

FAU Forschungen, Reihe B, Medizin, Naturwissenschaft, Technik 42

Daniel A. Kiefer

Elastodynamic quasi-guided waves
for transit-time ultrasonic flow metering



Daniel A. Kiefer

Elastodynamic quasi-guided waves for transit-time ultrasonic
flow metering

FAU Forschungen, Reihe B
Medizin, Naturwissenschaft, Technik
Band 42

Herausgeber der Reihe:
Wissenschaftlicher Beirat der FAU University Press

Daniel A. Kiefer

**Elastodynamic quasi-guided waves for
transit-time ultrasonic flow metering**

Erlangen
FAU University Press
2022

Bibliografische Information der Deutschen Nationalbibliothek:
Die Deutsche Nationalbibliothek verzeichnet diese Publikation in der Deutschen Nationalbibliografie; detaillierte bibliografische Daten sind im Internet über <http://dnb.d-nb.de> abrufbar.

Bitte zitieren als

Daniel A. Kiefer. 2022. *Elastodynamic quasi-guided waves for transit-time ultrasonic flow metering*. FAU Forschungen, Reihe B, Medizin, Naturwissenschaft, Technik Band 42. Erlangen: FAU University Press.

DOI: 10.25593/978-3-96147-550-6.

Erste Version: 28.05.2021

Zweite Version: 28.07.2021

Zur Begutachtung eingereicht: 26.10.2021

Endgültige Fassung: 18.05.2022

Das Werk, einschließlich seiner Teile, ist urheberrechtlich geschützt.
Die Rechte an allen Inhalten liegen bei ihren jeweiligen Autoren.
Sie sind nutzbar unter der Creative-Commons-Lizenz BY.

Der vollständige Inhalt des Buchs ist als PDF über den OPUS-Server der Friedrich-Alexander-Universität Erlangen-Nürnberg abrufbar:
<https://opus4.kobv.de/opus4-fau/home>

Verlag und Auslieferung:

FAU University Press, Universitätsstraße 4, 91054 Erlangen

Druck: docupoint GmbH

ISBN: 978-3-96147-549-0 (Druckausgabe)

eISBN: 978-3-96147-550-6 (Online-Ausgabe)

ISSN: 2198-8102

DOI: 10.25593/978-3-96147-550-6

**Elastodynamic quasi-guided waves
for transit-time ultrasonic flow
metering**

**Elastodynamische quasi-geführte
Wellen für die laufzeitbasierte
Ultraschall-Durchflussmessung**

Der Technischen Fakultät
der Friedrich-Alexander-Universität
Erlangen-Nürnberg

zur Erlangung des Doktorgrades Dr.-Ing.

vorgelegt von

Daniel A. Kiefer

geboren in Tumbaco Quito, Ecuador

Als Dissertation genehmigt
von der Technischen Fakultät
der Friedrich-Alexander-Universität Erlangen-Nürnberg

Tag der mündlichen Prüfung: 28.03.2022

Gutachter: Prof. Dr. techn. habil. Stefan J. Rupitsch
Prof. Dr.-Ing. habil. Paul Steinmann

*Schläft ein Lied in allen Dingen
die da träumen fort und fort,
und die Welt hebt an zu singen,
triffst du nur das Zauberwort.*

Joseph von Eichendorff

Preface – Vorwort

The material presented in this monograph is the result of my work as a research assistant at the *Lehrstuhl für Sensorik* (LSE), Friedrich-Alexander-Universität Erlangen-Nürnberg (FAU). Therein, my use of the pronoun “we” should be interpreted as stylistic as the work was written entirely by myself. Nonetheless, I must reckon having profited of much support and many helpful discussions during the development of the project. I desire to extend my thanks to all those who made this work possible in the following.

Zunächst geht ein großer Dank an Prof. Stefan J. Rupitsch, allzeit ein guter Mentor und Betreuer. Äußerst wertvoll und spannend waren für mich die häufigen und tiefgehenden Diskussionen über elastodynamische Wellenleiter mit Michael Ponschab. Des Weiteren war der stete Austausch mit den Kooperationspartnern von Diehl Metering – Dr. Andreas Benkert, Dr. Michael Mayle und Dr. Peter Ploß – sehr förderlich. Ferdinand Fischer, Michael Roas-Löffler, Bernd Meister sowie all den zuvor genannten danke ich für das Lektorieren meines Manuskripts, bzw. Teilen davon. Zudem möchte ich all meinen Kollegen des Lehrstuhls für die guten Diskussionen und die schöne gemeinsame Zeit danken. Sie sorgten so für ein stets gutes Arbeitsklima, welches ich sehr zu schätzen wusste. Insbesondere danke ich an dieser Stelle meinen langjährigen Bürokollegen Michael Ponschab, Michael Roas-Löffler und Manuel Weiß, mit welchen ich eine intensive, freundlich-kollegiale und aufbauende Atmosphäre genießen durfte.

Die experimentellen Arbeiten wären ohne dem Know-how und der Unterstützung von Ute Bollert, Hans Birkel, Hans-Michael Günther und Manfred Pelz in der Form nicht möglich gewesen. Den Partnern von Diehl Metering möchte ich für das Erheben von Messdaten an der Firmeneigenen Teststrecke danken. Des Weiteren hatte ich das Privileg viele begeisterte Studenten und Studentinnen im Rahmen ihrer Abschlussarbeit zu begleiten: L. Vogl, K. Schmid, D. Heilmeyer, J. Herterich, O. Umbeer, C. Ittner, H. Dai, S. Sivanesan und J. Freitag. Meine Arbeit profitierte in unterschiedlichster Form hiervon. Einige der dabei entstandenen Ergebnisse habe ich unter entsprechendem Verweis in vorliegender Arbeit verwendet. Ich habe auch all jenen zu danken, die hinter den Kulissen eine reibungslose Arbeit ermöglicht haben: Prof. Reinhard Lerch, Cornelia Salley-Sippel, Christine Peter und Simone Saalfrank.

Zu guter Letzt möchte ich mich bei all den lieben Menschen außerhalb des Lehrstuhls bedanken, die mich während dieser Zeit begleitet, unterstützt und ermutigt haben.

Paris, im Oktober 2021,

Daniel Nicker

Contents

Abstract	xi
Kurzfassung	xiii
1 Introduction to flow metering	1
1.1 Importance of flow metering and available devices	1
1.2 Ultrasonic transit-time devices	3
1.2.1 Classification of designs	4
1.2.2 Wave-path configurations	5
1.2.3 Normally vs. obliquely radiating transducers	7
1.2.4 Volumetric flow rate determination	7
1.2.5 Temperature compensation	9
1.2.6 Challenges and requirements for UFM water meters	10
1.3 Proposed design: Lamb wave-based flow metering	12
1.4 Goal and structure of this monograph	14
2 Elastodynamic field theory	17
2.1 Elastodynamic field in time-space domain	17
2.1.1 Fundamental equations of elastodynamics	17
2.1.2 Constitutive relations	19
2.1.3 Navier's equation: elastodynamic waves	21
2.1.4 Acoustics	22
2.1.5 Boundary and interface conditions	23
2.2 Elastodynamic field in frequency-wave vector domain	26
2.2.1 Fourier transforms	26
2.2.2 Governing equations in frequency-wave vector domain	27
2.2.3 Energy density	28
2.2.4 Power flux density: the elastodynamic Poynting vector	29
2.2.5 Equipartition of energy	29
2.2.6 Complex reciprocity relations	30
2.3 Homogeneous and inhomogeneous plane waves	31
2.3.1 Dispersion relations	33
2.3.2 Energy velocity	37
2.3.3 Group velocity	39
2.4 Concluding remarks	40
3 Guided and quasi-guided waves	43
3.1 Guided waves in plates	43
3.1.1 Waveguide problem formulation	44
3.1.2 Dispersion curves of an anisotropic plate	45

3.1.3	Classification of modes	47
3.1.4	Dispersion curves of an isotropic plate	50
3.1.5	Wave field of Lamb modes	52
3.1.6	Power flux considerations	53
3.1.7	Orthogonality relations between modes	55
3.1.8	Excitation of guided waves	56
3.1.9	Perturbation theory	59
3.2	Quasi-guided waves in fluid-coupled plates	60
3.2.1	Models for the fluid-coupled plate	60
3.2.2	QGW problem formulation	65
3.2.3	Polynomial form of the QGW problem through change of variable	69
3.2.4	Structure of the QGW problem	70
3.2.5	Classification of waves	72
3.2.6	Dispersion of quasi-guided waves	76
3.2.7	Wave field of trapped and leaky waves	79
3.2.8	Radiation	85
3.2.9	Immersed plate: double sided fluid coupling	89
3.2.10	Strongly fluid-loaded plate	91
4	Numerical Solution Methods	93
4.1	Solving waveguide problems	93
4.1.1	Root-finding of the characteristic equation	93
4.1.2	Eigenvalue problem discretization	96
4.2	Spectral collocation for waveguide problems	97
4.2.1	Chebyshev spectral collocation method	97
4.2.2	Discretization of the quasi-guided wave problem	98
4.2.3	Integration on Chebyshev-Gauß-Lobatto points	102
4.3	Polynomial eigenvalue problems	102
4.4	Elastodynamic Acoustic Toolbox (EDAT)	104
5	Experimental methods and verification	105
5.1	Transducers for waveguide excitation and sensing	105
5.1.1	Bonded piezoelectric ceramics	106
5.1.2	Comb array and comb transducers	108
5.2	Laser Doppler measurement of waveguide spectra	109
5.3	Schlieren photography	117
6	Modeling Lamb wave-based flow meters	121
6.1	Convection of ultrasound: ray tracing	121
6.2	Time-of-flight model of flow meters	123
6.2.1	Lamb wave-based flow meter	124
6.2.2	Piston type transducer-based flow meter	127
6.2.3	Comparison of flow meter setups and models	129

6.3	Incidence and reflection from the pipe wall	131
6.3.1	Excitation of a leaky Lamb wave by an incident acoustic beam	131
6.3.2	Nonspecular reflection from the pipe wall	135
7	Sensitivity and interference errors	141
7.1	Flow meter sensitivity to flow rate	141
7.2	Flow rate cross-sensitivities	141
7.3	Waveguide parameter cross-sensitivities	144
7.3.1	Thickness and frequency: Abrasion and manufacturing tolerances	144
7.3.2	Mechanical parameters: Material uncertainty and aging	145
7.3.3	Deposited layer: Scaling and dezincification	146
7.4	Temperature cross-sensitivity	150
7.4.1	Temperature dependence of the pipe material	151
7.4.2	Temperature dependence of the fluid wave speed	152
7.4.3	Overall differential effect of temperature	154
7.5	Flow meter sensitivity including temperature	156
8	Flow meter: model validation and measurements	159
8.1	Validation: experimental data of a prototype	159
8.1.1	LDV measurements	159
8.1.2	Ultrasonic pitch-catch measurements	161
8.2	Flow rate determination from the V-path	166
8.3	Temperature determination from direct path	169
8.4	A general inversion method: compensation of arbitrary effects	171
9	Conclusions and outlook	175
A	Appendix: Material data	179
	Bibliography	181
	References	181
	Publications	198
	List of supervised student theses	201
	Table of symbols	203

Abstract

Flow meters measure the amount of a fluid passing through a pipe per unit of time. Devices based on ultrasound are popular due to their robustness, low pressure loss and ease of installation. These strengths are best harnessed in a noninvasive setup like clamp-on meters, when the pipe is not perforated and the insonification of the pipe is performed from the outside. This leads to some unresolved difficulties: transmission loss through the pipe wall, critical transducer alignment, and excitation of guided waves inside the pipe wall. These waves travel along the pipe wall, exhibit intricate dispersive propagation behavior, and may interfere with the fluid-borne ultrasonic signal that is to be evaluated. For these reasons, guided waves are usually undesired. However, as they represent the generalized pipe wall resonances, the guided waves are difficult to avoid.

Subject of this dissertation is a noninvasive transit-time ultrasonic flow meter which explicitly excites leaky guided waves to resolve the aforementioned challenges. Leaky waves gradually transfer their energy into the fluid and efficiently insonify the interior of the pipe. A model of the flow meter is developed that accounts for the exact pipe wall mechanics. Thereby, all wave paths through the device are treated in a consistent manner and the effects of dispersion, wave convection and temperature are included. The resulting ultrasonic time-of-flight expression from transducer to transducer is simpler than the conventional expression obtained by considering an effective wave speed. The discrepancies are examined and explained in detail.

An extensive analysis of cross-sensitivities is performed using the model. It reveals that guided wave-based meters are significantly less affected by temperature. This is a result of the temperature-dependent radiation angle of leaky waves, which partly compensates temperature-induced changes in the fluid wave speed. Furthermore, the analysis exposes the device's robustness with regard to material and geometry uncertainties, aging as well as scaling inside the pipe.

The interaction between the pipe wall and the fluid is of major interest. It is analyzed by means of a fluid-coupled plate model, thereby accounting for the analytically exact fluid-structure interaction. Waves in this system are described by an intricate nonlinear eigenvalue problem. A robust solution technique is devised that allows to reliably obtain all eigensolutions. Trapped

and leaky waves are found and their complex physical behavior is discussed in detail.

Experiments substantiate the validity of the model. Dispersion curves of leaky guided waves in plates are acquired via laser Doppler vibrometry, while their radiation field is visualized with schlieren photographs. A flow meter prototype is tested under varying flow rate and temperature, whereby the upstream and downstream signals are recorded. The signal analysis reveals a very good agreement between the measured data and the developed theoretical transit-time model, in particular, it confirms the reduced cross-sensitivity to temperature of the device.

Kurzfassung

Durchflussmesser bestimmen die Menge eines Fluides welches pro Zeiteinheit durch ein Rohr fließt. Geräte basierend auf Ultraschall sind beliebt, da sich diese durch hohe Robustheit, geringen Druckverlust und leichte Installation auszeichnen. Diese Stärken werden bei nicht-invasiven Aufbauten wie Clamp-on Geräten ausgespielt, bei denen das Rohr verschlossen bleibt und die Beschallung von außen stattfindet. Hierbei treten jedoch einige ungelöste Schwierigkeiten auf: Transmissionsverluste durch die Rohrwand, kritische Ausrichtung der Wandler und Anregung von geführten Wellen in der Rohrwand. Diese Wellen breiten sich entlang der Rohrwand aus, weisen kompliziertes dispersives Ausbreitungsverhalten auf und können mit dem Nutzsignal interferieren. Aus diesen Gründen sind die geführten Wellen üblicherweise unerwünscht. Allerdings sind sie schwer zu vermeiden, da sie die verallgemeinerten Dickenresonanzen der Rohrwand darstellen.

Gegenstand dieser Dissertation ist ein nicht-invasives, laufzeitbasiertes Ultraschall-Durchflussmessgerät, welches explizit geführte abstrahlende Wellen anregt, um die genannten Schwierigkeiten zu überwinden. Diese Wellen geben ihre Energie graduell an das Fluid ab und beschallen effizient das Innere des Rohres. Das Durchflussmessgerät wird unter Betrachtung der exakten Mechanik der Rohrwand modelliert. Dabei werden alle akustischen Pfade durch das Gerät konsistent behandelt und die Effekte von Dispersion, Schallkonvektion und Temperatur berücksichtigt. Der resultierende Ausdruck für die Ultraschalllaufzeit zwischen den Wandlern ist einfacher als der konventionelle Ausdruck, der durch betrachten einer effektiven Schallgeschwindigkeit hervorgeht. Die Unterschiede werden untersucht und im Detail erklärt.

Eine ausführliche Analyse der Querempfindlichkeiten wird anhand des Modells durchgeführt. Sie offenbart, dass Durchflussmesser auf Basis geführter Wellen deutlich weniger temperaturabhängig sind. Dies ist ein Resultat des temperaturabhängigen Abstrahlwinkels der geführten Welle, welcher der Änderung der Schallgeschwindigkeit im Fluid entgegenwirkt. Des Weiteren quantifiziert die Analyse die Robustheit des Geräts hinsichtlich Unsicherheiten im Material und der Geometrie, Alterung sowie Kalkablagerungen.

Die Interaktion zwischen der Rohrwand und dem Fluid ist von zentralem Interesse. Dies wird anhand einer fluidbelasteten Platte modelliert, wobei die analytisch exakte Fluid-Struktur-Interaktion berücksichtigt wird. Wellen in

diesem System werden durch ein kompliziertes nichtlineares Eigenwertproblem beschrieben. Eine robuste Lösungsmethodik wird entwickelt welche es erlaubt, zuverlässig alle Eigenlösungen zu bestimmen. Ideal geführte sowie abstrahlende Wellen werden als Lösungen gefunden und deren komplexes physikalisches Verhalten wird im Detail diskutiert.

Experimente belegen die Gültigkeit des aufgestellten Modells. Dispersionskurven geführter abstrahlender Wellen in Platten werden mittels Laser-Doppler-Vibrometrie erfasst, während das abgestrahlte Feld mit Schlierenfotografien visualisiert wird. Ein Prototyp des Durchflussmessers wird unter variablem Durchfluss und Temperatur getestet, wobei die Ultraschallsignale flussauf- und flussabwärts aufgezeichnet werden. Die Signalanalyse offenbart eine sehr gute Übereinstimmung der Messdaten zum aufgestellten Laufzeitmodell, insbesondere bestätigt es die geringere Temperaturempfindlichkeit des Gerätes.

1 Introduction to flow metering

This monograph is a contribution to *transit-time ultrasonic flow metering (UFM)*. The research is performed in context of low-cost household water metering, but the presented concepts and ideas are equally applicable to any other UFM system. This chapter discusses the general relevance, challenges and requirements of flow metering. The need for flow metering and, in particular, water metering is addressed in Sec. 1.1. The basic concepts of ultrasonic flow meters and the corresponding classical design principles are introduced in Sec. 1.2. Lastly, in Sec. 1.3 and 1.4 we present and discuss the device that is proposed and studied in this project and explain the need for new modeling approaches.

1.1 Importance of flow metering and available devices

Flow meters measure the amount of fluid, i.e., liquid or gas, passing through a pipe per unit time [1–3]. Knowledge of the flow rate is essential for process monitoring and control as well as billing. For instance, it facilitates correct dosing in production processes of the pharmaceutical, chemical and food industry. The market share by end user is shown in Fig. 1.1a. The biggest field of application is custody transfer in the oil and gas industry (26 %) [4]. The purpose of billing and leak detection is also pursued in the water supply and wastewater industries (12 %) [4].

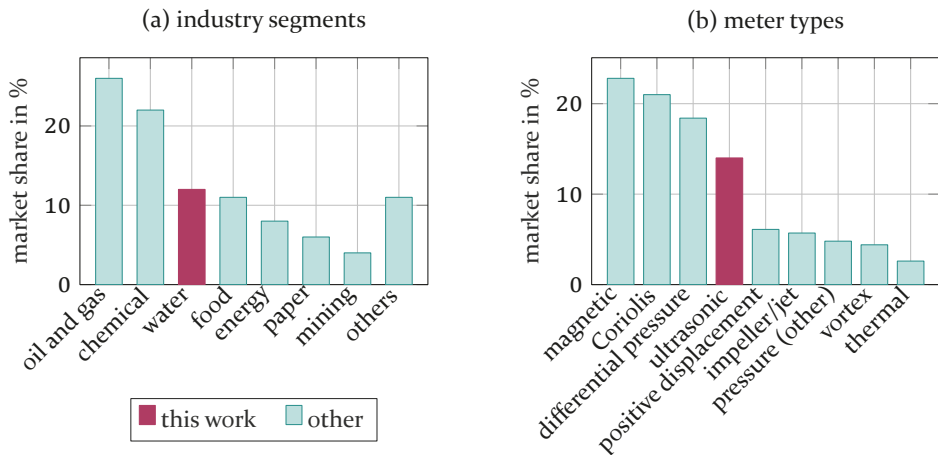


Figure 1.1: Global flow meter market share in 2015 according to [4].

The total flow meter market value in 2018 was estimated at \$7.3 billion [5]. With increasing degree of automation and sustainability demands of industrial processes, the market is expected to show a compound annual growth rate (CAGR) of about 6 % from 2019 to 2026 [5].

A large variety of flow meter types is available. An estimate of the allocation of the market by meter type is presented in Fig. 1.1b. Ultrasonic flow meters hold about 14 % market share [4] and are regarded as one of the “major players” that will profit of the prognosticated market growth. They can further be classified into transit-time, Doppler or hybrid meters, whereby transit-time ultrasonic flow meters are the most common, representing about 80 % of the ultrasonic devices [6].

The popularity of ultrasonic flow meters is attributed to (i) their relatively low cost, (ii) low pressure loss (possibly zero), (iii) ease of installation, (iv) high robustness and reliability, (v) universal applicability to different kind of fluids and gases, and (vi) good scalability to different pipe sizes and flow rates. Accordingly, UFM finds application in all industry segments.

Household water metering

Water is arguably more fundamental than any other resource - to life itself, supporting a huge array of ecosystem services, and to every economy and society.

Report of the United Nations Environment Programme [7]

The major argument for water metering is resource conservation. Billing per amount of consumption is an important incentive for usage reduction. Residential water use may thereby decrease by about 20 % [8]. This is the main justification for national policies mandating household water metering, e.g., in Germany. Another important benefit is that it enables leak detection in the supply infrastructure. Moreover, some argue that meter-based billing is fundamental for fairness reasons, as they do not want to subsidize those who have an above-average water usage.

Metering of household potable water consumption is widely practiced in most industrialized countries – an exception being the United Kingdom, with only about 50 % coverage [9]. Other countries, e.g., Germany, have almost complete coverage and are moving towards per-apartment accounting [10]. The degree of proliferation in developing countries varies from almost none to almost complete.

Singapore is probably the most advanced country in terms of water conservation and management, being one of the countries with highest decrease in per capita consumption in the past 40 years [7]. This was achieved through strong programs promoting water usage efficiency and efforts to reduce leakage (5 % unaccounted-for water, might be as high as 90 % in other cities). Consumption awareness was additionally increased by recent pilot projects using smart water meters that provide real-time data to the residents [11].

Despite the above mentioned relevance of efficient household water usage, it is important to keep in mind that other sectors are more relevant towards the overall goal. In Europe the water use by economic sector is: agriculture (58 %), energy (18 %), mining, manufacturing and construction (11 %), households (10 %) and service industries (3 %) [12]. Accordingly, the indirect water footprint of consumers is higher and should be given attention [7]. Having discussed the overall significance of water management, we will, hereinafter, focus on the technology of ultrasonic water metering.

Albeit their general popularity, UFM devices are not often employed for household water metering because of the high costs compared to the more common positive displacement and jet/impeller meters. Nonetheless, they exhibit evident advantages as water meters that distinguish them from the latter: (i) excellent robustness, (ii) no metering of airflow, (iii) correct sensing of reverse flow and (iv) low pressure drop. They achieve robustness by completely avoiding failure prone moving parts. This is of particular importance when extraneous particles (e.g., sand) are found in the pipe network. In many regions, loss of pressure in the pipes with consequent air rush is common. Conventional jet meters are very sensible to the fast flow of air, leading to wrong readings. In the same situation, back flow of water occurs which also leads to biased readings of the mechanical meters. By avoiding these difficulties, ultrasonic flow meters remain relevant in the water metering market.

1.2 Ultrasonic transit-time devices

The term UFM will, henceforth, implicitly refer to *transit-time* ultrasonic meters. Their fundamental working principle is simple: an ultrasonic wave traveling with the fluid flow is faster than against the flow [1, 2, 13]. This situation is sketched in Fig. 1.2. The phenomenon is called *wave convection*.

By measuring the upstream-downstream difference in transit time between two ultrasound emitters/receivers (i.e., transducers), the mean flow velocity of the fluid can be determined. The latter is then converted to a volumetric flow rate measured in m^3/s (or L/h), see Subsec. 1.2.4.

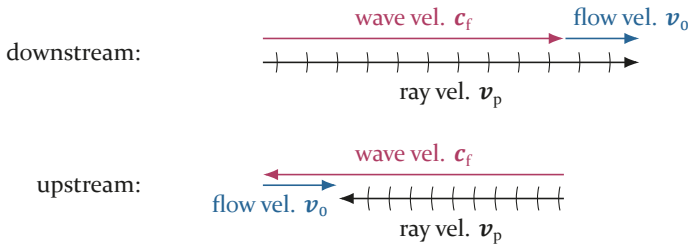


Figure 1.2: Physical phenomenon harnessed by transit-time UFM devices: convection of ultrasonic waves in a flowing medium. The phase fronts of the convected ray are also shown.

1.2.1 Classification of designs

The initially mentioned strengths of UFM are not equally met by every device. Instead, a wide variety of configurations exists that provide the desired properties. The main design traits are summarized in the following according to Ref. [1].

One can differentiate between two fundamental kind of configurations shown in Fig. 1.3:

in-line devices, which need to be inserted into the pipe system, and **clamp-on** meters that can be mounted on existing installations.

The latter are characterized by not possessing any special pipe section and can be mounted on existing installations without interrupting the fluid flow. Albeit the obvious advantages of clamp-on systems, two thirds of the market are served by in-line devices [14]. This can be attributed to the mounting difficulties as well as technical challenges of clamp-on meters [14, 15], which basically restricts their use to the high investment sectors (e.g., oil and gas).

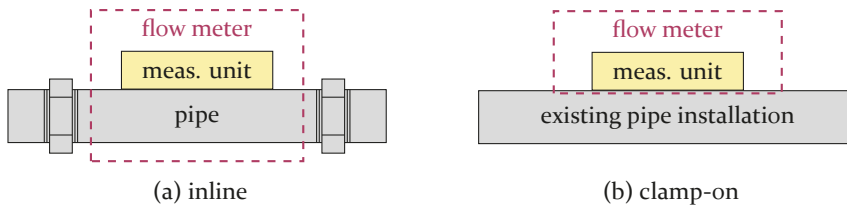


Figure 1.3: In-line and clamp-on configurations.

Clamp on systems are always *non-invasive* designs, while in-line variants could be either invasive or non-invasive as depicted in Fig. 1.4b. The pipe of

invasive systems is perforated, while for

non-invasive configurations it remains entirely sealed.

The former are technically simpler to realize and operate, as the ultrasonic transducers (T_1/T_2) are in direct contact with the fluid and, hence, independent of the pipe wall mechanics. However, non-invasive meters are regarded as superior, as they guarantee leak tightness and protect the fluid good against external contaminants.

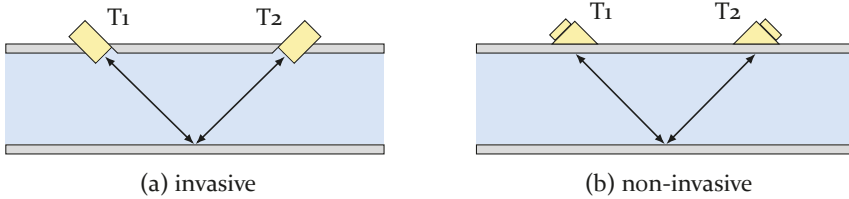


Figure 1.4: Invasive and non-invasive configurations. T_1/T_2 : transducers.

According to Fig. 1.5, a further important classification is into

intrusive setups that influence the fluid flow, and

non-intrusive ones, which leave the flow unaffected.

The former may cause swirls at the measurement point and thereby affect the flow profile v_0 . This is usually undesired, as it will lead to measurement errors if these complex fluid mechanical phenomena are not accounted for. Furthermore, the swirls lead to pressure loss in the pipe system.

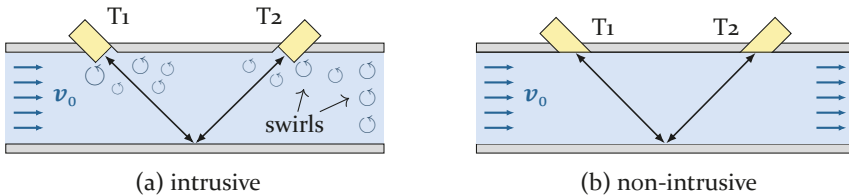


Figure 1.5: Intrusive and non-intrusive configurations (both invasive). v_0 : fluid flow velocity.

1.2.2 Wave-path configurations

Different ray paths between the sending and receiving elements can be exploited. Common setups are exemplarily sketched in Fig. 1.6 according to Ref. [1].

U-path systems (Fig. 1.6a) make use of acoustic mirrors to obtain a ray that is aligned with the fluid flow. Consequently, the upstream-downstream difference in transit time is maximized.

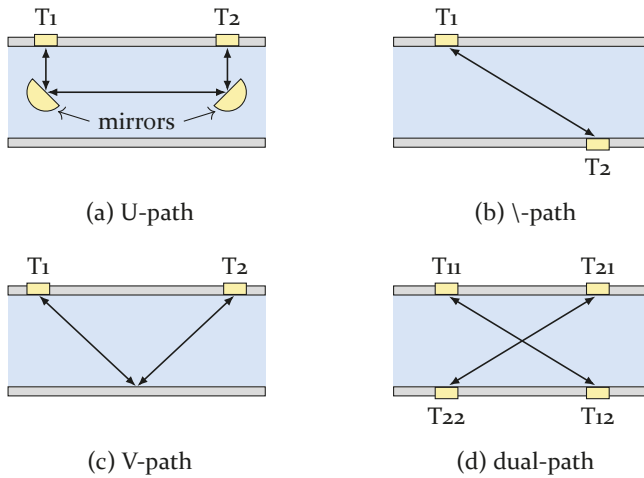


Figure 1.6: Common ultrasonic ray path configurations.

The mirrors can be avoided by installing an oblique ray path (Fig. 1.6b). This is not very convenient, as the transducers need to be mounted on opposite sides of the pipe. As a good alternative, a V-path (Fig. 1.6c) can be used by letting the beam reflect at the lower pipe wall. The larger axial propagation distance leads to a beneficial increase in the upstream-downstream differential time of flight. This idea can be continued by exploiting more reflections. However, at every reflection the ultrasonic signal suffers an inconvenient loss in amplitude.

Moreover, **multi-path** systems are also used (Fig. 1.6d) [1, 14, 16, 17]. An arbitrary number of paths could be installed, e.g., by mounting the transducers eccentrically on the pipe. The advantage of these devices is that they can (partly) acquire the flow profile and correctly account for it. Usually, an increased number of transducers is required to operate the ray paths, albeit just two phased array/matrix transducers are also feasible [14]. In any case, conventional multi-path systems lead to a massive increase in complexity of the electronics and are not suitable for low-cost meters.

Lastly, we remark that a ray propagating in transversal direction to the fluid flow could also be harnessed. Instead of changes in time of flight, this relies on the displacement of the beam in downstream direction as it is convected with the flow [2]. However, this form of operation is considered unstable [2] and is not commonly used in practice.

1.2.3 Normally vs. obliquely radiating transducers

Inspect again Fig. 1.5 (or 1.4), where an intrusive and a non-intrusive configuration is shown. They are different in a further aspect: while in Fig. 1.5b the transducer's active surface is aligned with the fluid flow, it is not in Fig. 1.5a. This is possible because the transducers in Fig. 1.5b insonify the fluid **obliquely** with respect to their own surface. On the other hand, transducers as in Fig. 1.5a radiate and receive ultrasound **normally** to their surface. The latter will be denoted as *piston-type* transducers hereon after.

A distinction according to the inclination of the transducer's active surface is not usually made in the literature. It will be shown in this monograph (see Chap. 6) that differences arise with regard to how their respective time of flight should be modeled. For this reason, we introduce this classification at this point.

1.2.4 Volumetric flow rate determination

The ultimate goal of flow metering is to determine the *volumetric flow rate* [1, 2], which represents the total fluid volume passing through a section of the pipe per unit time. It is defined as the integral of the flow velocity over the cross-sectional area of the pipe. For the rectangular cross-section seen in Fig. 1.7a, it is given by

$$Q \stackrel{\text{def}}{=} \int_0^d \int_0^b v_0(y, z) dy dz = bd\bar{v}_A, \quad (1.1)$$

where $v_0(y, z)$ is the flow velocity profile and $\bar{v}_A \stackrel{\text{def}}{=} \frac{1}{bd} \int_0^d \int_0^b v_0(y, z) dy dz$ is denoted as *average area velocity*.

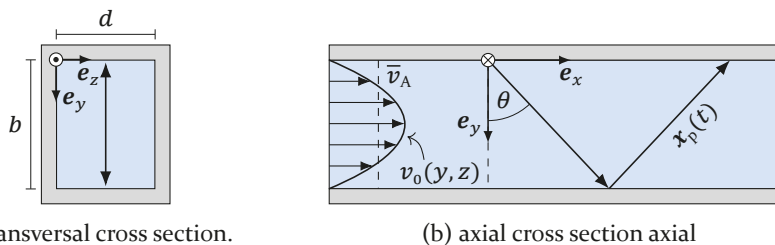


Figure 1.7: Schematic flow profile and a V-path ultrasonic ray through a rectangular pipe.

Neither the flow profile $v_0(y, z)$ nor the average area velocity \bar{v}_A are known in conventional UFM systems. Instead, the acquired upstream-downstream differential time of flight is proportional to the average \bar{v}_0 along the ray path $\mathbf{x}_p(t)$ sketched in Fig. 1.7b. This path is traced over time t as the wave packet propagates (for details refer to Sec. 6.1). The average over the ray path of length L is given by

$$\bar{v}_0 = \frac{1}{L} \int_0^L v_0(\mathbf{x}_p) dx_p = \frac{1}{b} \int_0^b v_0(x_p, y_p, z_p) dy_p, \quad (1.2)$$

where the latter equality holds because the flow velocity $v_0(y, z)$ is assumed to be independent of the axial coordinate x and the ray propagates in the x - y -plane. To handle the lack of information about \bar{v}_A in the ultrasonic signal, the *calibration factor* $K = \bar{v}_A/\bar{v}_0$ is conventionally introduced such that [1, 2]

$$Q = Kbd\bar{v}_0. \quad (1.3)$$

The calibration factor K depends on the *Reynolds number* Re , which is a dimensionless quantity characterizing the flow. For flow inside a pipe, it is defined as $Re = \frac{\bar{v}_0 D_H}{\nu_f}$ [1, 2], where ν_f is the kinematic viscosity of the fluid and D_H denotes the hydraulic diameter of the pipe. For a rectangular pipe of dimensions $b \times d$ and $b \approx d$, the latter is again defined as $D_H = \frac{2bd}{b+d}$. The Reynolds number essentially identifies the ratio between inertial and viscous force densities and in this way makes situations with different structural dimensions and flow velocities comparable [2]. Flow below the critical value of $Re = 2300$ is denoted as *laminar*, above $Re = 4000$ as *turbulent* and in between as *transitional*.

Any flow profile $v_0(y, z)$ always results in $K < 1$ [1]. In the laminar flow regime, K is a constant. For transitional flow it increases with the mean flow velocity \bar{v}_0 , tending to a value close to unity for turbulent flow [1, 3, 18]. With this, the flow rate Q is non-linearly dependent on \bar{v}_0 . In any case, once the calibration factor $K(\bar{v}_0)$ has been determined, it is possible to obtain Q from \bar{v}_0 using (1.3).

So far, the width of the ultrasonic beam has been neglected. In fact, the metering system does not only average along the infinitely thin ray path, but additionally over the beam's entire cross section. This corresponds to making the ray path – which is drawn in Fig. 1.7a as a thin line – wider. For a homogeneous insonification, when the beam width tends towards the pipe width d , the ray path average \bar{v}_0 tends towards the area average \bar{v}_A because the averaging is effectively performed on the whole cross section. This means that

a wide insonification of the pipe can lead to direct acquisition of the average area velocity \bar{v}_A [19, 20], as needed for UFM.

The above is a short and rather schematic delineation of the involved fluid dynamics. This intricate topic is outside the scope of this monograph. Instead, for description of ultrasonic wave propagation through the system, we will assume a steady and homogeneous “equivalent flow” profile, resulting in $v_0 = \bar{v}_0 = \bar{v}_A$ and $K = 1$. The factor K is kept in the equations for the sake of generality and later calibration.

1.2.5 Temperature compensation

There is one important practical difficulty in water metering with UFM: the sound speed of water $c_f(\mathcal{T})$ is highly dependent on the temperature \mathcal{T} . As a consequence, the upstream-downstream differential time of flight depends not only on the flow velocity \bar{v}_0 , but additionally on the temperature \mathcal{T} . It is crucial for conventional water meters to actively compensate this cross-sensitivity [2, 3].

A simple and common solution is to measure the temperature \mathcal{T} during operation and use a pre-determined look-up table to identify the effect on the meter’s sensitivity. However, this requires a temperature sensor inside the pipe. This is undesirable for non-invasive meters because the pipe needs to be perforated, the sensor disturbs the flow and additional components are required.

The conventional method for sensor-free temperature compensation consists in using the mean (or sum) of the upstream and downstream time of flights in addition to the difference of the two [1–3, 17]. The mean does not depend on the fluid flow and can directly be used to determine the wave speed $c_f(\mathcal{T})$. In a second step, the flow velocity (flow rate) is obtained from the differential time of flight. Overall, this leads to a wave speed-independent formulation. The method has, however, one caveat: the mean is an absolute time of flight, which in practice is biased by an unknown initial delay (due to the electronics and ultrasonic transit time through the transducers). This fact is a serious obstacle for practical implementation and is sometimes overcome by an additional calibration step.

1.2.6 Challenges and requirements for UFM water meters

All UFM devices have some common basic challenges, namely, (i) small time-of-flight differences, (ii) zero-flow error due to a non-reciprocity bias, (iii) non-linear dependence on the flow velocity, and (iv) dependency on the flow profile (e.g., asymmetric after a bent pipe section). Current electronics are able to precisely measure time differences, mostly resolving (i) and (ii). The read-out is classically done with analogue electronics that sense the zero-crossing of the signal. Microcontroller-based alternatives offering digital signal processing capabilities have only emerged recently for the low-power segment [21]. Furthermore, the calibration mentioned in Subsec. 1.2.4 is done to tackle (iii). With regard to (iv), the interior of the pipe is sometimes designed to “condition” the flow, that is, to homogenize it. Alternatively, it is also common to ensure that the flow meter is operated with a sufficiently long straight inlet.

Water meters for household applications compete in a diverse low-cost market segment. Ultrasonic meters are commonly in-line, invasive and possibly intrusive single-path designs, which represents the simplest setup. Unfortunately, some of the major potentials of ultrasonic systems are thereby not harnessed. Nonetheless, strong requirements are to be met by water meters: maintenance-free operation for many years in a mostly uncontrolled environment, where parameters like temperature, pressure, chemical properties of the fluid and particles in suspension may vary strongly. Therefore, robustness is a high priority and self-calibration is desired. The latter, however, may lead to difficulties at time of official verification. Furthermore, the devices are designed for low power consumption and may operate up to 16 years on a small form factor battery [22].

Lastly, non-invasive setups (e.g., clamp-on systems) suffer of some widely unresolved issues: (i) inefficient insonification due to transmission loss through the pipe wall, (ii) critical transducer alignment, and (iii) excitation of elastic *guided waves* that propagate along the pipe wall [14, 15]. The guided waves are also referred to as “structure-borne” ultrasound and are commonly undesired. This shall be discussed in more detail in the following.

Mechanics of the pipe wall

The traditional and widespread model to describe the insonification of the pipe’s interior with a non-invasive transducer is sketched in Fig. 1.8a [2, 3, 14, 15, 18, 23]. A single plane harmonic wave is expected to propagate through each of the three domains representing the transducer (wedge), the pipe wall

and the fluid. The ray is refracted at every interface according to Snell's law of matching traces, finally insonifying the fluid at certain angle.

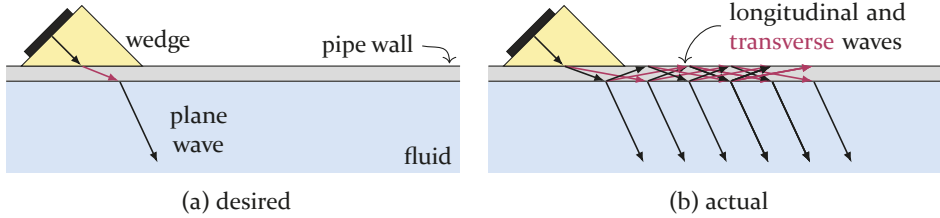


Figure 1.8: Non-invasive insonification of a pipe: comparison of desired and actual ray pattern.

In this classical model, a transverse wave is usually desired in the pipe wall because its impedance is better matched to the fluid. Even so, poor transmission factors from transmitter to receiver of typically 0.2% to 2% are obtained [3]. Some clamp-on systems are designed as *wide beam* flow meters [2, 3] by choosing the wedge angle so that the wave refracts into the pipe wall at 90° out of the surface normal, i.e., along the pipe. In this way, a wave is obtained that insonifies the interior over a large axial distance.

Unfortunately, these ideas are somewhat inaccurate and certainly incomplete to describe the pipe wall mechanics. A more accurate sketch of the actually arising situation is shown in Fig. 1.8b (still over-simplified in the wedge region). At every interface, the coupled longitudinal and transverse plane waves reflect and refract with mode conversion occurring thereby. In this way, a complex interference pattern builds up in the pipe wall, giving rise to the previously mentioned (*quasi*)-guided waves. These are intrinsic to the problem and unavoidable for thin-walled pipes.

Interference occurs whenever the ultrasonic pulse of duration D and longitudinal wave speed c_1 overlaps with its reflection, i.e., when the pipe wall thickness $h < c_1 D / 2$ (for the signal components propagating in direction normal to the pipe wall). For a metallic pipe ($c_1 \approx 6 \text{ mm}/\mu\text{s}$) at 1 MHz (assuming a short pulse with $D \approx 3 \mu\text{s}$), this is typically the case whenever the wall is thinner than $\approx 10 \text{ mm}$, which is practically always fulfilled. To some extent, it may be possible to mainly excite a transverse wave propagating at an angle out of the pipe wall normal. In this case, the range of validity of the plane wave model extends down to smaller wall thicknesses. However, this will always represent a rather strong simplification. Guided waves are a more appropriate concept to model the actual mechanics, in particular, when thin-walled pipes are of interest.

The guided elastic waves result in some undesired complications: (i) multiple waves propagating at different velocities exist, (ii) they propagate dispersively, i.e., their propagation velocity is frequency-dependent, and (iii) some of them reach the receiver without coupling out into the fluid. When these waves superpose with the desired V-path signal at the receiver, the time-of-flight read-out will be biased. To date, this is regarded the major difficulty of clamp-on devices [14]. For this reason, the guided waves are commonly understood as an undesired by-product, which needs to be suppressed or filtered out [1, 14, 15, 24, 25]. Given the fact that these waves represent the (practically) unavoidable thickness resonances of the thin pipe wall, this is an awkward position to take.

1.3 Proposed design: Lamb wave-based flow metering

A different standpoint is taken in this monograph: reckoning that the guided waves fully describe the wave motions of the pipe wall, they are regarded as the *foundation to precisely model* the flow meter. In particular, this approach extends the classical model, as it is also valid for operation at the (generalized) pipe wall thickness resonances, i.e., the guided waves. With such a model at hand, quasi-guided waves that radiate into the fluid – so-called *leaky Lamb waves* – are deliberately excited to operate the flow meter. Although rather uncommon, this idea is not new [26, 27] and Lamb wave-based devices already exist on the market [28, 29]. Nonetheless, the literature mostly focuses on classical modeling approaches and comparably few publications explicitly study Lamb wave-based meters [30, 31].

Subject of this dissertation is an *in-line, non-invasive* and *non-intrusive* transit-time ultrasonic flow meter in V-path configuration. The setup is sketched in Fig. 1.9. It consists of a specifically designed pipe section and a clamp-on measurement unit, which encloses the transducers and electronics. The sending transducer (S) generates a leaky Lamb wave, which propagates in axial direction inside the pipe wall and thereby radiates into the pipe's interior at an angle. The radiated ultrasonic wave propagates in a V-path through the flowing medium. After coupling back into the upper pipe wall, it is sensed by the receiver (R).

Albeit this meter cannot be mounted on existing pipelines, it inherits all remaining advantages of clamp-on devices:

- **Modular design:** the metering unit can easily and safely be exchanged without interrupting the fluid flow (once the pipe section has been mounted).

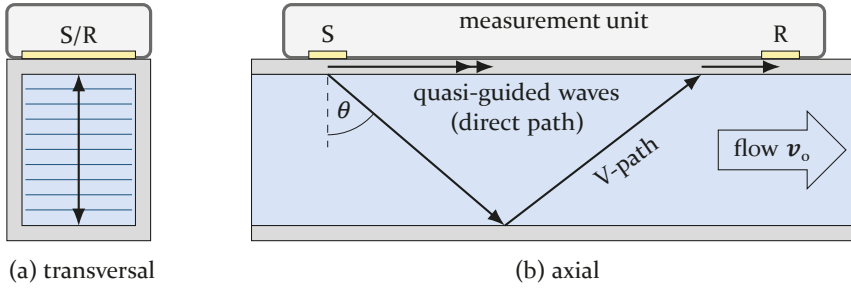


Figure 1.9: Setup of the proposed Lamb wave-based flow meter.

- The pipe interior is free of any components, avoiding obstruction and swirling of the flow. Furthermore, this counteracts the deposition of extraneous matter inside the pipe.
- With no perforations in the pipe, the system is guaranteed to be leak tight. Moreover, the fluid is protected against contamination from the exterior.

At the same time, the common difficulties of clamp-on systems associated with insufficient knowledge about the pipe material and geometry are avoided [14, 15].

Instead, it is even possible to design the pipe section according to the requirements of the metering task. We use a rectangular pipe that is designed to (i) condition the fluid flow [32], (ii) insonify the entire pipe cross section [19, 20], and (iii) support (quasi)-guided waves with desired properties. The excited quasi-guided wave easily extends over an entire face of the rectangular pipe. As shown in Fig. 1.9a, this leads to a wide insonification of the pipe's interior. Although difficult to achieve in practice, a homogeneous insonification would be desirable. As discussed in Sec. 1.2.4, in this case the acquired time of flight would be proportional to the desired average area velocity \bar{v}_A , which in turn is directly proportional to the volumetric flow rate Q . Under such ideal conditions, the calibration factor K would then be avoided entirely.

Further advantages will be obtained when operating the flow meter with leaky guided waves. The insonification is expected to be more efficient because the guided waves are directly associated with the transmission maxima of the pipe wall [33]. Moreover, lowly attenuated guided waves spread over a wide range along the pipe, reason for which the axial positioning of the transducers is uncritical. At the same time, the radiated wave is plane in good approximation, facilitating the use of simple ray models. However, the axial spreading of the

beam counteracts the good transmission rate, leading to lower signal-to-noise ratio at the receiver.

In addition to the V -path, *direct path* signals are obtained at the receiver. These are due to guided and quasi-guided waves that have not fully coupled out into the fluid. The direct path waves carry additional information about the system's state, e.g., temperature or scaling of the pipe. Within the (quasi)-guided wave framework, it is possible to leverage this additional information to compensate cross-sensitivities, as will be demonstrated in Chap. 7 and Chap. 8.

As discussed previously, multi-path flow metering can increase the measurement accuracy. With the proposed setup, it is feasible to radiate into the pipe at different angles by simply changing the excitation frequency and/or electrically re-configuring the transducers [34]. In this way, multiple ultrasonic paths through the fluid can be harnessed without installing more transducers.

1.4 Goal and structure of this monograph

The goals of this monograph are to

- Develop a model for non-invasive flow meters that accounts for the **exact pipe wall mechanics**.
- Include the effect of **wave convection** in the model.
- Account for **temperature** in the model and assess its impact.
- Perform an extensive analysis of **cross-sensitivities** (pipe wall thickness and material, frequency, scaling, dezincification, temperature).
- Provide a systematic quantitative assessment of all possible **operating points** (frequency, waveguide modes, pipe material and geometry, etc.).

Thereby, all possible wave paths through the device are modeled precisely in a consistent manner. The interaction of guided elastic waves with the fluid is studied in detail. The arising mathematical problem is uncommon and poses special challenges. Stable numerical solution methods are devised and implemented.

The monograph is structured as follows: CHAP. 2 is an introduction to general elastodynamic field theory and plane harmonic waves in solids and serves as ramp-up. CHAP. 3 is divided into two sections: 3.1 is a review on guided waves in elastic plates in vacuum, while 3.2 extends this idea to plates that are in contact with a fluid, denoted as quasi-guided waves. Although this

notion is not entirely new, the latter section presents mostly new findings developed in this project. CHAP. 4 presents both the traditional as well as the newly developed numerical solution methods for quasi-guided waves. CHAP. 5 introduces the experimental methods, principles and setups used to conduct the work. Not only electro-mechanical transducers are used, but also optical measurement methods. CHAP. 6 first introduces the well-known theory of ultrasonic convection and then proceeds to develop a time-of-flight model for Lamb wave-based flow meters. It also discusses the relationship to the conventional model that relies on effective wave speeds. Moreover, the incidence and reflection of ultrasound from the pipe wall is discussed here. CHAP. 7 deals with cross-sensitivities, especially the influence of temperature on the flow meter. CHAP. 8 validates the model experimentally with the help of a prototype and presents measurement results. Lastly, concluding remarks are given in CHAP. 9.

2 Elastodynamic field theory

Before turning attention to elastodynamic guided and quasi-guided waves, the general elastodynamic field theory shall be reviewed for the sake of reference and as a starting point. The presentation in this chapter is mainly based on an excellent book by Langenberg, Marklein and Mayer [35] (English translation [36]). Some adaptations and extensions are made to fit the following-up topic of guided waves. We first introduce the theory in the physical time-space domain in Sec. 2.1, before transitioning to the frequency-wave vector domain in Sec. 2.2. Finally, plane harmonic bulk waves in unbounded media are discussed in Sec. 2.3, which is a good preface for guided waves coming up in the following chapter.

An explanation of the mathematical notation and a list of symbols is provided in the *table of symbols* in the appendix.

2.1 Elastodynamic field in time-space domain

The elastodynamic field is described by the fundamental equations of elastodynamics in combination with constitutive relations. These two can be combined to obtain the Navier's equation. Each of the equations and some special cases thereof are discussed in the following.

2.1.1 Fundamental equations of elastodynamics

Consider the motion of a deformable, solid and continuous medium. The linearized evolution of the field in space \mathbf{x} and time t is described by the fundamental equations of linear *elastodynamics* given by [35]:

$$\partial_t \mathbf{j}(\mathbf{x}, t) = \nabla \cdot \mathbf{T}(\mathbf{x}, t) + \mathbf{f}(\mathbf{x}, t) \quad (2.1a)$$

$$\partial_t \mathbf{S}(\mathbf{x}, t) = \frac{1}{2} [\nabla \mathbf{v}(\mathbf{x}, t) + (\nabla \mathbf{v}(\mathbf{x}, t))^{\top}] + \mathbf{h}(\mathbf{x}, t), \quad (2.1b)$$

where ∇ is the *Nabla* operator and \bullet^{\top} means transposition. The involved quantities are denoted as momentum \mathbf{j} , stress \mathbf{T} , force density \mathbf{f} , strain \mathbf{S} , particle velocity \mathbf{v} and prescribed strain rate \mathbf{h} . The above equations are called the *Newton-Cauchy equation of motion* and the *strain rate equation*, respectively. In the following, we discuss each of the equations as well as the involved field quantities in more detail.

Let's first discuss (2.1b). We are interested in describing the deformation of the body, i.e., the change of particle displacement with respect to their “natural” position exhibiting no restoring forces [37]. In particular, rigid body motions are not of interest. The linearized differential change in particle displacement $\mathbf{u}(\mathbf{x}, t)$ is given by the displacement gradient $\nabla\mathbf{u}(\mathbf{x}, t)$. The gradient's symmetric part describes deformations of the body, while the antisymmetric part can be shown to account for rigid body rotations [35]. The 2nd order linear *strain tensor* $\mathbf{S}(\mathbf{x}, t)$ is, thus, defined as the symmetric part of the displacement gradient [35, 37], i.e.,

$$\mathbf{S}(\mathbf{x}, t) = \frac{1}{2} [\nabla\mathbf{u}(\mathbf{x}, t) + (\nabla\mathbf{u}(\mathbf{x}, t))^{\top}]. \quad (2.2)$$

Introducing the particle velocity vector as

$$\mathbf{v}(\mathbf{x}, t) = \partial_t\mathbf{u}(\mathbf{x}, t), \quad (2.3)$$

differentiating (2.2) with respect to time and adding the source term $\mathbf{h}(\mathbf{x}, t)$ results in the strain rate equation given in (2.1b). The injected or prescribed strain rate $\mathbf{h}(\mathbf{x}, t)$ is a symmetric 2nd order tensor. We remark that, as rigid body motions have been eliminated from (2.1b), this equation is directly connected to the stored elastic energy and the restoring internal forces.

The evolution of the restoring internal forces is described by (2.1a) as sketched in the following according to Langenberg et al. [35]. Imagine an arbitrary portion of the solid body with volume V and enclosing surface S as depicted in Fig. 2.1. The prescribed volume force density $\mathbf{f}(\mathbf{x}, t)$ acts on every differential volume element dV inside the volume and represents a source of the elastodynamic field. Moreover, the force area density $\mathbf{t}(\mathbf{x}, t)$, called the *traction*, acts on every differential, outward directed area segment $dS = \mathbf{e}_n dS$.

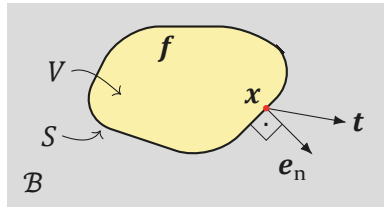


Figure 2.1: Cut out volume V of the body B .

A linear relationship between the traction $\mathbf{t}(\mathbf{x}, t)$ and the surface normal $\mathbf{e}_n(\mathbf{x}, t)$ is postulated by Cauchy in the form

$$\mathbf{t}(\mathbf{x}, t) = \mathbf{e}_n(\mathbf{x}, t) \cdot \mathbf{T}(\mathbf{x}, t), \quad (2.4)$$

where the proportionality is given by the 2nd order *stress tensor* $\mathbf{T}(\mathbf{x}, t)$. The change in total *linear momentum* $\mathbf{j}(\mathbf{x}, t)$ inside V can now be balanced with the overall forces acting inside V and on its surface S . In linearized form (assuming V constant), this may be stated as

$$\partial_t \iiint_V \mathbf{j}(\mathbf{x}, t) dV = \iint_S \mathbf{t}(\mathbf{x}, t) dS + \iiint_V \mathbf{f}(\mathbf{x}, t) dV. \quad (2.5)$$

Using (2.4) and applying Gauss' integral theorem results in

$$\iiint_V \partial_t \mathbf{j}(\mathbf{x}, t) dV = \iiint_V \nabla \cdot \mathbf{T}(\mathbf{x}, t) + \mathbf{f}(\mathbf{x}, t) dV. \quad (2.6)$$

Because the cut out volume V is arbitrary, the above balance of linear momentum is equivalent to the differential form given in (2.1a). Moreover, we note that restricting the stress tensor to be symmetric additionally enforces the conservation of angular momentum [35, 37]. In ferroelectric and ferromagnetic materials, a torque density may act as a source of the elastodynamic field, in which case the stress tensor is no longer symmetric [35]. This case will not be considered in this monograph and the stress tensor is always assumed to be symmetric.

2.1.2 Constitutive relations

Having discussed the two fundamental equations of elastodynamics given in (2.1a) and (2.1b), it is now necessary to relate the two. Notice that the equations make statements on different field quantities. The *constitutive equations* or *material laws* relate the two equations by introducing a dependence between the variables. The plentitude of possibilities for modeling the material will always be subject to the two criteria "close to reality" and "simplicity" [35]. In this monograph, we will restrict to linear, time-invariant, homogeneous and locally reacting models. Moreover, we will mostly be concerned with instantaneously reacting materials, which implies a nondissipative behavior. Such a material can be modeled by [35]

$$\mathbf{j}(\mathbf{x}, t) = \rho \mathbf{v}(\mathbf{x}, t), \quad (2.7a)$$

$$\mathbf{S}(\mathbf{x}, t) = \mathbf{s} : \mathbf{T}(\mathbf{x}, t), \quad (2.7b)$$

where ρ is called the *mass density* and \mathbf{s} the 4th order *compliance tensor*. We chose to model a scalar mass density as is conventional for ultrasonic NDT. This is not a requirement, however, and a tensorial mass density is sometimes

used in geophysics [35]. Inserting the constitutive relations (2.7) into the fundamental equations (2.1), we obtain

$$\rho \partial_t \mathbf{v}(\mathbf{x}, t) = \nabla \cdot \mathbf{T}(\mathbf{x}, t) + \mathbf{f}(\mathbf{x}, t), \quad (2.8a)$$

$$\mathbf{s} : \partial_t \mathbf{T}(\mathbf{x}, t) = \frac{1}{2} [\nabla \mathbf{v}(\mathbf{x}, t) + (\nabla \mathbf{v}(\mathbf{x}, t))^T] + \mathbf{h}(\mathbf{x}, t), \quad (2.8b)$$

which reveals that the linear elastodynamic field of the considered materials can be described by a system of coupled first order PDEs in terms of \mathbf{v} and \mathbf{T} – the so-called *state variables* [38].

Instead of (2.7b), we will usually prefer the inverted equation

$$\mathbf{T}(\mathbf{x}, t) = \mathbf{c} : \mathbf{S}(\mathbf{x}, t), \quad (2.9)$$

with the 4th order *stiffness tensor* \mathbf{c} defined through [35]

$$\mathbf{c} : \mathbf{s} = \mathbf{s} : \mathbf{c} = \frac{1}{2} \underbrace{[(\mathbf{II})^{1342} + (\mathbf{II})^{1324}]}, \quad (2.10)$$

symmetric part operator

where $\mathbf{I} = \delta_{ij} \mathbf{e}_i \mathbf{e}_j$ denotes the 2nd order identity tensor, δ_{ij} is the Kronecker delta, and the superindices denote the permutation of the tensors. The above linear relation between strain and stress is referred to as *Hook's law* or *Cauchy-Hook's law*. As \mathbf{S} and \mathbf{T} are symmetric, the stiffness tensor with coefficients c_{ijkl} is required to exhibit the symmetries [35, 37]

$$c_{ijkl} = c_{ijlk} = c_{jikl} = c_{jilk}. \quad (2.11)$$

Moreover, conservative systems are modeled with hermitian operators and the real-valued stiffness tensor of nondissipative media additionally fulfills the symmetry [35]

$$c_{ijkl} = c_{klij}. \quad (2.12)$$

The above symmetries reduce the number of independent coefficients of the tensor from 81 to 21 [35, 37].

An important specialization of the strain-stress relation in (2.9) is attained for *isotropic* materials. Their stiffness tensor is defined through rotational

invariance [37], which means that the material behavior does not depend on the orientation in space. The isotropic stiffness tensor can be written as [35]

$$\mathbf{c} \stackrel{\text{def}}{=} \lambda_L \overset{\text{I times trace of}}{\mathbf{\hat{I}}} + \mu_L \overset{\text{2 times symmetric part of}}{(\mathbf{II}^{1342} + \mathbf{II}^{1324})} \quad (2.13)$$

$$= (\lambda_L \delta_{ij} \delta_{kl} + \mu_L \delta_{il} \delta_{jk} + \mu_L \delta_{ik} \delta_{jl}) \mathbf{e}_i \mathbf{e}_j \mathbf{e}_k \mathbf{e}_l, \quad (2.14)$$

where the scalars λ_L and μ_L are called the Lamé parameters. We see that the number of independent coefficients are reduced to only 2. The over-braces describe the operations of \mathbf{c} when it acts on a 2nd order tensor (e.g., strain) through double contraction.

This work has a strong focus on isotropic materials and will mostly be using the above representation. Instead of the Lamé parameters, equivalent models might use the [37]

- Young's modulus $E = \mu_L(3\lambda_L + 2\mu_L)/(\lambda_L + \mu_L)$ and
- Poisson's ratio $\nu = \lambda_L/2(\lambda_L + \mu_L)$

or the [37]

- longitudinal wave speed $c_l = \sqrt{(\lambda_L + 2\mu_L)/\rho}$ and
- transverse wave speed $c_t = \sqrt{\mu_L/\rho}$.

The latter wave speeds correspond to special modal solutions of the homogeneous isotropic medium and we will recall their derivation in Subsec. 2.3.1.

2.1.3 Navier's equation: elastodynamic waves

The goal in the following is to express the governing equations of elastodynamics with only one equation and only one unknown field quantity. Using (2.10) and exploiting the symmetry $c_{ijkl} = c_{ijlk}$ of \mathbf{c} , (2.8b) reduces to

$$\partial_t \mathbf{T}(\mathbf{x}, t) = \mathbf{c} : \nabla \mathbf{v}(\mathbf{x}, t) + \mathbf{c} : \mathbf{h}(\mathbf{x}, t). \quad (2.15)$$

Inserting into the time derivative of (2.8a) yields [35]

$$\nabla \cdot [\mathbf{c} : \nabla \mathbf{v}(\mathbf{x}, t)] - \rho \partial_t^2 \mathbf{v}(\mathbf{x}, t) = -\partial_t \mathbf{f}(\mathbf{x}, t) - \nabla \cdot [\mathbf{c} : \mathbf{h}(\mathbf{x}, t)], \quad (2.16)$$

which is called *Navier's equation* or *elastodynamic wave equation* [35]. It is a second order PDE in time and space in terms of the single unknown \mathbf{v} . For

our purposes, we can assume that the prescribed strain rate is zero, i.e., $\mathbf{h} \equiv \mathbf{0}$. We may then write the wave equation in terms of the displacement [35] as

$$\nabla \cdot [\mathbf{c} : \nabla \mathbf{u}(\mathbf{x}, t)] - \rho \partial_t^2 \mathbf{u}(\mathbf{x}, t) = -\mathbf{f}(\mathbf{x}, t). \quad (2.17)$$

For isotropic and homogeneous materials, we replace the stiffness tensor given in (2.13) into (2.17) and pull the material parameters out of the derivatives to obtain

$$\mu_L \nabla \cdot \nabla \mathbf{u}(\mathbf{x}, t) + (\lambda_L + \mu_L) \nabla \nabla \cdot \mathbf{u}(\mathbf{x}, t) - \rho \partial_t^2 \mathbf{u}(\mathbf{x}, t) = -\mathbf{f}(\mathbf{x}, t). \quad (2.18)$$

The above equation can also be represented in the form [35]

$$(\lambda_L + 2\mu_L) \nabla \nabla \cdot \mathbf{u}(\mathbf{x}, t) - \mu_L \nabla \times \nabla \times \mathbf{u}(\mathbf{x}, t) - \rho \partial_t^2 \mathbf{u}(\mathbf{x}, t) = -\mathbf{f}(\mathbf{x}, t). \quad (2.19)$$

Herein, the first term is responsible for longitudinal waves (irrotational field), while the second term accounts for transverse waves (solenoidal field) [35].

2.1.4 Acoustics

UFM with leaky guided waves relies on the interaction of elastodynamic waves with a fluid and the propagation of acoustic waves inside the fluid. Acoustics is a special (degenerate) case of elastodynamics. It can be obtained from the elastodynamic fundamental equations by replacing in (2.1) [35]

1. the stress tensor \mathbf{T} with the *hydrostatic stress* state $-p\mathbf{I}$, where p is called the *acoustic pressure*, and
2. the strain \mathbf{S} and prescribed strain rate \mathbf{h} with their corresponding traces: $S \stackrel{\text{def}}{=} \text{tr} \mathbf{S}$ and $h \stackrel{\text{def}}{=} \text{tr} \mathbf{h}$, which are called *dilatation* and *prescribed dilatation rate*, respectively.

Using the constitutive relations

$$\mathbf{j}(\mathbf{x}, t) = \rho \mathbf{v}(\mathbf{x}, t), \quad (2.20a)$$

$$S(\mathbf{x}, t) = -\kappa p(\mathbf{x}, t) \quad (2.20b)$$

for linear, homogeneous, nondissipative acoustic materials with *adiabatic compressibility* κ , the fundamental equations of acoustics can be stated as [35]

$$\rho \partial_t \mathbf{v}(\mathbf{x}, t) = -\nabla p(\mathbf{x}, t) + \mathbf{f}(\mathbf{x}, t) \quad (2.21a)$$

$$-\kappa \partial_t p(\mathbf{x}, t) = \nabla \cdot \mathbf{v}(\mathbf{x}, t) + h(\mathbf{x}, t). \quad (2.21b)$$

Similar to the elastodynamic case, these are coupled first order PDEs. The number of degrees of freedom, however, have been reduced substantially because the deviatoric stress $\mathbf{T} - \frac{1}{3}\mathbf{I} \text{tr} \mathbf{T}$ is set to zero a-priori, allowing to use the scalar acoustic pressure p instead of the symmetric stress tensor. While the elastodynamic case has 9 state-space variables (3 for \mathbf{v} + 6 for symmetric \mathbf{T}), the acoustic equations has only 4 (3 for \mathbf{v} + 1 for p).

By taking the divergence of (2.21a) and inserting into the time derivative of (2.21b), we obtain the wave equation for pressure acoustics [13, 35, 39]:

$$\nabla \cdot \nabla p(\mathbf{x}, t) - \frac{1}{c_f^2} \partial_t^2 p(\mathbf{x}, t) = \nabla \cdot \mathbf{f}(\mathbf{x}, t) + \rho \partial_t h(\mathbf{x}, t), \quad (2.22)$$

with the speed of sound c_f defined as

$$c_f \stackrel{\text{def}}{=} \frac{1}{\sqrt{\kappa \rho}}. \quad (2.23)$$

Lastly, by inspecting the rotation of (2.21a), we see that in regions without forcing, i.e., $\mathbf{f} = \mathbf{0}$, the causal acoustic velocity field is free of rotations. This is sometimes referred to as the *compatibility condition* [35]. As a consequence, only longitudinal waves propagate in fluid media (see Sec. 2.3).

2.1.5 Boundary and interface conditions

Without the need for constitutive relations, the fundamental equations of elastodynamics make statements on the field's behavior across the boundary S_i of different materials with normal vector \mathbf{e}_n . This means that we have a discontinuity of the material parameters on the surface S_i . The situation is sketched in Fig. 2.2.

In the following sections, we cite the conditions for several different cases as derived in Langenberg et al. [35]. Thereby, we omit the explicit dependence on \mathbf{x} and t for the sake of conciseness. The boundary and interface conditions are

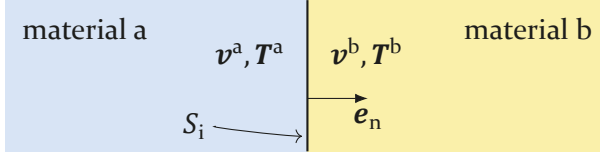


Figure 2.2: Interfacing region of two materials.

needed to describe waves confined within a structure, which will be studied in Chap. 3.

Interface conditions

In order to obtain the interface conditions, the equations (2.1) can be balanced over a cut-out volume that includes a portion of both materials. After applying Gauß's integral theorem and the mean value theorem, one obtains the continuity conditions [35] as

$$\mathbf{e}_n \cdot \mathbf{T}^a - \mathbf{e}_n \cdot \mathbf{T}^b = -\mathbf{t}, \quad (2.24a)$$

$$\frac{1}{2} [\mathbf{e}_n \mathbf{v}^a + \mathbf{v}^a \mathbf{e}_n - \mathbf{e}_n \mathbf{v}^b - \mathbf{v}^b \mathbf{e}_n] = -\mathbf{g}, \quad (2.24b)$$

where the superindices “a” and “b” denote the fields in each of the materials and the equations hold on the surface of the discontinuity. The right sides represent surface source densities on S_i . If no sources are present, the equations can be simplified [35] to

$$\mathbf{e}_n \cdot \mathbf{T}^a - \mathbf{e}_n \cdot \mathbf{T}^b = \mathbf{0}, \quad (2.25a)$$

$$\mathbf{v}^a - \mathbf{v}^b = \mathbf{0}, \quad (2.25b)$$

i.e., the normal traction and the particle velocity must be continuous across the interface. For causal fields, (2.25b) can also be expressed in terms of the particle displacement [35] as

$$\mathbf{u}^a - \mathbf{u}^b = \mathbf{0}. \quad (2.26)$$

Boundary conditions

A special case of interface conditions is obtained when one of the materials does not support an elastodynamic field, i.e., when it is infinitely compliant

or infinitely dense. These cases are referred to as *perfectly soft* and *perfectly rigid* boundary conditions [35]. The former imposes

$$\mathbf{e}_n \cdot \mathbf{T} = \mathbf{0}, \quad (2.27a)$$

$$\frac{1}{2} [\mathbf{e}_n \mathbf{v} + \mathbf{v} \mathbf{e}_n] = -\mathbf{g}, \quad (2.27b)$$

while the second results in the conditions

$$\mathbf{e}_n \cdot \mathbf{T} = -\mathbf{t}, \quad (2.28a)$$

$$\mathbf{v} = \mathbf{0}. \quad (2.28b)$$

In contrast to the interface conditions, the boundary conditions are powerless conditions, meaning that the power flux through the boundary S_i vanishes. They are important because they are necessary to describe closed finite domains. Finally, we remark that the sources in (2.27b) and (2.28a) are not allowed to be zero, as this would immediately imply that the field is zero everywhere [35].

Interface between solid and fluid media

We will be interested in the boundary between solid and fluid media. The sourceless interface equations in (2.25) then reduce to [35]

$$\mathbf{e}_n \cdot \mathbf{T}^a + p^b \mathbf{e}_n = \mathbf{0}, \quad (2.29a)$$

$$\mathbf{e}_n \cdot \mathbf{u}^a - \mathbf{e}_n \cdot \mathbf{u}^b = \mathbf{0}, \quad (2.29b)$$

where we have rewritten the second equation in terms of displacements. The change in sign for p^b in (2.29a) is because the hydrostatic stress state in the fluid results in the stress $\mathbf{T}^b = -p^b \mathbf{I}$. It should be remarked that the traction $\mathbf{e}_n \cdot \mathbf{T}^a$ is not generally normal to the surface S_i . Condition (2.29a) is, however, demanding that this must be the case at the boundary to a fluid domain. Additionally, instead of demanding the continuity of the displacement vectors, (2.29b) requires only the normal component to be continuous across the solid-fluid boundary.

2.2 Elastodynamic field in frequency-wave vector domain

The elastodynamic field has so far been introduced and discussed in the physical \mathbf{x} - t -domain. In the following, we will transition to the easier to deal with ω - \mathbf{k} -domain, where $\omega \in \mathbb{R}$ and $\mathbf{k} \in \mathbb{C}^3$ denote the angular frequency and the wave vector, respectively.

2.2.1 Fourier transforms

The relations $\omega \leftrightarrow t$ and $\mathbf{k} \leftrightarrow \mathbf{x}$ are given by Fourier transforms. It is convenient to use a different sign convention in the exponent of the temporal Fourier transform than for the spatial Fourier transform [35]. Using $i = \sqrt{-1}$, we define the *temporal Fourier transform* of $u(\mathbf{x}, t)$ and its inverse as

$$u(\mathbf{x}, \omega) = \mathcal{F}_t u(\mathbf{x}, t) \stackrel{\text{def}}{=} \int_{-\infty}^{\infty} u(\mathbf{x}, t) e^{i\omega t} dt, \quad (2.30)$$

$$u(\mathbf{x}, t) = \mathcal{F}_t^{-1} u(\mathbf{x}, \omega) = \frac{1}{2\pi} \int_{-\infty}^{\infty} u(\mathbf{x}, \omega) e^{-i\omega t} d\omega, \quad (2.31)$$

respectively. On the other hand, our *spatial Fourier transform* and its inverse shall be given by

$$u(\mathbf{k}, t) = \mathcal{F}_x u(\mathbf{x}, t) \stackrel{\text{def}}{=} \iiint_{-\infty}^{\infty} u(\mathbf{x}, t) e^{-i\mathbf{k}\cdot\mathbf{x}} d^3\mathbf{x}, \quad (2.32)$$

$$u(\mathbf{x}, t) = \mathcal{F}_x^{-1} u(\mathbf{k}, t) = \frac{1}{(2\pi)^3} \iiint_{-\infty}^{\infty} u(\mathbf{k}, t) e^{i\mathbf{k}\cdot\mathbf{x}} d^3\mathbf{k}, \quad (2.33)$$

where $d^3\mathbf{x} = dx dy dz$ and $d^3\mathbf{k} = dk_x dk_y dk_z$. The integrals (2.30) to (2.33) do not necessarily exist for all functions u . Nonetheless, in most cases of interest, they do exist in a distributional sense, for details refer to [35]. Vectorial quantities are transformed component-wise.

It is possible to concatenate the temporal and spatial transforms. This leads to the representation

$$u(\mathbf{x}, t) = \mathcal{F}_t^{-1} \mathcal{F}_x^{-1} u(\mathbf{k}, \omega) = \frac{1}{(2\pi)^4} \int_{t=-\infty}^{\infty} \iiint_{\mathbf{k}=-\infty}^{\infty} u(\mathbf{k}, \omega) e^{i\mathbf{k}\cdot\mathbf{x}} e^{-i\omega t} d^3\mathbf{k} d\omega \quad (2.34)$$

of the physical domain. In the above space-time Fourier synthesis, the function $u(\mathbf{k}, \omega)$ is called a *plane wave spectrum*. The different choice of signs in the Fourier transforms guarantees that the kernel $e^{i\mathbf{k}\cdot\mathbf{x}} e^{-i\omega t}$ represents a *forward*

propagating plane wave (see Sec. 2.3), i.e., the field is represented as a weighted superposition of such waves.

2.2.2 Governing equations in frequency-wave vector domain

The transition to the ω - \mathbf{k} -domain is achieved by considering a spectral plane wave representation of the particle displacement vector, i.e.,

$$\mathbf{u}(\mathbf{x}, t) = \mathbf{u}(\mathbf{k}, \omega) e^{i(\mathbf{k} \cdot \mathbf{x} - \omega t)}, \quad (2.35)$$

and an analogous ansatz for all other field quantities. Note that the *displacement spectrum* $\mathbf{u}(\mathbf{k}, \omega)$ is a complex-valued function. It is implicitly assumed that we are only interested in the real part of (2.35).

Inserting this kind of ansatz into any of the elastodynamic equations and eliminating the harmonic factor is equivalent to performing a Fourier transform in time and space of the equations, as described in the last section. Proceeding as mentioned, we obtain the

- velocity spectrum from (2.3)

$$\mathbf{v}(\mathbf{k}, \omega) = -i\omega \mathbf{u}(\mathbf{k}, \omega) \quad (2.36)$$

- strain spectrum from (2.2)

$$\mathbf{S}(\mathbf{k}, \omega) = \frac{i}{2} [\mathbf{k}\mathbf{u}(\mathbf{k}, \omega) + \mathbf{u}(\mathbf{k}, \omega)\mathbf{k}] \quad (2.37)$$

- stress spectrum form (2.9) (given that $c_{ijkl} = c_{ijlk}$)

$$\mathbf{T}(\mathbf{k}, \omega) = \frac{i}{2} \mathbf{c} : [\mathbf{k}\mathbf{u}(\mathbf{k}, \omega) + \mathbf{u}(\mathbf{k}, \omega)\mathbf{k}] \quad (2.38)$$

$$= i\mathbf{c} : \mathbf{k}\mathbf{u}(\mathbf{k}, \omega) = i\mathbf{c} : \mathbf{u}(\mathbf{k}, \omega)\mathbf{k}. \quad (2.39)$$

Moreover, transforming the equation of motion given in (2.17) into the ω - \mathbf{k} -domain results in [35]

$$\mathbf{k} \cdot \mathbf{c} : \mathbf{k}\mathbf{u}(\mathbf{k}, \omega) - \rho\omega^2 \mathbf{u}(\mathbf{k}, \omega) = \mathbf{f}(\mathbf{k}, \omega). \quad (2.40)$$

For isotropic media, the corresponding equation of motion according to (2.18) reads

$$\mu_L \mathbf{k} \cdot \mathbf{k} \mathbf{u}(\mathbf{k}, \omega) + (\lambda_L + \mu_L) \mathbf{k} \mathbf{k} \cdot \mathbf{u}(\mathbf{k}, \omega) - \rho \omega^2 \mathbf{u}(\mathbf{k}, \omega) = \mathbf{f}(\mathbf{k}, \omega). \quad (2.41)$$

2.2.3 Energy density

The *kinetic energy density* and the *elastic energy density* are defined as [35]

$$\mathcal{K}(\mathbf{x}, t) = \frac{1}{2} \rho \mathbf{v}(\mathbf{x}, t) \cdot \mathbf{v}(\mathbf{x}, t), \quad (2.42a)$$

$$\mathcal{E}(\mathbf{x}, t) = \frac{1}{2} \mathbf{S}(\mathbf{x}, t) : \mathbf{c} : \mathbf{S}(\mathbf{x}, t), \quad (2.42b)$$

respectively. The transition to the ω - \mathbf{k} -domain involves a peculiarity explained in the following.

Let's consider the plane wave ansatz from (2.35) for \mathbf{v} and \mathbf{S} , allowing $\mathbf{k} = \Re \mathbf{k} + i \Im \mathbf{k}$ but $\omega \in \mathbb{R}$. As the energy densities are quadratic forms, we need to form the real part of the complex ansatz (2.35) before inserting into (2.42). This leads to a time-harmonic term at 2ω and one at -2ω , as well as two constant terms [35]. When averaging in time over one period, the harmonic terms vanish. The *average* [40] kinetic and elastic energy densities are then given by

$$\overline{\mathcal{K}}(\mathbf{x}, \mathbf{k}, \omega) = \frac{\rho}{4} \mathbf{v}(\mathbf{k}, \omega) \cdot \mathbf{v}^*(\mathbf{k}, \omega) e^{-2\Im \mathbf{k} \cdot \mathbf{x}}, \quad (2.43a)$$

$$\overline{\mathcal{E}}(\mathbf{x}, \mathbf{k}, \omega) = \frac{1}{4} \mathbf{S}(\mathbf{k}, \omega) : \mathbf{c} : \mathbf{S}^*(\mathbf{k}, \omega) e^{-2\Im \mathbf{k} \cdot \mathbf{x}}, \quad (2.43b)$$

respectively. Notice that the spatial dependence does not vanish for $\Im \mathbf{k} \neq \mathbf{0}$. Moreover, purely in terms of the displacements, the energy densities read

$$\overline{\mathcal{K}}(\mathbf{x}, \mathbf{k}, \omega) = \frac{\rho \omega^2}{4} \mathbf{u}(\mathbf{k}, \omega) \cdot \mathbf{u}^*(\mathbf{k}, \omega) e^{-2\Im \mathbf{k} \cdot \mathbf{x}}, \quad (2.44a)$$

$$\overline{\mathcal{E}}(\mathbf{x}, \mathbf{k}, \omega) = \frac{1}{4} \mathbf{u}^*(\mathbf{k}, \omega) \mathbf{k}^* : \mathbf{c} : \mathbf{k} \mathbf{u}(\mathbf{k}, \omega) e^{-2\Im \mathbf{k} \cdot \mathbf{x}}, \quad (2.44b)$$

where the symmetries of \mathbf{c} have been exploited.

Lastly, the *average total stored energy density* is given by

$$\overline{\mathcal{H}} = \overline{\mathcal{K}} + \overline{\mathcal{E}}. \quad (2.45)$$

2.2.4 Power flux density: the elastodynamic Poynting vector

The *power flux density* is given by the elastodynamic Poynting vector defined as [35, 37]

$$\mathbf{p}(\mathbf{x}, t) = -\mathbf{v}(\mathbf{x}, t) \cdot \mathbf{T}(\mathbf{x}, t). \quad (2.46)$$

The transition to the ω - \mathbf{k} -domain is performed as for the energy densities in Subsec. 2.2.3. The resulting *average power flux density* is then given by

$$\bar{\mathbf{p}}(\mathbf{x}, \mathbf{k}, \omega) = -\frac{1}{4} [\mathbf{v}(\mathbf{k}, \omega) \cdot \mathbf{T}^*(\mathbf{k}, \omega) + \mathbf{v}^*(\mathbf{k}, \omega) \cdot \mathbf{T}(\mathbf{k}, \omega)] e^{-2\Im \mathbf{k} \cdot \mathbf{x}} \quad (2.47)$$

$$= -\frac{1}{2} \Re \{ \mathbf{v}(\mathbf{k}, \omega) \cdot \mathbf{T}^*(\mathbf{k}, \omega) \} e^{-2\Im \mathbf{k} \cdot \mathbf{x}} \quad (2.48)$$

In terms of displacements, the above can also be written as

$$\bar{\mathbf{p}}(\mathbf{x}, \mathbf{k}, \omega) = \frac{\omega}{2} \Re \{ \mathbf{u}(\mathbf{k}, \omega) \cdot \mathbf{c} : \mathbf{k}^* \mathbf{u}^*(\mathbf{k}, \omega) \} e^{-2\Im \mathbf{k} \cdot \mathbf{x}} \quad (2.49)$$

$$= \frac{\omega}{2} \Re \{ \mathbf{c} : \mathbf{k}^* \mathbf{u}^*(\mathbf{k}, \omega) \mathbf{u}(\mathbf{k}, \omega) \} e^{-2\Im \mathbf{k} \cdot \mathbf{x}}. \quad (2.50)$$

$$(2.51)$$

2.2.5 Equipartition of energy

It can be shown that for unforced motion in nondissipative media with real-valued wave vectors $\mathbf{k} = \mathbf{k}^*$ (so-called homogeneous waves), the average kinetic energy density $\bar{\mathcal{K}}$ is equal to the average elastic energy density $\bar{\mathcal{E}}$ [35][37, pp. 221]. This property is known as *equipartition of energy*. It can be used to avoid the rather complicated computation of the elastic energy density given in (2.43b). Contraction of the homogeneous equation of motion (2.40) from the left with $\mathbf{u}^*(\mathbf{k}, \omega)$ yields

$$\underbrace{\mathbf{u}^*(\mathbf{k}, \omega) \mathbf{k} : \mathbf{c} : \mathbf{k} \mathbf{u}(\mathbf{k}, \omega)}_{4\bar{\mathcal{E}}} - \underbrace{\rho \omega^2 \mathbf{u}^*(\mathbf{k}, \omega) \cdot \mathbf{u}(\mathbf{k}, \omega)}_{4\bar{\mathcal{K}}} = 0, \quad (2.52)$$

which immediately provides the desired result $\bar{\mathcal{E}} = \bar{\mathcal{K}}$. Under the mentioned restrictions, the total energy density $\bar{\mathcal{H}}$ simplifies to

$$\bar{\mathcal{H}}_{\text{lossless}} = 2\bar{\mathcal{K}} = \frac{1}{2} \rho \omega^2 \mathbf{u}^*(\mathbf{k}, \omega) \cdot \mathbf{u}(\mathbf{k}, \omega) = 2\bar{\mathcal{E}}. \quad (2.53)$$

2.2.6 Complex reciprocity relations

A pair $(\mathbf{v}(\mathbf{x}, t), \mathbf{T}(\mathbf{x}, t))$ solving the elastodynamic fundamental equations (2.8) is called an *elastodynamic state* [38]. Several different relations between one elastodynamic state $(\mathbf{v}_1, \mathbf{T}_1)$ and a second one, which we denote $(\mathbf{v}_2, \mathbf{T}_2)$, can be derived and are called *reciprocity relations* [41]. The situation is illustrated in Fig. 2.3. These relations are important to derive orthogonality relations between waveguide modes, see Subsec. 3.1.7. Moreover, given that one elastodynamic state is known, these relations can be used to obtain estimates of the unknown state without explicitly solving the elastodynamic equations again (see Subsec. 3.1.9).

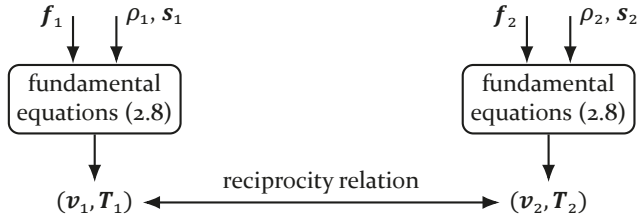


Figure 2.3: Sketch of reciprocity relations.

The *complex elastodynamic reciprocity relation* is valid for time-harmonic fields, i.e., of the form $\mathbf{v}(\mathbf{x}, t) = \mathbf{v}(\mathbf{x}) e^{-i\omega t}$, etc. The derivation according to Auld [41] is as follows: (i) write (2.8) for $(\mathbf{v}_1, \mathbf{T}_1)$ and multiply the equations with $(\mathbf{v}_2^* \cdot)$ and $(\mathbf{T}_2^* \cdot)$, respectively; (ii) obtain a second similar system of equations by exchanging the indices and the complex conjugation; and, finally, (iii) sum all four equations. Under the condition that ρ and \mathbf{s} are real and $s_{ijkl} = s_{klij}$, i.e., for nondissipative media, the result can be reduced to^{1,2}

$$\nabla \cdot (-\mathbf{v}_2^* \cdot \mathbf{T}_1 - \mathbf{v}_1 \cdot \mathbf{T}_2^*) = -\partial_t (\rho \mathbf{v}_2^* \cdot \mathbf{v}_1 + \mathbf{T}_2^* : \mathbf{s} : \mathbf{T}_1) + \mathbf{v}_2^* \cdot \mathbf{f}_1 + \mathbf{v}_1 \cdot \mathbf{f}_2^*. \quad (2.54)$$

Note that, in general, the above two states may be of different frequencies. More general reciprocity relations, e.g., for dissipative media, can also be formulated [41].

¹ Here, we assume that the prescribed strain rate $\mathbf{h} = \mathbf{0}$. Excitation with volume force densities \mathbf{f} are retained for perturbation analysis.

² We have made use of the fact that if \mathbf{A} is a symmetric 2nd order tensor, then $\mathbf{A} : \frac{1}{2}(\mathbf{B} + \mathbf{B}^\top) = \mathbf{A} : \mathbf{B}$. Moreover, $\nabla \cdot (\mathbf{v} \cdot \mathbf{T}) = \mathbf{v} \cdot \nabla \cdot \mathbf{T} + \mathbf{T} : \nabla \mathbf{v}$.

2.3 Homogeneous and inhomogeneous plane waves

We turn to analyze the *unforced motion* of an *unbounded* elastic medium, i.e., we set $\mathbf{f} = \mathbf{0}$ in (2.40). In Sec. 2.2, we already discussed the governing equations for solutions of the form

$$\mathbf{u}(\mathbf{x}, t) = \mathbf{u}(\mathbf{k}, \omega) e^{i(\mathbf{k} \cdot \mathbf{x} - \omega t)} \quad (2.55a)$$

$$= \mathbf{u}(\mathbf{k}, \omega) e^{-\Im \mathbf{k} \cdot \mathbf{x}} e^{i(\Re \mathbf{k} \cdot \mathbf{x} - \omega t)}, \quad (2.55b)$$

which, for a single fixed \mathbf{k} and ω , are called *plane harmonic bulk waves* [35]. Above $\mathbf{k} = k \mathbf{e}_k = \Re \mathbf{k} + i \Im \mathbf{k}$ denotes the complex wave vector with magnitude $k = \sqrt{\mathbf{k} \cdot \mathbf{k}^*}$ and complex unit directional vector \mathbf{e}_k . The vector's real part $\Re \mathbf{k} = \Re k \mathbf{e}_p$ is called the *propagation vector*. From (2.55b), we see that the field amplitude varies exponentially along the vector $\Im \mathbf{k} = \Im k \mathbf{e}_a$, reason for which it is termed the *attenuation vector*. In contrast to \mathbf{e}_k , the unit directional vectors \mathbf{e}_p and \mathbf{e}_a are real-valued.

Important properties of plane waves are due to their *phase* φ , which refers to the argument

$$\varphi(\mathbf{x}, t) \stackrel{\text{def}}{=} \Re \mathbf{k} \cdot \mathbf{x} - \omega t \quad (2.56)$$

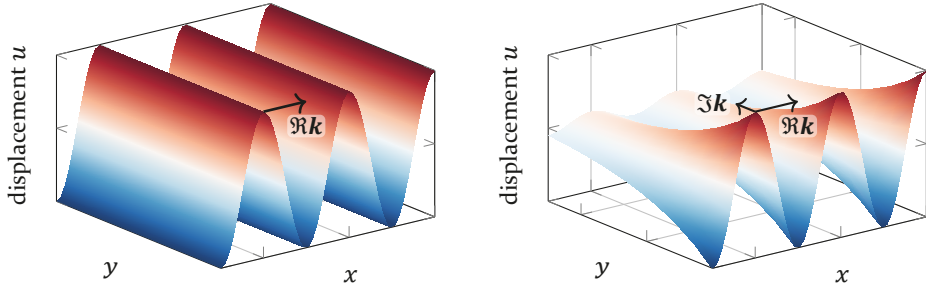
of the complex exponential in (2.55b). Its level sets are all points \mathbf{x}_p with the same phase and these sets are called *phase fronts* [35]. The vectors \mathbf{e}_t that are tangential to the phase front are characterized by a stationary phase φ along \mathbf{e}_t and, hence, the derivative in direction \mathbf{e}_t fulfills

$$\nabla \varphi \cdot \mathbf{e}_t = \Re \mathbf{k} \cdot \mathbf{e}_t \stackrel{!}{=} 0. \quad (2.57)$$

From the above result, we conclude that the tangential vectors are orthogonal to the propagation vector $\Re \mathbf{k}$ everywhere. Therefore, the phase fronts are planes orthogonal to $\Re \mathbf{k}$ spanned by the two linearly independent solutions \mathbf{e}_{t1} and \mathbf{e}_{t2} . This is the reason why solutions proportional to $e^{i\mathbf{k} \cdot \mathbf{x}}$ are called *plane waves*.

Two simplified examples of plane waves are visualized in Fig. 2.4, where all quantities have been normalized. The examples are in two-dimensional space $\mathbf{x} = [x, y]^T$ and the displacement $\mathbf{u}(\mathbf{k}, \omega)$ has been reduced to the scalar $u(\mathbf{k}, \omega) = 1$. The phase fronts of the 2D plane waves reduce to lines with $\mathbf{e}_t = \mathbf{e}_y$.

Depending on the relation between the propagation vector $\Re \mathbf{k}$ and the attenuation vector $\Im \mathbf{k}$, two kind of plane waves can be distinguished [35, 42]:



(a) homogeneous plane wave: attenuation vector vanishes.

(b) inhomogeneous plane wave: attenuation along the phase fronts.

Figure 2.4: Visualization of plane waves with scalar displacement u in the two-dimensional x - y -space. The wave fields are shown at $t = 0$ in a nondissipative medium.

Homogeneous plane waves: When the propagation vector $\Re\mathbf{k}$ and the attenuation vector $\Im\mathbf{k}$ are parallel, i.e., $\mathbf{e}_p = \mathbf{e}_a$, the plane waves are said to be homogeneous. The attenuation $\Im k$ of the wave is then solely due to dissipation of energy in the material [35]. In nondissipative materials, we have $\Im k = 0$, $\mathbf{k} = \Re\mathbf{k}$ and $\mathbf{e}_k = \mathbf{e}_p$. The latter case is shown in Fig. 2.4a.

Inhomogeneous plane waves: In this case, the propagation vector $\Re\mathbf{k}$ and the attenuation vector $\Im\mathbf{k}$ are not parallel. $\Im\mathbf{k}$ may then be decomposed into a component along the propagation direction \mathbf{e}_p and an orthogonal component. While the first component is due to dissipation of energy, the second is not. As will be shown, in nondissipative materials $\Im\mathbf{k}$ is always orthogonal to $\Re\mathbf{k}$ – this is the case displayed in Fig. 2.4b.

The phase fronts of harmonic plane waves move with time, as the following analysis shows [13]. Any point \mathbf{x}_p on a given phase front remains on this phase front by tracing a path $\mathbf{x}_p(t)$ determined by the invariance of the phase with respect to time, i.e.,

$$\frac{d}{dt}\varphi(\mathbf{x}_p(t), t) = \Re\mathbf{k} \cdot \frac{d\mathbf{x}_p(t)}{dt} - \omega \stackrel{!}{=} 0. \quad (2.58)$$

As the phase fronts are infinite planes, they can only move perpendicularly, i.e., in direction of $\Re\mathbf{k} = \Re k \mathbf{e}_p$. This component of the velocity vector $\frac{d\mathbf{x}_p}{dt}$ is given by

$$c_p \stackrel{\text{def}}{=} \mathbf{e}_p \cdot \frac{d\mathbf{x}_p(t)}{dt} = \frac{\omega}{\Re k}, \quad (2.59)$$

which is called the *phase velocity* [35]. Additionally, it makes sense to define the *phase velocity vector* [35] to be directed in the same direction as the propagation vector $\Re \mathbf{k}$, i.e.,

$$\mathbf{c}_p \stackrel{\text{def}}{=} c_p \mathbf{e}_p = \frac{\omega}{\Re \mathbf{k}} \mathbf{e}_p. \quad (2.60)$$

It should be remarked that plane waves are physically not realizable because of their infinite extend and energy. They are, nonetheless, interesting because they can be used to represent physical solution according to (2.34).

2.3.1 Dispersion relations

The discussed properties of harmonic plane waves are solely a consequence of the ansatz (2.55) and independent of the underlying physics. The elastodynamic field equations are consulted next to find out more about plane waves.

In (2.55), we have postulated elastodynamic solutions with two parameters, namely ω and \mathbf{k} . Not all combinations thereof form valid elastodynamic solutions. The dependence between ω and \mathbf{k} is described by the so-called *dispersion relations* [35, 37, 38]. They are obtained by inspecting the homogeneous equation of motion (2.40), which reads

$$[\mathbf{k} \cdot \mathbf{c} \cdot \mathbf{k} - \rho \omega^2] \cdot \mathbf{u}(\mathbf{k}, \omega) = \mathbf{0}. \quad (2.61)$$

For the given ρ - \mathbf{c} -material, we need to find the values \mathbf{k} , ω and \mathbf{u} that fulfill the above equation and, thus, arise as physical solutions. We factorize $\mathbf{u} = u(\mathbf{k}, \omega) \mathbf{e}_u(\mathbf{k}, \omega)$ in the above equation and divide the resulting equation by the arbitrary spectral amplitude u as well as the mass density ρ to obtain

$$\left[\frac{1}{\rho} \mathbf{k} \cdot \mathbf{c} \cdot \mathbf{k} - \omega^2 \mathbf{I} \right] \cdot \mathbf{e}_u(\mathbf{k}, \omega) = \mathbf{0}. \quad (2.62)$$

The above equation is called the *Kelvin-Christoffel equation* [35, 37]. As we are not interested in the trivial solution $\mathbf{e}_u = \mathbf{0}$, we need to find the values \mathbf{k} and ω for which the *wave tensor* [35]

$$\mathbf{W}(\mathbf{k}, \omega) = \frac{1}{\rho} \mathbf{k} \cdot \mathbf{c} \cdot \mathbf{k} - \omega^2 \mathbf{I} \quad (2.63)$$

becomes singular, i.e., we have to find the eigenvalues $\omega^2(\mathbf{k})$ of the second order *Kelvin-Christoffel tensor* [35, 37]

$$\mathbf{D} = \frac{1}{\rho} \mathbf{k} \cdot \mathbf{c} \cdot \mathbf{k}. \quad (2.64)$$

Instead of prescribing \mathbf{k} , it would be possible to prescribe \mathbf{e}_k and ω and solve for k . Even a third option is to prescribe \mathbf{e}_k and solve for the eigenvalues $c^2 \stackrel{\text{def}}{=} (\omega/k)^2$ determined by

$$\left[\frac{1}{\rho} \mathbf{e}_k \cdot \mathbf{c} \cdot \mathbf{e}_k - c^2 \mathbf{I} \right] \cdot \mathbf{e}_u(\mathbf{k}, \omega) = \mathbf{0}. \quad (2.65)$$

The latter form has the advantage that c is frequency-independent given that \mathbf{c} and ρ are independent of frequency, i.e., in nondissipative materials [35]. Note that in the case of homogeneous plane waves (real \mathbf{e}_k), c is the phase velocity – not for inhomogeneous waves, however.

In addition to the eigenvalues, also the eigenvectors \mathbf{e}_u can be obtained from (2.62) or (2.65). These unit directional vectors are called *polarization vectors* [35] and describe the direction of particle motion for each of the plane wave solutions. They might be complex, in which case they also specify a relative phase.

The solutions of the above eigenvalue problems (EVPs) are the modes of the unbound solid medium. As such, they form a complete orthogonal basis capable of expanding any arbitrary wave field with a plane wave *spectrum* [35] – this works even in bounded domains and is the starting point for several methods for computing guided wave propagation (see Subsec. 4.1.1). So far, we have only sketched the solution procedure. In order to find explicit solutions, the specific structure of the stiffness tensor \mathbf{c} needs to be considered.

Plane waves in anisotropic nondissipative media

In nondissipative media, the stiffness tensor \mathbf{c} and the mass density ρ are real-valued and independent of frequency. As a consequence, the Kelvin-Christoffel tensor in (2.65) and, hence, its eigenvalues c are independent of frequency [35]. This property is referred to as *nondispersive* wave propagation and is equivalent to demanding $\mathbf{k}(\omega)$ to be a linear relation. Otherwise, the wave propagation is said to be *dispersive* [35, 37, 38]. We remark that only for unbounded nondissipative media, one obtains nondispersive wave propagation. Waves confined within a structure are in general dispersive even if the medium is nondissipative, as we will see in Chap. 3. The latter

might be called *geometric dispersion* to distinguish it from dispersion due to dissipation.

We see in (2.65) that in general, the Kelvin-Christoffel tensor and, therefore, the plane wave solutions depend on the prescribed directional vector \mathbf{e}_k . Remember that $\mathbf{e}_k = \frac{\Re k}{k} + i \frac{\Im k}{k}$ might be complex, as it prescribes both a normalized phase propagation and a normalized attenuation. As a consequence, the resulting wave propagation properties (e.g., wave velocities) depend on both the propagation direction and the wave's inhomogeneity [35].

In order to find and discuss specific solutions to the EVP (2.62), additional assumptions on the material need to be made. In this thesis, isotropic nondissipative media are of central importance and will be discussed in the following.

Plane waves in isotropic nondissipative media

We use the isotropic stiffness tensor given in (2.13) and insert into (2.63) to obtain the isotropic wave tensor [35]

$$\mathbf{W} = \frac{\mu_L}{\rho} \mathbf{k} \cdot \mathbf{k} \mathbf{I} + \frac{\lambda_L + \mu_L}{\rho} \mathbf{k} \mathbf{k} - \omega^2 \mathbf{I}. \quad (2.66)$$

The eigenvalues are computed with the characteristic equation [35] given by

$$\det \mathbf{W} = \left(\frac{\mu_L \mathbf{k} \cdot \mathbf{k} - \rho \omega^2}{\lambda_L + \mu_L} \right)^2 \left(\frac{\mu_L \mathbf{k} \cdot \mathbf{k} - \rho \omega^2}{\lambda_L + \mu_L} + \mathbf{k} \cdot \mathbf{k} \right) = 0. \quad (2.67)$$

The three roots define the *dispersion relations* [35] and are given by

$$\text{longitudinal: } \mathbf{k} \cdot \mathbf{k} = \frac{\rho}{\lambda_L + 2\mu_L} \omega^2 \stackrel{\text{def}}{=} \kappa_l^2 \in \mathbb{R}^+, \quad (2.68a)$$

$$\text{transverse: } \mathbf{k} \cdot \mathbf{k} = \frac{\rho}{\mu_L} \omega^2 \stackrel{\text{def}}{=} \kappa_t^2 \in \mathbb{R}^+. \quad (2.68b)$$

The two equations (2.68a) and (2.68b) can be summarized by

$$\mathbf{k} \cdot \mathbf{k} = \kappa_{l/t}^2 \in \mathbb{R}^+, \quad (2.69)$$

Note that the values κ_l and κ_t , are fixed by the medium in which the wave propagates and the frequency. As only the scalar $\mathbf{k} \cdot \mathbf{k}$ is involved in the dispersion relations, the solutions are independent of propagation direction of the wave. This is a direct consequence of the structure of the isotropic stiffness tensor given in (2.13). While the solution κ_l is a single eigenvalue,

the solution κ_t is a double eigenvalue – which is a peculiarity of isotropic media [35].

Homogeneous plane waves

One possibility to fulfill requirement (2.69) is to set $\mathbf{k} = \kappa_{l/t} \mathbf{e}_p$, i.e., considering *homogeneous plane waves* [35, 38]. According to (2.59), the two solutions (2.68a) and (2.68b) then lead to the phase velocities of homogeneous plane waves in isotropic media, namely

$$\text{longitudinal: } c_l \stackrel{\text{def}}{=} \frac{\omega}{\kappa_l} = \sqrt{\frac{\lambda_L + 2\mu_L}{\rho}}, \quad (2.70a)$$

$$\text{transverse: } c_t \stackrel{\text{def}}{=} \frac{\omega}{\kappa_t} = \sqrt{\frac{\mu_L}{\rho}}. \quad (2.70b)$$

The above solutions are named according to the corresponding particle motion of the waves, which is determined by the eigenvector \mathbf{e}_u . For the eigenvalue κ_l^2 of (2.68a), we find that $\mathbf{e}_u = \mathbf{e}_p$, i.e., the particle motion is in the same direction as the phase propagation [35]. For this reason, it is called a *longitudinal wave*, sometimes also *primary wave* or *pressure wave*. On the other hand, the two eigenvectors corresponding to the double eigenvalue κ_t^2 of (2.68b) are required to be orthogonal to \mathbf{e}_p , but are otherwise arbitrary [35]. The waves are, hence, denoted as *transverse waves* – sometime also *secondary waves* or *shear waves*.

Inhomogeneous plane waves

We remark that the wave vector $\mathbf{k} = \Re \mathbf{k} + i \Im \mathbf{k}$ does not need to be real. Writing out the scalar product in (2.69) in terms of real and imaginary parts requires that

$$\mathbf{k} \cdot \mathbf{k} = |\Re \mathbf{k}|^2 - |\Im \mathbf{k}|^2 + 2i \Re \mathbf{k} \cdot \Im \mathbf{k} = \kappa_{l/t}^2 \in \mathbb{R}^+. \quad (2.71)$$

The above can also be satisfied with a complex wave vector \mathbf{k}^i fulfilling

$$\Re \mathbf{k}^i \cdot \Im \mathbf{k}^i = 0. \quad (2.72)$$

These kind of solutions are referred to as *inhomogeneous plane waves* [35, 38, 42]. According to (2.72), the propagation vector $\Re \mathbf{k}^i$ and the attenuation vector $\Im \mathbf{k}^i$ are required to be orthogonal in nondissipative isotropic media. Their phase fronts are attenuated along $\Im \mathbf{k}^i$, as sketched in Fig. 2.4b. While the

existence of inhomogeneous waves was much debated [42], it is now known that they often emerge naturally at the interface between two media [35, 42]. They also happen to be essential to understand wave propagation in leaky waveguides – as will become clear in Sec. 3.2.

The phase velocity of inhomogeneous waves is different to that of homogeneous waves [35, 43]. The real part of the wave vector \mathbf{k}^i is given by $\Re \mathbf{k}^i = (\mathbf{k}^i + \mathbf{k}^{i*})/2$. Its phase velocity is then

$$c_{1/t}^i \stackrel{\text{def}}{=} \frac{\omega}{|\Re \mathbf{k}^i|} = \frac{\omega}{\sqrt{\Re \mathbf{k}^i \cdot \Re \mathbf{k}^i}} = \frac{2\omega}{\sqrt{\mathbf{k}^i \cdot \mathbf{k}^i + \mathbf{k}^{i*} \cdot \mathbf{k}^{i*} + 2\mathbf{k}^i \cdot \mathbf{k}^{i*}}} \quad (2.73)$$

As \mathbf{k}^i fulfills the dispersion relation (2.69), it is known that $\mathbf{k}^{i*} \cdot \mathbf{k}^{i*} = \mathbf{k}^i \cdot \mathbf{k}^i = \kappa_{1/t}^2$. Forming the phase velocity ratio of inhomogeneous and homogeneous waves gives [35]

$$\frac{c_{1/t}^i}{c_{1/t}} = \sqrt{\frac{2}{1 + (\mathbf{k}^i \cdot \mathbf{k}^{i*})/\kappa_{1/t}^2}}. \quad (2.74)$$

Note that $\mathbf{k}^i \cdot \mathbf{k}^{i*} = |\Re \mathbf{k}^i|^2 + |\Im \mathbf{k}^i|^2$ and because $\Re \mathbf{k}^i \perp \Im \mathbf{k}^i$, the product $\mathbf{k}^i \cdot \mathbf{k}^i = |\Re \mathbf{k}^i|^2 - |\Im \mathbf{k}^i|^2 = \kappa_{1/t}^2$. With these observations we may write $\mathbf{k}^i \cdot \mathbf{k}^{i*} = \kappa_{1/t}^2 + 2|\Im \mathbf{k}^i|^2$. Inserting into the previous equation finally yields [35]

$$c_{1/t}^i = \sqrt{\frac{1}{1 + |\Im \mathbf{k}^i|^2/\kappa_{1/t}^2}} c_{1/t}. \quad (2.75)$$

As a consequence, the phase velocity of inhomogeneous plane waves depends on its attenuation and is always lower than that of homogeneous ones.

2.3.2 Energy velocity

Waves usually transport energy. The speed and direction of energy transport is called the *energy velocity* \mathbf{c}_e [35, 37, 38]. It is given by the ratio of average power flux density $\overline{\mathbf{p}}$ to the average total stored energy density $\overline{\mathcal{H}}$:

$$\mathbf{c}_e \stackrel{\text{def}}{=} \frac{\overline{\mathbf{p}}}{\overline{\mathcal{H}}}. \quad (2.76)$$

Using (2.44) and (2.50) the energy velocity can be stated purely in terms of the displacements as

$$\mathbf{c}_e = \frac{\frac{\omega}{2} \Re\{\mathbf{c} : \mathbf{k}^* \mathbf{u}^*(\mathbf{k}, \omega) \mathbf{u}(\mathbf{k}, \omega)\}}{\frac{\rho \omega^2}{4} \mathbf{u}(\mathbf{k}, \omega) \cdot \mathbf{u}^*(\mathbf{k}, \omega) + \frac{1}{4} \mathbf{u}^*(\mathbf{k}, \omega) \mathbf{k}^* : \mathbf{c} : \mathbf{k} \mathbf{u}(\mathbf{k}, \omega)}}. \quad (2.77)$$

For the special case of homogeneous plane waves in nondissipative media we can exploit equipartition of energy given in (2.53) and simplify the above to [35]

$$\mathbf{c}_e = \frac{\mathbf{c} : \mathbf{k} \mathbf{u}^*(\mathbf{k}, \omega) \mathbf{u}(\mathbf{k}, \omega)}{\rho \omega \mathbf{u}^*(\mathbf{k}, \omega) \cdot \mathbf{u}(\mathbf{k}, \omega)} = \frac{1}{\rho \omega} \mathbf{c} : \mathbf{k} \mathbf{e}_u \mathbf{e}_u. \quad (2.78)$$

For isotropic media $\mathbf{c}_e = \mathbf{c}_p$, but this does usually not hold for anisotropic materials [35, 37]. This means that in the latter case, energy propagates in a different direction and with different velocity as compared to the phase fronts [35, 37]. This will become visible only when inspecting a wave beam of finite width, as the phase fronts are then not orthogonal to the beam itself.

For dispersive homogeneous plane wave propagation, another useful formula to compute the energy velocity can be obtained by considering the $\nabla_{\mathbf{k}}$ -gradient of the equation of motion (2.61), where $\nabla_{\mathbf{k}}$ denotes the gradient with respect to the wavenumber components. The derivation is given in Langenberg et al. [35] and will be sketched in the following. Considering that $\nabla_{\mathbf{k}} \mathbf{k} = \mathbf{I}$ and $\nabla_{\mathbf{k}} (\mathbf{k} \cdot \mathbf{c} \cdot \mathbf{k}) = 2\mathbf{c} \cdot \mathbf{k}$, we find from (2.61) that

$$\nabla_{\mathbf{k}} \{[\mathbf{k} \cdot \mathbf{c} \cdot \mathbf{k} - \omega^2(\mathbf{k})\rho \mathbf{I}] \cdot \mathbf{u}\} \quad (2.79)$$

$$= \nabla_{\mathbf{k}} [\mathbf{k} \cdot \mathbf{c} \cdot \mathbf{k} - \omega^2(\mathbf{k})\rho \mathbf{I}] \cdot \mathbf{u} + \nabla_{\mathbf{k}} \mathbf{u} \cdot [\mathbf{k} \cdot \mathbf{c} \cdot \mathbf{k} - \omega^2(\mathbf{k})\rho \mathbf{I}]^{\top} \quad (2.80)$$

$$= 2[\mathbf{c} \cdot \mathbf{k} - \omega(\mathbf{k})\nabla_{\mathbf{k}} \omega(\mathbf{k})\rho \mathbf{I}] \cdot \mathbf{u} + \nabla_{\mathbf{k}} \mathbf{u} \cdot [\mathbf{k} \cdot \mathbf{c} \cdot \mathbf{k} - \omega^2(\mathbf{k})\rho \mathbf{I}] = \mathbf{0}. \quad (2.81)$$

In the latter equation, the transposition can be omitted because $\mathbf{k} \cdot \mathbf{c} \cdot \mathbf{k} - \omega^2(\mathbf{k})\rho \mathbf{I}$ is symmetric. Next, the result is contracted from the right with \mathbf{u}^* . Considering that $\mathbf{k}^* = \mathbf{k}$, the last term vanishes as \mathbf{k} and \mathbf{u} satisfy the equation of motion (2.61). This gives

$$\mathbf{c} : \mathbf{k} \mathbf{u} \mathbf{u}^* - \omega(\mathbf{k})\nabla_{\mathbf{k}} \omega(\mathbf{k})\rho \mathbf{u} \cdot \mathbf{u}^* = \mathbf{0}. \quad (2.82)$$

Forming the complex conjugate of the above equation and solving for $\nabla_{\mathbf{k}} \omega(\mathbf{k})$ finally yields

$$\nabla_{\mathbf{k}} \omega(\mathbf{k}) = \frac{\mathbf{c} : \mathbf{k} \mathbf{u}^* \mathbf{u}}{\rho \omega(\mathbf{k}) \mathbf{u}^* \cdot \mathbf{u}} = \mathbf{c}_e. \quad (2.83)$$

Comparing to (2.78), we see that $\nabla_{\mathbf{k}}\omega(\mathbf{k})$ gives the energy velocity of homogeneous plain waves in nondissipative media. We conclude by remarking that the energy velocity can be determined from the dispersion relation $\omega(\mathbf{k})$ alone without knowledge of the wave's displacement field \mathbf{u} .

2.3.3 Group velocity

So far, the concepts were developed for plane harmonic waves, i.e., at fixed \mathbf{k} and ω . Ultrasonic measurements are often based on the time of flight of a wave packet of finite extend by referring to the maximum of its envelope. We are, therefore, interested in knowing the propagation velocity of the envelope [35, 37, 38]. The below derivation is performed according to Langenberg et al. [35].

Consider a wave packet $\mathbf{u}(\mathbf{x}, t)$ with plane wave spectrum $\mathbf{u}(\mathbf{k}, \omega)$ which is continuous in the wave vector \mathbf{k} and – according to (2.34) – can be synthesized by

$$\mathbf{u}(\mathbf{x}, t) = \frac{1}{(2\pi)^3} \iiint_{-\infty}^{\infty} \mathbf{u}(\mathbf{k}, \omega) e^{i\mathbf{k}\cdot\mathbf{x} - i\omega(\mathbf{k})t} d^3\mathbf{k}. \quad (2.84)$$

Let's assume that $\omega(\mathbf{k})$ changes slowly with \mathbf{k} , such that the truncated Taylor series expansion

$$\omega(\mathbf{k}) \approx \omega(\mathbf{k}_0) + (\mathbf{k} - \mathbf{k}_0) \cdot \nabla_{\mathbf{k}}\omega(\mathbf{k})\big|_{\mathbf{k}=\mathbf{k}_0} \quad (2.85)$$

is a good approximation. Defining the *group velocity* of the wave packet as

$$\mathbf{c}_g(\mathbf{k}_0) := \nabla_{\mathbf{k}}\omega(\mathbf{k})\big|_{\mathbf{k}=\mathbf{k}_0} \quad (2.86)$$

and inserting (2.85) and (2.86) into (2.84), we obtain

$$\begin{aligned} \mathbf{u}(\mathbf{x}, t) &= \frac{1}{(2\pi)^3} \iiint_{-\infty}^{\infty} \mathbf{u}(\mathbf{k}, \omega) e^{i\mathbf{k}\cdot\mathbf{x} - i[\omega(\mathbf{k}_0) + (\mathbf{k} - \mathbf{k}_0) \cdot \mathbf{c}_g(\mathbf{k}_0)]t} d^3\mathbf{k} \\ &= \frac{1}{(2\pi)^3} \underbrace{\iiint_{-\infty}^{\infty} \mathbf{u}(\mathbf{k}, \omega) e^{i(\mathbf{k} - \mathbf{k}_0) \cdot \mathbf{x} - i(\mathbf{k} - \mathbf{k}_0) \cdot \mathbf{c}_g(\mathbf{k}_0)t} d^3\mathbf{k}}_{A_{\mathbf{k}_0}(\mathbf{x} - \mathbf{c}_g(\mathbf{k}_0)t)} e^{i\mathbf{k}_0 \cdot \mathbf{x} - i\omega(\mathbf{k}_0)t}. \end{aligned} \quad (2.87)$$

After integration, the argument of the envelope $A_{\mathbf{k}_0}$ is of the form $(\mathbf{k} - \mathbf{k}_0)(\mathbf{x} - \mathbf{c}_g(\mathbf{k}_0)t)$. Hence, the defined group velocity corresponds – in first order approximation – to the propagation speed and direction of the wave packet's envelope with carrier wave vector \mathbf{k}_0 and carrier frequency $\omega(\mathbf{k}_0)$. The retardation of

phases of the wave packet, on the other hand, is given by the phase velocity $\mathbf{c}_p = \omega(\mathbf{k}_0)/\Re k_0 \mathbf{e}_p$, as should be expected.

Comparing (2.86) to (2.83), we conclude that for homogeneous waves in nondissipative media, the group velocity is the same as the energy velocity, see also Refs. [35, 38, 40, 44, 45]:

$$\mathbf{c}_g = \mathbf{c}_e \quad (\text{for } \mathbf{k}, \mathbf{c} \text{ and } \rho \text{ real}). \quad (2.88)$$

This is intuitively clear because energy cannot travel passed the nodes of the wave's envelope [38]. In contrast to the energy velocity, which is a dynamical definition, the concept of group velocity is a purely kinematic definition.

Alternative representations of the group velocity may be found in terms of the phase velocity [38]. Here, we derive these expressions in full vectorial form. Considering that $\omega(\mathbf{k}) = \mathbf{c}_p(\mathbf{k}) \cdot \mathbf{k}$, one can write the group velocity as

$$\mathbf{c}_g = \mathbf{c}_p + \nabla_{\mathbf{k}} \mathbf{c}_p \cdot \mathbf{k}. \quad (2.89)$$

Moreover, for $\mathbf{c}_p = \mathbf{c}_p(\omega(\mathbf{k}))$ and real \mathbf{k} , we may also write

$$\mathbf{c}_g = \mathbf{c}_p + \frac{\omega}{c_p} \mathbf{c}_g \frac{\partial \mathbf{c}_p}{\partial \omega} \cdot \mathbf{e}_p, \quad (2.90)$$

which will reduce to

$$\mathbf{c}_g = \mathbf{c}_p \left(1 - \frac{\omega}{c_p} \frac{\partial c_p}{\partial \omega} \right)^{-1} \quad (2.91)$$

if $\mathbf{c}_p(\omega) = c_p(\omega) \mathbf{e}_p$ does not change direction with frequency, i.e., for isotropic media having collinear group and phase velocities.

Remember that \mathbf{c}_p is independent of frequency for nondispersive wave propagation. From the above equations, we may conclude that the phase velocity and group velocity are identical in this case.

2.4 Concluding remarks

The elastodynamic field theory was reviewed in this chapter. The presented concepts are essential to describe and understand mechanical waveguides, which are the core of this monograph. The governing equations of waveguides will be obtained from Navier's equation in combination with appropriate boundary and/or interface conditions (Sec. 2.1). Thereby, the analysis will be performed in the frequency-wavenumber domain (Sec. 2.2). The main

difference between wave propagation in unbounded media and in a waveguide is that the latter is always dispersive, even for isotropic media. Consequently, the concepts of dispersion relation, phase velocity, group velocity and energy velocity are indispensable (Sec. 2.3). By presenting them in this chapter, we emphasize that these concepts are not exclusive to guided waves, but are rather very fundamental.

3 Guided and quasi-guided waves

The theory of elastodynamic wave propagation confined within a structure is presented in the following. Thereby, we concentrate on plates, the simplest form of waveguides, as they are appropriate to describe thin structures like a pipe's wall. Two conceptually and mathematically very different kind of waveguides will be introduced: closed and open waveguides. While energy is perfectly confined within the former, it may flow across the waveguide's boundary in the latter case. Open waveguides are of practical interest in UFM because elastic waves inside the pipe wall leak into the pipe's interior in the form of acoustic waves. Conversely, an incident acoustic wave excites mechanical waves in the pipe wall. This is the mechanism by which ultrasonic waves are emitted and received into/from the pipe's interior.

The chapter is divided into two sections: closed waveguides in Sec. 3.1 and open waveguides in Sec. 3.2. Closed waveguides are well understood and Sec 3.1 gives a literature review on the topic. This is different for open waveguides: since they represent a non-conservative system, they are physically much more intricate. While Sec. 3.2 references existing literature, it mostly represents an adaptation and extension to the author's contributions [P3] and [P5].

3.1 Guided waves in plates

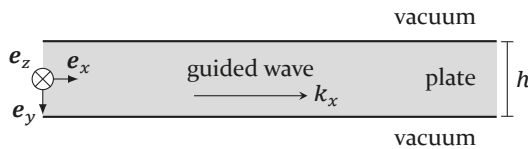


Figure 3.1: plate geometry.

Let's consider the geometry depicted in Fig. 3.1. The homogeneous plate is unbounded in the x - z -plane but has finite thickness h along e_y . The half-spaces above and below the plate are vacuum, i.e., no wave propagation is possible. For energy to be confined within the plate's interior, wave propagation must take place purely in the x - z -plane. We shall consider *plane waves* inside the plate. This implies displacements of the form $\mathbf{u}(\mathbf{x}, t) = \mathbf{u}(y, k_x, k_z, \omega) e^{i(k_x x + k_z z - \omega t)}$, which corresponds to a Fourier transform in x , z and t , while remaining in the physical domain y . This kind of ansatz makes sense because the formulated problem exhibits translational invariance along

x , z and t and, therefore, solutions that are harmonic in these coordinates are expected to exist [46]. Furthermore, the coordinate system is positioned such that the phases propagate purely in \mathbf{e}_x , i.e., we restrict attention to the waves with $k_z = 0$. This reduces the *guided wave ansatz* to

$$\mathbf{u}(\mathbf{x}, t) = \mathbf{u}(y, k_x, \omega) e^{i(k_x x - \omega t)}. \quad (3.1)$$

Note that this ansatz implies a *plain strain* state [1, 38] because the displacement field is clearly independent of the z -coordinate ($\partial_z \mathbf{u} = \mathbf{0}$).

3.1.1 Waveguide problem formulation

The field in the plate needs to satisfy the unforced elastodynamic wave equation (2.17) as well as the traction free BC (2.27a) at the plate's faces. The latter are located at $y = \pm h/2$ with normal vectors given by $\mathbf{e}_n = \pm \mathbf{e}_y$. Together with the guided wave ansatz (3.1), the named equations form the guided wave problem. In order to account for the ansatz, we introduce the mixed "spatial derivative operator"

$$\mathcal{G} := ik_x \mathbf{e}_x + \partial_y \mathbf{e}_y + 0 \mathbf{e}_z. \quad (3.2)$$

The stress tensor is then given by $\mathbf{T}(y, k_x, \omega) = \mathbf{c} : \mathcal{G} \mathbf{u}(y, k_x, \omega)$. Correspondingly, the *guided wave problem* for the free plate reads

$$\overbrace{[\mathcal{G} \cdot \mathbf{c} \cdot \mathcal{G} + \rho \omega^2 \mathbf{I}]}^{W(k_x, \omega)} \cdot \mathbf{u}(y, k_x, \omega) = \mathbf{0}, \quad (3.3a)$$

$$\underbrace{[\mathbf{e}_y \cdot \mathbf{c} \cdot \mathcal{G}]}_{B(k_x, \omega)} \cdot \mathbf{u}(y, k_x, \omega) \Big|_{y=\pm h/2} \stackrel{!}{=} \mathbf{0}. \quad (3.3b)$$

Writing out the components of \mathcal{G} , performing the contractions and grouping in terms of ik_x , finally results in

$$\overbrace{[(ik_x)^2 \mathbf{L}_2 + ik_x \partial_y \mathbf{L}_1 + \partial_y^2 \mathbf{L}_0 + \rho \omega^2 \mathbf{I}]}^{W(k_x, \omega)} \cdot \mathbf{u}(y, k_x, \omega) = \mathbf{0}, \quad (3.4a)$$

$$\underbrace{[ik_x \mathbf{B}_1 + \partial_y \mathbf{B}_0]}_{B(k_x, \omega)} \cdot \mathbf{u}(y, k_x, \omega) \Big|_{y=\pm h/2} \stackrel{!}{=} \mathbf{0}, \quad (3.4b)$$

where the constant 2nd order stiffness tensors \mathbf{L}_n are given by

$$\mathbf{L}_2 = c_{xj kx} \mathbf{e}_j \mathbf{e}_k, \quad \mathbf{L}_1 = (c_{xj ky} + c_{yj kx}) \mathbf{e}_j \mathbf{e}_k, \quad \mathbf{L}_0 = c_{yj ky} \mathbf{e}_j \mathbf{e}_k, \quad (3.5)$$

and the constant traction operators \mathbf{B}_n by

$$\mathbf{B}_1 = c_{yjkx} \mathbf{e}_j \mathbf{e}_k, \quad \mathbf{B}_0 = c_{yjk_y} \mathbf{e}_j \mathbf{e}_k. \quad (3.6)$$

As we seek nontrivial solutions for \mathbf{u} satisfying (3.4), it is necessary to find the values (k_x, ω) for which the wave operator $\mathbf{W}(k_x, \omega)$ subject to $\mathbf{B}(k_x, \omega)$ becomes singular. It is feasible to prescribe either ω or k_x in (3.4a) and consider the other parameter as eigenvalue to be solved for. However, if inhomogeneous (evanescent) waves are to be considered, it is more convenient to prescribe the real-valued angular frequency ω and solve for the complex values of the wavenumber k_x . Proceeding in this way results in a frequency-dependent quadratic EVP for $ik_x(\omega)$, as can be seen in (3.4) [47].

The above derivation shows that the guided wave problem is analogous to the plane bulk wave problem in Subsec. 2.3.1, with the difference that the problem remains continuous in the through-thickness coordinate y . As such, it represents a *differential EVP* on the one-dimensional domain $y \in [-h/2, h/2]$. This kind of problems is known in the literature as *Sturm-Liouville problems* [48–57] and is well studied in the context of functional analysis.

3.1.2 Dispersion curves of an anisotropic plate

A Matlab toolbox called Elastodynamic Acoustic Toolbox (EDAT), see Sec. 4.4, was developed in the course of this thesis that numerically solves a discrete and normalized version of the guided wave problem, for details refer to Chapter 4. As an example, the computed frequency-dependent wavenumbers $k_x(f)$ for a transversely isotropic (i.e., hexagonal symmetry) fibre reinforced graphite/epoxy plate with fibers in direction of wave propagation (material data is given in Appendix A) are plotted in Fig. 3.2a and Fig. 3.2b. Moreover, the corresponding phase velocities $c_p = \omega/\Re k_x$ are shown in Fig. 3.2c (compare to [58]).

The frequency-dependent curves in Fig. 3.2 are collectively referred to as *dispersion curves*. Each single curve corresponds to one *mode* or *wave*. Note that the dispersion curves live in the three-dimensional space $[\Re k_x, \Im k_x, f]$ [41, 47], i.e., the wavenumber spectrum is in general complex valued. Real valued solutions are marked as “propagating” in the shown dispersion diagrams, while complex valued ones are denoted as “nonpropagating” (see next section). Even if difficult to see in Fig. 3.2a, the curves of propagating modes are connected to the nonpropagating ones. With this continuation of dispersion curves into the complex plane, all modes extend down to zero frequency [41].

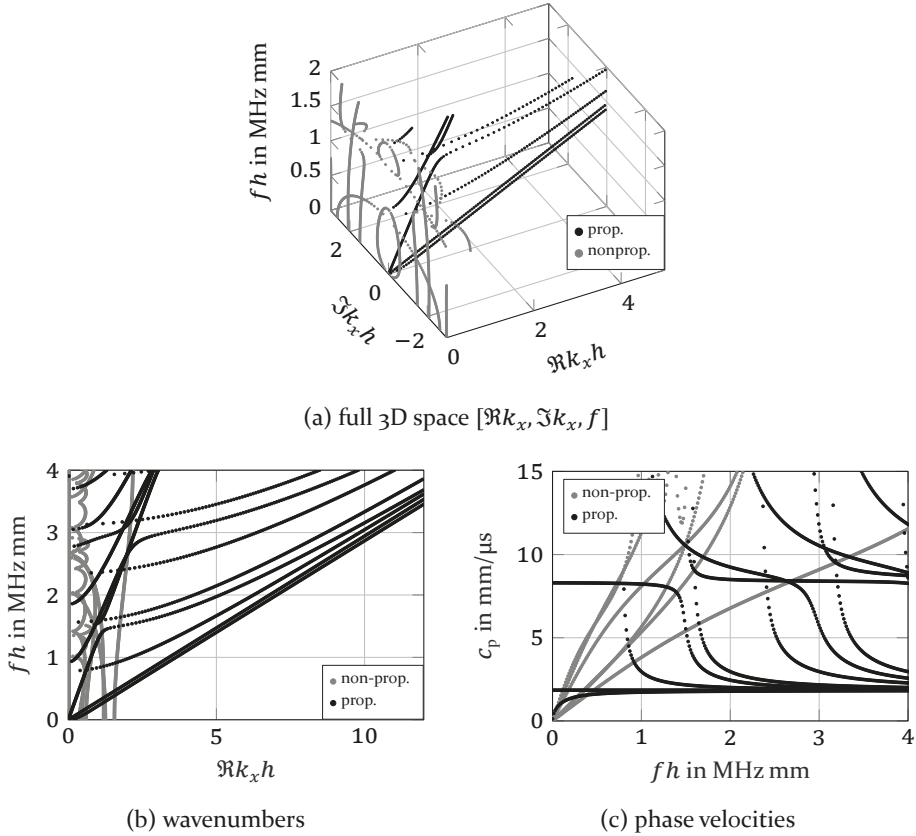


Figure 3.2: Dispersion curves of a transversely isotropic fibre reinforced graphite/epoxy plate.

We prefer to plot the dispersion curves in the wavenumber-thickness and frequency-thickness products because in this representation, they are independent of the plate's thickness itself. This can be seen when considering the guided wave problem on the normalized/stretched coordinate $\eta = y/h$ with $\partial_\eta = h\partial_y$. The problem given by (3.4a) and (3.4b) – scaled by h^2 and h , respectively – then yields

$$\text{PDE: } \left[(ik_x h)^2 \mathbf{L}_2 + ik_x h \partial_\eta \mathbf{L}_1 + \partial_\eta^2 \mathbf{L}_0 + \rho(\omega h)^2 \mathbf{I} \right] \cdot \mathbf{u}(\eta, k_x h, \omega h) = \mathbf{0}, \quad (3.7a)$$

$$\text{BCs: } \left[ik_x h \mathbf{B}_1 + \partial_\eta \mathbf{B}_0 \right] \cdot \mathbf{u}(\eta, k_x h, \omega h) \Big|_{\eta=\pm 1/2} \stackrel{!}{=} \mathbf{0}. \quad (3.7b)$$

Note that the differential operator ∂_η is dimensionless and operates on the unit thickness. Therewith, the above problem depends only on the products $k_x h$ (wavenumber-thickness) and ωh (angular frequency-thickness) and not

on the thickness h as such. We conclude that a change in the plate's thickness simply leads to accordingly scaled wavenumber and frequency [59].

3.1.3 Classification of modes

The waveguide modes separate into several independent sets with unique properties. This will be discussed in detail in the following.

Propagating and nonpropagating modes

Purely real wavenumbers exist and these solutions are called *propagating* modes. On the other hand, imaginary and complex wavenumbers do also exist. It can be shown that these modes do not propagate energy [41, 60], i.e., their power flux (and hence energy velocity) is identically zero. For this reason, they are termed *nonpropagating modes* [41, 60]. At some points in the dispersion diagram they meet with the propagating modes, which also exhibit vanishing power flux at this single point. These so-called zero-group-velocity (ZGV) modes represent local vibrations of the plate and are used for material characterization and nondestructive testing [61]. Note that fluid loading of the plate has the effect that propagating and nonpropagating waves merge into one non-separable physical entity called quasi-guided waves (QGWs), which will be treated in detail in Sec. 3.2. We will focus the remaining discussion in this section – which is concerned with free plates – on propagating modes.

Mode families

The multitude of modes seen in Fig. 3.2 can often be split into decoupled subsets, which are referred to as *mode families* [62]. As they are independent of each other, they can be computed and analyzed separately, leading to an according reduction in complexity. Moreover, the dispersion curves of modes belonging to the same family cannot cross. Instead, *eigenvalue veering/repulsion* [63, 64] can be observed when two modes in the same family get close to each other. From a computational point of view, this can be exploited to avoid tedious and unreliable mode tracing. Instead, the wavenumbers can simply be sorted by magnitude in order to match solutions at different frequencies to the same mode.

The mode families emerge due to two properties:

- coupling or decoupling between in-plane (x - y -plane) and out-of-plane motions (z -direction) and
- the parity of the eigenfunctions or lack thereof.

If the wave motions decouple, the in-plane motions $[u_x, u_y, 0]^T$ lead to the so-called *Lamb waves* [41, 65], while the out-of-plane motions $[0, 0, u_z]^T$ lead to *shear-horizontal (SH) waves* [41]. Their eigenfunctions $u_i(y)$ might exhibit symmetric (S) or anti-symmetric (A) parity, splitting the former families again into two independent subsets.

The number and type of mode families that exist in a plane waveguide depends on

- the existence of a plane of symmetry in the geometry and
- the anisotropy and orientation of the material.

An in-depth analysis was performed by Hernando Quintanilla et al. [62] and reveals that the anisotropy of the material leads to exactly five possible categories of plane and homogeneous waveguides (plates), each with a unique set of mode families summarized in Tab. 3.1. The denotation of the waveguide class seen in the table was introduced by the mentioned authors and refers to the applicable crystal class with fewest symmetries. For instance, $O_D^{S/A}$ stands for orthorhombic crystal class with decoupling (\bullet_D) of Lamb and SH waves, each with symmetric/anti-symmetric parity ($\bullet^{S/A}$). The classification is for a homogeneous single-layer plate. Breaking the waveguide's symmetry with respect to the mid-plane ($y = 0$), e.g., due to inhomogeneity of the material or fluid loading, does naturally also break the parity of the solutions, not, however, the decoupling of Lamb and SH polarizations.

Table 3.1: Summary of possible splitting into mode families according to [62]. Empty fields indicate no decoupling or no parity, respectively. For a full list of material configurations corresponding to each class refer to [62].

denotation	T_C	M_D		$M_C^{S/A}$	Tet_D^*		$O_D^{S/A}$				
decoupling		Lamb	SH		Lamb	SH	Lamb	SH			
parity				A	S	A	S	A	S	A	S

Let's first inspect the conditions under which Lamb waves decouple from SH waves, i.e., we are interested in knowing when motions of u_x and u_y are independent of u_z . This corresponds to waveguides of either class \bullet_D or class \bullet_C , see Tab. 3.1. Note that the coupling is due to the stiffness operators L_i and B_i in (3.4). We derive conditions on the Cartesian components c_{ijkl} of the stiffness tensor for which decoupled equations are obtained. Greek indices shall denote free indices for the x and y components – omitting the z -component – i.e., $\alpha, \beta \in \{x, y\}$. The components of the stiffness contribution

in (3.4a) can then be split into a contribution due to u_β and one due to u_z according to

$$\begin{aligned} & [(ik_x)^2 c_{xj\beta x} + ik_x \partial_y (c_{xj\beta y} + c_{yj\beta y}) + \partial_y^2 c_{yj\beta y}] u_\beta \\ & + [(ik_x)^2 c_{xjz x} + ik_x \partial_y (c_{xjz y} + c_{yjz y}) + \partial_y^2 c_{yjz y}] u_z. \end{aligned} \quad (3.8)$$

The three equations indexed by j will decouple when reference to u_z disappears for $j = \alpha$, i.e., $c_{\alpha z \alpha x} = c_{\alpha z \alpha y} = c_{y \alpha z x} = c_{y \alpha z y} = 0$, and when reference to u_β disappears for $j = z$, i.e., $c_{x z \beta x} = c_{x z \beta y} = c_{y z \beta x} = c_{y z \beta y} = 0$. In a similar way, redundant conditions are obtained from (3.4b). To summarize concisely, Lamb and SH waves decouple when

$$c_{\alpha \beta z \gamma} = 0 \quad \text{and} \quad c_{\alpha z \beta \gamma} = 0 \quad \text{for } \alpha, \beta, \gamma \in \{x, y\}. \quad (3.9)$$

In this case, the $\alpha \in \{x, y\}$ and z components of the guided wave problem given in (3.4) can be treated separately, leading to a 2×2 -system for Lamb waves and a scalar equation for SH waves, respectively. Each of them, having the same structure as before.

Next, let's inspect the segregation of waves according to the parity of their eigenfunctions $\mathbf{u}(y) = [u_x(y), u_y(y)]^\top$, which yields the waveguide classes without super-index, super-index S/A or super-index * in Tab. 3.1. When the functions exhibit a definite parity, the modes segregate into the following two families:

symmetric (S): u_x is even, i.e., $u_x(y) = u_x^*(-y)$, and u_y is odd, i.e., $u_y(y) = -u_y^*(-y)$.

anti-symmetric (A): u_x is odd and u_y is even.

Our toolbox classifies the waves into A and S by computing the scalar product of the eigenfunctions $\mathbf{u}_n(y)$ with the test functions $f_e(y) = 1$ and $f_o(y) = 2y$ and exploits the fact that even and odd functions are orthogonal. This procedure has the advantage that it results in a measure on “how close to symmetric or anti-symmetric” the modes are, i.e., it can be seen as a generalization to waves that do not exhibit perfect parity. This can be of interest for guided wave transducer selection [44, 66] when the parity is only “slightly altered”, e.g., light single-sided fluid loading.

Instead of an a-posteriori classification, it is also possible to compute only the symmetric or anti-symmetric solutions of (3.4) by

- using only even or odd interpolation functions in the numerical approximation [48] or

- modeling only half the plate's cross-section, i.e., $y \in [0, h]$, and imposing appropriate symmetry or anti-symmetry conditions at the center point $y = 0$ [58].

The implemented Matlab toolbox uses a full-tensor notation and is capable of computing waveguide problems of any crystal symmetry/anisotropy. This monograph focuses on the $O_D^{S/A}$ class, which includes isotropic materials as well as the example given in Fig. 3.2. As we are mostly interested in fluid-coupled plates (Sec. 3.2), decoupling of Lamb and SH waves is of particular interest because SH waves – having no displacements normal to the plate's surface – do not couple to the fluid medium (see Subsec. 2.1.5).

3.1.4 Dispersion curves of an isotropic plate

Let's discuss guided waves in a free, homogeneous and *isotropic plate* in more detail. It corresponds to the $O_D^{S/A}$ class, i.e., motions decouple into Lamb and SH polarization and each of them into symmetric and anti-symmetric families. The equations are obtained by inserting the isotropic stiffness tensor (2.13) into the guided wave problem (3.4). Additionally, we explicitly split the equations according to their polarization using the two-component displacement vector $\bar{\mathbf{u}} = u_\alpha \mathbf{e}_\alpha$ with $\alpha \in \{x, y\}$, as well as the reduced identity tensor $\bar{\mathbf{I}}$ and $\bar{\mathcal{G}}$ -operator, both consisting only of the x - and y -components¹. The equations of in-plane and out-of-plane plain strain motions then read

$$[(\lambda_L + \mu_L)\bar{\mathcal{G}}\bar{\mathcal{G}} + \mu_L\bar{\mathcal{G}} \cdot \bar{\mathcal{G}}\bar{\mathbf{I}} + \rho\omega^2\bar{\mathbf{I}}] \cdot \bar{\mathbf{u}} = \mathbf{0}, \quad (3.10a)$$

$$[\mu_L\bar{\mathcal{G}} \cdot \bar{\mathcal{G}} + \rho\omega^2] u_z = 0, \quad (3.10b)$$

respectively.

Shear-horizontal waves

The guided shear-horizontal waves are pure out-of-plane displacements described by (3.10b) together with traction free boundary conditions (BCs). Writing out in terms of ik_x and ∂_y , the waveguide problem reduces to the following scalar waveguide problem:

$$[\mu_L(ik_x)^2 + \mu_L\partial_y^2 + \rho\omega^2]u_z(y, k_x, \omega) = 0, \quad (3.11a)$$

$$\mu_L\partial_y u_z(y, k_x, \omega)|_{y=\pm h/2} = 0. \quad (3.11b)$$

¹ In the following, $\bar{\bullet}$ shall not denote a mean, but reduced tensors.

As an example, the dispersion curves of shear-horizontal waves in an isotropic brass plate (material data in Appendix A) have been computed and are displayed in Fig. 3.3.

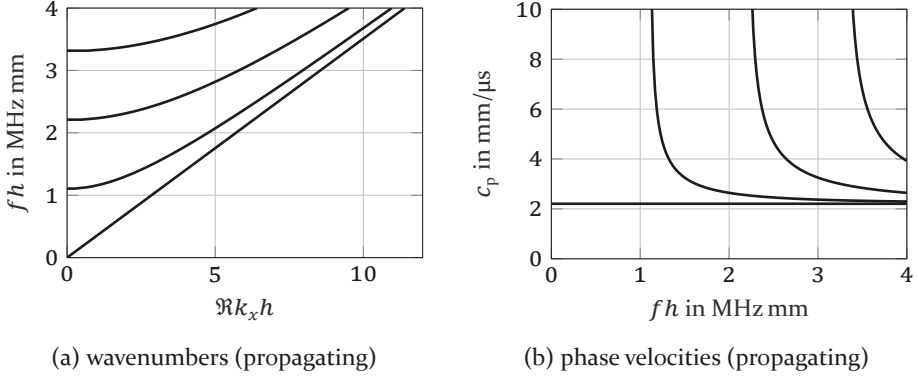


Figure 3.3: Dispersion curves of shear-horizontal (SH) modes in a brass plate.

Lamb waves

We turn to analyze wave motions in the x - y -plane described by (3.10a). Hereinafter, the over-bars denoting two-component tensors will be omitted, as only reduced tensors are involved. The structure of the guided wave equation is identical to the one of the anisotropic plate given in (3.4). However, the reduced stiffness tensors $\mathbf{L}_2 = c_{x\alpha\beta x} \mathbf{e}_\alpha \mathbf{e}_\beta$, $\mathbf{L}_1 = (c_{x\alpha\beta y} + c_{y\alpha\beta x}) \mathbf{e}_\alpha \mathbf{e}_\beta$ and $\mathbf{L}_0 = c_{y\alpha\beta y} \mathbf{e}_\alpha \mathbf{e}_\beta$ can now be stated explicitly in terms of the Lamé parameters in matrix representation as

$$[\mathbf{L}_2] = \begin{bmatrix} \lambda_L + 2\mu_L & 0 \\ 0 & \mu_L \end{bmatrix}, \quad [\mathbf{L}_1] = \begin{bmatrix} 0 & \lambda_L + \mu_L \\ \lambda_L + \mu_L & 0 \end{bmatrix}, \quad [\mathbf{L}_0] = \begin{bmatrix} \mu_L & 0 \\ 0 & \lambda_L + 2\mu_L \end{bmatrix}. \quad (3.12)$$

Similarly, the traction operators $\mathbf{B}_1 = c_{y\alpha\beta x} \mathbf{e}_\alpha \mathbf{e}_\beta$ and $\mathbf{B}_0 = c_{y\alpha\beta y} \mathbf{e}_\alpha \mathbf{e}_\beta$ for the isotropic plate can be written in matrix form as

$$[\mathbf{B}_1] = \begin{bmatrix} 0 & \mu_L \\ \lambda_L & 0 \end{bmatrix}, \quad [\mathbf{B}_0] = \begin{bmatrix} \mu_L & 0 \\ 0 & \lambda_L + 2\mu_L \end{bmatrix}. \quad (3.13)$$

The resulting dispersion curves of Lamb waves in a free brass plate (material parameters given in Appendix A) are shown in Fig. 3.4. The propagating modes have been split into symmetric and antisymmetric modes. Only three of the nonpropagating branches are included because waves with $\Im k_x h > 8$ have been cropped. This is also the reason why the uppermost of these branches stops at approx. (3, 3.1 MHz mm), i.e., this is merely an artifact of visualization. The propagating Lamb modes labeled Ao and So are denoted as *fundamental*

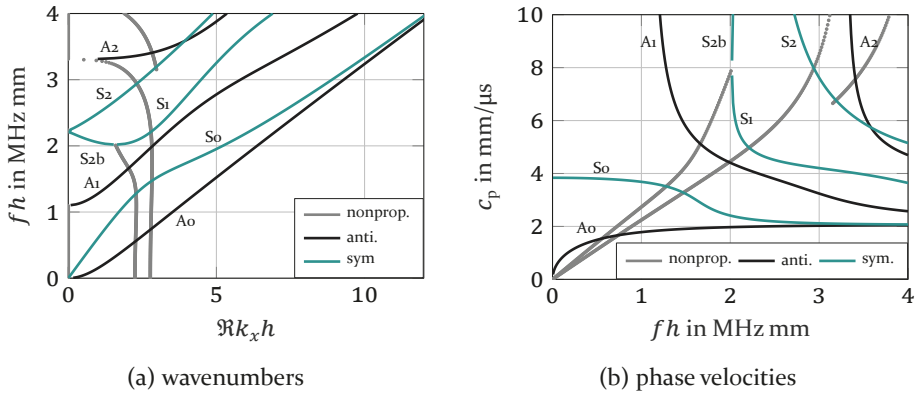


Figure 3.4: Dispersion curves of Lamb modes in a brass plate.

modes because they exist over the whole frequency range. With increasing frequency, more propagating modes are encountered. Those frequency points are called *cutoff frequencies*. Note that the discussed details also apply to Fig. 3.2, where no classification into SH/Lamb nor symmetric/anti-symmetric waves has been performed although the plate is also of class $O_D^{S/A}$.

3.1.5 Wave field of Lamb modes

The wave field of propagating Lamb modes will be inspected more closely in the following. The displacement eigenfunctions $\mathbf{u}_n(y)$ describe the wave field of the modes [59]. They are depicted exemplarily for the fundamental modes in Fig. 3.5. Thereby, each mode is normalized to its maximum displacement magnitude. As the components $u_x(y)$ and $u_y(y)$ are always 90° out of phase [44], they are shown at the phase where they become maximal, respectively. The even and odd parity of the displacement functions discussed in Subsec. 3.1.3 can clearly be observed in the plots.

The displacements can be extruded to the x - y -plane using the ansatz (3.1), obtaining a more intuitive visualization. This has been done for the fundamental modes and is presented in Fig. 3.6. It illustrates the “flexural” nature of anti-symmetric waves as well as the “compressional” nature of the symmetric ones. Higher modes exhibit increasing number of nodal points in their displacement structure, but behave otherwise similar [59].

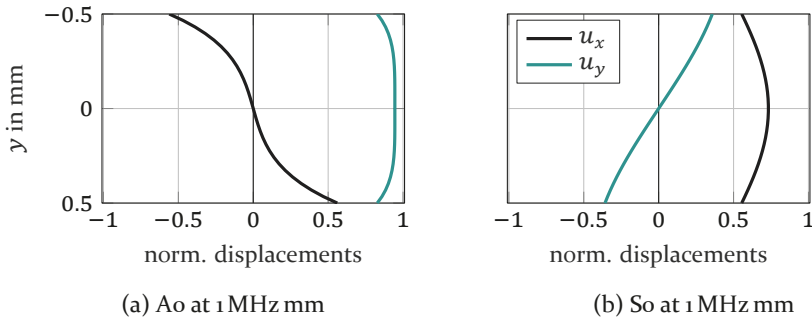


Figure 3.5: Displacement structure of the fundamental modes. The two components are shown 90° out of phase at their respective maximum.

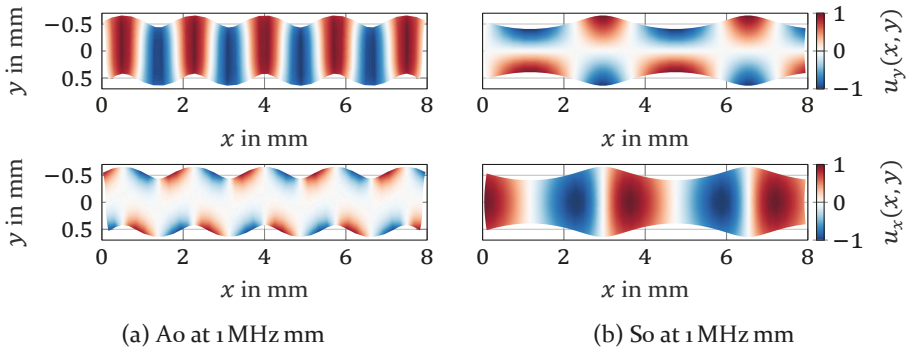


Figure 3.6: Displacement field of the fundamental modes.

3.1.6 Power flux considerations

As the energy is confined within the waveguide, the modal solutions carry power purely in x -direction. The average power flux density $\bar{\mathbf{p}}$ according to (2.48) can be integrated over the waveguide's cross section, i.e., along y , in order to obtain the *net average power flux* of the waves:

$$\bar{P} = \int_{-h/2}^{h/2} \bar{\mathbf{p}} \cdot \mathbf{e}_x dy. \quad (3.14)$$

The above expression is strictly zero for all nonpropagating waves, but nonzero for the propagating ones.

Energy and group velocity of guided waves

The *energy velocity* according to Subsec. 2.3.2 describes the speed and direction with which waves carry energy. This concept can be adapted to guided

waves [41], where we may now consider their total average energy flux \bar{P} along the plate given in (3.14) and the total average stored energy $\bar{H} = \int_{-h/2}^{h/2} \bar{\mathcal{H}} dy$, where $\bar{\mathcal{H}}$ is the time-averaged energy density from (2.45) or (2.53). The energy velocity of guided waves is then given by [40, 41, 44]

$$c_e \stackrel{\text{def}}{=} \frac{\bar{P}}{\bar{H}}. \quad (3.15)$$

As the power flux of the guided waves is purely in x -direction, it is sufficient to specify the energy velocity as a scalar.

The energy velocities of propagating Lamb modes in the fibre reinforced graphite/epoxy plate according to (3.15) are plotted in Fig. 3.7a, while the one for the brass plate are shown in Fig. 3.7b. In general, the energy velocity of modes can be negative even if $\Re k_x > 0$. Such waves propagate energy in opposite direction as compared to the phases and are, hence, called *backward waves* [67–69]. Such a wave – labeled S2b in the figures – is supported by the brass plate, displaying negative energy velocities in Fig. 3.7b.

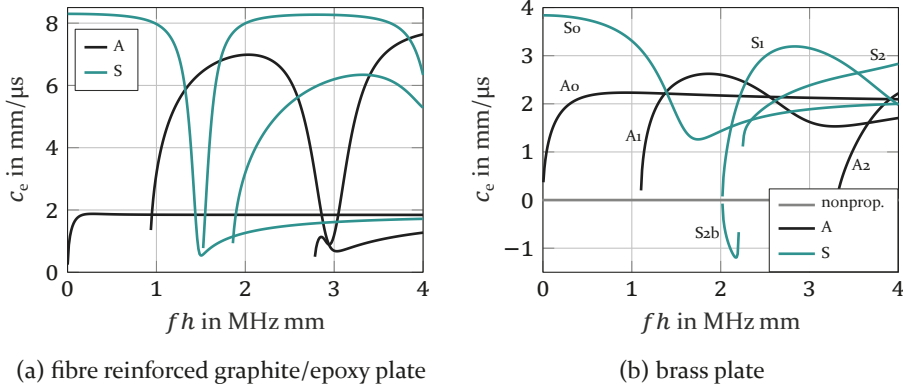


Figure 3.7: Energy velocity of Lamb modes

The concept of *group velocity*, defined for plane waves in Subsec. 2.3.3, is equally applicable to guided waves [41] and is especially appropriate for propagating modes, as they have purely real wavenumbers [44]. The group velocity of propagating guided waves is defined as

$$c_g \stackrel{\text{def}}{=} \frac{\partial \omega}{\partial \Re k_x}. \quad (3.16)$$

This means that for propagating modes, it can be identified as the slope in the ω - $\Re k_x$ -diagram, e.g., in Fig. 3.4a. For nondissipative and closed waveguides, it can be shown that the group- and energy velocities are identical [40, 44]. However, energy velocity is the more general concept, as it extends to dissipative waveguides [44].

3.1.7 Orthogonality relations between modes

Guided waves in plates – albeit they are eigensolutions of a non-Hermitian system² – form a *complete orthogonal set*, i.e., they can be used to uniquely expand arbitrary fields in the plate. Orthogonality is shown and discussed in Ref. [41, 70–72]. Their completeness is usually assumed [73], but recent work presents a proof [74]. Accordingly, guided waves form the natural basis to describe wave phenomena in plates – analogous to what plane waves are for unbounded media. The field expansion requires an orthogonality relation, which is then used to project the arbitrary field onto each of the modal solutions, yielding the desired expansion coefficients.

An orthogonality condition for the waveguide solutions can be derived from the reciprocity relation given in (2.54). We provide the derivation according to Auld [41]. For this end, both considered elastodynamic states are modal solutions obtained from (3.4) at one given frequency, i.e.,

$$\mathbf{v}_1 = \mathbf{v}_m(\mathbf{y}) e^{i(k_{xm}x - \omega t)}, \quad \mathbf{T}_1 = \mathbf{T}_m(\mathbf{y}) e^{i(k_{xm}x - \omega t)}, \quad \text{and} \quad (3.17)$$

$$\mathbf{v}_2 = \mathbf{v}_n(\mathbf{y}) e^{i(k_{xn}x - \omega t)}, \quad \mathbf{T}_2 = \mathbf{T}_n(\mathbf{y}) e^{i(k_{xn}x - \omega t)}. \quad (3.18)$$

The term in (2.54) with the time derivative vanishes in this case because the products $\mathbf{v}_2^* \cdot \mathbf{v}_1$, etc., are time-independent. Considering that $\mathbf{f}_1 = \mathbf{f}_2 = 0$, and inserting into the reciprocity relation (2.54) yields

$$i(k_{xn}^* - k_{xm}) \mathbf{e}_x \cdot (-\mathbf{v}_n^* \cdot \mathbf{T}_m - \mathbf{v}_m \cdot \mathbf{T}_n^*) = \mathbf{e}_y \partial_y \cdot (-\mathbf{v}_n^* \cdot \mathbf{T}_m - \mathbf{v}_m \cdot \mathbf{T}_n^*), \quad (3.19)$$

where summation over repeated free indices is not implied. Furthermore, we integrate the above equation over the cross section of the waveguide, i.e., along y . Then, using the divergence theorem (fundamental theorem of calculus), the integral of the ∂_y -term reduces to the boundary term $\mathbf{e}_y \cdot (-\mathbf{v}_n^* \cdot \mathbf{T}_m - \mathbf{v}_m \cdot \mathbf{T}_n^*)|_{-h/2}^{h/2}$. With these considerations, the integral of (3.19) reads

$$i(k_{xn}^* - k_{xm}) 4P_{mn} = \mathbf{e}_y \cdot (-\mathbf{v}_n^* \cdot \mathbf{T}_m - \mathbf{v}_m \cdot \mathbf{T}_n^*)|_{-h/2}^{h/2}, \quad (3.20)$$

² Remember that the wavenumbers (eigenvalues) are complex valued [56].

with

$$P_{mn} \stackrel{\text{def}}{=} \frac{1}{4} \int_{-h/2}^{h/2} (-\mathbf{v}_n^* \cdot \mathbf{T}_m - \mathbf{v}_m \cdot \mathbf{T}_n^*) \cdot \mathbf{e}_x \, dy. \quad (3.21)$$

Moreover, for the free waveguide modes, we know that $\mathbf{e}_y \cdot \mathbf{T}_n = \mathbf{e}_y \cdot \mathbf{T}_m = \mathbf{0}$, which means that the boundary term in (3.20) vanishes. This yields the *orthogonality relation*

$$P_{mn} = 0 \quad \text{for} \quad k_{xm} \neq k_{xn}^*. \quad (3.22)$$

We conclude that, at given frequency, an eigensolution with propagation constant k_{xn} is orthogonal to all other eigensolutions for which the propagation constant $k_{xm} \neq k_{xn}^*$. In particular, this means that such solutions are mutually independent. P_{mn} can be interpreted as the *cross power flow* between mode m and mode n . When $m = n$, the term P_{mn} reduces to the mode's total average power flux, i.e., $P_{nn} = \bar{P}$ according to (3.14). In a similar manner, orthogonality relations between solutions at different frequencies but constant wavenumber can be obtained [72].

The deduced orthogonality relation is used to describe (i) how guided waves are excited by tractions applied on the plate's surfaces (next subsection); (ii) how small changes in/at the waveguide alter the solutions (Subsec. 3.1.9); and (iii) how an ultrasonic beam is reflected from the pipe wall (Subsec. 6.3.2).

3.1.8 Excitation of guided waves

It is of interest to determine how waveguide modes will be excited when tractions are prescribed at the boundary of the guide or when body forces act in its interior. This will be used in Sec. 5.1 to describe the response of waveguide transducers and in Sec. 6.3 to describe the incidence and reflection of acoustic waves from a plate.

The configuration is presented in Fig. 3.8. Traction $\mathbf{t}(x, y)$ are prescribed at the plate's surfaces over the segment $x \in [0, w]$. The region of excitation may also contain an applied force density distribution $\mathbf{f}(x, y)$ in its interior. As a result, guided waves propagate away to both sides of the source region, but we restrict attention to the right-propagating ones as the others are analogous. We seek the amplitudes $A_n(x)$ at axial position x of each of the propagating modes with $c_e > 0$. Note that sufficiently far away from the sources, the field is fully determined by the propagating waves because nonpropagating modes are evanescent.

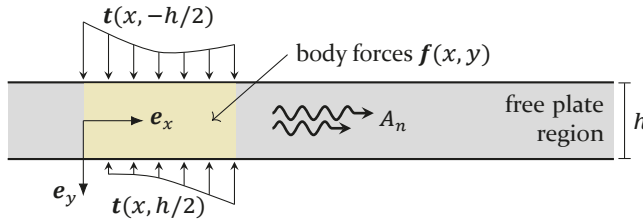


Figure 3.8: Plate with prescribed tractions and applied body forces over the region $x \in [0, w]$. Guided waves are excited in the free plate region to the right.

The general idea on how the excitation of guided waves can be modeled is laid out first. The prescribed forces and tractions lead to motions inside the waveguide, which can be regarded as a superposition of modal motions, as seen in the previous section. The interaction of the imposed forces/tractions with the waveguide motions results in mechanical power that is injected into the waveguide. The injected power needs to be found in the power flux of all modes. Due to their orthogonality property, it is also possible to uniquely determine the allocation of power in each of the modes.

The reciprocity relation given in (2.54) can be used together with the mode orthogonality property in (3.22) to determine the excitation of modes. The theory is presented according to Auld [41] and is also found in more detail in Kino [70]. Recall that all fields vary as $e^{-i\omega t}$. The elastodynamic state 1 shall be an arbitrarily prescribed state $(\mathbf{v}(x, y), \mathbf{T}(x, y))$, while state 2 is the field of the n th mode, i.e., $(\mathbf{v}_n(y), \mathbf{T}_n(y)) e^{ik_x n x}$, for which $\mathbf{f}_2 = \mathbf{0}$. Inserting into (2.54), integrating over the waveguide cross section $y \in [-h/2, h/2]$ and dropping the exponential term yields

$$\begin{aligned} & (\partial_x - ik_{xn}^*) \int_{-h/2}^{h/2} (-\mathbf{v}_n^* \cdot \mathbf{T} - \mathbf{v} \cdot \mathbf{T}_n^*) \cdot \mathbf{e}_x dy \\ & + \mathbf{e}_y \cdot \int_{-h/2}^{h/2} \partial_y (-\mathbf{v}_n^* \cdot \mathbf{T} - \mathbf{v} \cdot \mathbf{T}_n^*) dy = \int_{-h/2}^{h/2} \mathbf{v}_n^* \cdot \mathbf{f} dy, \end{aligned} \quad (3.23)$$

where no summation over the index n is implied.

The first term needs further treatment. For this, we assume that the arbitrary state 1 is expandable in terms of the modal solutions as

$$\mathbf{v} = \sum_m a_m(x) \mathbf{v}_m(y), \quad \mathbf{T} = \sum_m a_m(x) \mathbf{T}_m(y), \quad (3.24)$$

Thereby, the scalar weighting functions $a_m(x)$ denote the *axial field variations* of mode m that are to be determined. The above expansions together with definition (3.21) further simplify (3.23) to

$$(\partial_x - ik_{xn}^*)4 \sum_m a_m(x)P_{mn} = f_{sn}(x) + f_{vn}(x), \quad (3.25)$$

where

$$f_{sn}(x) \stackrel{\text{def}}{=} \mathbf{e}_y \cdot [\mathbf{v}_n^* \cdot \mathbf{T}]_{y=-h/2}^{y=h/2} = [\mathbf{v}_n^* \cdot \mathbf{t}]_{y=h/2} + [\mathbf{v}_n^* \cdot \mathbf{t}]_{y=-h/2}, \text{ and} \quad (3.26)$$

$$f_{vn}(x) \stackrel{\text{def}}{=} \int_{-h/2}^{h/2} \mathbf{v}_n^* \cdot \mathbf{f} \, dy \quad (3.27)$$

denote the surface sources and the volume sources, respectively. The expression for f_{sn} was obtained by integrating the second term in (3.23) and taking into account the stress free BCs of the waveguide modes, i.e., $\mathbf{e}_y \cdot \mathbf{T}_n|_{y=\pm h/2} = 0$.

According to the orthogonality relation given in (3.22), the sum $\sum_m a_m(x)P_{mn}$ is nonzero only for one value of m . For propagating modes, this is the case when $m = n$, in which case we also have $k_{xn}^* = k_{xn}$ and P_{nn} is given by \bar{P}_n in (3.14). With this in mind, the equation governing the variations $a_n(x)$ of propagating modes finally reduces to [41]

$$4\bar{P}_n(\partial_x - ik_{xn})a_n(x) = f_{sn}(x) + f_{vn}(x). \quad (3.28)$$

The modal field is harmonic in x , therefore, the axial variations must be of the form $a_n(x) = A_n(x) e^{ik_{xn}x}$, where $A_n(x)$ denotes the *modal envelope/amplitude*. The above equation is solved by multiplying with $e^{-ik_{xn}x}$, grouping the left hand side terms as $\partial_x(a_n(x) e^{-ik_{xn}x}) = \partial_x A_n(x)$ and integrating. This yields the modal envelope [70]

$$A_n(x) = \frac{1}{4\bar{P}_n} \int_{-\infty}^x [f_{sn}(\xi) + f_{vn}(\xi)] e^{-ik_{xn}\xi} \, d\xi. \quad (3.29)$$

Special interest might lie on the free plate region without sources, when the mode's envelope has settled to its final amplitude. In this case, the upper integral limit can be extended to $+\infty$ because $f_{sn} = f_{vn} = 0$ outside $[0, w]$.

It is then identified as the spatial Fourier transform defined in (2.32). The resulting constant amplitude in the free plate region can be expressed as

$$A_n = \frac{1}{4\bar{P}_n} [\mathcal{F}_x f_{sn}(x) + \mathcal{F}_x f_{vn}(x)]|_{k_x=k_{xn}}, \quad \text{for } x > w. \quad (3.30)$$

3.1.9 Perturbation theory

Given a waveguide solution, perturbation calculations can be used to approximate the solution under slightly changed waveguide conditions, e.g., changed boundary conditions or material parameters. The great advantage is that an *analytical expression* relating the perturbed and the unperturbed fields is obtained. Auld [41] derives both interior as well as boundary perturbation formulas for waveguides and this is presented in the following. We will make use of the resulting perturbation formulas in Chap. 7 for sensitivity analysis of waveguide parameters.

Boundary perturbations are obtained using the reciprocity relation (2.54). Solution “2” is taken to be the known solution, which is required to be a nondissipative and closed waveguide solution with real wavenumber k_x [41]. On the other hand, solution “1” shall represent the perturbed solution with wavenumber k'_x . Note that the perturbation might be lossy, leading to complex valued k'_x . With this, the two fields are of the form $\mathbf{v}_2 = \mathbf{v}(y) e^{ik_x x}$, $\mathbf{v}_1 = \mathbf{v}'(y) e^{ik'_x x}$, etc., where the time dependence $e^{-i\omega t}$ has been dropped. The procedure is the same as for derivation of the mode orthogonality relation (except that here k'_x is not modal and $k'_x \approx k_x$) and the result may be taken from (3.20), yielding the *boundary perturbation formula* [41]:

$$\Delta k_x = k_x - k'_x \approx \frac{-i\mathbf{e}_y \cdot (-\mathbf{v}^* \cdot \mathbf{T}' - \mathbf{v}' \cdot \mathbf{T}^*)|_{-h/2}^{h/2}}{4\bar{P}}, \quad (3.31)$$

where the factor P_{mn} given in (3.21) has been approximated by $P_{mn} \approx P_{nn} = \bar{P}$ assuming a small perturbation. In order to obtain the change in wavenumber, the perturbed field \mathbf{v}' , \mathbf{T}' needs to be approximated according to the current situation, e.g., fluid loading, a thin layer overlay, etc.

Interior perturbations can be performed by first deriving a reciprocity relation similar to (2.54) but where solution “2” corresponds to nondissipative material parameter ρ , \mathbf{c} , while solution “1” corresponds to different (possibly dissipative) constitutive parameters denoted as ρ' , \mathbf{c}' . The resulting relation includes the parameter differences $\Delta\rho = \rho' - \rho$ and $\Delta\mathbf{c} = \mathbf{c}' - \mathbf{c}$. For details refer to Ref. [41].

With the same steps and field ansatz as for the above boundary perturbation, the following *interior perturbation formula* is obtained [41]:

$$\Delta k_x = k_x - k'_x \approx \frac{\omega}{4P} \int_{-h/2}^{h/2} \Delta \rho \mathbf{v}^* \cdot \mathbf{v}' - \mathbf{S}^* : \Delta \mathbf{c} : \mathbf{S}' dy. \quad (3.32)$$

Note that, thereby, the boundary terms have vanished in virtue of the traction-free boundary conditions satisfied by both the perturbed and unperturbed fields.

3.2 Quasi-guided waves in fluid-coupled plates

We now turn to analyze the propagation of waves in an *open plate*, i.e., energy is allowed to flow across the plate's boundaries. This is achieved by replacing one or both vacuum half-spaces in Fig. 3.1 by a material that supports mechanical wave propagation. We will consider a perfectly inviscid fluid for this purpose. An elastodynamic wave propagating in the plate may then radiate an acoustic wave into the fluid, thereby transporting energy away from the plate. The reverse process is also feasible. Moreover, perfectly guided waves that do not radiate energy also exist. Overall, we will collectively refer to these waves as *quasi-guided waves (QGWs)*.

A novel representation, solution procedure and analysis for QGWs is developed in Subsecs. 3.2.2 to 3.2.5 as well as 3.2.8. Most of these discussions have been presented by the author in [P3] and [P5]. The dispersive behavior and wave field of leaky waves is known in the literature, but we revisit the topics in more detail in the remaining subsections. Therewith, we hope to achieve a mostly complete presentation of the current state of knowledge on this open research topic.

This section restricts to Lamb-polarized waves in isotropic media. According to (2.29) the SH waves – exhibiting displacements purely tangential to the plate's faces – do not interact with the fluid. Consequently, the SH modes of the plate will remain unchanged when it is loaded by a fluid, see Subsec. 3.1.4.

3.2.1 Models for the fluid-coupled plate

Before deriving the QGW model, some remarks on how it relates to other models are in order. In principle, there are two substantially different kind of models for a plate that is in contact with a fluid half-space: (a) a full plate-fluid model and (b) an open plate model. Additionally, a mixture between the

two is obtained when truncating the fluid half-space at a finite distance from the plate. These three models and their advantages and disadvantages are discussed in the following.

Remember the guided wave ansatz (3.1). All models consider wave fields of this form, i.e., harmonic in time as $e^{-i\omega t}$ and in the x -coordinate as $e^{ik_x x}$. As the solutions are given analytically in t and x , only the y -coordinate remains as computational domain. The models differ in the treatment of this coordinate, which is unbounded due to the infinite extend of the fluid.

Full plate-fluid model

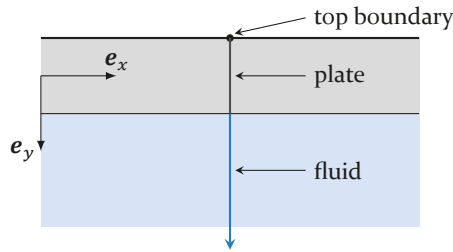


Figure 3.9: Plate with adjacent fluid half-space.

The plate and the fluid are described “as are”, i.e., on the unbounded domain $y \in [-h/2, \infty)$. The geometry is sketched in Fig. 3.9. This approach is necessary for a full description of the mechanics that includes the plate as well as its exterior, i.e., the fluid [50, 51, 75, 76]. For this reason, the corresponding eigensolutions, i.e., the solutions factorized in space and time [76], have been referred to as *modes of the universe* [76–78]. When considering nondissipative media, the model will be energy conserving because energy cannot “escape” the universe. Consequently, the eigensolutions form an orthonormal basis [76] in the conventional sense. This can be considered a major advantage of the model.

The spectrum, i.e., the possible values of k_x in the complex plane, consists of discrete and continuous parts [50, 75]. The discrete solutions are called *trapped modes* and describe waves that propagate along the plate without radiating into the half-space. The continuous parts are called *radiation modes* [50] and are required to describe exchange of energy between the plate and the fluid domain. The radiation modes are, hence, analogous to the plane bulk waves in an unbounded homogeneous medium (see Sec. 2.3), where we have two continua, one for the longitudinal waves and one for the transverse waves.

The radiation modes are different in that they include the inhomogeneity of the plate-fluid system.

To sum up, this model represents the overall wave field by a discrete sum of trapped modes plus an integral over the continuum of the radiation modes: $\mathbf{u}(x, y, \omega) = \sum \text{trapped modes} + \int \text{radiation modes}$ [75]. The main disadvantage of the model is that the continuum is difficult to handle mathematically and intricate to interpret physically. Moreover, if analytical solutions in the exterior domain are not known a-priori, it is difficult to compute the solutions [52].

Open plate model

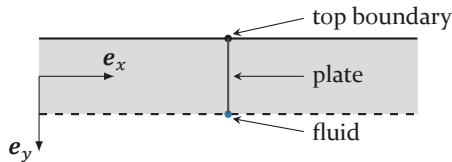


Figure 3.10: Geometry of the open plate: Energy can cross the bottom boundary.

Restricting attention to the plate itself leads to the open plate model. Thereby, the problem is reduced onto a bounded domain, namely $y \in [-h/2, h/2] \cup h^+$. The resulting geometry is depicted in Fig. 3.10. The plate is *open* in the sense that energy is not necessarily confined in the computational domain, but can leave or enter through the open boundary and is, therefore, not conserved. The boundary point denoted h^+ represents the region in the fluid next to the plate, i.e., $y \rightarrow h/2$ from above. As a consequence of the domain reduction, the degrees of freedom of the fluid domain have been reduced to just one scalar. This is sufficient to represent the effect that the fluid has on the plate, but not to fully describe the wave field in the fluid domain. In this sense, attention has indeed been *restricted* to the plate. However, we will see in Subsec. 3.2.7 that the exterior field is, nonetheless, approximated in restricted spatial and temporal regions.

The eigensolutions of this model will be denoted as *QGWs* throughout this monograph. They form a *purely discrete spectrum*, which represents the *resonances of the plate* [79]. It is, therefore, much easier to deal with mathematically and conceptually, because every field contribution is associated to one resonance instead of a continuum of modes. In most cases, just a few such eigensolutions are sufficient to represent an arbitrary field in the plate with high accuracy. This is possible because the overall wave field in the plate

is highly dominated by its resonances. In this sense, the model converges much faster.

There is one major difficulty with the open plate model: the eigenfunctions diverge with distance from the plate [75], see Subsec. 3.2.7 for details. As a consequence, the eigensolutions are not (normal) modes in the usual sense [46, 79]. Instead, a generalization was developed applicable to open systems called *quasinormal modes (QNMs)* [54, 76–80], also known as *resonant states* or *Gamow states*. This precise mathematical framework closely resembles normal modes of conservative systems and allows the existing mathematical tools to be utilized. For the best of the authors knowledge, this concept has not yet been introduced in ultrasonics. However, it is widely employed in other physical disciplines, e.g., in astrophysics to describe gravitational waves from black holes [55], in quantum physics to model confined particles [76] and in classical electromagnetism/optics to describe leaky resonators [77, 79]. More recently, leaky optical waveguides have also been studied in the context of QNMs [52].

According to Ref. [77], the QNMs of a resonator will form a complete set if (i) the material parameters exhibit one or more discontinuities and (ii) the material parameters approach a constant value sufficiently rapidly with $y \rightarrow \infty$. Thereby, the completeness property holds *only on the interior* of the resonator. Condition (i) is very intuitive because it provides a natural definition of the interior, namely the region between the two outermost discontinuities. Furthermore, the QNMs are orthogonal under a suitable definition of the inner product [77].

The two conditions for completeness are met by the fluid-coupled plate, where the discontinuities correspond to the plate's faces. Hence, we expect QNM theory to be applicable to wave propagation in the fluid-coupled plate. Although we are able to compute the QGW solutions, see Sec. 3.2.2 and 4.2, no accompanying QNM theory has been developed so far. This would be highly desirable because further in-depth analysis, e.g., perturbation of the solutions, would be possible.

Similar to the full plate-fluid model, the open plate accepts both outgoing as well as incoming solutions. These correspond to waves with power flux out of the plate or into the plate, respectively. The latter are usually disregarded a-priori by applying a radiation condition [49, 79, 81, 82]. Our approach is to keep the incoming solutions and (if necessary) discard them after solving the QGW problem. Note that incoming waves are easily identified, see Subsec. 3.2.5.

Truncated fluid model (PML model)

A third modeling approach is to truncate the fluid domain at certain distance from the plate with an additional finite or infinite layer, see Fig. 3.11. The wave field is damped in this layer until it has (hopefully) vanished. This ensures that the bottom of the computational domain does not affect the solutions. The finite truncation layer seen in Fig. 3.11b, for example, removes the effect of the undesired bottom boundary. The solutions obtained using a finite truncation layer are expected to be similar to the ones of the infinite layer if the wave field has been sufficiently attenuated when it reaches the artificially introduced bottom boundary, i.e., if the damping and the layer size are large enough.

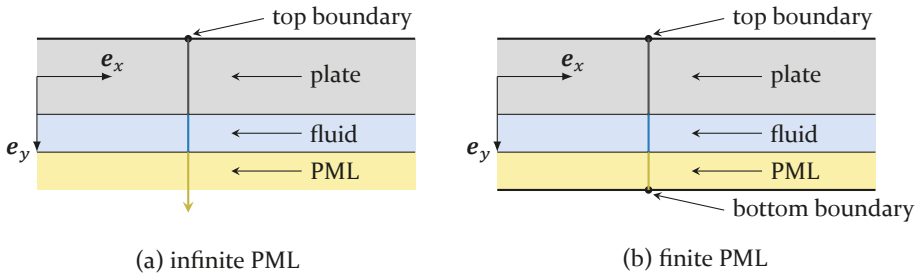


Figure 3.11: Plate with fluid truncated by a PML layer.

Two widely used methods exist to implement the truncation layer:

Absorbing layer: A medium with increasing dissipation is used in the truncating layer [83]. Careful design is necessary to minimize reflections at the interface between fluid and absorbing layer.

Perfectly matched layer (PML): The elastodynamic equations are extended onto complex x -coordinates on the truncating layer [75, 84]. Energy can smoothly transition from the real domain to the complex domain. If correctly designed, this will ensure an efficient damping of the wave field in the PML's domain and avoids reflections from the fluid-PML interface.

The consequences of introducing a truncation layer will be discussed by means of the PML method as presented in Ref. [75]. Such a model for the plate-fluid system can be regarded as a *mixture* between the full plate-fluid model and the open plate model [75]. Indeed, this is also reflected in the resulting spectrum. In case of the infinite PML, it consists of the trapped modes, a finite number of *QGWs* and a continuum of so-called *PML-modes*. By truncating the PML

to a finite domain, the continuum of PML-modes is sampled, resulting in a purely discrete spectrum in this case [84].

This model is applicable to general geometries and simple to implement. A further major advantage is that it leads to a complete set of eigensolutions, i.e., they are capable of representing arbitrary fields in the plate and the fluid [84]. Although the PML-modes have often been regarded as spurious and undesired [85], they are actually important for a full description of the field in the fluid [84]. Note, moreover, that the PML removes incoming waves.

For waveguide design and analysis, usually the dispersion curves are of foremost interest. In this case, it is necessary to elaborately discard the PML-modes with somewhat arbitrary conditions on the computed wavenumbers. This is a very common approach to obtain dispersion curves [83, 85–87] but results in an *incomplete open waveguide spectrum* because not all QGW are included. The number of “revealed” QGWs depends on the free parameters of the PML [75]. In general, the solutions are highly dependent on these free parameters, which are unrelated to the physics. Using inappropriate parameter values might lead to incorrect results, which means that a basic a-priori understanding of the solutions is required. A further disadvantage is that the truncated fluid model is computationally more expensive compared to the open plate because the fluid and the PML regions usually need to be discretized with many more degrees of freedom than the plate itself. The mentioned circumstances make this method somewhat unattractive. Nonetheless, if used correctly, it is a powerful method, especially in applications where the wave field in the fluid domain is of high relevance.

3.2.2 QGW problem formulation

After reviewing possible models for the fluid-coupled plate and the nature of the corresponding harmonic solutions, we will now derive the governing equations of the open plate problem. Consider for this end wave propagation in a homogeneous, isotropic, linearly elastic plate with single-sided fluid loading as depicted in Fig. 3.12.

Seeking plane harmonic solutions, the same ansatz as in (3.1) is used for the plate. The field in the fluid domain is known a-priori to be a longitudinal inhomogeneous plane wave (see Subsec. 2.1.4) with displacement amplitude U and has the form

$$\mathbf{u}_f(\mathbf{x}, t) = i \underbrace{\frac{\mathbf{k}_f}{\kappa_f}}_{\mathbf{u}_f(\mathbf{k}_f, \omega)} U e^{i(\mathbf{k}_f \cdot \mathbf{x} - \omega t)}, \quad (3.33)$$

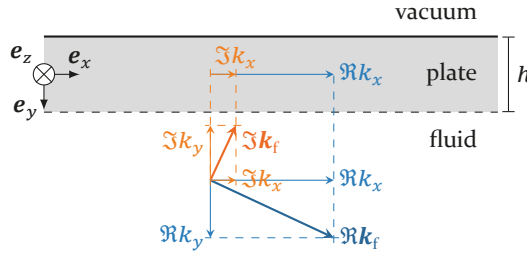


Figure 3.12: Plate with adjacent fluid.

with the wave vector $\mathbf{k}_f = k_x \mathbf{e}_x + k_y \mathbf{e}_y$, see Fig. 3.12. The QGW changes in amplitude as the wave propagates along the plate because it exchanges energy with the fluid half-space. This needs to be accounted for by allowing the wavenumber k_x to be complex, i.e., the problem consists of *inhomogeneous plane waves* according to Subsec. 2.3.1. According to the *generalized Snell's law* [42], the tangential wavenumber components in the plate and the fluid coincide, i.e., k_x in the fluid and the plate are identical, this is sketched in Fig. 3.12. We recall from (2.68a) that the wave in the nondissipative fluid half-space, which is a longitudinal wave, is required to fulfill the dispersion relation

$$\mathbf{k}_f \cdot \mathbf{k}_f = k_x^2 + k_y^2 = \rho \omega^2 / \lambda_L^f =: \kappa_f^2 = \omega^2 / c_f^2 \in \mathbb{R}. \quad (3.34)$$

Therefore, if k_x^2 is complex, k_y^2 also needs to be complex. Furthermore, with known k_x the *direction of the attenuation vector* $\Im \mathbf{k}_f$ is *uniquely determined*, as it is necessarily orthogonal to the propagation vector $\Re \mathbf{k}_f$ and at the same time satisfies Snell's law. For example in Fig. 3.12, the attenuation vector will point towards the plate if the QGW is attenuated in \mathbf{e}_x , i.e., $\Im k_x > 0$; otherwise it points away from the plate. With this restriction, $k_y = \pm \sqrt{\kappa_f^2 - k_x^2}$ is uniquely determined given k_x .

Plate-fluid interface conditions

Proceeding as in Sec. 3.1, we see that the equation of unforced motion of the plate is valid without modification. Merely the bottom boundary condition changes according to the interface conditions between solid and fluid media introduced in (2.29). For this end we need the acoustic pressure, which we write in terms of the displacement in the fluid \mathbf{u}_f as

$$p(\mathbf{k}_f, \omega) = -\lambda_L^f \mathbf{i} \mathbf{k}_f \cdot \mathbf{u}_f(\mathbf{k}_f, \omega) = \lambda_L^f \kappa_f(\omega) U = Z_f \omega U. \quad (3.35)$$

A formulation in terms of the displacement amplitude U yields a term that is linear in ω , while a formulation using a displacement potential would result in $\sim \rho_f \omega^2$. We opted for the former representation because U has units that are consistent with the unknown \mathbf{u} in the plate.

Using the differential operator \mathcal{G} defined in (3.2), it is now possible to write out the interface conditions stated in (2.25a) and (2.26) in terms of k_x and ∂_y . This gives

$$\overbrace{[(ik_x \mathbf{B}_1 + \mathbf{B}_0 \partial_y) \cdot \mathbf{u}(y)]}^{\mathbf{e}_y \cdot \mathbf{T}} \Big|_{y=h/2} + \overbrace{Z_f \omega U}^p \mathbf{e}_y \stackrel{!}{=} \mathbf{0}, \quad (3.36a)$$

$$Z_f \omega \mathbf{e}_y \cdot \mathbf{u}(y) \Big|_{y=h/2} - \underbrace{ik_y \lambda_L^f U}_{Z_f \omega \mathbf{e}_y \cdot \mathbf{u}_f} \stackrel{!}{=} 0, \quad (3.36b)$$

whereby the displacement continuity equation was multiplied with $Z_f \omega = \lambda_L^f \kappa_f$ in order to obtain equations with consistent units.

The quasi-guided wave problem

Compared to waves in a free plate, there is *one additional scalar degree of freedom*, namely U , which can be determined with the additional equation (3.36b). Introducing the new vector of unknowns

$$\underline{q}(y) = [\mathbf{u}(y), U]^\top, \quad (3.37)$$

and rewriting the equation of motion (3.4a) and the interface conditions (3.36) accordingly yields the *QGW problem*:

$$\left[(ik_x)^2 \underline{\underline{L}}_{=2} + ik_x \underline{\underline{L}}_{=1} \partial_y + \underline{\underline{L}}_{=0} \partial_y^2 + \omega^2 \underline{\underline{M}} \right] \cdot \underline{q}(y) = \underline{0} \quad \text{on } y \in (-h/2, h/2), \quad (3.38a)$$

$$\left[ik_x \underline{\underline{B}}_{=1} + \underline{\underline{B}}_{=0} \partial_y + \omega \underline{\underline{B}}_{=\omega} + ik_y \underline{\underline{B}}_{=y} \right] \cdot \underline{q}(y) = \underline{0} \quad \text{at } y = \pm h/2. \quad (3.38b)$$

Thereby, the introduced matrices $\underline{\underline{L}}_i$ and $\underline{\underline{M}}$ can be written with the tensors for Lamb waves given in (3.12) as

$$\underline{\underline{L}}_{=2} = \begin{bmatrix} \underline{\underline{L}}_2 & \mathbf{0} \\ \mathbf{0} & 0 \end{bmatrix}, \quad \underline{\underline{L}}_{=1} = \begin{bmatrix} \underline{\underline{L}}_1 & \mathbf{0} \\ \mathbf{0} & 0 \end{bmatrix}, \quad \underline{\underline{L}}_{=0} = \begin{bmatrix} \underline{\underline{L}}_0 & \mathbf{0} \\ \mathbf{0} & 0 \end{bmatrix}, \quad \underline{\underline{M}} = \begin{bmatrix} \rho \mathbf{I} & \mathbf{0} \\ \mathbf{0} & 0 \end{bmatrix}, \quad (3.39)$$

while the new boundary matrices $\underline{\underline{B}}_i$ make use of the Lamb boundary tensors from (3.13) and are given by

$$\underline{\underline{B}}_1 = \begin{bmatrix} \mathbf{B}_1 & \mathbf{0} \\ \mathbf{0} & \mathbf{0} \end{bmatrix}, \quad \underline{\underline{B}}_0 = \begin{bmatrix} \mathbf{B}_0 & \mathbf{0} \\ \mathbf{0} & \mathbf{0} \end{bmatrix}, \quad \underline{\underline{B}}_\omega = \begin{bmatrix} \mathbf{0} & Z_f \mathbf{e}_y \\ Z_f \mathbf{e}_y & 0 \end{bmatrix}, \quad \underline{\underline{B}}_y = \begin{bmatrix} \mathbf{0} & \mathbf{0} \\ \mathbf{0} & -\lambda_L^f \end{bmatrix}. \quad (3.40)$$

Note that the formulation of the BC (3.38b) is also valid for the plate's free surface by setting $\lambda_L^f = Z_f = 0$.

Nontrivial solutions for $q(y)$ satisfying (3.38) are sought. Hence, similar to Lamb waves in a free plate, quasi-guided waves are determined by an EVP.

Observe that the transversal wavenumber $k_y = \pm \sqrt{\kappa_f^2 - k_x^2}$ appears explicitly in the BC (3.38b). For this reason, the EVP is no longer a polynomial EVP in k_x but a more *generally nonlinear EVP*. This fact makes it substantially more difficult to obtain the QGW solutions. To point out the resulting complexity, the following remarks are in order:

Nonlinear: The square root term is highly nonlinear and poses a challenge even for modern nonlinear eigenvalue solvers.

Nonunique: The term is nonunique as the square root has two solutions (emphasized by the \pm -sign). Both satisfy the equations but correspond to different eigenvectors.

Nonholomorphic: The square root is nonholomorphic. As a consequence, an approximate representation using a power series is not feasible, i.e., this approach cannot be used to convert the problem to an easier to solve polynomial EVP.

Numerical methods exist to solve nonlinear EVPs [88, 89]. These are usually based on iterative linearization of the equations [88, 90, P11]. In contrast to linear eigenvalue solvers, these methods are often computationally demanding and might miss eigensolutions. Contour integration techniques are also employed to transform a holomorphic nonlinear EVP [91] to a linear one inside an appropriately chosen region of the complex k_x -plane. For this purpose, it is first necessary to remove singular points and ensure the uniqueness of the EVP. The method yields spurious solutions, which have to be discarded appropriately [91].

3.2.3 Polynomial form of the QGW problem through change of variable

A technique was developed in this work that avoids the difficulties inherent to nonlinear eigenvalue solvers. The procedure has been published and discussed in Refs. [P3, P9, P14]. It is based on a trigonometric change of variables inspired by Hood [92], where a somewhat different nonlinear EVP is solved that models a radio-frequency gun cavity (particle accelerator component). Independently, a similar procedure has been developed in Ref. [57] to obtain leaky wave solutions of optical waveguides in terms of the transversal wavenumber.

We transform the QGW problem into polynomial form by the change of variable

$$ik_x \stackrel{\text{def}}{=} \frac{i\kappa_f}{2}(\gamma + \gamma^{-1}), \quad (3.41a)$$

$$\Rightarrow ik_y = \pm \frac{\kappa_f}{2}(\gamma - \gamma^{-1}) = i\sqrt{\kappa_f^2 - k_x^2}, \quad (3.41b)$$

with the new variable $\gamma \in \mathbb{C} \setminus 0$. Substituting the above definitions into the QGW problem (3.38) results in a rational EVP of the form

$$\underbrace{\left[\gamma^2 \underline{G}_{\underline{2}} + \gamma i \underline{G}_{\underline{1}} \partial_y + (\underline{G}_{\underline{0}} \partial_y^2 + 2\underline{G}_{\underline{2}} + \omega^2 \underline{M}) + \gamma^{-1} i \underline{G}_{\underline{1}} \partial_y + \gamma^{-2} \underline{G}_{\underline{2}} \right]}_{\underline{W}_r(\gamma)} \cdot \underline{q}(\gamma) = \mathbf{0}, \quad (3.42a)$$

$$\underbrace{\left[\gamma i \underline{\Gamma}_{\underline{d}}^{\mp} + \underline{\Gamma}_{\underline{0}} \partial_y + \omega \underline{\Gamma}_{\underline{\omega}} + \gamma^{-1} i \underline{\Gamma}_{\underline{d}}^{\pm} \right]}_{\underline{B}_r^{\pm}(\gamma)} \cdot \underline{q}(\gamma)|_{y=\pm h/2} = \mathbf{0}, \quad (3.42b)$$

in γ , where $\underline{G}_{\underline{2}} = -\frac{\kappa_f^2}{4} \underline{L}_{\underline{2}}$, $\underline{G}_{\underline{1}} = \frac{\kappa_f}{2} \underline{L}_{\underline{1}}$, $\underline{G}_{\underline{0}} = \underline{L}_{\underline{0}}$ and $\underline{\Gamma}_{\underline{0}} = \underline{B}_{\underline{0}}$, $\underline{\Gamma}_{\underline{\omega}} = \underline{B}_{\underline{\omega}}$, $\underline{\Gamma}_{\underline{d}}^{\pm} = \frac{\kappa_f}{2} (\underline{B}_{\underline{1}} \pm i \underline{B}_{\underline{y}})$. The matrix $\underline{\Gamma}_{\underline{d}}^{\pm}$ is the only complex one and includes dissipation due to radiation losses. While $\underline{B}_r^+(\gamma)$ is due to the positive sign in (3.41b), $\underline{B}_r^-(\gamma)$ corresponds to the negative sign.

Furthermore, we can multiply (3.42a) and (3.42b) with γ^2 , which for our matters yields an equivalent [P₃] polynomial EVP:

$$\left[\gamma^4 \underline{\underline{G}}_2 + \gamma^3 i \underline{\underline{G}}_1 \partial_y + \gamma^2 (\underline{\underline{G}}_0 \partial_y^2 + 2 \underline{\underline{G}}_2 + \omega^2 \underline{\underline{M}}) + \gamma i \underline{\underline{G}}_1 \partial_y + \underline{\underline{G}}_2 \right] \cdot \underline{q}(y) = \mathbf{0}, \quad (3.43a)$$

$$\left[\gamma^3 i \underline{\underline{\Gamma}}_{+1} + \gamma^2 \left(\underline{\underline{\Gamma}}_0 \partial_y + \omega \underline{\underline{\Gamma}}_\omega \right) + \gamma i \underline{\underline{\Gamma}}_{-1} \right] \cdot \underline{q}(y)|_{y=\pm h/2} = \mathbf{0}. \quad (3.43b)$$

Polynomial EVPs as in (3.43) are very common and much easier to solve because they have a linear representation in a higher-dimensional state-space [88]. Note that this linearization is not an approximation, but rather an equivalent representation. It is worth remarking that the linearized representation is not unique and some might be more appealing for numerical implementation than others [88, 93]. The easiest and most widely used one is the *companion linearization* [88]. After linearization, the discretized problem can be solved using conventional linear numerical eigenvalue solvers, thereby inheriting all advantages that these solvers provide. This procedure is fast and reliable as it finds all solutions. After solving for the eigenvalue γ , the axial and transversal wavenumbers are easily obtained by substituting into the definition (3.41a) and (3.41b).

The implemented Elastodynamic Acoustic Toolbox (EDAT) relies on a spectral collocation (SC) scheme to discretize and solve the QGW problem, see Chap. 4 for details. The solution of a 1 mm thick aluminum plate coupled on one side to glycerol is shown in Fig. 3.13. Note the high degree of symmetry in the three spectra. Depending on the choice of sign in (3.41b), we obtain two different EVPs. In the next section, we will see that each one of them uniquely and fully describes the QGWs, i.e., only one needs to be solved.

3.2.4 Structure of the QGW problem

Let's discuss the structure associated to the change of variable (3.41) and the QGW problem (3.42) or (3.43). This structure provides valuable information about the expected spectrum.

Sign convention: The variable change $\gamma \mapsto \gamma^{-1}$ represents the choice of sign of k_y , see (3.41b). At the same time, k_x remains invariant.

Palindromicity: $\underline{\underline{W}}_r$ is palindromic [94], meaning that $\underline{\underline{W}}_r(\gamma) = \underline{\underline{W}}_r(\gamma^{-1})$, i.e., if the terms sorted by power of γ are reversed in order, the matrix

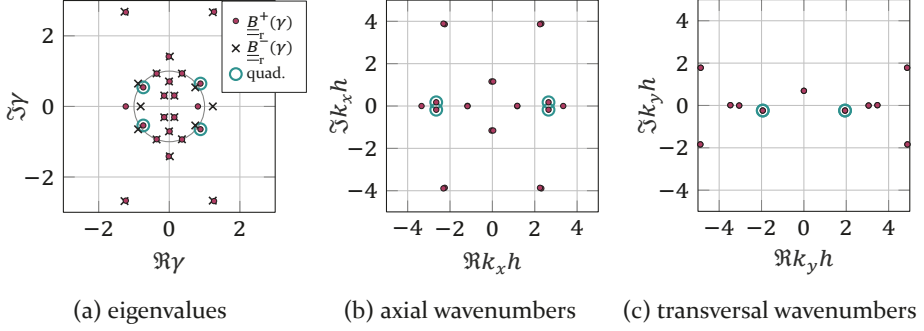


Figure 3.13: Spectrum of the eigenvalues and wavenumbers at 1 MHz mm. The unit circle is shown in (a) for reference. One quadruple solution (always appear together) has been marked. Note that in the k_y -domain, the four marked points collapse onto two double points.

function remains unaltered. This does not hold for $\underline{\underline{B}}_r^\pm$, however, we find the important relation $\underline{\underline{B}}_r^\mp(\gamma^{-1}) = \underline{\underline{B}}_r^\pm(\gamma)$. Hence, if γ_n is an eigenvalue corresponding to $\underline{\underline{B}}_r^+$, then γ_n^{-1} will be an eigenvalue due to $\underline{\underline{B}}_r^-$. We conclude that the two EVPs obtained by the choice of sign lead to inverted γ -spectra.

Conjugate parity: $\underline{\underline{W}}_r$ is conjugate even [94], i.e., $\underline{\underline{W}}_r(\gamma) = \underline{\underline{W}}_r^*(-\gamma) = \underline{\underline{W}}_r^*(-\gamma^{-1})$. Furthermore, the relation $\underline{\underline{B}}_r^{\pm*}(-\gamma^{-1}) = \underline{\underline{B}}_r^\pm(\gamma)$ holds because $\underline{\underline{\Gamma}}_d^{\pm*} = \underline{\underline{\Gamma}}_d^\mp$. As a result, if γ_n is an eigenvalue then $-\gamma_n^{*-1}$ will also be an eigenvalue.

The above properties have important consequences. Due to the first two, the choice of sign in (3.41b) and correspondingly (3.42b) or (3.43b) is irrelevant [P3]. $\underline{\underline{B}}_r^+$ and $\underline{\underline{B}}_r^-$ yield inverted γ -spectra. However, γ and γ^{-1} lead to the same axial wavenumbers k_x and – considering the respective choice of sign in (3.41b) – they also lead to the exact same transversal wavenumbers k_y . As a result, the two problems formulated by $\underline{\underline{B}}_r^+$ and $\underline{\underline{B}}_r^-$ are fully equivalent in terms of the wavenumbers (albeit not in γ) and any one of them *fully* and *uniquely* describes the QGW spectrum. Without loss of generality, we choose the positive sign in (3.41b), i.e., we set $\underline{\underline{B}}_r \stackrel{\text{def}}{=} \underline{\underline{B}}_r^+$, and solve the corresponding QGW problem obtaining the full set of solutions. This is a remarkable feature of the proposed solution method [P3].

Moreover, due to the geometric symmetry, if k_x is a solution, $-k_x$ must also be a solution corresponding to a wave propagating in opposite direction. This

implies that if γ_n is a solution, either $-\gamma_n$ or $-\gamma_n^{-1}$ must also be one. Together with the conjugate parity property, the truly complex eigenvalues due to \underline{B}_r^+ are seen to appear in quadruples, namely $\{\gamma_n, -\gamma_n^{-1}, \gamma_n^*, -\gamma_n^{*-1}\}$. Overall, the symmetries in the γ - and (k_x, k_y) -spectra are summarized in Table 3.2. An exemplary quadruple has been highlighted in Fig. 3.13.

Table 3.2: The eigenvalues γ appear in quadruples, which leads to the specified symmetries in the spectrum. The corresponding axial and transversal wavenumbers are specified exemplarily.

solution	wave vector	$\Re k_x$	$\Im k_x$	$\Re k_y$	$\Im k_y$	denotation
γ	(k_x, k_y)	+	+	+	-	outgoing forward
$-\gamma^{-1}$	$(-k_x, k_y)$	-	-	+	-	outgoing forward
γ^*	$(k_x^*, -k_y^*)$	+	-	-	-	incoming backward
$-\gamma^{*-1}$	$(-k_x^*, -k_y^*)$	-	+	-	-	incoming backward

3.2.5 Classification of waves

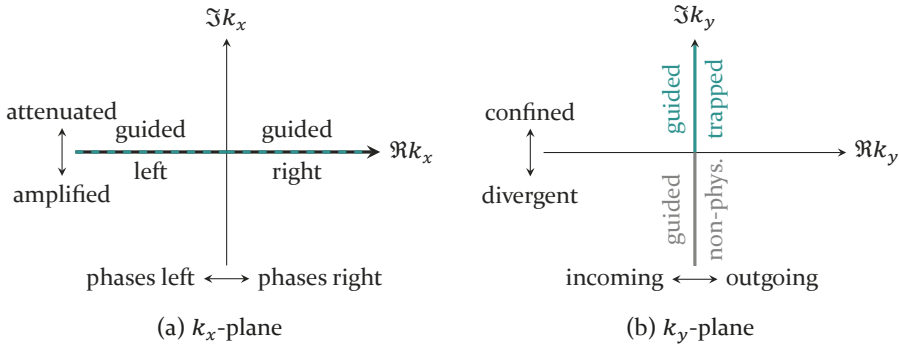


Figure 3.14: Classification of the QGWs according to their wavenumbers. The k_x -plane cannot distinguish between outgoing/incoming nor convergent/divergent waves. Similarly, in the k_y -plane it is not possible to identify the axial propagation direction of phases nor of attenuation.

The symmetry of the spectra leads to a natural classification of the waves according to their wavenumbers. Let's first examine the meaning of each of the wavenumber components before moving on to the actual classification.

First, the k_x -plane shown in Fig. 3.14a characterizes the wave field in the axial direction, i.e., along e_x . The real part identifies whether the phases of the waves **propagate right** (e_x) or **left** ($-e_x$), while the imaginary part leads to **attenuation** or **amplification** of the wave field in e_x . The imaginary part might also be zero, i.e., the waves propagate without attenuation, in which

case we call them (**perfectly**) **guided** or **trapped** if additionally $\Im k_y > 0$. The latter will be discussed in detail later on.

Second, the k_y -plane shown in Fig. 3.14b characterizes the wave field in transversal direction, i.e., along \mathbf{e}_y . Note that the energy flux in the fluid, and hence through the plate's boundary, is in direction $\Re k_f$. Therefore, $\Re k_y$ indicates whether energy flows out or into the plate. Moreover, based on $\Im k_y$ it is possible to differentiate between **divergent** and **confined** wave fields, depending on whether the field increases or decreases with distance from the plate. Notice that both solutions are physically possible in a limiting sense, i.e., for perfectly harmonic inhomogeneous plane waves. This will be discussed in detail in Subsec. 3.2.7.

Overall, based on both k_x and k_y it is possible to classify waves into the following three categories with two subcategories each:

Trapped waves: These waves have no transversal energy flux, i.e., $\Re k_y = 0$ and additionally they are confined within the proximity of the plate, i.e., $\Im k_y > 0$ (see Fig. 3.15). They could also be called *perfectly guided waves*, as in nondissipative media they propagate along the plate without attenuation, i.e., $\Im k_x = 0$. The trapped waves form the discrete modal spectrum [75] mentioned in Subsec. 3.2.1 that complements the radiation modes of the full plate-fluid model. In addition to the trapped waves, guided waves with diverging wave fields in transversal direction (Fig. 3.16), i.e., $\Im k_y < 0$, also satisfy the QGW-problem (3.43) [95–97]. This is considered unfeasible and the solutions are regarded as nonphysical [98]. Finally, we note that the confined and diverging guided waves form characteristic real-valued loops in the dispersion curves [96], a matter that will be discussed in more detail in Subsec. 3.2.9 and 3.2.10.



Figure 3.15: trapped wave



Figure 3.16: physically infeasible

Outgoing or leaky waves: The energy flux of outgoing/leaky waves is away from the plate, i.e., $\Re k_y > 0$. They describe acoustic radiation phenomena and attenuate as they propagate along the plate [46, 50, 75, 99]. If they are attenuated in the same direction as their phase propagation, i.e., if $\Im k_x$ is of same sign as $\Re k_x$, we call them **forward waves** (Fig. 3.17), otherwise we speak of **backward waves** [100] (Fig. 3.18). Note that energy considerations require that the attenuation of leaky waves must

always be in the same direction as their net energy flux in the plate.



Figure 3.17: forward leaky



Figure 3.18: backward leaky

Incoming waves: These waves exhibit energy flux towards the plate, i.e., $\Re k_y < 0$. They describe processes where energy in the fluid couples into the plate [101]. Incoming waves are the complementary waves to outgoing waves, having complex conjugate eigenvalues. They also appear as **forward** (Fig. 3.19) and **backward** (Fig. 3.20) waves but in this case the net energy flux in the plate is in opposite direction to the attenuation $\Im k_x$. This accounts for the fact that, as they propagate along the plate, they increase in amplitude due to the supply of energy. Incoming waves are most often disregarded a-priori by applying a *radiation condition* as discussed in Subsec. 3.2.1.



Figure 3.19: forward incoming

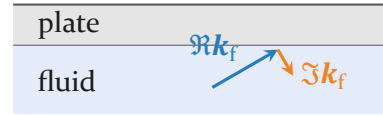


Figure 3.20: backward incoming

Only waves whose phases propagate to the right have been considered above. The same solutions propagating to the left also exist, giving a total of 12 categories. To characterize waves based on the wavenumbers, both their axial and transversal wavenumbers are required – one of them is not sufficient.

The eigenvalue γ is different to the wavenumbers in that it segregates each class of wave into a unique region in the γ -plane. The allocation of the 12 regions is displayed in Fig. 3.21. Explicitly in terms of the real part $\gamma_r = \Re \gamma$ and the imaginary part $\gamma_i = \Im \gamma$, the wavenumbers according to (3.41) read

$$k_x = \frac{\kappa_f \gamma_r (\gamma_r^2 + \gamma_i^2 + 1)}{2 \gamma_r^2 + \gamma_i^2} + i \frac{\kappa_f \gamma_i (\gamma_r^2 + \gamma_i^2 - 1)}{2 \gamma_r^2 + \gamma_i^2}, \quad (3.44a)$$

$$k_y = \frac{\kappa_f \gamma_i (\gamma_r^2 + \gamma_i^2 + 1)}{2 \gamma_r^2 + \gamma_i^2} + i \frac{\kappa_f (-\gamma_r) (\gamma_r^2 + \gamma_i^2 - 1)}{2 \gamma_r^2 + \gamma_i^2}, \quad (3.44b)$$

with $\gamma_r, \gamma_i \in \mathbb{R}$. As can be seen in the numerators, the real and imaginary parts of k_x and k_y will cross zero when crossing the $\Re \gamma$ -axis, the $\Im \gamma$ -axis and the unit circle. These define the regions in the γ -plane and are shown in Fig. 3.21.

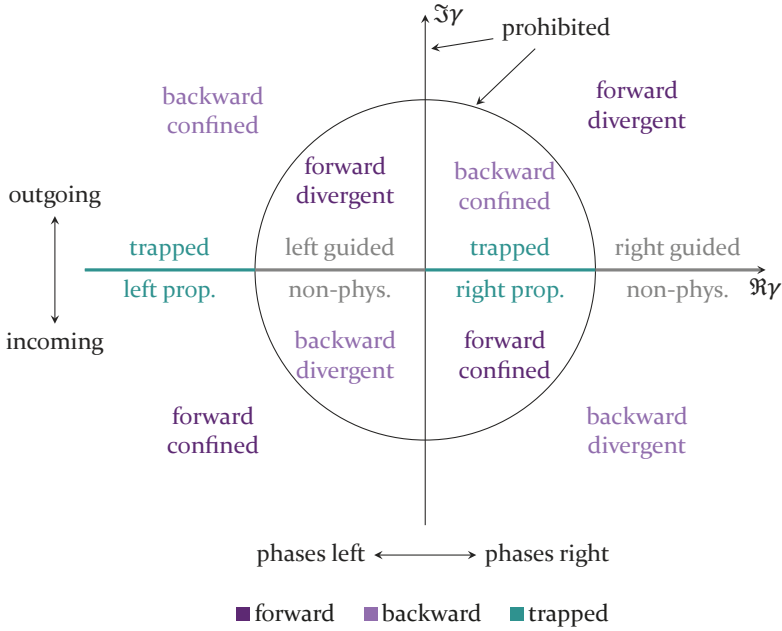


Figure 3.21: Classification of the QGWs in the γ -plane. Waves fully segregate into the 12 categories.

According to (3.44), waves on the $\Im\gamma$ -axis transport energy purely in \mathbf{e}_y . As the free plate surface is free of energy flux, energy considerations disallow such solutions. Waves whose eigenvalue is on the unit circle are perfectly guided, i.e., neither attenuated nor amplified. At the same time, the wave vector in the fluid would have a transversal component (except for real γ) with according energy flux. Therefore, this region is also prohibited. On the other hand, eigenvalues on the $\Re\gamma$ -axis can in fact be obtained and they do also represent perfectly guided waves. These can be trapped, i.e., confined to the proximity of the plate, or divergent. The latter are labeled “nonphysical”.

Due to the symmetry of the setup along the x -coordinate, the left propagating and right propagating waves must be identical if the coordinate is flipped. For the remainder, and throughout this monograph, only waves whose phases (or sometimes energy instead) propagate to the right will be discussed. Moreover, we will restrict attention to the outgoing waves, as the incoming ones are analogous. This leaves us with the first quadrant of Fig. 3.21, where we include the trapped waves on the real line but exclude the nonphysical guided waves. In terms of the wavenumbers, this is equivalent to restricting to $\Re k_x > 0$ with $\Re k_y \geq 0$ and $\Im k_y > 0$. Overall, three different kind of waves are found within

this restricted region, namely leaky forward, leaky backward and trapped waves. These will be examined in the following section.

3.2.6 Dispersion of quasi-guided waves

So far we examined and categorized the eigensolutions $(\gamma_n, \underline{q}_{-n})$ at one given frequency. The QGW problem can be solved for a range of frequencies to obtain dispersion curves $\gamma_n(\omega)$ and derived quantities. The frequency-dependent eigenvalues and wavenumbers of a brass plate coupled on one side to water are shown in Fig. 3.22. The eigenvalues in Fig. 3.22a move continuously with frequency – as would be expected – some of them on the real axis or close to the unit circle. These are the solutions of interest because they represent lowly attenuated waves (see Subsec. 3.2.5).

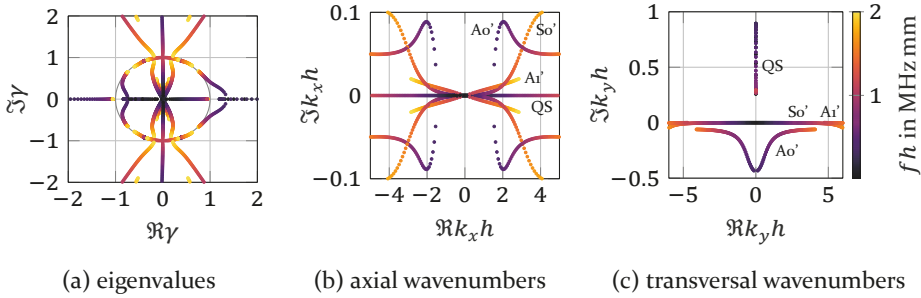


Figure 3.22: Dispersion curves parametrized by the frequency-thickness product fh .

The corresponding complex wavenumber planes are displayed in Fig. 3.22b and Fig. 3.22c. Thereby, all solutions except the nonphysical ones have been retained. The imaginary axis extends have been chosen such as to highlight the lowly attenuated waves. Note that the 14 branches in the $k_x(f)$ plane collapse onto 7 double-branches in the $k_y(f)$ domain because it cannot distinguish between left and right propagating waves, as was already observed in Fig. 3.13.

Fig. 3.23 takes a closer look at the dispersion curves in the three-dimensional $[f, \Re k_x, \Im k_x]$ domain. Thereby, the solutions have been split into forward and backward waves. As can be observed in Fig. 3.23a, the curves appear in pairs: for each leaky wave, there is one incoming wave with the same $\Re k_x$ but opposite $\Im k_x$. This is more clearly seen in Fig. 3.23b, which zooms into the region of Fig. 3.23a where four such waves meet. The wavenumbers of $S1'$ and $S2b'$ move closely along the real line but before meeting, they abruptly turn into the highly attenuated regime. This phenomenon has been interpreted as an “interaction” between propagating and nonpropagating solutions of the free plate spectrum induced by the loading of the fluid [102].

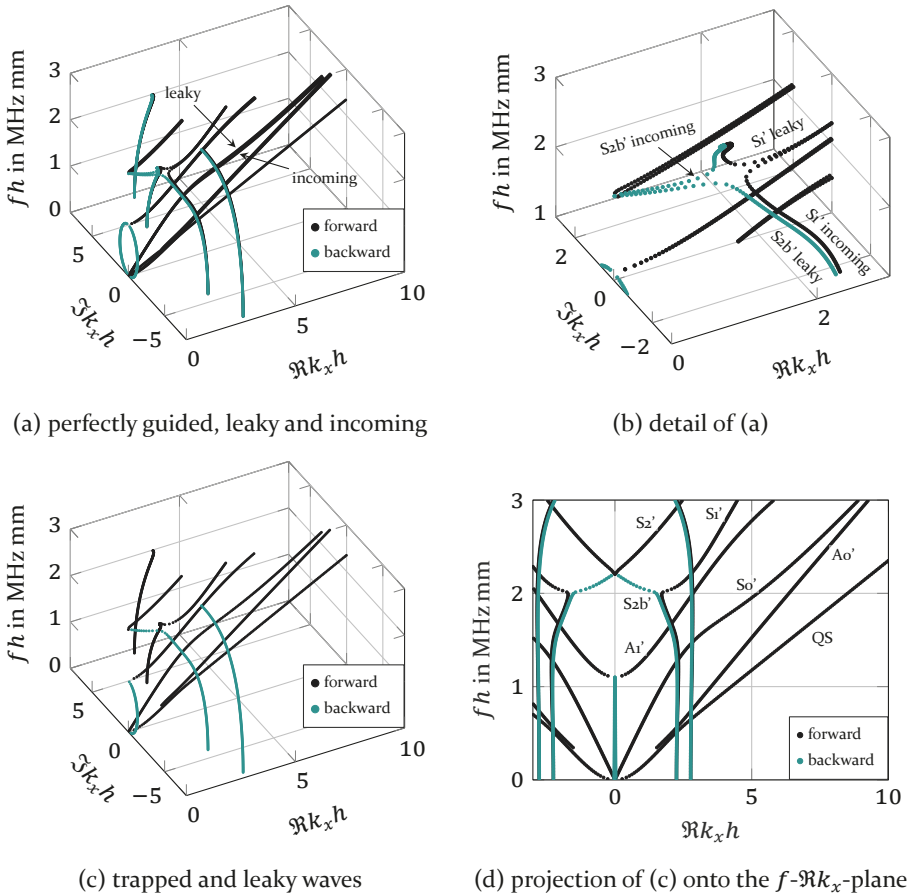


Figure 3.23: Dispersion curves of the axial wavenumbers $k_x(f)$ splitted into forward and backward waves: (a) and (b) show all solutions, while (c) and (d) restrict to trapped and leaky waves.

For the sake of clarity, we remove the incoming waves and retain only the trapped and leaky waves in Fig. 3.23c, yielding single branches for each wave. In many applications the incoming waves are not of relevance, i.e., when emitter and receiver are both located on the plate. Lastly, the projection onto the f - $\Re k_x$ plane is plotted in Fig. 3.23d. In this representation, we included a portion of the negative $\Re k_x$ plane to clarify that the curves extend symmetrically into this region. The similarity to the free brass plate spectrum (see Fig. 3.4a) is clearly noticeable. It is due to the high impedance mismatch between the plate and the fluid, hence, we may consider the plate to be “lightly fluid loaded”. Accordingly, we have adopted a mode labeling based on the free plate spectrum but appended with a dash, e.g., $A_0 \rightarrow A_0'$, albeit the solutions of the single-sided fluid-coupled plate do not exhibit a definite

parity. In comparison to the free plate, one more mode is obtained in the present example. It is called the quasi-Scholte (QS) mode and is the only trapped wave in this setup.

More dispersion curves of the same setup are presented in Fig. 3.24. The first plot, i.e., Fig. 3.24a, shows again the wavenumbers but includes color-coded information about the attenuation of the waves. The corresponding phase velocities $c_p = \omega/\Re k_x$ can be seen in Fig. 3.24b. The QS mode approaches the phase velocity c_f of water from below, as it increasingly confines to the fluid domain. While in the free plate the higher order waves exhibit a strict cut-off frequency where the phase velocity tends to infinity, this is no longer the case for the leaky waves. Instead, the attenuation of the waves increases strongly near “cut-off”, while the phase velocity reaches a maximum and then decreases steadily as it extends down to zero frequency. This is best seen with the S_i' wave in Fig. 3.24b.

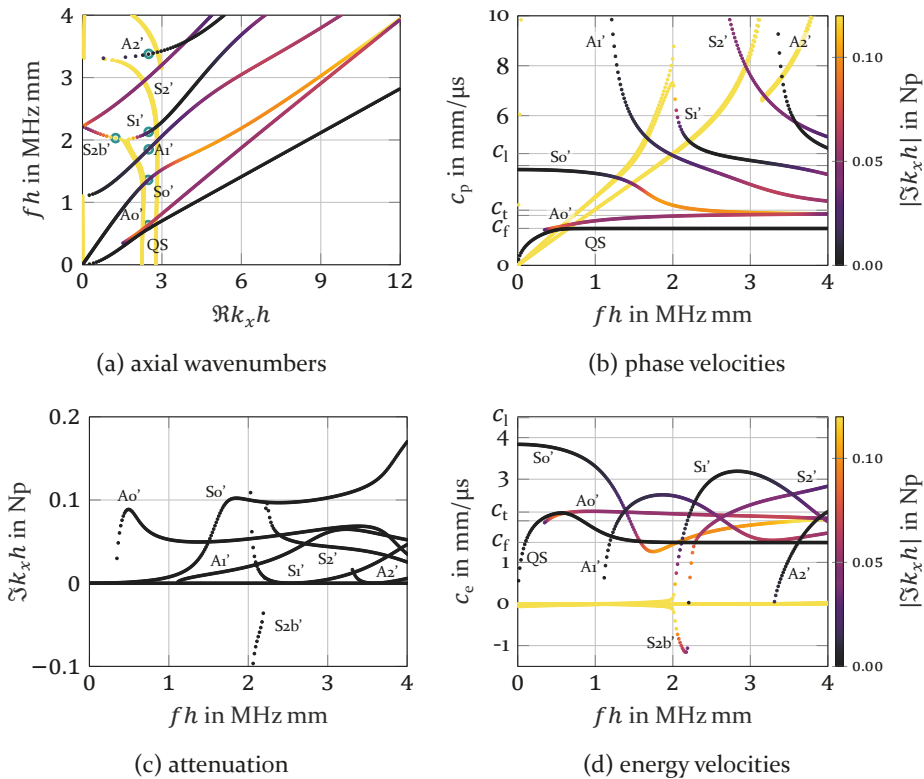


Figure 3.24: Dispersion characteristics of a brass plate with single-sided water contact.

A peculiarity of the water-coupled brass plate is the behavior of the A_0' wave [103]. At certain frequency (0.35 MHz mm in Fig. 3.24), it splits into two

non-attenuated branches. In the present example (not so in the water loaded PMMA plate, see Sec. 3.2.10), we find that they are all nonphysical according to Subsec. 3.2.5 and the solutions have been discarded. This phenomenon has been denoted as real-valued loops [95–97, 103, 104]. It is discussed in some more detail with the help of the brass plate immersed in water (Subsec. 3.2.9) and the water-coupled PMMA plate (Subsec. 3.2.10).

The attenuation of the waves is furthermore an important parameter for many applications. It is shown explicitly in Fig. 3.24c. Remember that for high frequencies, the Ao and So waves of the free plate converge towards Rayleigh surface waves. A similar behavior can be observed for the plate with single sided fluid loading, but each of the waves converges towards a wave confined to the proximity of either of the two plate’s surfaces. The So’ wave at high frequencies is confined at the plate-fluid interface and radiates strongly, thus exhibiting high attenuation. On the other hand, the Ao’ wave tends towards an actual Rayleigh wave at the free boundary and features small attenuation values.

Lastly, the energy velocities computed by (3.15) are shown in Fig. 3.24d. It is important to remark that equipartition of energy is no longer valid in the fluid-loaded case and both the kinetic and elastic energy need to be computed separately, see Subsec. 2.2.5. In the fluid-coupled case, we also obtain negative energy velocities associated with backward waves. Correspondingly, these waves must exhibit negative attenuation (attenuated in $-e_x$), which is confirmed by Fig. 3.24c. The energy velocity is always lower than the longitudinal plane wave velocity c_1 of the medium.

We remark that the energy velocities are computed as an integral over the plate alone according to (3.15), i.e., ignoring the fluid domain. This is conventionally considered a good approximation, at least for leaky waves with “light fluid loading” [91, 100, 105]. It is remarkable that no rigorous definition of energy velocity in open waveguides has yet been formulated [100]. For instance, the computed energy velocity of the QS mode is not valid in the dispersive region, as has been found experimentally [S2]. This wave exhibits real wavenumbers and, hence, it could be resorted to the group velocity in this case instead, which is given in (2.86).

3.2.7 Wave field of trapped and leaky waves

The wave field associated to QGWs is inspected in the following. The leaky forward waves, in particular, exhibit highly unusual properties that need to be explained in detail. We discuss the QS wave and leaky waves separately.

Trapped waves: The quasi-Scholte (QS) plate wave

As seen in the last section, one trapped wave is supported by the brass plate with single sided fluid loading and is called the QS mode. More trapped waves might appear in other configurations, see Subsec. 3.2.10. In contrast to the leaky or incoming waves, trapped waves are proper modes, as they form the discrete spectrum of the full plate-fluid model, see Subsec. 3.2.1.

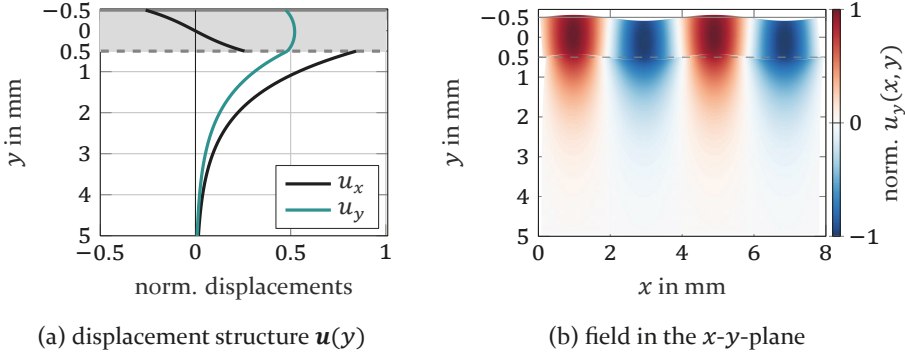


Figure 3.25: Wave field of the QS mode at 0.3 MHz in a 1 mm thick brass plate on water.

The QS wave is confined to the proximity of the plate, as can be observed in Fig. 3.25. The $u_x(y)$ and $u_y(y)$ displacement components represent the eigenfunctions of the QGW problem, whereby they are extrapolated in the fluid region using the plane wave ansatz (3.33). Similar to Lamb waves in a free plate, the displacement components are 90° out of phase everywhere, i.e., there are no losses. Fig. 3.25a shows the two components at their respective maximum phase normalized to the overall maximum magnitude. Due to the flexural wave character of the plate motions seen in Fig. 3.25b, it has also been called the “A-wave” [64, 106].

The QS wave exhibits a strong interaction with the fluid, while at the same time it does not attenuate as it propagates. This unique behavior makes it attractive for characterizing fluid properties, e.g., wave speed and viscosity [66, S2], or for fluid level metering [107].

Leaky Lamb waves

The wave field of leaky Lamb waves consists of a resonance pattern inside the plate and a radiating field in the fluid. This is depicted in Fig. 3.26, showing the normalized particle displacement along the y -coordinate. Unlike the trapped or perfectly guided waves, the complex displacement components $u_x(y)$ and $u_y(y)$ are no longer 90° out of phase. In the figure they are shown at

their corresponding phase where they become maximal. The cross-sectional displacements fully describe the wave fields. For visualization purposes, some exemplary wave fields have been extruded to the x - y -plane and are displayed in Fig. 3.27.

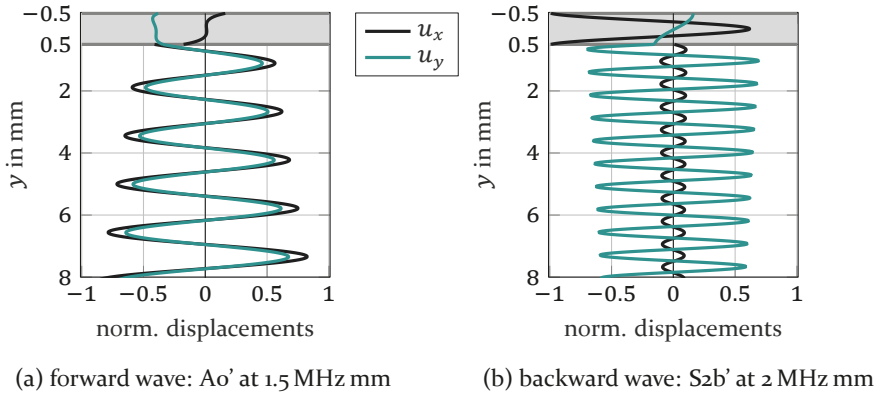


Figure 3.26: Cross-sectional displacements of forward and backward waves. Adapted from [P5].

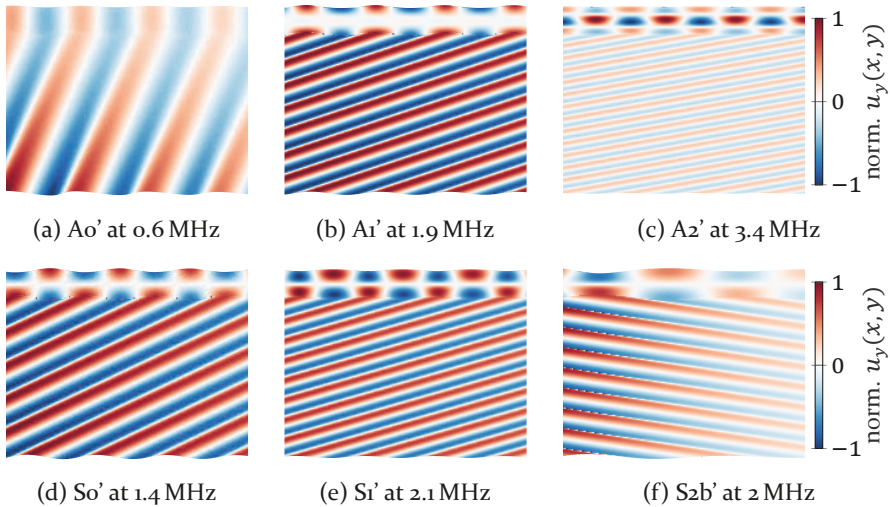


Figure 3.27: Wave field of some QGWs. The corresponding points in the dispersion diagram are marked in Fig. 3.24a. Adapted from [P5].

Backward waves decay with distance from the plate, while forward waves exhibit an acoustic field which increases exponentially in transversal direction. This behavior can clearly be observed in Fig. 3.26. Diverging wave fields are a well-known behavior of leaky waves in nondissipative media and are a direct consequence of energy conservation [46, 52, 57, 75, 78, 79, 86, 87, 91,

108]. This can be understood by inspecting Fig. 3.28, where the fields and the corresponding propagation and attenuation vectors are shown. The thickness of the arrows indicate schematically the evolution of the field's amplitude in this direction. The acoustic wave is radiated into the fluid in direction $\Re k_f$ and must propagate without attenuation in this direction. Consequently, a wave that is attenuated in e_x must necessarily increase in e_y . The converse situation applies to backward waves.

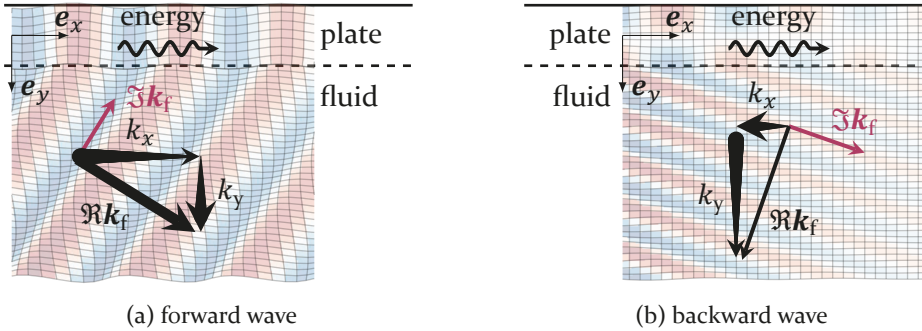


Figure 3.28: Wave fields of forward and backward waves. While backward waves are confined to the proximity of the plate, the perfectly harmonic field of leaky forward waves must diverge with distance from the plate. Reproduced from [P5].

The exponential growth in transverse direction needs to be understood as an asymptotic behavior for perfectly harmonic waves in time and space [52, 79]. Like any other infinite phenomenon, this is per se unfeasible. Incidentally, this also applies to homogeneous plane waves in unbounded media (see Sec. 2.3). There is, however, one significant difference between the two: while the wave structure $\mathbf{u}(y)$ of free waveguides is square integrable, the leaky wave structure diverges as $y \rightarrow \infty$ and is no longer square integrable. Arbitrary fields in the fluid domain (e.g., finite fields) cannot be represented as a linear combination of the QGWs. In other words, these waves are not part of the spectrum of the fluid half-space and for this reason, they have been denoted as *improper waves* [108]. This fact is not surprising, as QGWs restrict attention to the plate and its resonances.

The exponential growth in transverse direction is, nonetheless, physical in the sense that it corresponds to the observable behavior of the waves in limited spatial and temporal regions [52, 79]. This can be confirmed by a full-scale finite element (FE) simulation that is agnostic of the QGWs. Fig. 3.29a shows the geometry of the harmonic simulation consisting of a 1.5 mm brass plate in contact on one side with water (material parameters in Appendix A). The displacements over the plate's left boundary are prescribed using the complex $u_x(y)$ and $u_y(y)$ displacement structures of the Ao' wave at 1.5 MHz mm,

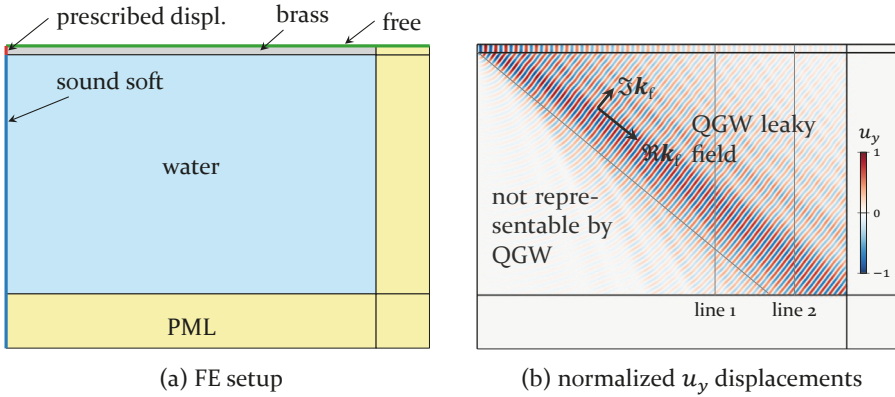


Figure 3.29: FE computation of the leaky field close to a source. The Ao' wave is excited at 1.5 MHz mm.

which was already presented in Fig. 3.26a. The unbounded fluid domain and the plate are cropped with a PML layer. Note that the excitation of a pure QGW is not guaranteed because the displacement structures of two different QGWs are not orthogonal on the plate's domain alone.

The surface plot in Fig. 3.29b shows the resulting $u_y(x, y)$ displacement field in plate as well as in the fluid. The inhomogeneous plane wave radiated by the QGW can clearly be identified on a wedge enclosed by the plate and a line inclined at the radiation angle of the QGW. The remaining part of the field is expected to be non-representable by the QGW solutions as the continuum of the radiation modes (see Subsec. 3.2.1) are required for that. Contrary to the leaky field, this part is highly dependent on the left BC.

The exponential growth in transverse direction can best be observed in Fig. 3.30, showing the field along the vertical lines marked in Fig. 3.29b. The exponential envelope expected from the QGW solution ($\Im k_y = 0.275 \text{ Np/cm}$) fits well to the FE result. The further away from the source, the larger is the y -range where the QGW approximation is valid. At the same time, the observable “ripples” in the leaky field become more visible. These are due to other QGWs (the A_1' wave in this setup) being excited in addition to the Ao' wave, albeit with a substantially lower amplitude [109]. As the A_1' 's attenuation is lower than that of the Ao' wave, it will become dominant when far enough away from the source. Moreover, non-representable contributions of the radiation modes are present everywhere, including in the leaky field region and they become visible once the leaky waves have attenuated sufficiently.

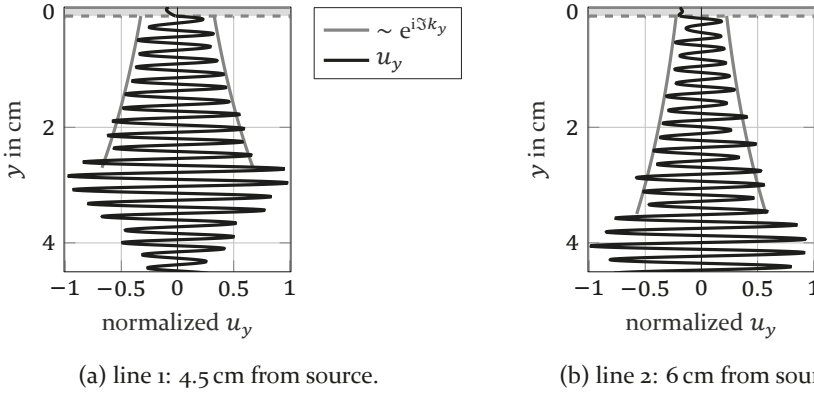


Figure 3.30: Normalized $u_y(y)$ displacements on the cross sectional lines marked in Fig. 3.29b. The expected exponential envelope from the QGW solution is also shown.

The leaky waves will separate best in a transient FE simulation when the energy velocity of the waves differ. This is the case for the Ao' and Ai' wave. The setup for the transient FE simulation is identical to the harmonic setup in Fig. 3.29a without the PML and a slightly larger fluid domain as to avoid reflections from the boundaries. The transient prescribed displacements across the plate's thickness are ramped-up by a raised cosine of 10 periods length, i.e.,

$$\text{RCR}(t) = \begin{cases} \frac{1}{2} - \frac{1}{2} \cos\left(\frac{\pi t}{10T}\right), & \text{for } 0 \leq t \leq 10T \\ 1 & \text{for } t > 10T, \end{cases} \quad (3.45)$$

where $T = 2\pi/\omega$ denotes the period. The overall prescribed displacements are then given by

$$u_{i,\text{exc}} = \text{RCR}(t) \sin \omega t \Re u_i(y) + \text{RCR}(t + T/4) \sin \omega(t + T/4) \Im u_i(y), \quad i = \{x, y\}, \quad (3.46)$$

where $u_i(y)$ denote the modal $u_x(y)$ or $u_y(y)$ displacements – in this case of the Ao' wave.

The result of the transient FE simulation at fixed time is presented in Fig. 3.31. The spatial excerpt is chosen such as to visualize the location where the Ao' and Ai' waves separate due to the difference in energy velocity. The leaky field in the fluid clearly shows the different radiation angles of the two waves.

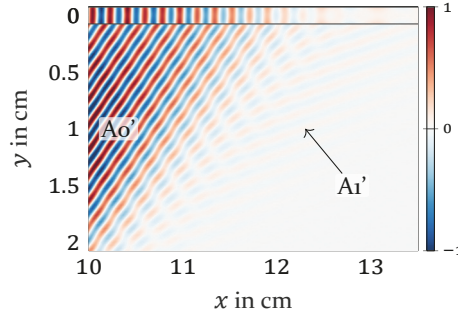


Figure 3.31: Transient leaky field at $t = 65 \mu\text{s}$: the A_1' wave is excited in addition to the A_0' wave. The fluid shows the pressure, while the plate domain shows the u_y displacements, each normalized to their respective maximum.

3.2.8 Radiation

Radiation denotes the transport of energy away from a given system or domain. The QGW model considers the plate as a waveguide which radiates inhomogeneous plane acoustic waves into the fluid (see Subsec. 3.2.2). The waves in the plate and in the fluid are, thereby, strongly linked through the interface conditions. Two essential aspects of the radiation process will be discussed in the following: (i) geometric characteristics, and (ii) balance of power flux through the plate-fluid interface.

Radiation angle

First, we analyze the geometric properties of the radiated field. The setting of the brass plate coupled on one side to water is sketched in Fig. 3.32a. The plot reveals the possible locations of the propagation vectors \mathbf{k}_f in the fluid. Thereby, we have exploited the fact that the developed solution procedure allows us to uniquely obtain both components k_x and k_y . This immediately yields the *radiation angles*, which describe the inclination of the plane wave fronts (see Sec. 2.3) with respect to the plate's normal. They are given by

$$\theta = \arctan \frac{\Re k_x}{\Re k_y} = \arcsin \frac{\Re k_x}{|\Re \mathbf{k}_f|}. \quad (3.47)$$

The radiation angles are plotted in Fig. 3.32b. We see that at given frequency, only a discrete set of radiation angles are in resonance with the plate. Note that the QS wave, which has been omitted in Fig. 3.32b, is perfectly guided along the plate, i.e., it does not radiate, but rather propagates with 90° along the plate. According to the symmetry in Fig. 3.23d, the plot of the radiation

3 Guided and quasi-guided waves

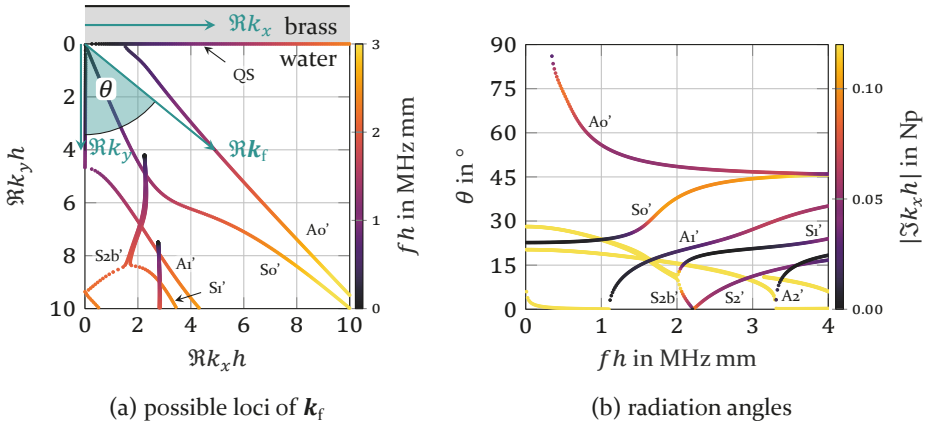


Figure 3.32: Propagation vectors and radiation angles of the brass plate with single sided water coupling.

angles is symmetric across the frequency axis because negative $\Re k_x$ lead to negative θ . If we had chosen to plot only waves which propagate energy to the right – instead of the ones that propagate phases to the right – then backward waves would be characterized by negative radiation angles [P5]. The S_{2b}' wave could, for example, be regarded as a continuation of $S_{2'}$ into the negative θ regime.

Albeit the definition (3.47) is very evident from a geometrical point of view, it is not conventional. The reason is presumably that most computational methods do not easily yield both wavenumber components (nor $|\Re \mathbf{k}_f|$!). For the best of the authors knowledge, the literature exclusively relies on approximative computations which neglect the inhomogeneity of the radiated plane waves, namely $\theta_{\text{approx}} = \arcsin \frac{\Re k_x}{\kappa_f}$, see Ref. [59, 70, 110, 111]. In order to relate the approximation to (3.47), we recall that the radiated waves are inhomogeneous waves satisfying the dispersion relation (2.71) with $\Re \mathbf{k}_f \cdot \Im \mathbf{k}_f = 0$. Accordingly, we may re-write (3.47) as $\theta = \arcsin \frac{\Re k_x}{\sqrt{\kappa_f^2 + |\Im \mathbf{k}_f|^2}}$. This expression reduces to

θ_{approx} for $\Im \mathbf{k}_f = \mathbf{0}$, i.e., when the inhomogeneity of the wave is neglected. While θ_{approx} is based on the homogeneous plane wave phase velocity with $\kappa_f = \omega/c_f$, definition (3.47) uses the actual phase velocity of the inhomogeneous plane wave according to (2.75). Note that the inhomogeneity of the wave tends to increase with the radiation rate. Hence, the conventional radiation angle computation represents a good approximation for lowly radiative waves.

Radiation rate: balance of power flux

Second, we analyze the balance of average power flux as sketched for a section of the plate in Fig. 3.33 assuming nondissipative media. A QGW transports

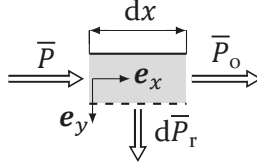


Figure 3.33: balance of power flux

the net power \bar{P} through the plate's cross section at $x = 0$ and carries \bar{P}_0 out of this section at an infinitesimal distance dx . Thereby, it has lost the power $d\bar{P}_r$ to the fluid by means of acoustic radiation. The power flux \bar{P} can be computed with the elastodynamic Poynting vector $\bar{\mathbf{p}}(x, y)$ given in (2.50) as

$$\bar{P} = \int_{-h/2}^{h/2} \mathbf{e}_x \cdot \bar{\mathbf{p}}(y) dy, \quad (3.48)$$

where $\bar{\mathbf{p}}(y)$ denotes the average power flux density at $x = 0$, i.e., $\bar{\mathbf{p}}(y) = \bar{\mathbf{p}}(0, y)$. The power flux leaving at the end of the section can be written in linear approximation by

$$\bar{P}_0 = \bar{P} + \partial_x \left(\bar{P} e^{-2\alpha x} \right) \Big|_{x=0} dx = \bar{P} - 2\alpha \bar{P} dx. \quad (3.49)$$

Note that the QGW loses a fraction of its power per dx to the fluid and, therefore, the wave field must be attenuated as $e^{-\alpha x}$. Accordingly, the power flux is proportional to $e^{-2\alpha x}$. Lastly, the radiated power flux is obtained by

$$d\bar{P}_r = \mathbf{e}_y \cdot \bar{\mathbf{p}}(h/2) dx. \quad (3.50)$$

With the above considerations, the balance of power flux, i.e., $\bar{P} = \bar{P}_0 + d\bar{P}_r$, then reads

$$2\alpha \bar{P} = \mathbf{e}_y \cdot \bar{\mathbf{p}}(h/2), \quad (3.51)$$

which finally yields the *radiation rate*

$$\alpha = \frac{\mathbf{e}_y \cdot \bar{\mathbf{p}}(h/2)}{2\bar{P}}. \quad (3.52)$$

The radiation rate describes how fast the QGW field decays in axial direction *due to radiation* and is, hence, a measure for power leakage into the fluid. We conclude from (3.52) that it is basically determined by the average power flux density through the plate-fluid interface, i.e., the component normal to the boundary. This can be observed in Fig. 3.34, which compares the power flux density vectors in the free brass plate to the one coupled to water. While energy flux is confined inside the free plate as expected, the Poynting vectors in the fluid-coupled plate incline towards the fluid half-space.

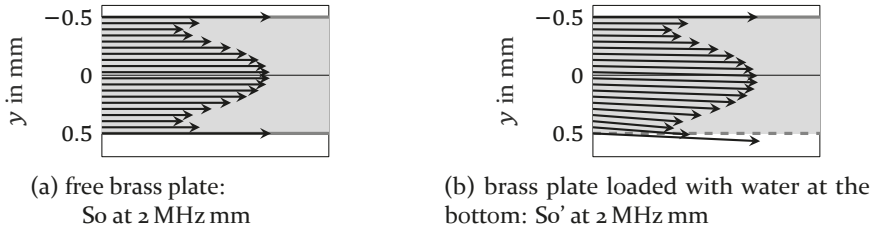
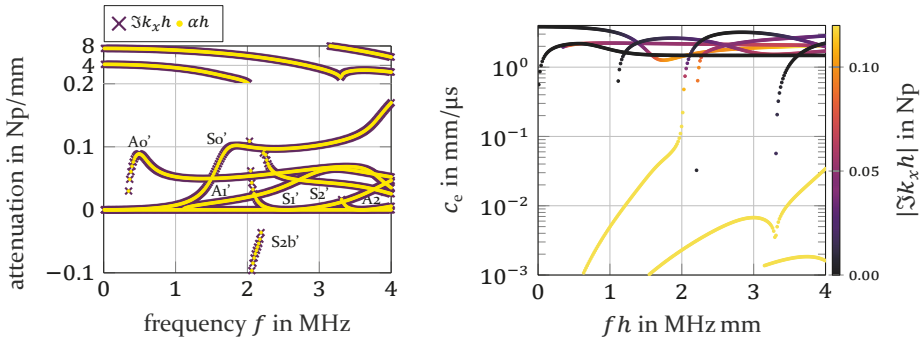


Figure 3.34: Average power flux density vectors $\bar{\mathbf{p}}(y)$. Adapted from [P5].

The radiation rate given in (3.52) was computed for the fluid-coupled brass plate and the result is compared to the overall attenuation $\Im k_x$ in Fig. 3.35a. The radiation rate α coincides with the axial attenuation $\Im k_x$ even for the highly attenuated waves. We conclude that *attenuation is always due to radiation*. This result is not trivial! Remember that the free plate exhibits attenuated modes (see Subsec 3.1.3) – called nonpropagating modes – albeit it exhibits no losses, in particular, it does certainly not radiate. Traditionally, leaky Lamb waves are regarded as a perturbation to the free solutions, where the non-attenuated modes become attenuated due to radiation. The above calculation shows that this point of view is correct and that it additionally holds for the attenuated modes of the free plate.

The finding that attenuation is always due to radiation has a further consequence: nonpropagating waves do not exist in the fluid-coupled plate. The nonpropagating modes in the free plate are attenuated and exhibit no net power flux, i.e., $\bar{\mathbf{P}} = 0$. According to (3.52), this will not be possible if $\alpha = \Im k_x$ is to remain bounded. This finding is analogous to waves in dissipative plates [44]. Contrary to the free plate, waves in the fluid-coupled plate *always carry energy*. Consequently, the energy velocity of QGW might be low but never zero (except on isolated frequency points). This is visualized in Fig. 3.35b, where the waves with low energy velocity are seen to gradually propagate more energy as the frequency is increased. The higher the fluid



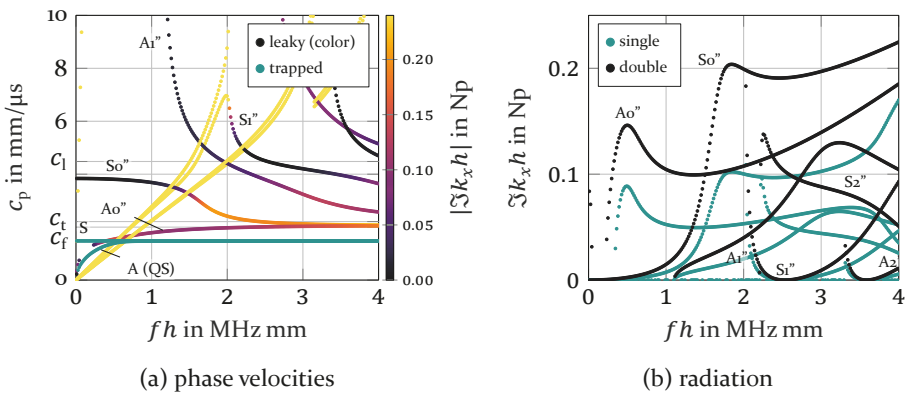
(a) Comparison of radiation rate α and (b) Logarithmic scale of the energy velocities given attenuation $\Im k_x$ in Fig. 3.24d.

Figure 3.35: Radiation rate and energy velocity: Adapted from [P5].

loading of the plate, the more energy is propagated by these waves – limiting zero when the fluid loading vanishes, as expected.

3.2.9 Immersed plate: double sided fluid coupling

Plates in contact with a fluid on one side were considered so far. It is straightforward to extend the presented model to immersed plates, i.e., plates in contact with the same fluid on both sides. For this end, one additional scalar degree of freedom is added to the problem, which describes the amplitude of the inhomogeneous plane wave on the other side of the plate. The linearization procedure presented in Subsec. 3.2.3 can then be applied as previously.



(a) phase velocities

(b) radiation

Figure 3.36: Dispersion curves of a brass plate immersed in water. The radiation in (b) shows both single and double sided fluid loading.

Dispersion curves of a brass plate immersed in water are displayed in Fig. 3.36. Waves in the the plate with double-sided fluid loading are marked with two dashes, e.g., Ao'' . The phase velocities are similar to the ones with single sided fluid loading. However, one additional trapped wave is obtained, labeled “S” in Fig. 3.36a. As the symmetry of the problem’s geometry across $y = 0$ has been restored, the solutions have again a definite parity. One anti-symmetric (QS, A-wave) and one symmetric (S-wave) trapped wave is obtained [106]. As would be assumed by perturbation models [41] (see Subsec. 3.1.9), the radiation rate is approximately doubled compared to single sided fluid loading. However, as Fig. 3.36b shows, this should rather be considered a rule of thumb. Observe the opposite attenuation behavior of the Ao' and Ao'' waves when the frequency is increased. The wave can no longer tend towards an unloaded surface wave and always radiates, hence, contrary to single-sided fluid loading, the attenuation keeps increasing.

The splitting of the Ao'' wave into a “real-valued loop” [P3, 96, 97, 104, 112, 113] shall be discussed with the help of the present example, but occurs similarly in the plate with single sided fluid contact. The relevant region of the dispersion diagram is shown in detail in Fig. 3.37a and – contrary to the previously presented dispersion curves – includes the solutions that we consider to be nonphysical (diverge in the transversal direction, see Subsec. 3.2.5). The Ao'' leaky wave is seen to split into two curves with real-valued wavenumbers/phase velocities, which later on merges again into a leaky wave – labeled again Ao'' . Splitting also occurs in the PMMA plate with single-sided water contact shown in Fig. 3.37b and discussed in Subsec. 3.2.10.

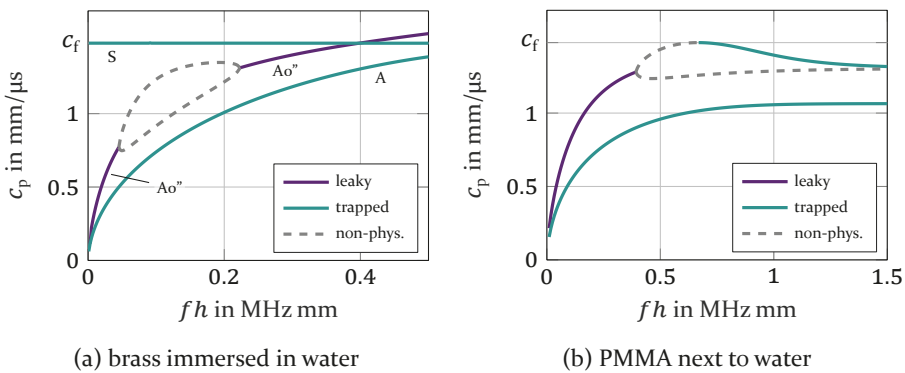


Figure 3.37: Splitting of dispersion curves.

It is often assumed a-priori that the Ao'' wave is cut-off at the *coincident frequency* [59, 67, 70, 91, 102, 104, 112, 114], which is defined as the frequency where the phase velocity of the wave matches the velocity of homogeneous

plane waves in the fluid medium. As seen due to the crossing with the S-wave – whose phase velocity is basically the same than that of the fluid medium – the splitting of the A_0 wave happens well below the coincident frequency. This can be regarded to be a consequence of the reduced phase velocity of inhomogeneous plane waves according to Subsec. 2.3.1 [43]. For a detailed explanation refer to [115]. We conclude that, contrary to what is widely assumed, *subsonic radiation* is possible [43, 115]. A remarkable example is a water-loaded aluminum plate, where the A_0 wave does not split at all and continues down to zero-frequency [P5, 97].

3.2.10 Strongly fluid-loaded plate

So far the discussion focused on plates with “light fluid loading”, i.e., the impedance mismatch between plate and fluid was high [116]. Most relevantly, the ratio of fluid mass density to plate mass density was low [102], see eq. (4.2). The developed model includes an analytically exact fluid-structure interaction, i.e., it is applicable for arbitrary material combinations. This is demonstrated by considering a plate made of poly(methyl methacrylate) (PMMA), i.e., plexiglass, which is in contact on one side with water (material parameters in A). Fig. 3.38 shows the corresponding dispersion curves. The strong interaction between the PMMA plate and the fluid lead to qualitatively and quantitatively very different dispersion curves as compared to the free plate case [P5]. This is presumably because the transverse wave speed in the plate is below the fluid wave speed in the present example.

In the inspected range, three trapped waves are found and are displayed separately from the leaky waves. The latter are plotted color coded according to their attenuation. Note that the “higher order” trapped waves appear after a leaky wave has split into a real-valued loop which closes at $f \rightarrow \infty$ [96]. This is illustrated in detail in Fig. 3.37b, which includes the nonphysical solutions (diverge in the transversal direction, see Subsec. 3.2.5). The trapped wave consist of a section of one of the branches of the real-valued loop, while the remaining parts are nonphysical solutions. Rostyne et al. [98] have confirmed this behavior experimentally.

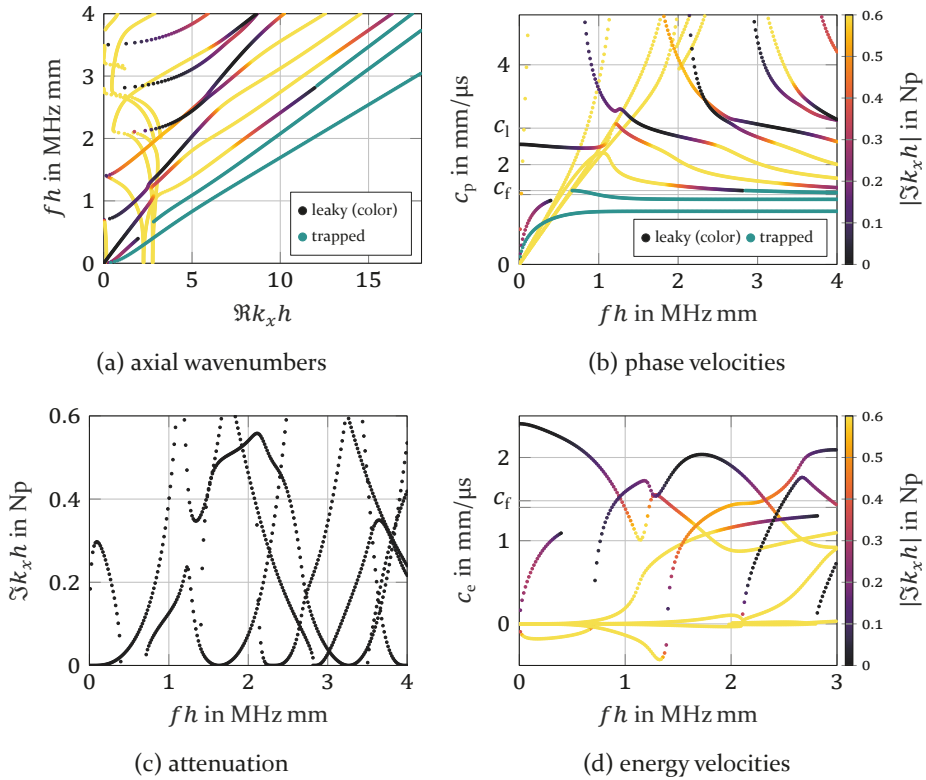


Figure 3.38: Dispersion characteristics of a PMMA plate with single-sided water contact. (a) adapted from [P5].

4 Numerical Solution Methods

With the theoretical description of the wave propagation phenomena in hand, we now proceed to discuss numerical solution techniques. The two fundamental approaches to solve waveguide problems are discussed and compared in Sec. 4.1. We use a special discretization procedure denoted as spectral collocation, which is introduced in Sec. 4.2. Next, Sec. 4.3 explains how to deal with the polynomial eigenvalue problems resulting from discretization. Lastly, a software tool has been implemented that handles waveguide problems and it is presented in Sec. 4.4.

4.1 Solving waveguide problems

Two fundamentally different approaches exist to solve the derived guided and quasi-guided wave problems: (i) root-finding of the characteristic equation, and (ii) discretization of the eigenvalue problem. These will be presented and discussed separately in the following. Emphasis is put on approach (ii), which is used by the `Elastodynamic Acoustic Toolbox (EDAT)` implemented for Matlab, see Sec 4.4.

4.1.1 Root-finding of the characteristic equation

Root-finding of the characteristic equation(s) is the most wide spread solution technique [117]. It is reviewed in the following as background information to the EVP-based technique developed in the next section. The EVP-based technique is used throughout this work.

The main idea of the method consists in resolving the y -dependence of the eigenfunctions analytically as a superposition of plane waves [38, 41, 118]. The resulting representation is called a *partial wave decomposition* [41, 118], see Subsec. 2.3.1. The situation is sketched in Fig. 4.1 for a plate loaded with two different fluids on either side.

For instance, inside the plate this yields the ansatz

$$\mathbf{u}(y, k_x, \omega) := A \mathbf{e}_u^{1+} e^{ik_y^1 y} + B \mathbf{e}_u^{t+} e^{ik_y^t y} + C \mathbf{e}_u^{1-} e^{-ik_y^1 y} + D \mathbf{e}_u^{t-} e^{-ik_y^t y}, \quad (4.1)$$

where k_y^1 and k_y^t fulfill the plane bulk wave dispersion relations $k_x^2 + (k_y^1)^2 = \kappa_1^2$ and $k_x^2 + (k_y^t)^2 = \kappa_t^2$, see Subsec. 2.3.1. As a consequence, the ansatz is

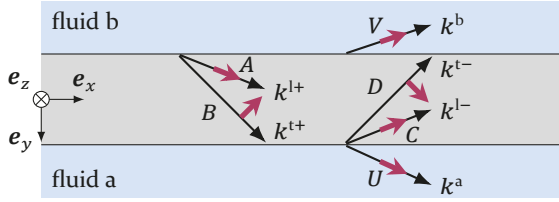


Figure 4.1: Partial wave decomposition of a leaky wave inside a plate in contact with two different fluids a and b . The polarization vectors are also indicated.

guaranteed to fulfill the equations of motion. For leaky waves, a similar ansatz is used for the fluid domains, having only one (longitudinal) partial wave. Note, moreover, that the polarization vectors of longitudinal waves are known to be $\mathbf{e}_u^{l+} = 1/\kappa_l[k_x, k_y^l]^\top$ and $\mathbf{e}_u^{l-} = 1/\kappa_l[k_x, -k_y^l]^\top$. Similarly, for the transverse waves we have $\mathbf{e}_u^{t+} = 1/\kappa_t[-k_y^t, k_x]^\top$ and $\mathbf{e}_u^{t-} = 1/\kappa_t[k_y^t, k_x]^\top$.

The plate-fluid interface conditions (or BCs at free surfaces) still need to be satisfied. Inserting the partial wave decompositions into the appropriate conditions yields a homogeneous algebraic system of equations for the unknown plane wave amplitudes. For instance, the single sided fluid plate case is retrieved by setting $V = 0$ and inserting (4.1) into (3.36), resulting in a 5×5 linear system for A, B, C, D and U . The lengthy derivation could be simplified somewhat by introducing a potential formulation [41]. The fact that symmetric and antisymmetric solutions decouple could additionally be exploited for symmetric waveguide problems, see Sec. 3.1.

The resulting linear system can always be written in the general form $\underline{\underline{P}}(k_x, \omega) \cdot \underline{a} = \underline{0}$, where \underline{a} denotes the vector of wave amplitudes [118]. The *characteristic equation* is then given as $\det \underline{\underline{P}}(k_x, \omega) = 0$. For the case with symmetries, $\underline{\underline{P}}$ consists of two independent blocks and the characteristic equation segregates into $\det \underline{\underline{P}}(k_x, \omega) = A(k_x, \omega)S(k_x, \omega) = 0$, where S and A describe symmetric and antisymmetric solutions, respectively. For a free plate, each of them results in an implicit transcendental nonlinear dispersion relation, the so-called *Rayleigh-Lamb frequency equations* [33, 59, 65]. In any case, the roots of the characteristic equation can now be searched numerically using conventional methods, yielding the desired solutions $k_x(\omega)$. This, however, is not a simple task [117, 118].

The procedure discussed above is very general and can be extended to multi-layered, anisotropic, dissipative and fluid-coupled plates [105, 117]. Several methods exist to derive the corresponding characteristic equations in an automated way on the computer, for instance, the global matrix method

(GMM) or the direct matrix method (DMM) could be used [118]. Albeit these methods deliver analytically equivalent results, they differ from a numerical point of view. This is very important because zero-finding of the equations is badly conditioned for numerical treatment. It can be shown that the field scales exponentially from one interface to another, resulting in numerical instabilities for high frequency-thickness products [57, 118].

The characteristic equations of immersed or single-sided fluid loaded plates are given explicitly in a variety of forms in Refs. [64, 95, 102, 113, 116, 119, 120]. For the sake of reference, we reproduce the characteristic equation of a plate loaded by two different fluids on either side, characterized by the mass densities ρ_a, ρ_b and the wave speeds c_a, c_b , respectively. After slight adaptations in notation, the characteristic equation is given according to Ref. [64] by

$$S_a A_a + S_b A_b - \underbrace{\frac{1}{\rho^2} \left(\frac{\rho_a}{k_y^a} - \frac{\rho_b}{k_y^b} \right)^2}_{\text{loading asymmetry}} \kappa_t^8 k_y^1{}^2 = 0, \quad (4.2)$$

where $S_i, i \in \{a, b\}$ is defined by

$$S_i = \overbrace{4k_x^2 k_y^t k_y^l \tanh(ik_y^l h/2) + (k_x^2 - k_y^t{}^2)^2 \tanh(ik_y^t h/2)}^{\text{free plate}} + \underbrace{\kappa_t^4 \frac{\rho_i k_y^l}{\rho k_y^i} \tanh(ik_y^l h/2) \tanh(ik_y^t h/2)}_{\text{fluid loading}}, \quad (4.3)$$

and A_i is obtained by replacing all \tanh by \coth in the above expression. The Rayleigh-Lamb frequency equations are recovered by setting $\rho_i = 0$. The case $\rho_i/\rho \rightarrow \infty$ yields the dispersion relations for a plate with slip BCs, i.e., $u_y = 0$ and $T_{xy} = 0$ [102].

Although very popular, root-finding of the characteristic equations suffers of two inherent problems: (i) it exhibits the mentioned instabilities and (ii) it is impossible to know if all roots have been found [57, 121]. In general, it is not even known how many (real) roots are to be expected at given frequency. This will be particularly detrimental when studying new problems, where the researcher does barely have a “feeling on how the solutions should look”. Moreover, root-finding becomes significantly more difficult when complex valued k_x are sought. This makes the method especially unattractive for open waveguides, where most solutions of interest are complex valued. These difficulties are resolved with the alternative approach presented next.

4.1.2 Eigenvalue problem discretization

The waveguide problems derived in Chap. 3 are ordinary boundary value problems (BVPs) and can, therefore, be approximated by conventional discretization methods. The result is an algebraic system of equations approximating the continuous waveguide problem on a discrete set of degrees of freedom $i \in \{1 \dots N\}$. Fluid loading adds an additional degree of freedom for the unknown longitudinal wave amplitude U . The idea is depicted in Fig. 4.2.

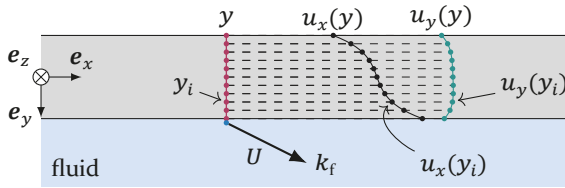


Figure 4.2: Through-thickness discretization of a plate in contact with a fluid.

Note that the general structure of the equations remains thereby unchanged. After discretization, conventional numerical eigenvalue solvers can be used to compute the approximated eigenvalues (wavenumbers) for every prescribed frequency. The discretized eigenfunctions $\mathbf{u}(y_i)$ are, thereby, obtained at no extra cost, which is useful for post-processing and visualization. Advantages of this method are that [57, 121]

1. it does not suffer of numerical instabilities;
2. all eigenvalues are guaranteed to be found as long as the discretization order N is sufficiently high;
3. complex-valued solutions k_x are dealt with naturally at no extra cost; and
4. it is very fast.

A comprehensive discussion on the topic is found in Ref. [121].

A very popular discretization scheme is the FE method. As the x -coordinate is resolved analytically by the initial ansatz (3.1) of the waveguide problem, some authors refer to this procedure as the “semi-analytical finite element” (SAFE) method [91, 122–124]. Personally, I think that this terminology is deceptive as well as obscuring and should not be used because the conventional FE method is being applied to the *guided wave problem* without any modifications. Note that the ansatz (3.1) is inherent to the problem of guided waves under consideration, not to the discretization method. To the best of the author’s

knowledge, FE discretization of elastodynamic waveguide problems was first performed by Gavrić [125, 126] without use of the above terminology.

Any other numerical discretization scheme could also be used to solve the waveguide problem. For instance, spectral methods [48, 121, 127–129], finite differences [130], discontinuous Galerkin FEs [131] and scaled-boundary FEs [132, 133] have been employed. We use Chebyshev SC for this purpose, which is subject of the next section.

4.2 Spectral collocation for waveguide problems

The Chebyshev spectral collocation (SC) method is used to discretize waveguide problems in this work. The technique and its application is discussed in detail in the following.

4.2.1 Chebyshev spectral collocation method

The continuous domain of plane waveguide problems is $y \in [-h/2, h/2]$. Such simple geometries are particularly well discretized by *SC methods* [134, 135]. Thereby, the unknown function $u(y)$ – which is a solution of the waveguide problem – is approximated by $u^h(y) = \sum_i u_i \phi_i(y) \approx u(y)$, consisting of a weighted sum of known ansatz functions $\phi_i(y)$. In contrast to FE methods, a *spectral method* [134] is characterized by a global approach, i.e., the ansatz functions $\phi_i(y)$ are nonzero on the whole domain $y \in [-h/2, h/2]$ (except possibly on discrete points). *Collocation methods* [134] determine the unknown weights u_i by requiring that the residuum $u(y) - u^h(y)$ should vanish on selected N points y_i , $i \in \{1 \dots N\}$, which are called the *collocation points*. This is sometimes regarded as a special instance of the weighted residual method, where the weighting functions of the residuum are chosen as Dirac delta functions at the collocation points.

Different choices for the ansatz functions $\phi_i(y)$ are possible. On finite domains the Chebyshev polynomials exhibit optimal behavior [134]. Moreover, the collocation points y_i should cluster quadratically to the borders of the domain in order to avoid the Gibbs phenomenon [135]. Chebyshev-Gauß-Lobatto points [134] fulfill this requirement and are used together with Chebyshev polynomials in the *Chebyshev SC method*.

For simple geometries and smooth solutions $u(y)$, the SC method is considered superior to the FE method. This is mainly due to the fact that the SC

method converges exponentially for sufficiently smooth solutions, a property denoted as *spectral convergence* [134, 135]. For non-smooth solutions, polynomial convergence can still be expected in most cases [135]. Another advantage is that no prior meshing of the domain is required, leading to simpler implementations. On the other hand, for complex geometries, the FE method should be preferred. Another disadvantage of the SC method is that it leads to fully populated matrices. However, this is usually compensated by the fact that the matrices are substantially smaller due to the spectral convergence property.

4.2.2 Discretization of the quasi-guided wave problem

The SC method allows to express differentiation explicitly in the form of a $N \times N$ differentiation matrix $\underline{\underline{D}}_y$ [135, 136]. If \underline{u} is the vector with coefficients $u(y_i)$, then $\underline{\underline{D}}_y \cdot \underline{u}$ will be the vector of corresponding derivative values, i.e., $\partial_y u(y)|_{y=y_i}$. This can be harnessed for simple discretization of the waveguide problem, which is realized by performing the following formal exchanges in the equations:

- unknowns: e.g., $u(y) \rightarrow \underline{u}$,
- derivatives: e.g., $\partial_y \rightarrow \underline{\underline{D}}_y$, and
- constants: e.g., $\lambda_L \rightarrow \lambda_L \underline{\underline{I}}_d$,

where $\underline{\underline{I}}_d$ is the $N \times N$ identity matrix. Furthermore, in the BCs only the relations for $y = \pm h/2$ are needed. For this end, it is sufficient to use the corresponding rows $\underline{\underline{D}}_y|_{\pm h/2}$ and $\underline{\underline{I}}_d|_{\pm h/2}$ that describe the local mappings.

As a concrete example, we discuss how to solve the quasi-guided wave problem. The procedure follows along the same lines as the discretization of the displacement potential formulation of the same problem presented in [P3]. We discretize the generally nonlinear form of the problem instead of the polynomial one. The governing equations of the former are recalled from (3.38), namely

$$\left[(ik_x)^2 \underline{\underline{L}}_{\underline{\underline{2}}} + ik_x \underline{\underline{L}}_{\underline{\underline{1}}} \partial_y + \underline{\underline{L}}_{\underline{\underline{0}}} \partial_y^2 + \omega^2 \underline{\underline{M}}_{\underline{\underline{}}} \right] \cdot \underline{q}(y) = \underline{0} \text{ on } y \in (-h/2, h/2), \quad (4.4a)$$

$$\left[ik_x \underline{\underline{B}}_{\underline{\underline{1}}} + \underline{\underline{B}}_{\underline{\underline{0}}} \partial_y + \omega \underline{\underline{B}}_{\underline{\underline{\omega}}} + ik_y \underline{\underline{B}}_{\underline{\underline{y}}} \right] \cdot \underline{q}(y) = \underline{0} \text{ at } y = \pm h/2, \quad (4.4b)$$

where $k_y = \sqrt{\kappa_f^2 - k_x^2}$; while the equations of the polynomial equivalent are restated from (3.43):

$$\left[\gamma^4 \underline{\underline{G}}_2 + \gamma^3 i \underline{\underline{G}}_1 \partial_y + \gamma^2 (\underline{\underline{G}}_0 \partial_y^2 + 2\underline{\underline{G}}_2 + \omega^2 \underline{\underline{M}}) + \gamma i \underline{\underline{G}}_1 \partial_y + \underline{\underline{G}}_2 \right] \cdot \underline{q}(y) = \mathbf{0}, \quad (4.5a)$$

$$\left[\gamma^3 i \underline{\underline{\Gamma}}_{+1} + \gamma^2 \left(\underline{\underline{\Gamma}}_0 \partial_y + \omega \underline{\underline{\Gamma}}_\omega \right) + \gamma i \underline{\underline{\Gamma}}_{-1} \right] \cdot \underline{q}(y)|_{y=\pm h/2} = \mathbf{0}. \quad (4.5b)$$

Lastly, we also recall the change of variables (3.41) given by

$$i k_x \stackrel{\text{def}}{=} \frac{i \kappa_f}{2} (\gamma + \gamma^{-1}), \text{ and} \quad (4.6a)$$

$$i k_y = \pm \frac{\kappa_f}{2} (\gamma - \gamma^{-1}) = i \sqrt{\kappa_f^2 - k_x^2}, \quad (4.6b)$$

which transforms (4.4) into (4.5). The former problem statement is discretized instead of the more readily solvable polynomial one because the matrices are all independent of frequency, which means that the discretization can be performed once before iteration. The change of variables is subsequently applied iteratively at every frequency. The resulting discrete version of the polynomial problem is then solved with standard techniques, for details refer to Sec. 4.3.

Only the continuous components $u_x(y)$ and $u_y(y)$ of the vector of unknowns $\underline{q}(y) = [u_x, u_y, U]^T$ are discretized component-wise on the whole domain $y \in [-h/2, h/2]$. The scalar unknown U of the fluid remains unaffected. Note that the fluid interacts with the plate at the boundary, in this example at the bottom surface. The interaction is strictly local, i.e., the above mentioned rows $\underline{\underline{D}}_{+h/2}$ and $\underline{\underline{I}}_{+h/2}$ are used instead of the whole matrices.

The goal is to find discrete representations of the matrices and partial derivatives appearing in (4.4). The matrices are given explicitly in (3.39) and (3.40), which make use of the Lamb wave tensors $\underline{\underline{L}}_i$ and $\underline{\underline{B}}_i$ defined in (3.12) and (3.13). To begin with, the latter tensors are discretized with the method introduced at the beginning of the section. Using the Cartesian matrix representation $[\underline{\underline{L}}_i]$ of the tensors $\underline{\underline{L}}_i$ yields the $(2N \times 2N)$ -matrices

$$\underline{\underline{L}}_2^d = [\underline{\underline{L}}_2] \otimes \underline{\underline{I}}_d, \quad \underline{\underline{L}}_1^d = [\underline{\underline{L}}_1] \otimes \underline{\underline{D}}_y, \quad \underline{\underline{L}}_0^d = [\underline{\underline{L}}_0] \otimes \underline{\underline{D}}_{yy}, \quad \underline{\underline{M}}^d = \rho [\underline{\underline{I}}] \otimes \underline{\underline{I}}_d, \quad (4.7)$$

where \otimes denotes the Kronecker product¹. Similarly, the Lamb BC-tensors \mathbf{B}_i result in the $(4 \times 2N)$ -matrices

$$\underline{\underline{B}}_{-1}^d = [\mathbf{B}_1] \otimes \underline{\underline{I}}_{-d} |_{\pm h/2}, \quad \underline{\underline{B}}_{=0}^d = [\mathbf{B}_0] \otimes \underline{\underline{D}}_{=y} |_{\pm h/2}. \quad (4.8)$$

With the above matrices, a full discretization of the Lamb wave problem in a *free plate* has been obtained. Thereby, the partial derivatives ∂_y and ∂_y^2 have been “absorbed” into the matrices through the discrete approximations $\underline{\underline{D}}_{=y}$ and $\underline{\underline{D}}_{=yy}$, respectively.

The plate-fluid interaction is incorporated next. The additional scalar degree of freedom U of the fluid needs to be accounted for. Accordingly, the matrices in (4.7) and (4.8) are all expanded by one additional zero-row and zero-column, resulting in matrices of size $2N+1 \times 2N+1$ and $5 \times 2N+1$, respectively. The fluid-structure interaction is represented by the matrices $\underline{\underline{B}}_{=\omega}$ and $\underline{\underline{B}}_{=y}$ appearing in (4.4b) and given in (3.40). The discretized versions make use of $\underline{\underline{e}}_y^d = [\mathbf{e}_y]^T \otimes \underline{\underline{I}}_{=d} |_{+h/2}$, where $[\mathbf{e}_y]^T$ is the row vector $[0, 1]$. This yields the $(2N+1 \times 2N+1)$ -matrices:

$$\underline{\underline{B}}_{=\omega}^d = \begin{bmatrix} \mathbf{0}_{2N \times 2N} & Z_f \underline{\underline{e}}_y^{dT} \\ Z_f \underline{\underline{e}}_y^d & 0 \end{bmatrix}, \quad \underline{\underline{B}}_{=y}^d = \begin{bmatrix} \mathbf{0}_{2N \times 2N} & \mathbf{0} \\ \mathbf{0} & -\lambda_f \end{bmatrix}. \quad (4.9)$$

Finally, using the above matrices, the discrete version of the QGW problem (4.4) can be written as

$$\left[(ik_x)^2 \underline{\underline{L}}_{=2}^d + ik_x \underline{\underline{L}}_{=1}^d + \underline{\underline{L}}_{=0}^d + \omega^2 \underline{\underline{M}}^d \right] \cdot \underline{\underline{q}}^d = \underline{\underline{0}}, \quad (4.10a)$$

$$\left[ik_x \underline{\underline{B}}_{=1}^d + \underline{\underline{B}}_{=0}^d + \omega \underline{\underline{B}}_{=\omega}^d + ik_y \underline{\underline{B}}_{=y}^d \right] \cdot \underline{\underline{q}}^d = \underline{\underline{0}}, \quad (4.10b)$$

Note that the general structure of the matrices $\underline{\underline{L}}_i^d$ is as described in Fig. 4.3 but without yet incorporating the BCs $\underline{\underline{B}}_i^d$.

¹ The Kronecker product is defined by the block matrix: $\underline{\underline{A}} \otimes \underline{\underline{B}} \stackrel{\text{def}}{=} [A_{ij} \underline{\underline{B}}]$. If $\underline{\underline{A}}$ is of size $n \times m$ and $\underline{\underline{B}}$ of size $p \times q$, then $\underline{\underline{A}} \otimes \underline{\underline{B}}$ will be of size $pn \times qm$.

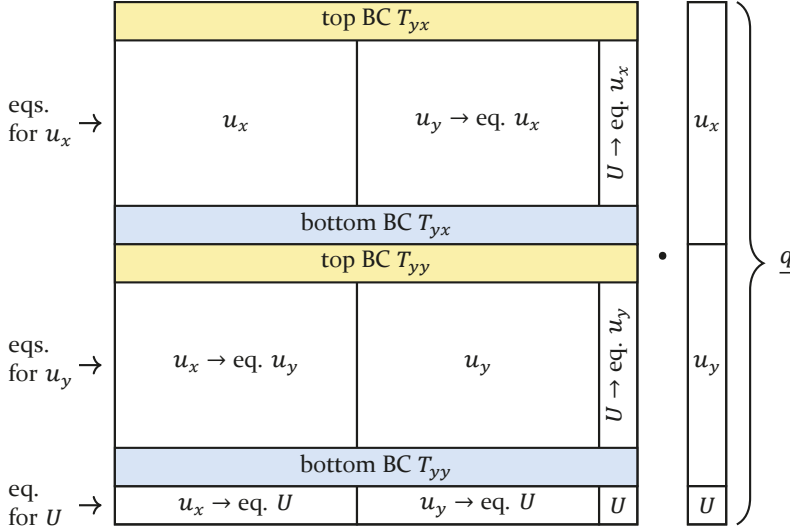


Figure 4.3: Allocation of the matrix sub-blocks in $\underline{P}_{\underline{i}}^d$ incorporated into $\underline{G}_{\underline{i}}^d$.

The change of variables will be performed prior to incorporating the BCs. At given frequency f , we have $\omega = 2\pi f$ and $\kappa_f = \frac{\omega}{c_f}$. With this, the change of variable (4.6) can be performed using the matrices obtained so far. This yields the discrete version of (4.5), which represents an algebraic polynomial EVP:

$$\left[\gamma^4 \underline{G}_{\underline{2}}^d + \gamma^3 \mathbf{i} \underline{G}_{\underline{1}}^d + \gamma^2 (\underline{G}_{\underline{0}}^d + 2\underline{G}_{\underline{2}}^d + \omega^2 \underline{M}^d) + \gamma \mathbf{i} \underline{G}_{\underline{1}}^d + \underline{G}_{\underline{2}}^d \right] \cdot \underline{q}^d = \underline{0}, \quad (4.11a)$$

$$\left[\gamma^3 \mathbf{i} \underline{\Gamma}_{\underline{+1}}^d + \gamma^2 (\underline{\Gamma}_{\underline{0}}^d + \omega \underline{\Gamma}_{\underline{\omega}}^d) + \gamma \mathbf{i} \underline{\Gamma}_{\underline{-1}}^d \right] \cdot \underline{q}^d = \underline{0}. \quad (4.11b)$$

As a last step, the BCs are incorporated into the equations of motion. This is achieved by replacing the rows 1, N , $N + 1$, $2N$ and $2N + 1$ of the polynomial coefficient matrices in (4.11a) by the rows of the matrices in (4.11b). Note that the mentioned rows are the degrees of freedom at the boundaries $y = \pm h/2$ for u_x and u_y , respectively, as well as U . The final structure of the matrices is shown in Fig. 4.3.

With the incorporated BCs, we obtain a simple polynomial algebraic EVP in γ , namely

$$\sum_{i=0}^4 \gamma^i \underline{P}_{\underline{i}} \cdot \underline{q} = \underline{0}, \quad (4.12)$$

where we omit the superscript \bullet^d for conciseness. This formulation fully and uniquely describes the QGWs in the fluid-coupled plate [P3]. It can quite readily be solved using standard techniques, see Sec. 4.3.

It is worth mentioning that (4.11b) can be multiplied by any power of γ . Accordingly, there is some flexibility in where the BCs are actually incorporated. We found that all options work equally well, but this presumably depends on the used eigenvalue solver.

Our code solves (4.12) iteratively for all frequencies. At time of implementation, all parameters are normalized. Moreover, the y coordinate is normalized so that the domain reduces to $[-1/2, 1/2]$ and the differentiation matrices operate on the unit domain. The computation of the differentiation matrices relies on the DMSUITE package by Weideman and Reddy [136]. Apart from normalization, the code closely resembles the equations from last section.

4.2.3 Integration on Chebyshev-Gauß-Lobatto points

After computing solutions, the results are not only meaningful by themselves but also very useful for further analysis. For instance, many of the studies showcased in Chap. 6 and Chap. 7 rely on the orthogonality relation (3.22), which involves the wave's total average power flux \bar{P} . For this purpose, it is crucial to be able to accurately integrate the field, e.g., the power flux density $p_x(y)$, over the waveguide cross section.

The numerical results require a numerical integration technique. Gauss quadrature is optimal, being exact for polynomials of order $2N - 1$ [135, 137]. However, this requires the integrand to be known at the Legendre points. Remember that the solution has been obtained at the Chebyshev points instead. An interpolation would be required in order to use Gauss quadrature.

On Chebyshev points, the optimal integration technique is *Clenshaw-Curtis quadrature* [135], which is exact for N th-order polynomials. We use a procedure provided by von Winckel [138] to calculate the quadrature weights. The implementation is based on the fast Fourier transform. Note that it might be possible to improve thereon, as the weights can be specified analytically [135].

4.3 Polynomial eigenvalue problems

Polynomial EVPs [88, 139] are common because they appear when modeling dynamical systems with losses [140]. The nondissipative, closed waveguide problem also leads to a polynomial EVP. The mentioned examples usually

result in 2nd order polynomial EVPs. In contrast to this, QGWs in the fluid coupled plate are described by the 4th order polynomial EVP given in (4.12). While the numerical solution procedures are the same regardless of the polynomial order, the required computational resources increase.

The conventional solution technique consist in first finding a linear EVP, i.e., of the form

$$(\gamma \underline{\underline{B}} - \underline{\underline{A}}) \cdot \underline{\underline{c}} = \underline{\underline{0}}, \quad (4.13)$$

in a higher-dimensional “state space” $\underline{\underline{c}}$ that has the same eigenvalues γ as the original problem. This new formulation can then be solved using standard numerical methods. The linearization procedure is not unique, i.e., many different linear representations can be found [88]. Commonly, the first *companion linearization* is employed [88], which for (4.12) results in the companion matrices

$$\underline{\underline{B}} = \begin{bmatrix} \underline{\underline{P}}_1 & \underline{\underline{P}}_2 & \underline{\underline{P}}_3 & \underline{\underline{P}}_4 \\ -\underline{\underline{I}}^d & 0 & 0 & 0 \\ 0 & -\underline{\underline{I}}^d & 0 & 0 \\ 0 & 0 & -\underline{\underline{I}}^d & 0 \end{bmatrix}, \quad \underline{\underline{A}} = \begin{bmatrix} \underline{\underline{P}}_0 & 0 & 0 & 0 \\ 0 & \underline{\underline{I}}^d & 0 & 0 \\ 0 & 0 & \underline{\underline{I}}^d & 0 \\ 0 & 0 & 0 & \underline{\underline{I}}^d \end{bmatrix}, \quad (4.14)$$

with the companion vector field $\underline{\underline{c}} = [\gamma^3 \underline{\underline{q}}, \gamma^2 \underline{\underline{q}}, \gamma \underline{\underline{q}}, \underline{\underline{q}}]^T$. From this representation it is evident that the quartic EVP may have $4(2N + 1)$ eigenvalues and eigenvectors, as the coefficient matrices $\underline{\underline{P}}_i$ are of size $2N + 1 \times 2N + 1$.

We use Matlab’s `polyeig` function to solve (4.12) directly. It performs the companion linearization described above and subsequently applies the QZ-algorithm to solve the resulting linear EVP. Overall, this method guarantees to find all QGW solutions. It is stable for all frequency-thickness products and it is more efficient than root-finding. Furthermore, complex valued eigenvalues/wavenumbers are naturally dealt with, representing no complication.

Some comments on possible further improvements of the EVP solution technique are in order. As pointed out by Mehrmann and Voss [88], nonlinear eigenvalue solvers do currently not meet the standards of their linear counterparts and are the topic of current research. Any numerical method should be accurate, efficient and thereby exploit and preserve the structure of the problem. These requirements are not met by the companion linearization [88]. The increased size of the companion matrices lead to deteriorated efficiency and the linearized problem may be less well conditioned then the original one [88]. Furthermore, this linearization does not preserve the structure that

is evident in the original problem, see Subsec. 3.2.4. Improvements could be achieved by choosing a structure preserving linearization [88, 93, 94, 141]. Higher efficiency could additionally be achieved using a carefully designed nonlinear solver that directly operates on the polynomial EVP and, thereby, exploits and preserves the inherent structure [88].

4.4 Elastodynamic Acoustic Toolbox (EDAT)

A Matlab toolbox called Elastodynamic Acoustic Toolbox (EDAT)² was developed that assembles, solves, post-processes and visualizes plane elastodynamic waveguide problems. The toolbox is the result of a close cooperation between an adjunct project [142, P7, P8] and the project of this dissertation. While the former focuses on the effect of pre-stress on the mechanical waveguides, the latter is concerned with the effects of fluid-structure interaction.

EDAT is entirely based on SC discretization of waveguide problems as exemplarily presented in the previous sections. It is capable of handling multi-layered, fluid-coupled and pre-stressed plane elastodynamic waveguides in arbitrary anisotropy. For the best of the author's knowledge, it is currently the only software package that provides a reliable EVP-based solution of leaky elastodynamic waves.

² © 2017 - 2022 Miturheber: Daniel A. Kiefer, einige Rechte vorbehalten. Einige Befugnisse liegen bei Diehl Metering GmbH, Ansbach, Deutschland.

5 Experimental methods and verification

Several different methods for generation and measurement of ultrasound and (quasi)-guided waves are used in this work. This chapter gives an overview of the working principles and how the experimental setups were realized. Moreover, measurement results validating the theory presented in Sec. 3.2 are presented and discussed.

5.1 Transducers for waveguide excitation and sensing

Ultrasonic transducers serve the purpose of converting electrical energy into mechanical energy and vice versa. In this section, we review, model and analyze transducer setups capable of exciting guided and quasi-guided elastodynamic waves.

Different physical energy conversion mechanisms can be exploited. Transducers may rely on piezoelectric [1], magnetostrictive [143], Lorentz force [143], electrostatic [144] or thermal expansion principles [145]. Piezoelectric and Lorentz force (eddy current) transduction is most common for ultrasonic elastodynamic waves. We focus on the former in this work. Optical excitation is also common and is based on thermal expansion. In contrast to the previously mentioned transduction mechanisms, the latter one is not reversible. Optical sensing of mechanical waves is, nonetheless, possible via interferometry, e.g., with a laser Doppler vibrometer (LDV).

The basic properties of the relevant transduction mechanisms can be summed up as follows:

Piezoelectric: Advantages: good impedance matching, efficient, robust, small form factor, relatively low cost. Disadvantages: coupling medium required.

Lorentz forces: Advantages: contactless, no coupling medium required, broadband, force distribution is well definable, controllable directivity. Disadvantages: inefficient, must be very close to the waveguide, only suitable for electrically conductive waveguides, magnet required, electrical impedance matching required, quite large setup.

Optical interferometry: Advantages: contactless, reactionless, broadband, highly localized. Disadvantage: only suited for (diffusively) reflecting or coated waveguides, very large setup, expensive.

For many applications it is desirable to selectively excite one desired mode [146], but sometimes transducers that excite a brought range of waves are preferred instead. Accordingly, we distinguish between selective and multi-modal transducers. In general, the aim is to ensure a distribution of forces – prescribed either inside the waveguide or at its boundary – that excites the desired mode(s). For this end, several different transducer designs are conceivable for each of the transduction mechanisms [59, 143]. The relevant ones will be discussed in detail in the following subsections. Note that independent of the specific transducer under study, the excitation of waves is described by the modal expansion theory [147], see Subsec. 3.1.8.

5.1.1 Bonded piezoelectric ceramics

The setup of a surface bonded piezoelectric ceramic [1] (sometimes referred to as piezoelectric waver active sensors, PWAS) is shown in Fig. 5.1. These transducers exhibit good coupling into the plate, operate out of resonance and are capable of broadband excitation and sensing [148, 149], both in time and space. This makes them a good choice to measure dispersion curves. Due to their simplicity and efficiency, they are frequently used in structural health monitoring.

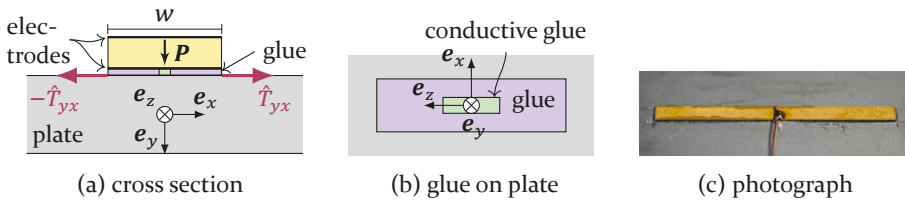


Figure 5.1: Bonded piezoelectric ceramic.

The transduction is dominated by the shear stresses $T_{yx}(x)$. For a stiff and thin bonding layer, the stresses highly concentrate at the two edges of the piezoelectric element and are oppositely directed. This leads to a pin-force model [148], where the Dirac delta like tractions are distributed in odd symmetry with respect to the transducer’s center. The idealized stresses are drawn into Fig. 5.1a.

We are interested in the frequency and mode-dependent surface normal velocities generated by the transducer. This can be modeled using the modal expansion technique [147] presented in Subsec. 3.1.8. The tractions prescribed by the transducer are idealized as discussed above, i.e., they are assumed to be given by $[\hat{T}_{yx}\delta(x - w/2) - \hat{T}_{yx}\delta(x + w/2)]\mathbf{e}_x + 0\mathbf{e}_y$, where w is the width of the piezoelectric ceramic. Hence, the source seen by the mode $(\mathbf{v}_n, \mathbf{T}_n)$ is

$f_{sn} = v_{xn}^* [\hat{T}_{yx} \delta(x - w/2) - \hat{T}_{yx} \delta(x + w/2)]$, using the x -component of the mode's velocity vector at the surface, i.e., $v_{xn} = \mathbf{v}_n \cdot \mathbf{e}_x|_{y=h/2}$. With this, the modal envelopes/amplitudes A_n are given according to (3.30) by

$$A_n = \frac{\mathcal{F}_x f_{sn}(x)|_{k_x=k_{xn}}}{4\bar{P}_n} = \frac{-i}{2\bar{P}_n} v_{xn}^* \hat{T}_{yx} \sin(k_x w/2). \quad (5.1)$$

The above computation has been done iteratively for a set of frequency values. The result for a piezoelectric element of width $w = 2.95$ mm on a 1 mm thick brass plate is displayed exemplarily in Fig. 5.2.

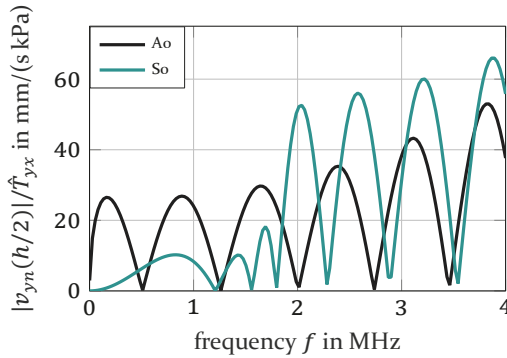


Figure 5.2: Prediction of wave amplitudes excited by the bonded piezoelectric ceramic.

The transducers are seen to exhibit a wavelength tuning effect [148], whereby the width w of the piezoelectric element strongly determines which wavenumbers are excited. Zero excitation is found when the width w corresponds to multiples of the wavelength λ , as can be seen in (5.1). On the other hand, maxima will be found when its width is close to odd multiples of half the wavelength [149]. In general, the sensitivity tends to increase for narrower elements due to an averaging effect [149]. The ideal transducer to excite a broad wavenumber range is a line source. For these two reasons, the transducer should be narrow in axial direction [149].

In this work, bonded piezoelectric ceramics are used to measure dispersion curves. They consist of a rectangular piezoelectric ceramic (PIC255, PI Ceramic GmbH, Lederhose, Germany) of size $35 \times 2.95 \times 0.3$ mm³ (length \times width \times thickness) polarized in thickness direction. It is bonded to the specimen using a dual-component epoxy adhesive (UHU Plus Endfest 300, UHU GmbH, Bühl, Germany) in addition to a spot of electrically conductive glue (Elecolit 325, Panacol-Elosol GmbH, Steinbach, Germany) in the center, see Fig. 5.1b. The latter allows to contact the lower electrode through

the conductive plate, as it is mechanically inaccessible after bonding. The adhesives are cured at 70 °C with approx. 2 kg weight for about 2 h. Such a transducer mounted to a steel plate is depicted in Fig. 5.1c.

5.1.2 Comb array and comb transducers

Piezoelectric comb array and comb transducers [33, 59] are surface mounted transducers designed to predominantly excite certain mode. The geometries are shown in Fig. 5.3. Both rely on wavelength matching, i.e., they preferentially excite wavelengths λ that are equal to the periodicity w_p of the transducer's geometry. They are usually pressed onto the structure and coupled through a fluid layer, e.g., glycerol (glycerine). Due to this layer, when modeling the transducers it is usually assumed that they cause a purely normal stress T_{yy} over the comb's fingers [33, 150, 151].

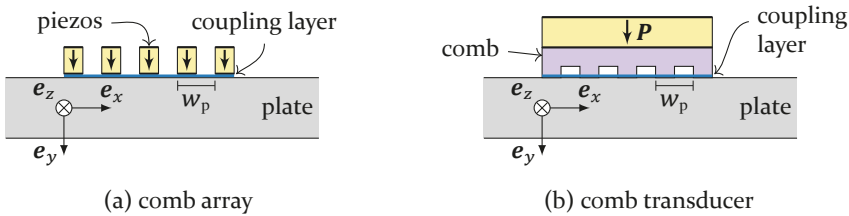


Figure 5.3: Geometry of comb array and comb transducers.

Each piezoelectric rod of the array depicted in Fig. 5.3a can be driven separately. This is known as a *phased array transducer* [33, 152, 153, S6] and is widespread in medical ultrasonic imaging and also used in nondestructive testing (NDT). This allows for dynamical matching to any desired mode (phase velocity) through introduction of a phase delay between the excitation of the elements. However, the resulting electrical driving unit is highly complex and costly. Instead, it might be preferable to drive the array as a single unit. In this case, the matching condition will be fixed to $\lambda = w_p$; unless the polarization direction of the piezoelectric elements alternates, in which case $\lambda = w_p/2$. The comb transducer shown in Fig. 5.3b is a simpler variant [59, 150, 151], as it requires only one piezoelectric ceramic.

For simplicity, we use a comb array transducer¹ with only two piezoelectric ceramics that are polarized in the same direction. It is matched to the Ao mode of either a 1 MHz mm brass plate or 1.5 MHz mm steel plate. The elements are held inside a polymer enclosure, which also ensures the electrical connectivity.

¹ Developed and build by the project partner Diehl Metering GmbH.

Thereby, the lower electrode of the piezoelectric elements is extended to the edge of the ceramic for accessibility. The transducer is clamped onto the waveguide and coupled with a thin layer of glycerol.

We demonstrate exemplarily how the transducer excites the fundamental modes in the pipe wall. The modeling is performed again according to Subsec. 3.1.8 and the result is presented in Fig. 5.4. As was discussed previously, we thereby assume that the transducer generates pure normal stresses $T_{yy}(x)$ beneath the piezoelectric elements. The corresponding source seen by the waveguide is $f_{sn} = v_{yn}^* T_{yy}(x)$, where v_{yn} is the normal velocity at the boundary, i.e., $v_{yn} = \mathbf{v}_n \cdot \mathbf{e}_y|_{y=h/2}$. The spatial distribution of the stresses is taken to be constant beneath the piezoelectric elements and zero otherwise, as shown in Fig. 5.4. The spacing w_p between the elements is matched to the Ao wave and the width of the elements is $w_p/2$. A high amplitude is obtained for the Ao wave but not for the So mode. The process of Ao wave build-up can clearly be observed in Fig. 5.4a, while Fig. 5.4b demonstrates the mostly destructive interference seen by the So wave.

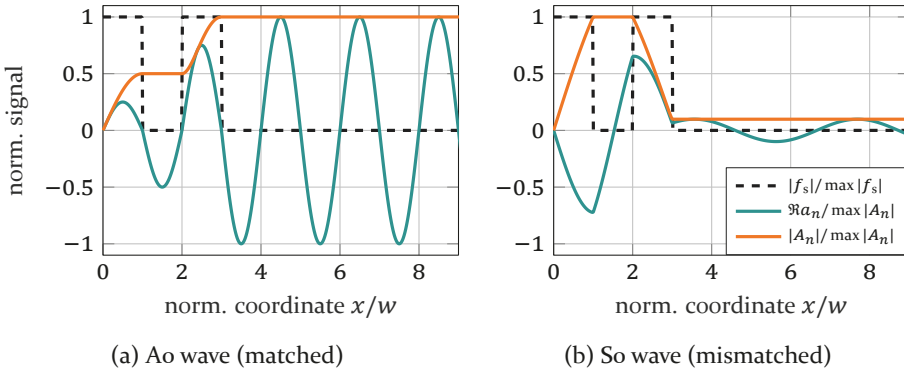


Figure 5.4: Excitation of the Ao and So wave by the comb array transducer.

5.2 Laser Doppler measurement of waveguide spectra

Laser Doppler vibrometry is a great tool to verify the dispersion curves calculated in Chap. 3. It is an optical measurement method that works without contact and it is easy to sample the specimen's surface with high resolution. This makes it perfect to acquire spatial data, such as wavenumbers and phase velocity. The method is based on interferometric measurement of the Doppler frequency shift of a laser beam reflected from a moving surface. The Doppler shift is proportional to the velocity with which the reflector moves axially to

the laser beam. Hence, this method provides direct access to the local surface normal velocity of a mechanical waveguide.

The used vibrometer (PSV-500, Polytec GmbH, Waldbronn, Germany) [154] is a modified Mach-Zehnder interferometer based on a helium-neon laser. It is a heterodyne interferometer, which means that it is sensitive to the direction of vibration of the object. This is achieved by adding a constant frequency shift to the reference beam (using a Bragg cell), to which the Doppler shift then adds with the correct sign. After mixing the reference beam and the object beam, a signal with beating envelope reaches the photo-sensor. The beat frequency is equal to the Doppler shift and provides direct access to the normal velocity of the specimen. Moreover, the optical setup includes an actuated mirror to deflect the laser beam in order to scan the surface of the specimen.

An overview of the measurement setup used to acquire dispersion curves of leaky Lamb waves is given in Fig. 5.5. The plate under test (specimen) is fixed on one side onto a tank filled with water. The excitation signal is generated on a computer and programmed onto a function generator (33220A, Keysight, Santa Rosa, CA, USA). After amplification by factor 20 (A 1230-02, Dr. Hubert GmbH, Bochum, Germany), resulting in 100 V amplitude, it drives a bonded piezoelectric transducer on the plate. The plate's surface normal velocities are scanned by the LDV (PSV-500, Polytec GmbH, Waldbronn, Germany) and fed back to the computer for post-processing and visualization.

A chirp is used as broadband excitation signal to drive a bonded piezoelectric ceramic, see Subsec. 5.1.1. The signal is exemplarily shown together with its magnitude spectrum in Fig. 5.6. It has a center frequency $f_c = 1.9$ MHz, bandwidth $B = 3.8$ MHz and a total duration between $D = 100$ μ s and $D = 150$ μ s. The time-bandwidth product is therewith $380 \leq DB \leq 570$, which guarantees a better signal-to-noise ratio as compared to pulsed excitation [P4]. Injecting as much energy as possible into the plate is important because the leaky waves gradually loose energy to the fluid. The higher the initial energy in the wave, the larger is the range where the wave can be measured with the LDV. Furthermore, the chirp is windowed with a raised cosine window with a tapering factor of 0.15 to reduce the Fresnel ripples [P4].

The LDV scans the transducer's center line marked in Fig. 5.5c, obtaining a discrete set of the time- and space-dependent surface normal velocities $v_m(x, t)$. The obtained data can immediately be visualized in a time-space diagram as in Fig. 5.7. The broadband space-time signal is difficult to interpret. However, some of the wave and frequency components isolate. For example, a portion

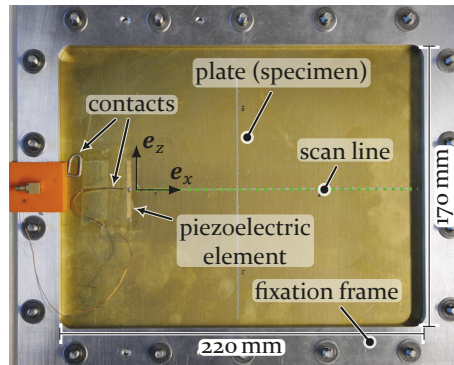
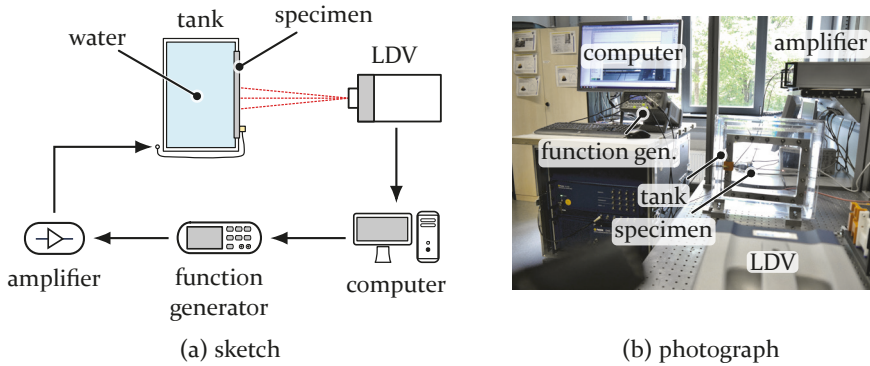


Figure 5.5: Experimental setup to measure leaky QGW. The water tank and connector was designed and constructed as part of [S4].

of the So' and Ao' waves separate after propagating about 10 cm. The phase velocity of the waves can be read-off as the slope of the phase lines, while the energy velocity is given by the slope of the beams. Observe that the phase fronts of the labeled So' wave beam have approximately the same slope as the beam itself, meaning that it is barely dispersive at all. This suggests that it is a low frequency component of the So' wave (see Fig. 3.24b), which agrees with the fact that low frequency components come first in the used up-chirp excitation signal. The plate is clamped at about 15.3 cm from the transducer and the plate edge is about 2 cm further out. A reflection of the So' wave from this edge can clearly be seen in the plot, which propagates in negative x -direction. On the other hand, the Ao' wave beam shows lower phase velocity than energy velocity and is clearly dispersive. Overall, wave components strongly overlap in the x - t -domain and are difficult to interpret both quantitatively as well as qualitatively.

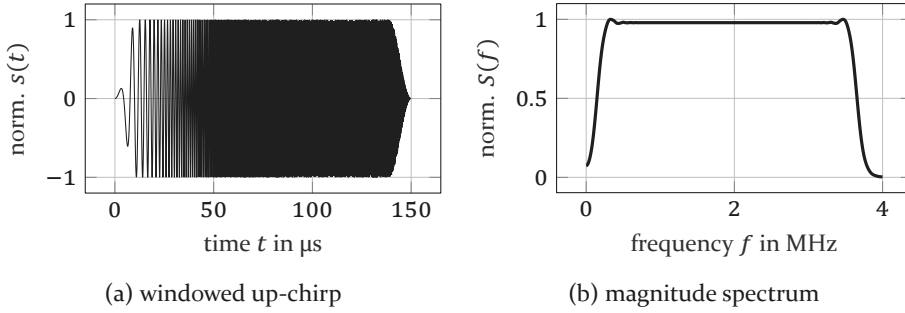


Figure 5.6: Excitation signal and its spectrum.

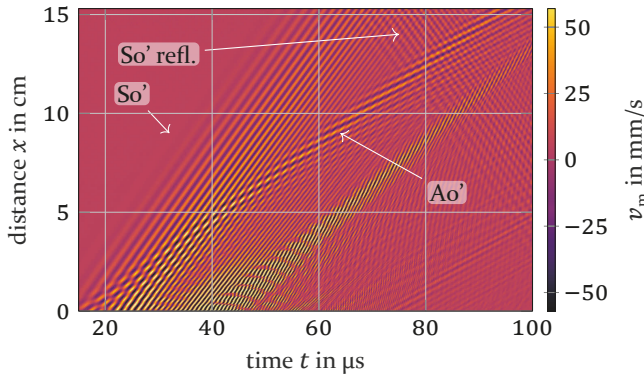


Figure 5.7: Wave field obtained by laser Doppler vibrometry of a 1 mm brass plate on water ($D = 100 \mu\text{s}$).*

* The data was obtained by Dai [S4]. Post-processing and visualization by the author.

For this reason, it is desirable to transform the measured surface normal velocities $v_m(x, t)$ into the k_x - ω -domain. We use a 2D-Fourier transform for this end [155, 156, P2]. First, a Fourier transform in time according to (2.30) maps $t \rightarrow \omega$ for all x . Then, a subsequent spatial Fourier transform as defined in (2.32) – albeit only for the x -coordinate – maps $x \rightarrow k_x$ for all ω . Overall, this results in

$$V_m(k_x, \omega) \stackrel{\text{def}}{=} \mathcal{F}_x \mathcal{F}_t v_m(x, t) = \int_{-\infty}^{\infty} \int_{-\infty}^{\infty} v_m(x, t) e^{-ik_x x} e^{i\omega t} dt dx. \quad (5.2)$$

Due to the different sign conventions used in the definitions of the temporal and spatial Fourier transforms, the inverse space-time Fourier transform matches the initial ansatz for QGWs given in (3.1). This has the consequence that waves whose phases travel in positive x -direction are mapped to (k_x, ω) with equal sign. Accordingly, waves with forward propagating phases are found

in the first and third quadrants of the k_x - ω -plane – as would be expected from ansatz (3.1).

The acquired LDV data is sampled in time and space. The discrete version of the 2D-Fourier transform (5.2) is computed using Matlab's `fft2` function. Matlab's sign convention is a negative exponent in the Fourier transform, which fits to our spatial Fourier transform. We achieve the flipped sign in the temporal Fourier transform by flipping the temporal axis using `flip1r` before performing the transform². The effect of this operation on the result in the f - k_x -domain can be observed in Fig. 5.8. The lower plane, i.e., quadrants three and four, is point symmetric to the upper one as the measured time-space signals are real-valued.

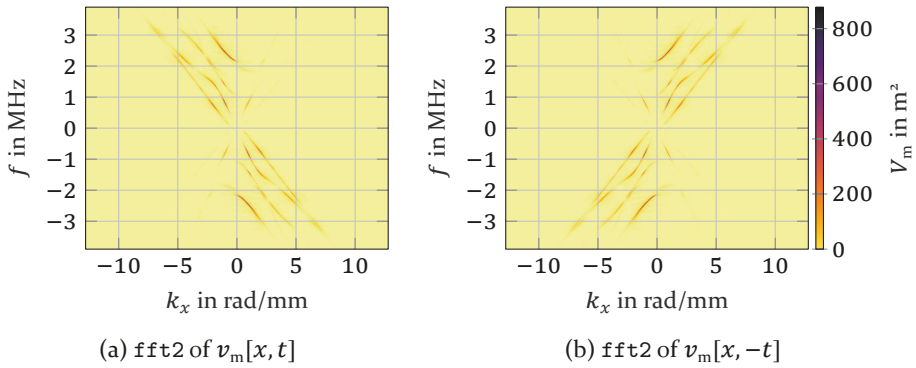


Figure 5.8: Effect of flipping the temporal coordinate, i.e., using a switched sign in the temporal Fourier transform (1.5 mm steel plate on water).*

* The data was obtained by Dai [S4]. Post-processing and visualization by the author.

Some notes on the sampling of time and space are in order. The LDV's sampling frequency is set to $f_s = 7.8125$ MHz and it scans the transducers' normal line with a sampling distance of $245 \mu\text{m}$, i.e., a sampling wavenumber of $k_s = 25.6$ rad/mm. Fig. 5.8 shows the full f - k_x -domain limited by the sampling frequency f_s and sampling wavenumber k_s . No wave components are excited outside this range, hence, no aliasing is seen. Furthermore, the vibrometer averages each scanned point 100 times to suppress noise.

The thus obtained dispersion curves of a 1 mm brass plate on water is depicted in logarithmic scale in Fig. 5.9. For the purpose of comparison, the axial wavenumbers computed according to Subsec. 3.2.3 are plotted on top. In general, we observe a very good match between experimental results and

² Instead, it would also be possible to use `fft` for the spatial coordinate and `ifft` for the time variable. The normalization conventions used by Matlab need to be considered when doing so.

the numerical model. For higher frequencies, a slight drift can be observed, which is related to uncertainties in the model parameters like the plate's thickness and elastic parameters. The material parameters used to compute the dispersion curves were taken from the literature, see Appendix A. An inverse method could be applied to determine accurate values for the material parameters as well as the plate's thickness [P2, 157–159].

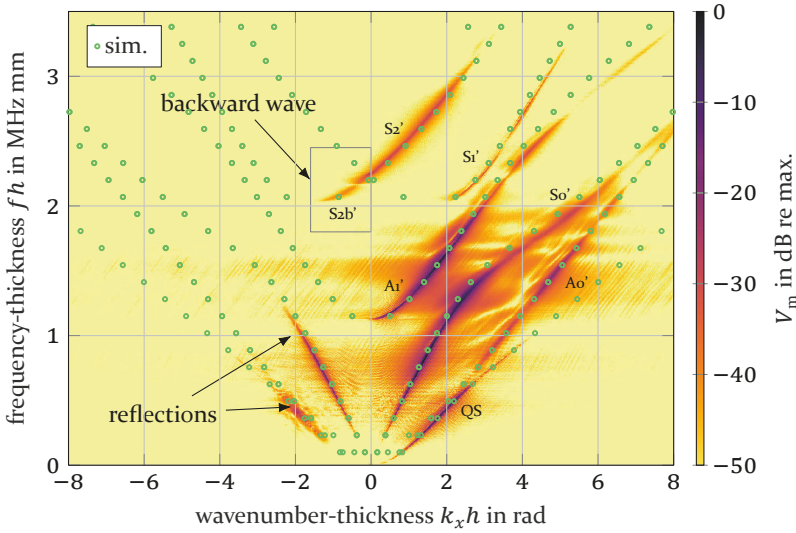


Figure 5.9: Measured axial wavenumbers of a 1 mm thick brass plate on water obtained as the 2D-Fourier transform of Fig. 5.7.*

* The data was obtained by Dai [S4]. Post-processing and visualization by the author.

The wave components are seen to isolate in the f - k_x -plane. Reflections separate from the direct waves and are found on the negative k_x axis together with the backward S_{2b}' wave. The latter has positive energy velocity, as can be deduced from the curve's slope. We remark that in the previous analysis, we mostly separated waves with positive phase propagation from the ones with negative phase propagation. When inspecting experimental data, however, it is more meaningful to separate waves according to the direction of their energy flux (energy velocity) because only the corresponding waves arrive at the receiver, which is located to one side of the transducer.

The fact that waves isolate in the f - k_x -domain can be harnessed to separate wave components. We utilize a rectangular pass-band filter as shown in Fig. 5.9 to obtain the isolated spectrum of the S_{2b}' wave. An inverse Fourier transform yields its wave field and is displayed in Fig. 5.10. Note that the wave is confined to a very limited x - t -domain and the axis extends have been

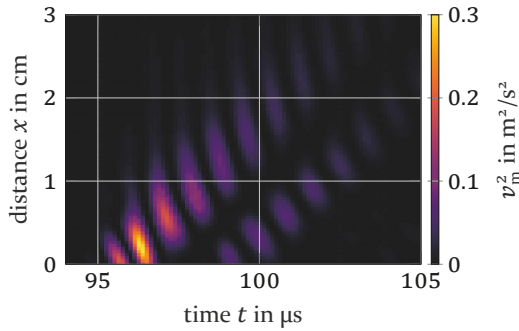


Figure 5.10: Isolated wave field as squared velocities of the S2b' wave obtained by filtering in the f - k_x -domain.*

* The data was obtained by Dai [S4]. Post-processing and visualization by the author.

zoomed accordingly. This is because it limits to a narrow frequency band (remember the chirp excitation) and has high attenuation. As expected, the wave beam propagates in positive x -direction, while the phases “propagate” in negative direction. Backward waves have also been observed in Refs. [68, 160–162].

Guided and QGWs in other plate samples have also been measured and give similar results. The obtained dispersion curves are provided in the following for reference without further comments.

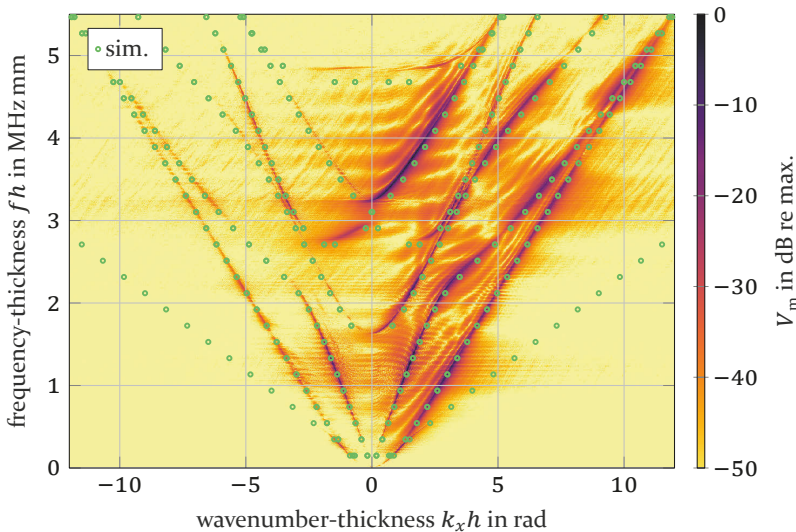


Figure 5.11: Steel plate on water.

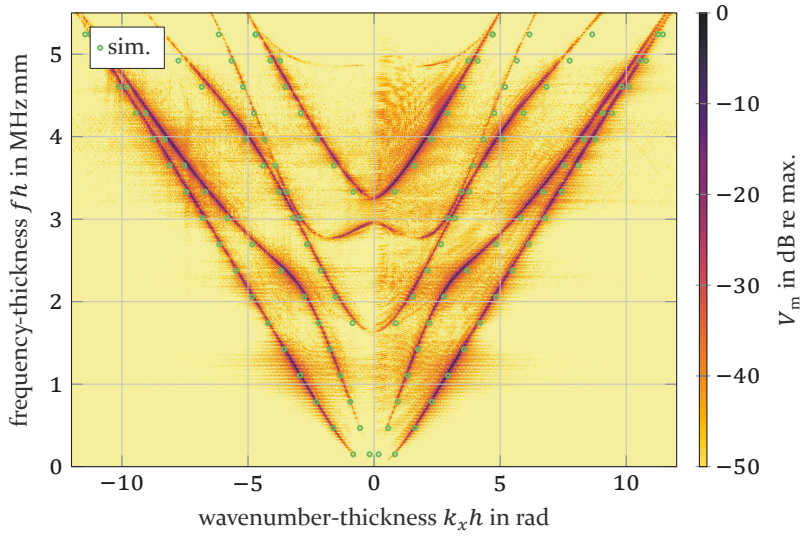


Figure 5.12: Free steel plate.

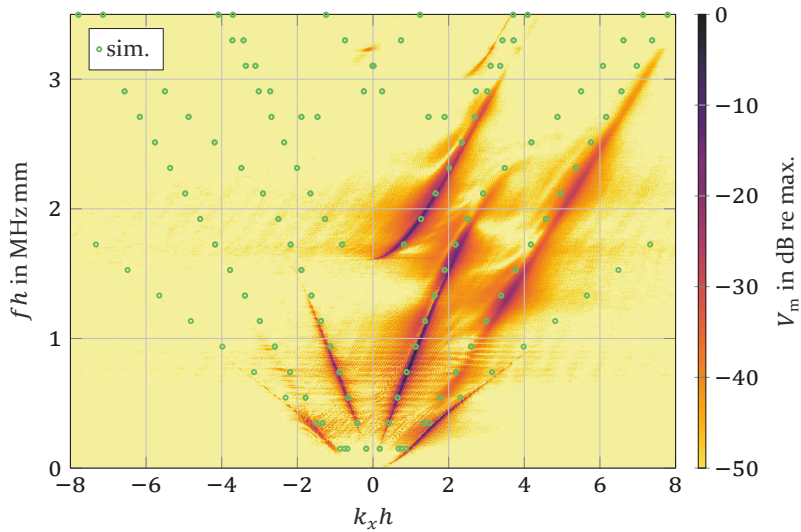


Figure 5.13: Aluminum plate on water.*

* The data was obtained by Dai [S4]. Post-processing and visualization by the author.

5.3 Schlieren photography

Ultrasound in transparent media can be made visible using a schlieren system [163]. The term *schliere* refers to small disturbances of the optical refractive index. Ultrasound are local variations in pressure (and density) and through the piezooptic effect, it also causes local changes in the refractive index. Therefore, from an optical point of view, ultrasound represents a schliere and when light travels through it, its phase gets modulated. With a schlieren system the phase variations are translated into intensity variations [163], enabling us to see or photograph the small variations in refractive index.

The schlieren system at Lehrstuhl für Sensorik (LSE) is a classical dual-field-lens arrangement [163]. The setup is sketched in Fig. 5.14 and photographs are depicted in Fig. 5.15. A 532 nm solid state laser (FDSS532-Q1, CryLas GmbH, Berlin, Germany) with 1.3 ns pulse duration is used as light source. A neutral density (ND) filter can be used to adjust the intensity. A beam expander widens the laser beam, which is then collimated by a lens. This ensures a homogeneous illumination of the water tank, where ultrasound waves are to be made visible. A second lens acts as a Fourier transformer. At the focal distance – which is the Fourier plane of the lens [164] – a filter is responsible of translating phase variations of the light into intensity variations at the imaging plane, where the monochromatic CCD camera (Grasshopper3, Point Grey Research Inc., Richmond, Canada) is located.

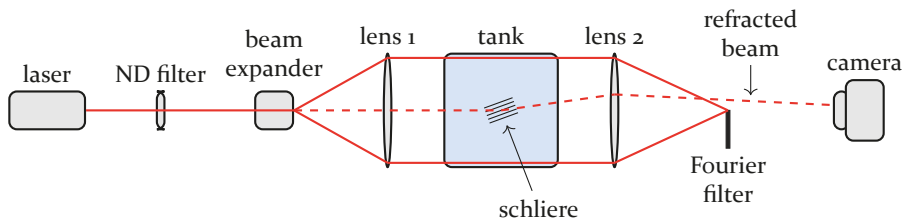


Figure 5.14: Sketch of the optical schlieren system at LSE.

In ray-optical terms, the homogeneous illumination focused onto the center point is filtered out, while the rays refracted by the schliere pass above the filter and eventually reach the camera. In this way, an image of the schliere is formed. Although the ray model is intuitive, a Fourier optics [164] model is preferred, as it is a familiar tool capable of representing asymptotically the wave nature of refractive phenomena.

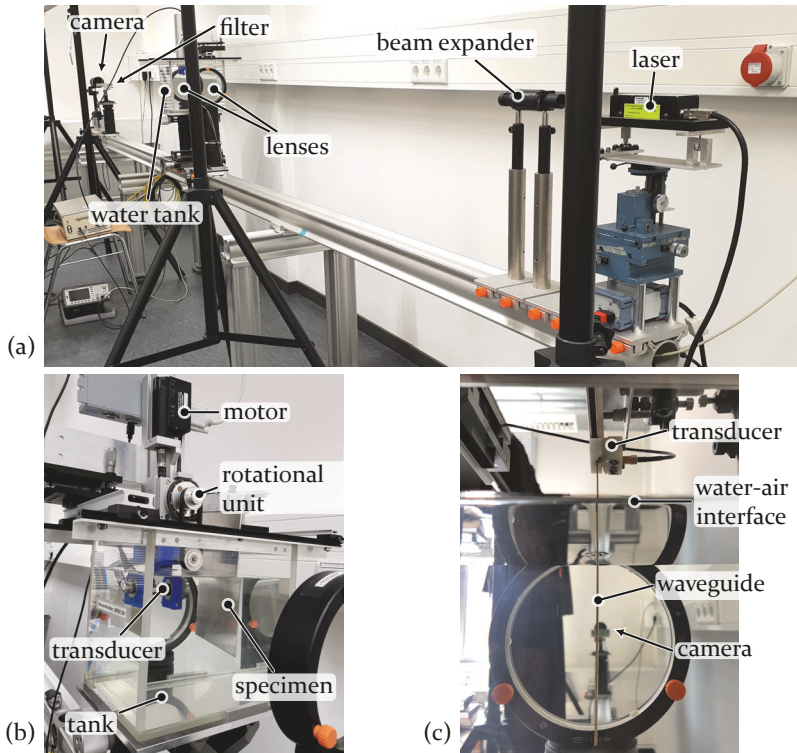


Figure 5.15: Photographs of the schlieren system at LSE: (a) full optical system; (b) water tank with immersed transducer mounted onto a motorized rotational unit; and (c) immersed waveguide with transducer.*

* Photograph (a) taken by Sivanesan [S3]; (b) and (c) are from Schmid [S9].

As Fourier filter we use a razor blade, thereby blocking almost half of the wavenumber spectrum. This is known as the classical “knife-edge cutoff”. The combination of coherent illumination and knife-edge cutoff is not optimal [163], but we obtain satisfactory results for our purposes. Improved filtering could be achieved using a digital micromirror device [165]. Fourier optical simulations of our system with different filters were performed as part of a student’s thesis [S3]. The $\varnothing 150$ mm lenses have a focal length of 2.25 m. For ultrasound with a wavelength of 1.5 mm, this results in 0.8 mm between the diffraction orders in the Fourier plane. Hence, the diffraction peaks separate well in space and a simple mechanical filter in the Fourier plane is suitable.

In general, schlieren photography does not, in a simple manner, provide quantitative data on the ultrasonic field, i.e., acoustic pressure distributions. Although such work exists [163], other methods do more readily yield quantitative acoustic data. For instance, *light refractive tomography* [166–168] is

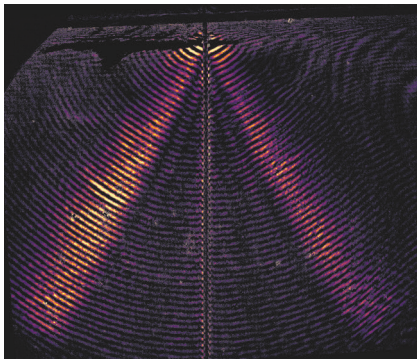
more suitable for such purposes. Nonetheless, schlieren photographs provide accurate quantitative data about the geometry of the wave field [15, 169]. Moreover, its advantage is speed, as the entire projection of the wave field is acquired with a single shot. As a consequence, it is feasible to make videos of propagating ultrasonic waves.

Schlieren images of leaky ultrasonic fields were obtained of the immersed plate/strip depicted in Fig. 5.15c as part of the student thesis [S9]. A comb array transducer is mounted on the free strip region and mainly excites the Ao Lamb wave at 1 MHz in the 1 mm thick brass strip, see Subsec. 5.1.2. The wave travels down the guide and eventually reaches the section immersed in water. While part of the wave's energy is reflected at this point, most of it is converted into the Ao" wave of the double-sided fluid loaded plate. Its radiated field is then captured by the schlieren system.

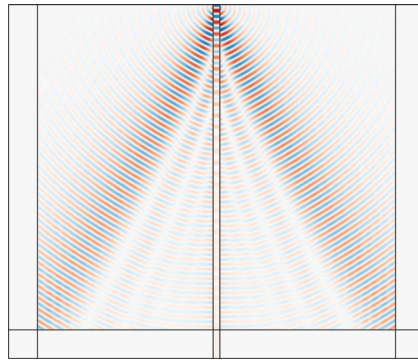
The resulting schlieren photograph of the leaky Ao" wave is shown in Fig. 5.16. A corresponding FE computation of the field is also shown for comparison. The high attenuation of the Ao" wave ($\Im k_x \approx 1 \text{ Np/cm}$) leads to radiation in a clearly visible main lobe due to the small effective aperture of radiation ($\sim 1/\Im k_x$). This does not correspond to the plane inhomogeneous wave field expected for leaky waves, see Subsec. 3.2.7. Remember that QGWs are not able to fully represent the wave field in the fluid domain. Nonetheless, the leaky wave solution correctly predicts the radiation angle at which the main lobes are formed, as they represent the resonances of the plate-water system.

The radiation lobes will gradually transition into an inhomogeneous plane wave field when the radiation rate of the QGW decreases. Consider, for instance, the So" wave field shown in Fig. 5.16c. In this case, the low attenuation ($\Im k_x \approx 0.1 \text{ Np/cm}$) leads to radiation over a large plate section compared to the wavelength and, therewith, to the formation of the expected inhomogeneous, nearly plane wave front.

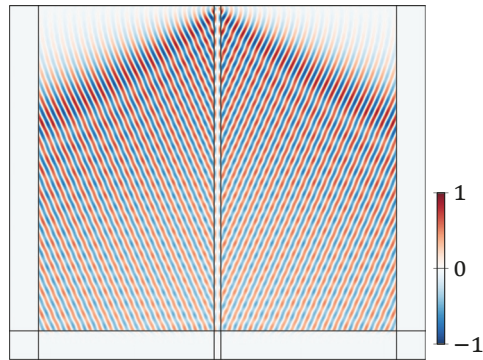
Nonspecular reflections were also photographed as part of [S9]. Thereby, the motorized rotational unit seen in Fig. 5.15a serves to adjust the critical angle of incidence onto the plate. The results are presented jointly with the theory in Subsec. 6.3.2.



(a) Schlieren image: A_0



(b) FE validation: A_0



(c) Less attenuated wave: FE simulation of S_0

Figure 5.16: Schlieren photograph of the acoustic field radiated by an A_0 leaky wave*. The corresponding FE simulation in (b) serves as qualitative comparison and (c) for discussion. The computed field shows the normalized pressure in the water and the normalized x -displacement in the plate (through-thickness direction). Parameters: 1 mm thick brass plate immersed in water, excited with A_0 wave at 1 MHz in the free plate region.

* Photograph acquired by Schmid [S9]. Post-processing and visualization by the autor.

6 Modeling Lamb wave-based flow meters

This chapter is concerned with the adequate modeling of the flow metering principle, i.e., the details of the V-path signal. In general, for this we need to describe: (a) the radiation of QGW into the fluid, (b) the effect of the flowing medium on the acoustic wave, (c) the reflection at the bottom pipe wall, (d) the back-coupling into the upper pipe wall at incidence. While (a) has been treated in detail in Sec. 3.2, (b) through (d) will be discussed in the remainder of this chapter.

6.1 Convection of ultrasound: ray tracing

Wave propagation in quiescent media has been considered so far. Transit-time UFM relies on changed wave propagation due to flow of the medium, i.e., large scale motion. In this case, *convective terms* need to be included in the equations of motion for an appropriate description [13]. Instead of developing a full wave theory of convected ultrasound, we shall rather use the *ray theory* to obtain explicit approximations of the time of flight through the pipe's interior.

The ray theory is provided in this section as a reference according to the exposition by Pierce [13]. It assumes that the field's amplitude does not vary much over one wavelength and that the radii of curvature of the phase fronts are larger than the wavelength [13]. These conditions will both be fulfilled if the wave is generated by a leaky Lamb wave with moderate radiation rate, i.e., when $\Im k_x \ll \Re k_x$.

The theory predicts the path taken by an arbitrary point on a wave front, hereinafter, denoted as \mathbf{x}_p . According to Sec. 2.3, in a medium at rest, the point moves with the phase speed c_f in direction \mathbf{e}_p , which is normal to the phase front, resulting in the vectorial phase velocity $\mathbf{c}_f = c_f \mathbf{e}_p$. If the medium is flowing with velocity \mathbf{v}_o , the point needs to move with the *ray velocity*

$$\mathbf{v}_p \stackrel{\text{def}}{=} \frac{d\mathbf{x}_p(t)}{dt} = \mathbf{c}_f + \mathbf{v}_o \quad (6.1)$$

with respect to a coordinate system at rest, in order to remain on the phase front. This situation is depicted in Fig. 6.1a. As the point $\mathbf{x}_p(t)$ moves with time, it traces the so-called *ray path*.

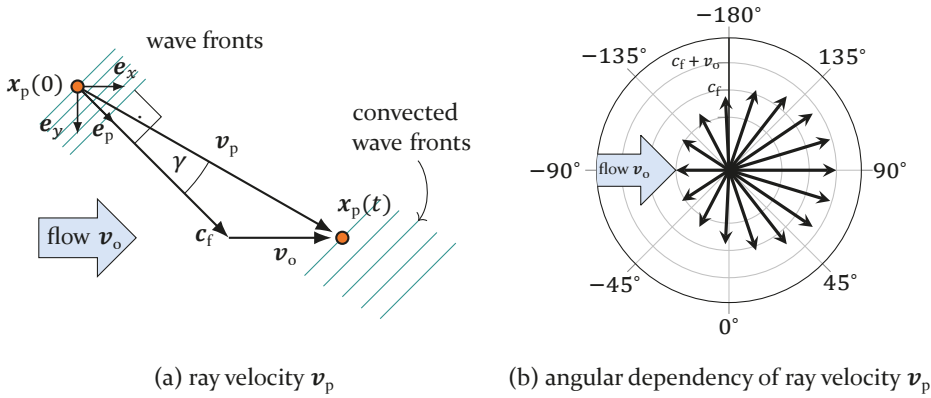


Figure 6.1: convection of ultrasound

When v_o and c_f are not collinear, both the direction and the magnitude of the wave propagation will change due to the fluid flow v_o . Fig. 6.1b illustrated this by showing the ray velocities in a horizontally flowing medium with different orientations e_p of the wave fronts. The propagation of the wave fronts is no longer normal to themselves, but under an angle

$$\gamma = \arccos\left(\frac{\mathbf{v}_p \cdot \mathbf{e}_p}{v_p}\right) \quad (6.2)$$

with respect to the normal vector e_p , where $v_p = |\mathbf{v}_p|$.

Ray tracing equations can be derived that predict the ray path [13]. This is usually done in terms of the *slowness vector* introduced as

$$\mathbf{s} = \frac{1}{c_f + \mathbf{v}_o \cdot \mathbf{e}_p} \mathbf{e}_p. \quad (6.3)$$

It can be interpreted as the reciprocal of the velocity of x_p normal to the phase front under effect of the flow. In the following, it will be used to describe the change in orientation of the phase front as the wave propagates, i.e., the quantity $\frac{d\mathbf{s}}{dt}$. The ray tracing equations according to Ref. [13] then read

$$\frac{d\mathbf{x}_p}{dt} = \frac{c_f^2}{1 - \mathbf{v}_o \cdot \mathbf{s}} \mathbf{s} + \mathbf{v}_o, \quad (6.4a)$$

$$\frac{d\mathbf{s}}{dt} = -\frac{1 - \mathbf{v}_o \cdot \mathbf{s}}{c_f} \nabla c_f - \mathbf{s} \times (\nabla \times \mathbf{v}_o) - (\mathbf{s} \cdot \nabla) \mathbf{v}_o. \quad (6.4b)$$

The above model accounts for full material and flow inhomogeneity, i.e., $c_f = c_f(\mathbf{x})$ and $\mathbf{v}_o = \mathbf{v}_o(\mathbf{x})$.

Henceforth, we assume a homogeneous medium, i.e., $\nabla c_f = 0$. Moreover, the fluid flow shall be purely in x -direction and depend only on the transversal y -coordinate, i.e., $\mathbf{v}_o(y) = v_o(y)\mathbf{e}_x$. For this *stratified flow* [13], the ray tracing equations in the Cartesian x - y -plane simplify to

$$\frac{d}{dt} \begin{bmatrix} x_p \\ y_p \end{bmatrix} = \frac{c_f^2}{1 - v_o s_x} \begin{bmatrix} s_x \\ s_y \end{bmatrix} + \begin{bmatrix} v_o \\ 0 \end{bmatrix}, \quad (6.5a)$$

$$\frac{d}{dt} \begin{bmatrix} s_x \\ s_y \end{bmatrix} = \begin{bmatrix} 0 \\ -s_x \partial_y v_o \end{bmatrix}. \quad (6.5b)$$

If, moreover, the flow is steady and homogeneous, i.e., $\partial_t v_o = 0$ and $\partial_y v_o = 0$, then the orientation of the phase front does not change as the wave propagates. Ray tracing becomes particularly simple in this case as it results in *rectilinear wave propagation* [13]. Eq. (6.5a) is then sufficient and, using the initial value of \mathbf{s} given by (6.3), it reduces to the local and instantaneous definition of the ray velocity given in (6.1).

Let the phase front be inclined at an angle θ with respect to \mathbf{e}_y , such that the Cartesian components of \mathbf{e}_p are given by $[\sin \theta, \cos \theta]^\top$. In Cartesian components, we may then write

$$[\mathbf{v}_p] = \frac{d}{dt} \begin{bmatrix} x_p \\ y_p \end{bmatrix} = c_f \begin{bmatrix} \sin \theta \\ \cos \theta \end{bmatrix} + \begin{bmatrix} v_o \\ 0 \end{bmatrix}. \quad (6.6)$$

This equation is solved by integrating once, yielding the ray path as desired, namely

$$\mathbf{x}_p(t) = \mathbf{x}_p(0) + \mathbf{v}_p t. \quad (6.7)$$

6.2 Time-of-flight model of flow meters

While the wave propagates through the pipe's interior, it is convected by the medium flowing with velocity $\mathbf{v}_o = [v_o, 0]^\top$. According to (6.7), this leads to changed ray paths, which is shown in Fig. 6.2. The axial distance l traveled by the wave though the fluid is flow-dependent, ultimately enabling to measure the flow velocity. A detailed physical description will be given in the following and the resulting metering principle will be compared to the conventional UFM setup and its classical modeling approach.

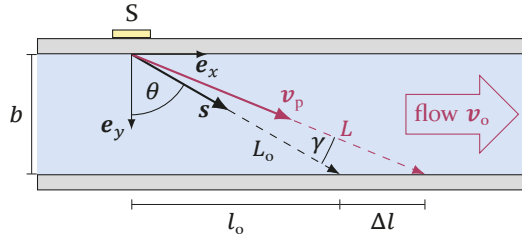


Figure 6.2: Ray convector by fluid flow.

6.2.1 Lamb wave-based flow meter

For the Lamb wave-based UFM system, the pipe wall itself constitutes the radiating and receiving elements. They radiate and receive ultrasound under an angle θ with respect to the transducer's normal, which for the sending element is \mathbf{e}_y . The radiating and receiving surfaces are parallel to each other and aligned with the fluid flow. For this reason, using the ray velocity in (6.6), we find that the transit time through the fluid is given by

$$\tau_f = \frac{b}{\mathbf{v}_p \cdot \mathbf{e}_y} = \frac{b}{c_f \cos \theta}, \quad (6.8)$$

which is independent of the flow velocity v_0 [31].

Convective ray displacement

The setup can, nonetheless, be used for flow metering because within this fixed transit time, the propagated axial distance $l = l_0 + \Delta l$ of the wave beam changes with the fluid flow. Using the transit time in (6.8), this distance can be determined as

$$l = \mathbf{v}_p \cdot \mathbf{e}_x \tau_f = (c_f \sin \theta + v_0) \tau_f \quad (6.9)$$

$$= b \left(\tan \theta + \frac{v_0}{c_f \cos \theta} \right) = l_0 \left(1 + \frac{v_0}{c_f \sin \theta} \right). \quad (6.10)$$

Accordingly, the axial displacement of the beam relative to zero-flow is

$$\Delta l = \frac{b}{c_f \cos \theta} v_0. \quad (6.11)$$

Summarizing, we may state that, independent of the flow velocity, the ultrasonic wave always couples into the pipe wall at $t = \tau_f$ but displaced by the

axial distance $\Delta l(v_o)$ closer to the receiver, hence, causing a flow-dependent change in arrival time. This is the working principle of Lamb wave-based UFM. Note that the distances will double for the V-path flow meter setup (cf. Fig. 6.4).

The displacement of the ultrasonic beam can be verified by a FE simulation of convected ultrasound. We remark that this computation is not based on ray tracing, but rather on solving the full convected wave equation [13, 170]. The simulation was performed for the geometry sketched in Fig. 6.3a. The beginning and ending sections of the pipe are closed by an *absorbing layer* in order to avoid reflections. The transient simulation is excited by a prescribed acoustic pressure at the marked boundary segment. Radiation under an angle is achieved by prescribing the pressure as $p(x, t) = p_o g_e(x) g_t(t) \Re e^{i(k_x x - \omega t - \pi)}$, with $k_x = 3.52$ rad/mm and $\omega = 2\pi$ rad/s, which corresponds to a radiating Ao' wave in the pipe wall with $\theta = 56^\circ$. The gaussian pulse $g_e(x)$ in the spatial domain is centered on the excitation line and has a standard deviation of one sixth of the line length. The gaussian pulse $g_t(t)$ is centered at $t = 20/f$ with a standard deviation of $8/f$. The mesh results in 1.2 million degrees of freedom and the two simulation runs for both flow velocities take about 40 min on an Intel Core i9 processor at 2.3 GHz.

The simulation results are presented in Figs. 6.3a to 6.3c at the time instant $t = 2\tau_f + 20/f = 68.3 \mu\text{s}$, i.e., when the pulse's center impinges at the top pipe wall. The acoustic pressure field seen in Fig. 6.3a is a superposition of incident and reflected fields. Fig. 6.3b compares the acoustic intensity distribution with and without fluid flow. The result for $v_o = 0$ m/s is shown at the bottom, while the corresponding solution with $v_o = 10$ m/s is flipped on top. Lastly, the acoustic pressure along the pipe wall ($y = 0$) is shown in Fig. 6.3c. A displacement of the two signals of about 0.48 mm can be identified in the figure. This compares to $2\Delta l = 0.483$ mm computed from (6.11) with minimal computational demands. The points of incidence predicted by ray tracing for $v_o = 0$ m/s and $v_o = 10$ m/s are marked with vertical lines in Fig. 6.3c.

The good agreement with the FE simulation suggests that the ray tracing model is well suited to predict the effect of ultrasonic convection. The above analysis confirms that the ultrasonic beam is actually *displaced due to convection* in a Lamb wave-based meter – not merely accelerated, as is conventionally assumed in UFM. Nonetheless, the beam displacement leads to a change in time of flight between the transducers, as will be explained next.

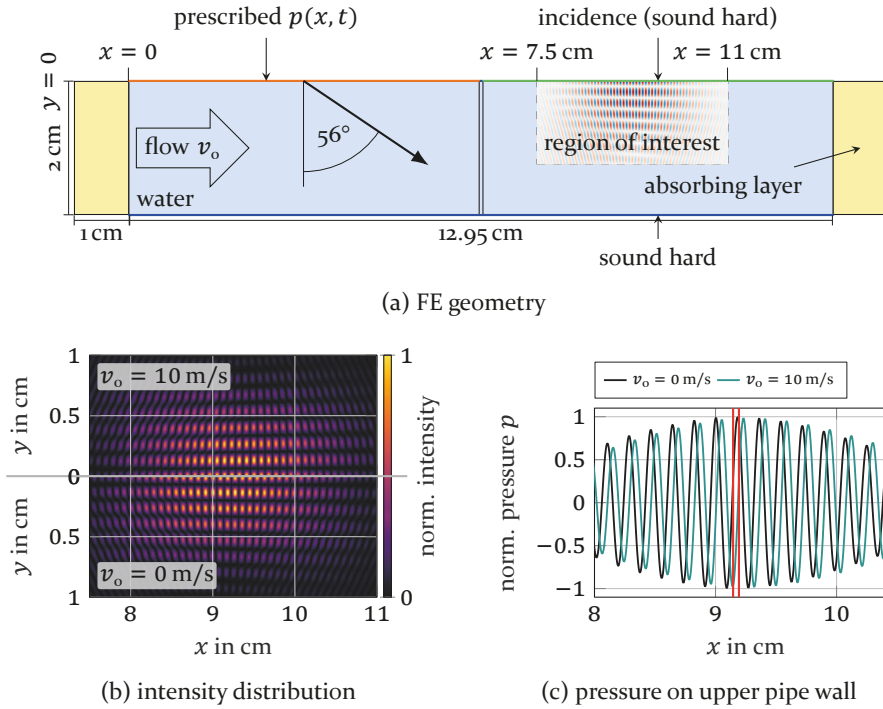


Figure 6.3: FE simulation results of convected ultrasound at $t = 68.3 \mu\text{s}$.

Convective transit time

The total time of flight τ_p from sender (S) to receiver (R) changes with the fluid flow even if the transit time through the fluid medium τ_f does not. For this we inspect the full geometry of the V-path flow meter depicted in Fig. 6.4 and take a closer look at the travel time inside the pipe wall.

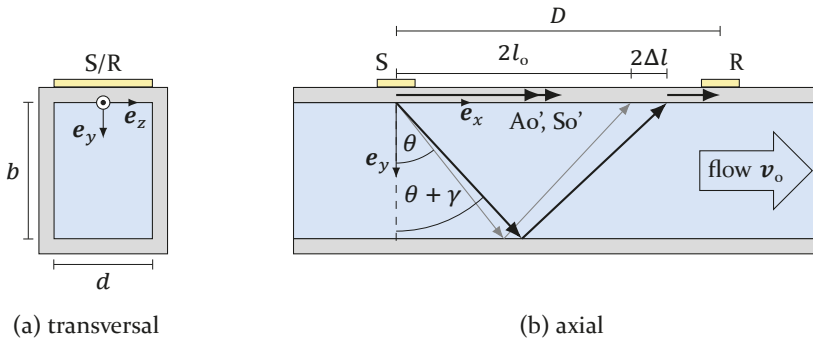


Figure 6.4: Flow meter geometry including transducers and wave paths.

If D is the axial distance of the transducers, then the propagation distance inside the pipe wall will be $D - 2l$, where $l = l_0 + \Delta l$ is known from (6.10). Due to the dispersive behavior of the Lamb waves, the corresponding travel time differs depending on whether propagation of phases or energy is being considered. The total time of flight of phase fronts is obtained using (6.10) and the phase velocity c_p of the QGW, which yields

$$\tau_p(v_o) = \frac{D - 2b \tan \theta}{c_p} + \frac{2b}{c_f \cos \theta} \left(1 - \frac{v_o}{c_p}\right). \quad (6.12)$$

Accordingly, the time of flight of the pulse envelope is determined by replacing c_p by the energy velocity c_e . In the following, all equations are written for phase fronts only and the envelope equations can be obtained by the mentioned replacement.

The metering principle is based on the *change* in travel time due to fluid flow. As conventional [1], we exploit the fact that the role of sender and receiver can be exchanged and inspect the difference between upstream and downstream signals, instead of the total time of flight. This *differential time of flight* is determined by

$$\Delta\tau_p = \tau_p(-v_o) - \tau_p(v_o) = \frac{4\Delta l}{c_p} = \frac{4b}{c_f \cos \theta} \frac{v_o}{c_p}. \quad (6.13)$$

The linear dependence on the flow velocity seen above is very advantageous for the metering system. It should be noted, however, that this is an approximation resulting from the assumptions of the model, namely homogeneous and laminar flow. When the flow is inhomogeneous and/or turbulent, it is still possible to consider an “effective homogeneous flow velocity”, which then needs to be corrected with the calibration factor K (see Subsec. 1.2.4) in order to obtain correct volumetric flow rates [1]. This represents the conventional approach taken for flow metering.

6.2.2 Piston type transducer-based flow meter

The working principle of Lamb wave-based flow meters is different to conventional UFM. Even the differential time of flight derived in (6.13), which is central to flow metering, differs from the well known standard expression. This discrepancy arises due to the geometric differences between noninvasive meters (e.g., Lamb wave-based devices) and invasive setups with piston type transducers, as will be explained in detail in the next section. Before doing so, we shall introduce the piston type devices in the following.

The piston transducers radiate normally to their surface into the pipe's interior, as depicted in Fig. 6.5. According to (6.7), the transit time of a phase point x_p through the fluid from sender (S) to receiver (R) is given by

$$\tau_f = \frac{L(v_o)}{v_p(v_o)}, \quad (6.14)$$

where L denotes the flow-dependent ray path length. Considering that for the piston type transducer $L_{\text{piston}} = L_o / \cos \gamma$ and using (6.2), the actual propagation distance is $L_{\text{piston}} = L_o v_p / (c_f + v_o \sin \theta)$. According to (6.14) the resulting transit time through the fluid is obtained for the piston transducer setup as

$$\tau_{f,\text{piston}} = \frac{L_{\text{piston}}}{v_p} = \frac{L_o}{c_f + v_o \sin \theta}. \quad (6.15)$$

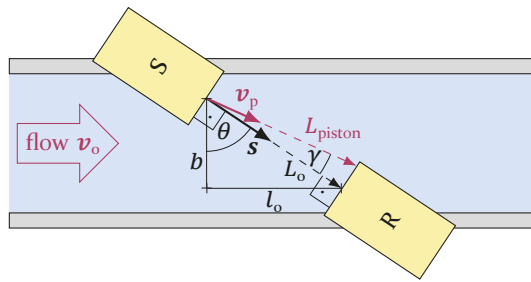


Figure 6.5: Geometry of conventional UFM with piston type transducers.

Conventionally, an *effective wave speed* [1, 2, 14] formalism is adopted in place of the above derivation. The idea consists in projecting the ray velocity onto the original propagation direction e_p , i.e., $v_p \cdot e_p = c_f + v_o \sin \theta$. This wave speed will result in the same transit time as given in (6.15) when using the fixed distance L_o between the transducers. The reason why the effective wave speed yields the correct result is that the transducer surface is aligned with the phase fronts and the actual ray path is irrelevant, i.e., it does not matter which point on the phase front is actually considered because it impinges on the transducer's surface everywhere at the same time. It is important to stress that this transit time is, strictly speaking, only valid for piston-type transducer setups. We conclude that – in contrast to the Lamb wave-based flow meters – the transit time of an ultrasonic pulse through the pipe's interior changes with the fluid flow velocity, directly enabling its measurement.

Ray tracing vs. effective wave speed

The time-of-flight model derived in Subsec. 6.2.1 is based on simple unaltered ray tracing. Instead, an *effective wave speed* formalism is traditionally used in flow metering systems. The question arises, whether it is possible to apply this framework to Lamb wave-based flow meters.

As already mentioned, the effective wave speed is obtained by projecting the ray velocity onto the original propagation direction, i.e., $\mathbf{v}_p \cdot \mathbf{e}_p = c_f + v_o \sin \theta$. Using this wave speed, it is possible to determine the transit time τ_f^{eff} to the point where the wave would be reflected without fluid flow, i.e., the L_o ray path in Fig. 6.2. This transit time, given by

$$\tau_f^{\text{eff}} = \frac{L_o}{c_f + v_o \sin \theta}, \quad (6.18)$$

is seen to be flow-dependent, which is in disagreement with the convected ray model in (6.8). Moreover, after some algebra, the corresponding upstream-downstream differential time of flight can be written as [1]

$$\Delta\tau_p^{\text{eff}} = \frac{4b}{\cos \theta} \frac{v_o \sin \theta}{(c_f^2 - v_o^2 \sin^2 \theta)}. \quad (6.19)$$

Comparing (6.19) to (6.13), we see that the two models yield different results – one is linear, while the other is hyperbolic in v_o .

The two models differ in the treatment of the wave propagation on the segment Δl . The situation is sketched in Fig. 6.7, where the effective ray impinges on the plate at l_o at time τ_p^{eff} , whereas the convected ray impinges at a later time τ_p on $l_o + \Delta l$. While (6.19) assumes that the wave propagates with $c_p = c_f / \sin \theta$ inside the plate, (6.13) instead accounts for the fact that the wave is still being convected inside the fluid and propagates with the trace velocity $c_f / \sin \theta + v_o$ in axial direction. As a consequence, the “effective ray” reaches $x = l_o + \Delta l$ at time $\tau_p^{\text{eff}} + \frac{\Delta l}{c_p}$, which is slightly later than the convected ray because in practice Δl is substantially smaller than one wavelength.

From a mathematical point of view, the differential time of flight given in (6.19) differs from the one in (6.13) due to the term $v_o^2 \sin^2 \theta$ in the denominator. Note that this term is conventionally disregarded under the assumption that $v_o \ll c_p$ [1]. Neglecting this term and considering that $c_p = c_f / \sin \theta$ reduces the effective wave model to the convected ray model. For Lamb wave-based flow meters, disregarding the mentioned term does not represent an approximation. It translates the “imprecise” model into the actual model.

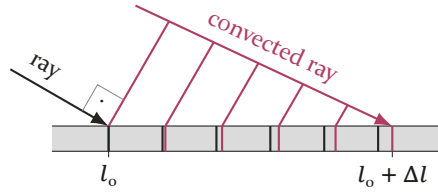


Figure 6.7: Comparison of phase fronts: two different trace velocities are assumed over the range Δl . “Effective ray”: $c_p = c_f / \sin \theta$; convected ray: $c_p = c_f / \sin \theta + v_o$. In practice $\Delta l \ll c_p / f$, leading to small deviations between the two models.

Using the effective wave model without the mentioned simplification leads to errors. Using (6.19) and (6.13) results in a relative deviation between the two models of

$$\frac{\Delta\tau_p^{\text{eff}} - \Delta\tau_p}{\Delta\tau_p} = \frac{v_o^2}{(c_p^2 - v_o^2)} \approx \left(\frac{v_o}{c_p}\right)^2, \quad (6.20)$$

where the approximation holds for $v_o \ll c_p$. In practice, this deviation is in the order of $1 \cdot 10^{-4}$ and, therefore, negligible. Nonetheless, the convected ray model should be preferred because:

- it is the physically meaningful model,
- it reveals the linear dependence of $\Delta\tau$ on v_o ,
- it yields mathematically simpler expressions, and
- it is also valid for the ultrasonic pulse envelope.

6.3 Incidence and reflection from the pipe wall

The radiated ultrasonic beam propagates through the pipe and then impinges on the opposite pipe wall, where it partially reflects and partially couples into a QGW, e.g., a leaky Lamb wave. This coupled process of “incidence” and “reflection” will be modeled in this section as inspired by Jia et al. [171] but using a pressure formulation. All field quantities are thereby assumed to vary as $e^{-i\omega t}$.

6.3.1 Excitation of a leaky Lamb wave by an incident acoustic beam

The goal is to obtain the axial variations $a_n(x)$ of the wave inside the pipe wall/plate due to an acoustic pressure $p_i(x)$ incident on the plate surface.

The resulting $a_n(x)$ is purely a consequence of the spatial distribution of the incident beam $p_i(x)$ and the considered mode. It should be remarked that it is not allowed to disregard the fluid-structure interaction at this point. This means that the pressure on the plate's surface is a consequence of the incident and reflected pressure as well as the radiated acoustic field of the thereby generated QGW [171].

We consider a QGW propagating to the right. The field variations $a_n(x)$ are known to start from zero at the left edge of the exciting region and increase thereon, see (3.29). This means that the plate is initially not under motion and the incident acoustic beam suffers – at first – a sound hard reflection [111], i.e., the pressure is doubled. The motions of the plate increase along x , thereby generating a leaky pressure field that adds to the total pressure. Overall, the pressure at the plate's boundary may then be written [111, 171]

$$p(x) = 2p_i(x) + p_{ln}(x), \quad (6.21)$$

where p_{ln} is the leaky pressure field. If the leaky Lamb wave radiates under an angle θ_n , the resulting acoustic pressure will be

$$p_{ln}(x) = -\frac{Z_f}{\cos \theta_n} v_{yn} a_n(x), \quad (6.22)$$

where the negative sign is due to radiation in $-\mathbf{e}_y$, the acoustic impedance $Z_f = \rho_f c_f$ and v_{yn} denotes the y -component of the mode's velocity eigenvector at the plate-fluid boundary, i.e., $v_{yn} = \mathbf{e}_y \cdot \mathbf{v}_n(y = -h/2)$. The subindex n for the modal variables is dropped henceforth for conciseness.

The corresponding hydrostatic stress state acting on the plate's surface is $\mathbf{T} = -p(x)\mathbf{I}$, see Subsec. 2.1.4. The traction on the upper plate surface with normal vector $-\mathbf{e}_y$ is then given by $\mathbf{t}(x) = -\mathbf{e}_y \cdot \mathbf{T} = p(x)\mathbf{e}_y$. According to (3.26), the total pressure (6.21) at the plate's surface leads to a source $f_s(x)$ seen by the waveguide mode, which may be written as

$$f_s(x) = v_y^* p(x) = 2v_y^* p_i(x) - \frac{Z_f}{\cos \theta} |v_y|^2 a(x). \quad (6.23)$$

With this, the mode's axial variation according to (3.29) is governed by

$$(\partial_x - ik'_x) a(x) = \frac{v_y^* p_i(x)}{2\bar{P}}, \quad (6.24)$$

where we use $k'_x = k_x + i\alpha'$, and the abbreviation

$$\alpha' = \frac{Z_f}{4\bar{P} \cos \theta} |v_y|^2, \quad (6.25)$$

which is seen to represent an estimate for the radiation rate, i.e., axial attenuation $\Im k_x$ of the QGW, compare to Subsec. 3.2.8. Therefore, even if the wave field of the free plate mode is being used for the computation, radiation losses are being considered – as it needs to be. The governing equation for $a(x)$ is of the same form as (3.28) and the solution can be taken from (3.29), i.e.,

$$A(x) = \frac{v_y^*}{2\bar{P}} e^{-\alpha'x} \int_{-\infty}^x p_i(\xi) e^{-ik'_x\xi} d\xi, \quad (6.26)$$

where we include the attenuation in the “modal envelope” A , so that the axial variation is given by $a(x) = A e^{ik_x x}$. Comparing to (3.29), we conclude that the interaction of the prescribed external field and radiated field can be considered by merely using an appropriate complex wavenumber instead of the real wavenumber of the free plate mode. Note that the obtained result is an approximation because it assumes that the modes of the free plate are a good approximation to the QGWs of the fluid-coupled plate.

As a simple but insightful example, we begin with an incident acoustic pressure with matching axial wavenumber, i.e., its wavenumber along x corresponds to the Lamb wave’s wavenumber k_x . Moreover, it shall exhibit a rectangular envelope. The incident pressure is, therefore, $p_i(x) = p_o e^{ik_x x}$ on $x \in [0, w]$ and zero otherwise. The situation is sketched in Fig. 6.8a. Inserting p_i into (6.26), we see that in the exciting region $A(x) = \frac{v_y^* p_o}{2\alpha' \bar{P}} (1 - e^{-\alpha'x})$ and for $x > w$, $A(x) = \frac{v_y^* p_o}{2\alpha' \bar{P}} (e^{\alpha'w} - 1) e^{-\alpha'x}$. The resulting envelope $A(x)$ and axial variations $a(x)$ are both shown in Fig. 6.8b. Thereby, the modal field (\mathbf{v}, \mathbf{T}) has been normalized such that the waves carry unit power per waveguide width, i.e., $\bar{P} = 1 \text{ W/m}$.

If radiation losses had been disregarded, the mode’s amplitude would increase linearly with the excitation length [70]. This will no longer be the case when changing from real to complex valued k_x . Instead, the guided wave’s envelope is seen to exponentially approach a limiting value of $A(x) \rightarrow \frac{v_y^* p_o}{2\alpha' \bar{P}}$, which is the case when incoming and radiated power are balanced [111]. Outside the exciting region, the QGW then attenuates exponentially, as would be expected. Note that the behavior of leaky wave excitation is similar to transient phenomena in resonant systems. This analogy was already noted by

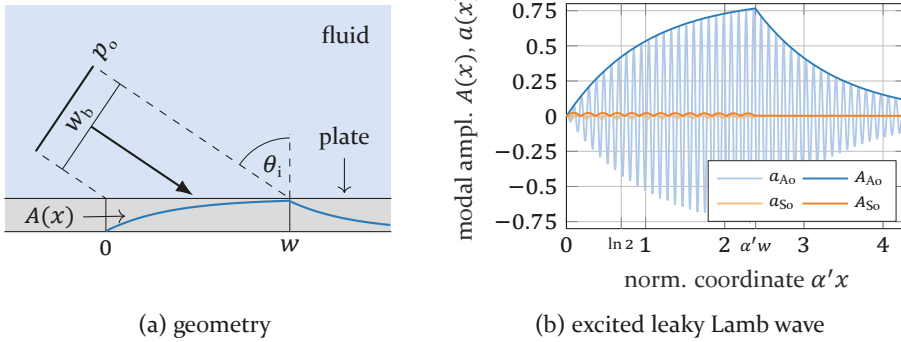


Figure 6.8: Rectangular acoustic beam incident onto a brass plate under the A_0' critical angle. The dimensionless modal envelope $A(x)$ and the dimensionless axial variations $a(x)$ are w.r.t. a modal field with $\bar{P} = 1 \text{ W/m}$. Parameters: 1 mm thick brass plate coupled to water, frequency $f = 1 \text{ MHz}$, angle of incidence $\theta = 56^\circ$, attenuation $\alpha' = 53 \text{ rad/m}$, tracing beam width $w = 4.5 \text{ cm}$.

Cremer [172], although Schoch [116] remarks that the two phenomena are not exactly equivalent.

There exists an optimal beam width under which the coupling into the plate is most efficient [111]. This is expected because the power coupled into the plate reaches saturation with increasing w , while the power carried by the incident beam does not. The maximum power contained in the QGW is found at $x = w$ and its value is $\bar{P}(w) = A^*(w)A(w)\bar{P}$, where \bar{P} denotes the power for $A = 1$, as before. On the other hand, the total power carried by the incident acoustic beam is $\bar{P}_{\text{acou}} = \frac{p_0^2 w \cos \theta_i}{2Z_f}$, where $w \cos \theta_i$ is the width of the beam incident under angle θ_i . The efficiency with which acoustic energy is converted to a QGW is then determined by $\eta(w) = \frac{\bar{P}(w)}{\bar{P}_{\text{acou}}(w)} = \frac{2}{\alpha' w} (1 - e^{-\alpha' w})^2$ [111]. The maximum is found at $w_{\text{opt}} \approx 1.26/\alpha'$ with $\eta_{\text{opt}} \approx 81\%$. This result is a direct consequence of the nature of leaky fields, namely, inhomogeneous plane waves (see Subsec. 2.3.1 and 3.2.7) – which are not “matched” to the incident homogeneous plane wave.

A more realistic example would be an incident pressure pulse with Gaussian envelope [171] as sketched in Fig. 6.9a. The pressure at the plate’s surface is $p_i(x) = p_0 e^{-\frac{1}{2}(\frac{x}{w})^2} e^{ik_x x}$, where w is its 1-sigma width along x . According to (6.26), the excited QGW’s envelope is then given by

$$A(x) = \frac{v_y^* p_0}{2\bar{P}} e^{-\alpha' x} \int_{-\infty}^x e^{-\frac{1}{2}(\frac{\xi}{w})^2} e^{-ik'_x \xi} d\xi. \quad (6.27)$$

The integration was performed numerically using the Chebfun toolbox [173] and the result is depicted in Fig. 6.9b for $w = 5.66$ mm ($\alpha'w = 0.3$). The envelope A of the excited A_0 wave reaches a maximum and then gradually transitions into the exponential decay expected due to leakage.

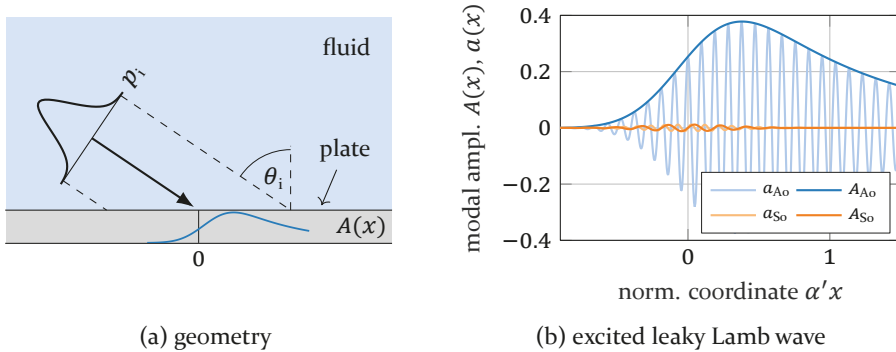


Figure 6.9: Ultrasonic beam with Gaussian envelope incident onto a plate under the A_0 critical angle. The dimensionless modal envelope $A(x)$ and the dimensionless axial variations $a(x)$ are w.r.t. a modal field with $\bar{P} = 1$ W/m. Parameters: 1 mm thick brass plate coupled to water, frequency $f = 1$ MHz, angle of incidence $\theta_i = 56^\circ$, attenuation $\alpha' = 53$ rad/m, normalized 1-sigma tracing beam width $\alpha'w = 0.3$.

6.3.2 Nonspecular reflection from the pipe wall

In addition to the wave field inside the pipe wall, the acoustic pressure in the fluid is also fully determined by the computation presented in the previous section [171]. Remember that the axial variations of the leaky Lamb wave are $a(x) = A(x) e^{ik_x x}$, with the modal envelope A given in (6.26). The leaky pressure field is then obtained using (6.22) and the total pressure field at the plate's boundary through (6.21).

The acoustic field is discussed by virtue of the incident Gaussian pressure pulse example calculated in the previous section. The resulting A_0 wave envelope was already shown in Fig. 6.9. The corresponding acoustic pressure at the plate's boundary is displayed in Fig. 6.10. The reflected pressure field is the superposition of the specularly reflected beam p_i and the leaky wave pressure p_l . These two components are 180° out of phase [111], leading to wave field extinction where they exhibit the same envelope. This manifests in a zero-crossing of the pressure's envelope. Left to the crossing point, the pressure is dominated by the specular reflection and is in phase with it. On the other hand, to the right of the crossing point, it is dominated and in phase with the leaky field.

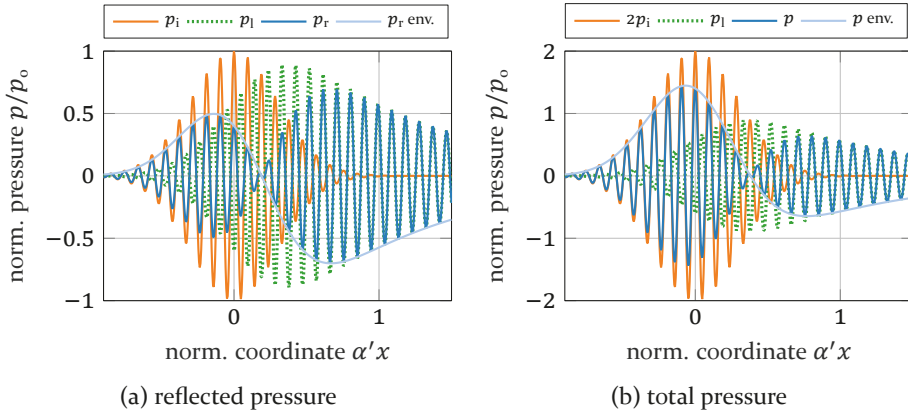


Figure 6.10: Nonspecular reflection from the pipe wall: (a) the reflected pressure is a consequence of a specularly reflected beam interfering with the leaky wave field; (b) the total pressure acting on the plate’s surface is composed of the incident and reflected pressure. The parameters are taken from Fig. 6.9.

Effects due to interference of a specular reflection with a leaky field are denoted as *nonspecular reflection* [171, 174]. The first reports in ultrasonics were due to Schoch [116, 175], where they were already interpreted as an interaction with free waves in the plate. Roughly speaking, three effects can be observed: (i) an axial displacement of the beam, (ii) a region of wave extinction and (iii) widening of the beam. The axial displacement of the reflected beam’s maximum with respect to the one of the specular reflection is known as the *Schoch displacement* [174, 176]. The larger the incident beam width-radiation rate product wa' , the more energy concentrates in the leaky field and the more pronounced is the Schoch displacement [174]. On the other hand, whenever the incident beam is sufficiently narrow, a region of acoustic extinction will be found [174] – as in Fig. 6.10.

The nonspecular reflection was validated using a FE simulation. The used geometry and BCs are explained in Fig. 6.11a, which also presents the resulting ultrasonic field. The region of extinction is clearly visible in the reflected beam. With the FE simulation it is only possible to separate the reflected and incident field components geometrically. Especially the logarithmic scale of the pressure field illustrates clearly the widening of the nonspecularly reflected beam with respect to the incident beam. This effect can be exploited to obtain beams with a very narrow angular spectrum [116], albeit inhomogeneous plane waves are thereby generated. By reversing this process, it is possible to achieve beam narrowing [101].

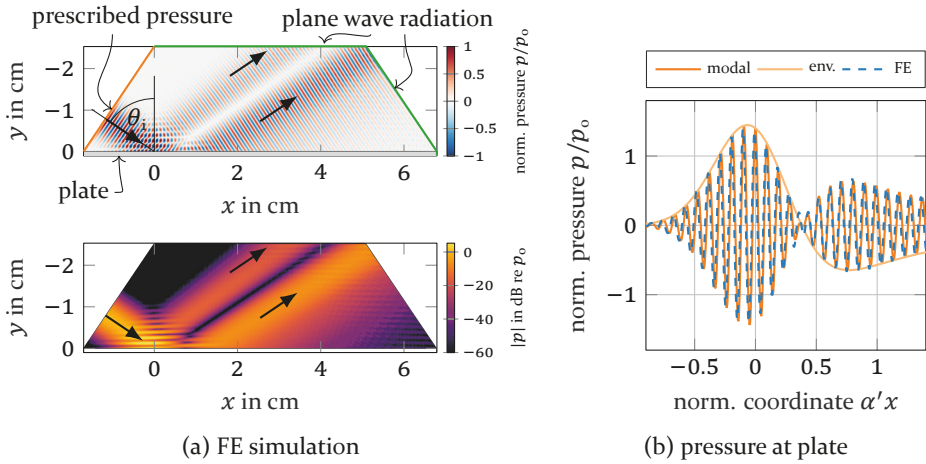


Figure 6.11: FE simulation of a nonspecularly reflected ultrasonic beam: (a) pressure and pressure level fields. (b) The total pressure along the plate's surface shows excellent agreement to the modal solution (already presented Fig. 6.10). The parameters are taken from Fig. 6.9.

A direct comparison of the total acoustic pressure at the plate's surface to the one computed via modal expansion is provided in Fig. 6.11b. The results nearly coincide, demonstrating the accuracy of the modal computation for the current example¹. The modal computation has a significant conceptual advantage: it reveals the nature of the nonspecular phenomena in terms of specular reflections and leaky waves [171]. Moreover, it has a significant computational advantage, as only the plate's surface needs to be discretized. We conclude that the combination of guided/leaky waves and modal expansion leads to a very natural setting to describe nonspecular phenomena.

Nonspecular reflections of ultrasound were made visible as part of [S9] using *Schlieren photography*, see Sec. 5.3. An ultrasonic transducer (V302-SU, Panametrics) with 25 mm aperture and 1 MHz center frequency was utilized to illuminate a 3 mm thick steel plate immersed in water. The processed photographs are presented in Fig. 6.12. The null field in the nonspecularly reflected field is clearly visible, both for incidence under the Ao'' angle as well as the So'' wave angle. The widening of the beam can also be observed.

¹ The accuracy depends on the locus on the dispersion curves. Good accuracy is expected when the eigenfunction and wavenumber of the fluid loaded plate are comparable to the ones of the free plate.

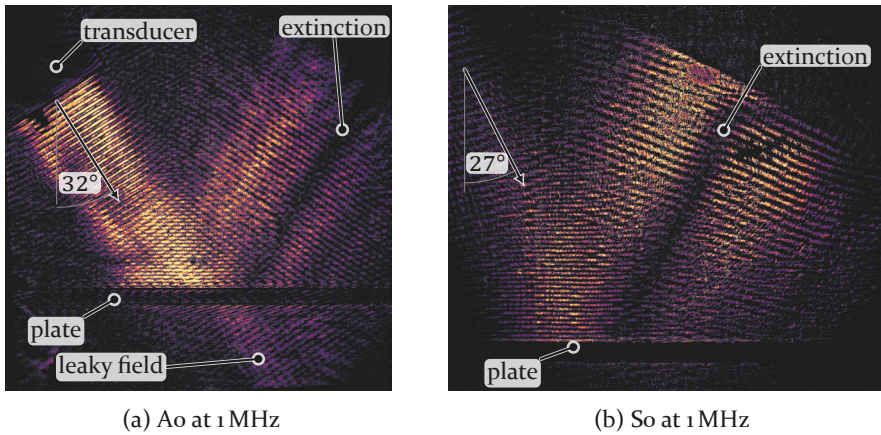


Figure 6.12: Schlieren photographs of ultrasonic beams reflected nonspecularly from a 3 mm thick steel plate in water.*

* Experimental data obtained by Schmid [S9]. Post-processing and visualization by the author.

Effects on the Lamb wave-based flow metering system

Some remarks with regard to Lamb wave-based UFM and nonspecular reflections are in order. Depending on whether the signal portion to the left or to the right of the zero crossing of the envelope is evaluated, the time-of-flight model of phase fronts might need to be adjusted by one half-period in order to conform to the 180° phase shift in the leaky field region [31]. Note, however, that the effects of reflection are reciprocal, while the convection of ultrasound is not. This means that changes in phase due to reflection will not appear in the differential time of flight given in (6.13) and do, consequently, not affect the flow measurement directly.

Nonetheless, nonspecular reflection does affect the flow metering system in other ways. To assess this, the analysis can be extended to cover the entire V-path. After reflection from the bottom pipe wall, the beam propagates back towards the upper pipe wall and impinges on it with an axial displacement of $2l$, see Fig. 6.4. The generated QGW can again be computed with (6.26) after having obtained p_r from the first reflection. Thereby, p_r constitutes the pressure incident onto the top pipe wall. This has been done for the exponential beam example given in Fig. 6.9. The result is shown in Fig. 6.13 together with the original and the nonspecularly reflected pressure signals. The beam's axial displacement has been omitted for the sake of comparison, i.e., $a(x-2l)$ is actually plotted. Note that the signal $a(x)$ reaching the receiver is much wider than the initial Gaussian pulse. In this example, its maximum is displaced by about 3 cm. Note that the signal reaching the receiver is highly

dependent on the initially emitted pressure distribution and a per-case study is required.

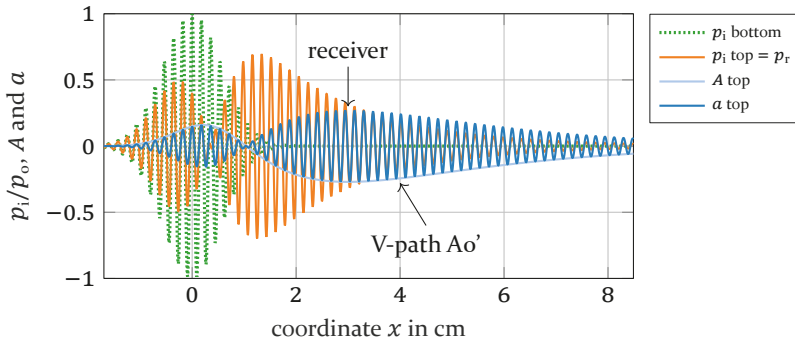


Figure 6.13: V-path signal resulting from an emitted Gaussian pulse. “ p_i bottom” is the initially emitted Gaussian, which is incident onto the bottom pipe wall. After nonspecular reflection, the pressure “ p_i top” reaches the upper pipe wall and excites an Ao' wave with axial field “ a top” and envelope “ A top”.

The consequences of nonspecular reflections on the UFM system can be summed up as follows: If the sender and receiver are arranged in a V-path, the local extinction and the widening of the beam upon reflection will lead to a decreased signal amplitude and, thus, lower signal-to-noise ratio at the receiver [1]. The Schoch displacement and widening of the reflected beam affects the optimal position of the receiver. This either needs to be considered in the flow meter design or the nonspecular reflection should be avoided. The latter is achieved by choosing the upper and lower pipe walls to be either (i) of different thickness or (ii) non-parallel.

7 Sensitivity and interference errors

The upcoming sensitivity studies reveal the dependence of the Lamb wave-based UFM on its parameters. This information is pertinent for the choice of a good operating point, i.e., the desired nominal parameter values. Furthermore, it reveals which disturbances are the most relevant ones and it yields a framework for active compensation of undesired effects.

7.1 Flow meter sensitivity to flow rate

The quantity acquired by the flow meter is the differential time of flight $\Delta\tau_p(v_0)$, which depends on the sought volumetric flow rate Q through $\bar{v}_0 = v_0 = \frac{Q}{Kbd}$. The model needs to be inverted in order to calculate the flow rate corresponding to a given $\Delta\tau_p$. This is achieved by inserting \bar{v}_0 from (6.13) into (1.3), yielding

$$Q = \mathcal{S}\Delta\tau_p, \quad (7.1)$$

with the *sensitivity* of the flow meter defined by

$$\mathcal{S} \stackrel{\text{def}}{=} \frac{1}{4}Kdc_f c_p \cos\theta. \quad (7.2)$$

Note that the smaller \mathcal{S} , the larger is the physical metering effect for a given Q because the measured time delay is $\Delta\tau_p = Q/\mathcal{S}$.

Measurement error analysis is performed in this chapter. In general, errors occur either due to imprecise acquisition of $\Delta\tau_p$ (electronics and signal processing) or unexpected deviations in the sensitivity \mathcal{S} (ultrasonic system). The latter effect is studied in Sec. 7.2 through 7.4. The thus gained knowledge is exploited in Sec. 7.5 to include the effect of temperature into the above sensitivity, which then becomes $\mathcal{S}(\mathcal{T})$.

7.2 Flow rate cross-sensitivities

Deviations between the actual and assumed meter sensitivity \mathcal{S} are a result of uncertainties in the system parameters, i.e., K , d , c_f , c_p , or unexpected changes therein. They directly lead to errors in the measured flow rate, which are denoted as *interference errors* and are said to be due to *cross-sensitivities*. These are studied in-depth in the following. The analysis aids in choosing an

appropriate operating point, which would ideally be unaffected by parameter changes.

The *relative measurement error* due to a change Δp of an arbitrary parameter from its assumed *nominal value* p is given by

$$\epsilon_Q^p \stackrel{\text{def}}{=} \frac{Q_m - Q}{Q} = - \left. \frac{\Delta Q}{Q} \right|_p \approx - \left. \frac{\partial Q}{\partial p} \right|_p \frac{\Delta p}{Q} = - \left. \frac{\partial S}{\partial p} \right|_p \frac{\Delta p}{S}, \quad (7.3)$$

where Q and Q_m are the actual and the measured flow rate, respectively, and the approximation is the first order Taylor expansion. This means that differential changes are being considered for now. Large changes will also be considered where necessary. According to (7.3), it is irrelevant whether the analysis is performed using either Q or S .

The ratio of ϵ_Q^p to the relative change of the parameter, i.e., $\epsilon_p = \frac{\Delta p}{p}$, given by

$$\frac{\epsilon_Q^p}{\epsilon_p} = - \frac{p}{Q} \left. \frac{\partial Q}{\partial p} \right|_p = - \frac{p}{S} \left. \frac{\partial S}{\partial p} \right|_p, \quad (7.4)$$

is especially advantageous as it is independent of Δp . This differential *relative cross-sensitivity* of the sensor will be studied systematically for all of the parameters. Thereby, the inhomogeneity of the leaky wave field is disregarded and the approximation $\theta \approx \arcsin(\frac{c_f}{c_p})$ is utilized¹ to eliminate θ . Simple expressions for the cross-sensitivities can then be obtained from (7.4) and (7.2), namely²

$$\frac{\epsilon_Q^{c_p}}{\epsilon_{c_p}} = \frac{-c_p^2}{c_p^2 - c_f^2}, \quad \frac{\epsilon_Q^{c_f}}{\epsilon_{c_f}} = \frac{2c_f^2 - c_p^2}{c_p^2 - c_f^2}, \quad \frac{\epsilon_Q^d}{\epsilon_d} = -1, \quad \frac{\epsilon_Q^K}{\epsilon_K} = -1. \quad (7.5)$$

While the wave speed c_f of the fluid is fixed by the medium to be measured, the phase velocity c_p can be adjusted by choice of the leaky Lamb wave and the operating frequency f . The cross-sensitivities to c_p and c_f are plotted in Fig. 7.1 as a function of the nominal phase velocity. The sensitivity to changes in c_p is observed to steadily decrease with higher nominal phase velocity c_p . With regard to the sensitivity on c_f , a sweet spot exhibiting zero local sensitivity

¹ Strictly speaking, θ additionally depends on the field's inhomogeneity $\Im k_x$, or alternatively the radiation rate $\Im k_x$, see Subsec. 3.2.8.

² Note that $\cos \arcsin \frac{c_f}{c_p} = \sqrt{1 - \frac{c_f^2}{c_p^2}}$.

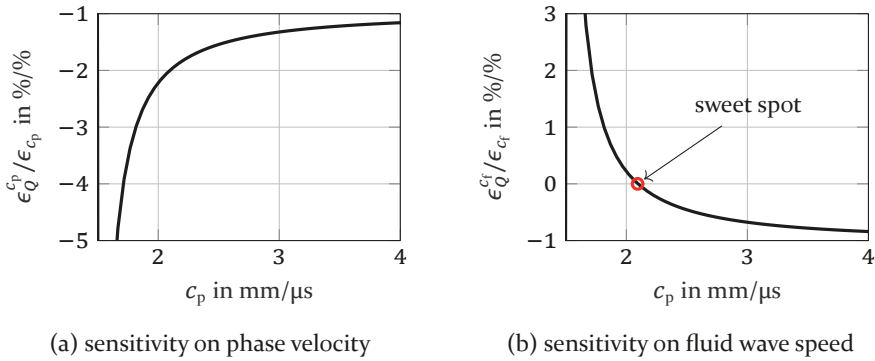


Figure 7.1: Cross-sensitivity to c_p and c_f as a function of the nominal phase velocity of the excited leaky Lamb wave (nominal $c_f = 1.48 \text{ mm}/\mu\text{s}$).

is found at $c_p = \sqrt{2}c_f$. This operating point could be achieved using the Ao' wave at about 700 kHz mm in a steel pipe.

The preceding discussion shows that the accuracy of the metering system with parameter uncertainties is dependent upon the chosen operating point. The phase velocity c_p at which the device is operated is essential to control its cross-sensitivities. Other parameters, for instance temperature, also lead to interference errors. These act on the system through one or more of the parameters considered so far. Fig. 7.2 displays an error chain, i.e., which parameters influence other parameters. Most of them act on the phase velocity and, hence, this quantity is again of central importance.

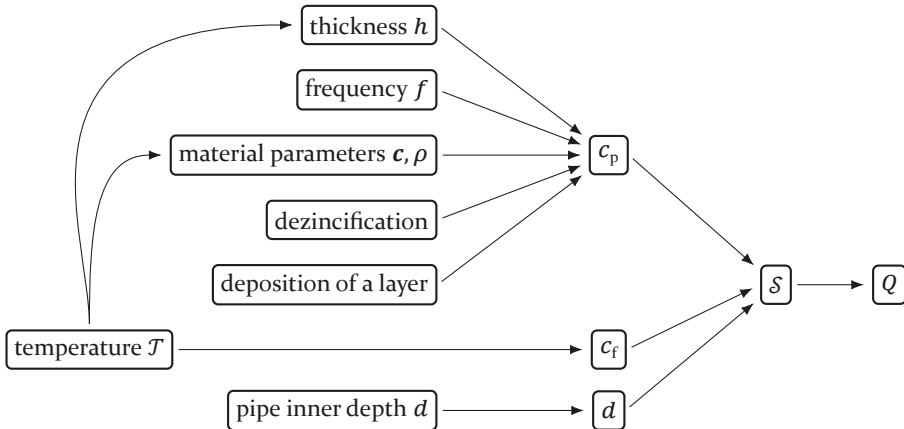


Figure 7.2: Error dependence diagram.

Parameters that act on c_p will collectively be denoted as waveguide parameters and are discussed more closely in Sec. 7.3. Furthermore, the effect of

temperature is essential because the water meter should be operational in a very wide temperature range from 0 °C to 100 °C, for heat meters even up to 150 °C. This is treated in Sec. 7.4 and 7.5.

7.3 Waveguide parameter cross-sensitivities

The waveguide parameters affect the phase velocity of the leaky wave excited inside the pipe wall. Uncertainties, tolerances and environmental circumstances lead to deviations in the pipe's wall thickness, material parameters, excitation frequency, etc., from the corresponding assumed nominal values. Each of the effects is discussed individually in the following.

7.3.1 Thickness and frequency: Abrasion and manufacturing tolerances

Manufacturing tolerances lead to uncertainties in the actual pipe wall thickness h . Moreover, the thickness might change over time due to abrasion and thermal expansion. This leads to changes in the phase velocity of the excited leaky Lamb wave. For a single layer pipe wall, the dispersion curves depend on the frequency-thickness product fh (see Subsec. 3.1.2), i.e., $c_p = c_p(fh)$, relative changes in frequency have the same effect as in thickness.

Three different approaches to obtain the sensitivity of the phase velocity, i.e., $\frac{\partial c_p}{\partial f}$ and $\frac{\partial c_p}{\partial h}$, may be thought of: (i) implicit differentiation of the characteristic equation, (ii) numerical differentiation of the dispersion curves, or (iii) exploiting the relation to the group velocity. The latter is obtained from (2.91), wherein the phase and group velocities are both scalars in the Lamb wave case. A change of variable in the differentiation and resorting terms results in

$$\frac{\epsilon_{c_p}^f}{\epsilon_f} \stackrel{\text{def}}{=} \frac{f}{c_p} \frac{\partial c_p}{\partial f} = \frac{c_g - c_p}{c_g} = \frac{h}{c_p} \frac{\partial c_p}{\partial h} \stackrel{\text{def}}{=} \frac{\epsilon_{c_p}^h}{\epsilon_h}. \quad (7.6)$$

These frequency-dependent sensitivities are exemplarily plotted for a brass plate in Fig. 7.3a. Thereby, $c_g = c_e$ has been assumed and the energy velocity is used for the computations to avoid differentiation of the curves.

The frequency is a property of the employed excitation signal and can dynamically be adjusted during operation. In principle, this could be harnessed to *compensate* for other changes in the waveguide parameters. Evidently, this method will only work if a dispersive wave is used, which is reflected in the

above sensitivity expression, where the group and phase velocities need to differ in order to obtain a non-zero sensitivity to frequency.

7.3.2 Mechanical parameters: Material uncertainty and aging

The material parameters are usually not known exactly and may vary from batch to batch. Moreover, the parameters might change in long-time processes, i.e., aging. We are interested in the consequences for the guided wave's phase velocity. For this end, the volume perturbation formula given in (3.32) can be used. For small changes in the material parameter, the approximations $\mathbf{v}' = \mathbf{v}$ and $\mathbf{S}' = \mathbf{S}$ can be made [41]. This yields the relative changes in phase velocity as

$$\epsilon_{c_p}^{\text{mat}} \stackrel{\text{def}}{=} \frac{\Delta c_p}{c_p} = -\frac{\Delta k_x}{k_x} = -\frac{c_p}{4P} \int_{-h/2}^{h/2} \Delta \rho \mathbf{v}^* \cdot \mathbf{v} - \mathbf{S}^* : \Delta \mathbf{c} : \mathbf{S} \, dy. \quad (7.7)$$

The first term yields the relative sensitivity to changes in mass density, namely

$$\frac{\epsilon_{c_p}^{\rho}}{\epsilon_{\rho}} \stackrel{\text{def}}{=} \frac{\rho}{\Delta \rho} \frac{\Delta c_p}{c_p} = -\frac{c_p}{2P} \int_{-h/2}^{h/2} \frac{1}{2} \rho \mathbf{v}^* \cdot \mathbf{v} \, dy = -\frac{1}{2} \frac{c_p}{c_e}. \quad (7.8)$$

Thereby, we have used the definition of energy velocity given in (3.15) and we have assumed equipartition of energy according to (2.53).

Next, changes in stiffness are examined. These are due to the second term in (7.7). For this we note that the stiffness tensor of isotropic materials can be factorized as $\mathbf{c} = EN(\nu)$, where E is the Young's modulus and \mathbf{N} is a 4th order tensor depending only on the Poisson's ratio ν . Taking the change in stiffness to be of the form $\Delta \mathbf{c} = \frac{\Delta E}{E} \mathbf{c} = \Delta E \mathbf{N}(\nu)$, the sensitivity due to changes in Young's modulus are determined by

$$\frac{\epsilon_{c_p}^E}{\epsilon_E} \stackrel{\text{def}}{=} \frac{E}{\Delta E} \frac{\Delta c_p}{c_p} = \frac{c_p}{4P} \int_{-h/2}^{h/2} \mathbf{S}^* : \mathbf{c} : \mathbf{S} \, dy = \frac{1}{2} \frac{c_p}{c_e}. \quad (7.9)$$

Again, the definition of energy velocity (3.15) and equipartition of energy (2.53) has been exploited therein.

The resulting frequency-dependent sensitivities to the mechanical parameters of a brass plate are exemplarily depicted in Fig. 7.3b. It is remarked that the relative sensitivities to mass and Young's modulus are equal but of opposite sign. The phase velocity of forward waves increases with the Young's modulus

but decreases with mass. The opposite holds for backward waves. Note that the S2b wave exhibits sensitivities of about > 10 and is outside the range of Fig. 7.3b.

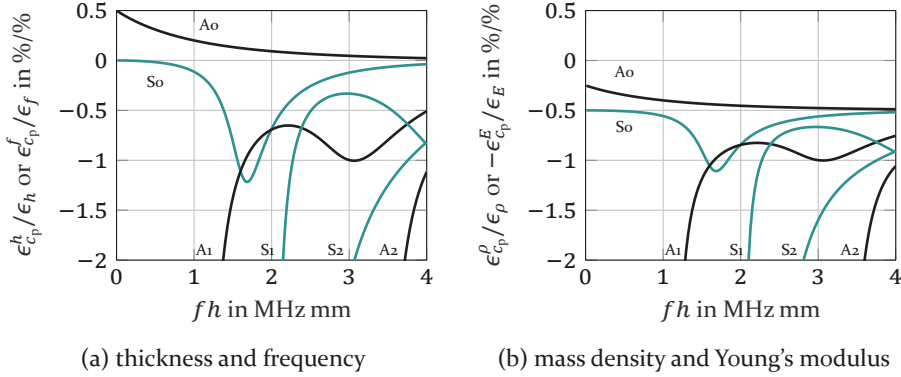


Figure 7.3: Relative changes in phase velocity due to frequency, thickness and material parameters (brass plate).

Changes in the Poisson's ratio can also be accounted for using (7.7). Due to its tensorial form, it does not reduce to a simple expression in terms of phase and energy velocity. Numerical calculations have been performed and the corresponding relative sensitivities are all $< 0.3 \%$, except at the cut-off frequencies.

The full nonlinear behavior due to large perturbations has been obtained by computing the waveguide problem for a set of material parameters. A very good agreement to the above linear predictions is found for up to about 10 % relative change in the material parameters (brass plate). We conclude that the linear behavior is sufficient for our purposes.

7.3.3 Deposited layer: Scaling and dezincification

UFMs for potable water supply stay in operation for extended periods of time. Thick layers of extraneous material may form on the inner pipe wall. This occurs by sedimentation of particles in suspension or by precipitation of dissolved substances. Two relevant phenomena leading to layer buildup will be analyzed in the following: scaling and dezincification.

Perturbation theory according to Subsec. 3.1.9 could be used in case of very thin layers [41], i.e., when the deposited layer thickness h_1 fulfills $k_x h_1 \ll 1$. For thick layers – which can be the case for both scaling as well as dezincification – perturbation theory is no longer valid. Instead, the exact mechanics are

considered to analyze the effect of a deposited layer. That is, wave propagation in the bi-layered waveguide as depicted in Fig. 7.4 is considered. Thereby, we assume the formation of an isotropic and homogeneous layer. Modeling of multi-layered waveguides has been included in the developed EDAT toolbox. Each layer is modeled as described in Subsec. 4.2.2 and coupled to the adjacent layer by imposing the interface conditions given in (2.25). For implementation details, refer to Refs. [P3, 121, 127].

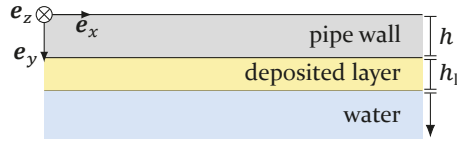


Figure 7.4: Pipe wall with deposited layer (e.g., limescale) in contact with water.

Fluid loading is included into the multi-layered mechanical waveguide using the method developed in Subsecs. 3.2.3 and 4.2.2. In this way, valuable information about the radiation rate into the pipe's interior under the effect of a deposited layer is obtained in addition to the phase velocity.

Scaling: formation of a calcite layer

Of particular interest is the precipitation of dissolved salts, mainly of calcium and magnesium. Thereby, a hard layer is deposited on the pipe that is commonly referred to as *limescale*, the material is also called *limestone*, while the process of formation is denoted as *scaling* or *fouling*. Limescale mostly consists of calcium carbonate in the form of *calcite*, which is the most stable crystal structure of the mineral [177]. The formation of limescale is a complicated process dependent on temperature (variation), pressure, time scales, pH level, water hardness and an interaction of the different polymorphs of calcium carbonate as well as other minerals [177]. As a result, the rate of formation and the mechanical properties may vary significantly, for instance, the layer may exhibit different kind of micro-structures.

Albeit the above mentioned difficulties, formation of a homogeneous and isotropic calcite (material parameters in Appendix A) layer is assumed for simplicity. Solving for the guided waves in the bi-layered plate yields the dispersion curves shown in Fig. 7.5. The layer thickness h_1 is varied from 0 mm to 1 mm, which corresponds to the thickness of the brass pipe wall. The phase velocity dispersion curves are shown in Fig. 7.5a, while the relative changes with respect to $h_1 = 0$ mm are depicted in Fig. 7.5b.

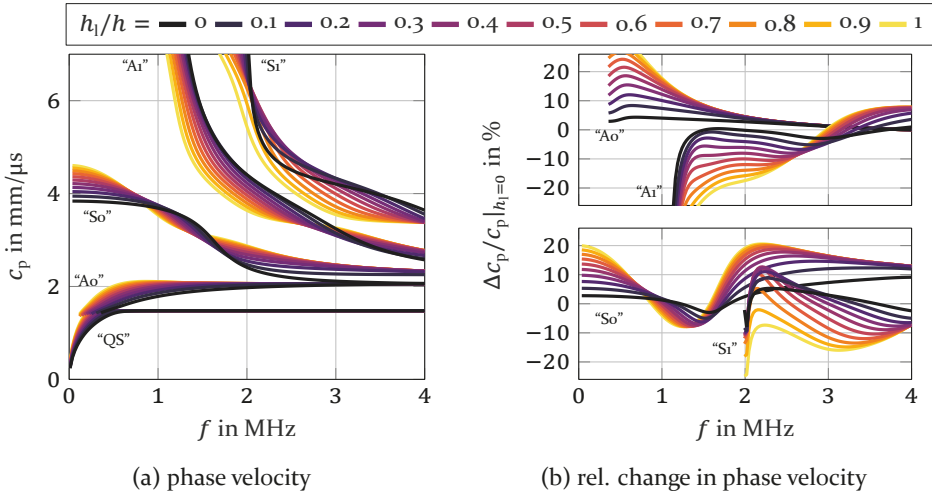


Figure 7.5: Scaling: phase velocity changes with increasing calcite layer thickness h_1 deposited on the pipe wall (brass pipe with thickness $h = 1$ mm).

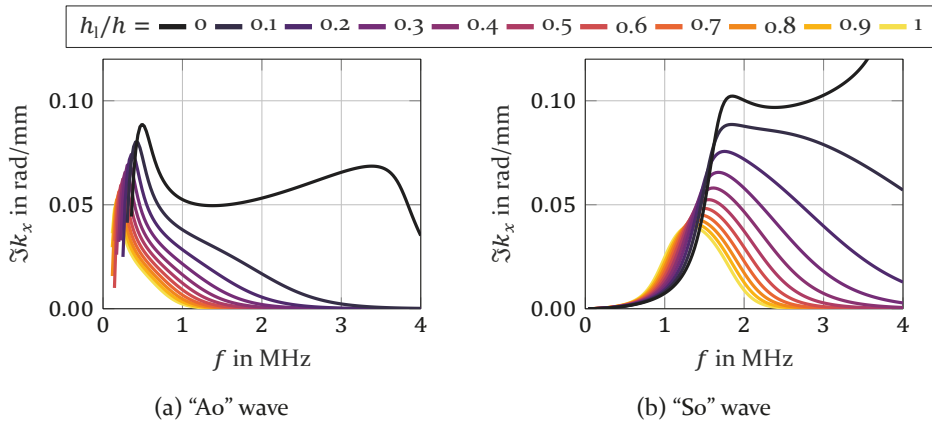


Figure 7.6: Scaling: radiation rate changes with increasing calcite layer thickness h_1 deposited on the pipe wall (brass pipe with thickness $h = 1$ mm).

For high frequencies, the wave labeled "Ao" is not sensitive to the calcite layer thickness, as can be seen in Fig. 7.5. Albeit low sensitivity to undesired environmental changes is desired, this region should be avoided. This is because the radiation into the pipe's interior is lost, as can be concluded from Fig. 7.6, which shows the radiation rate of the "Ao" and "So" waves. The reason for the low radiation is that the wave confines to the brass layer, which has no longer direct contact to the water. The UFM device requires that the radiation be guaranteed even under calcite deposition.

Dezincification

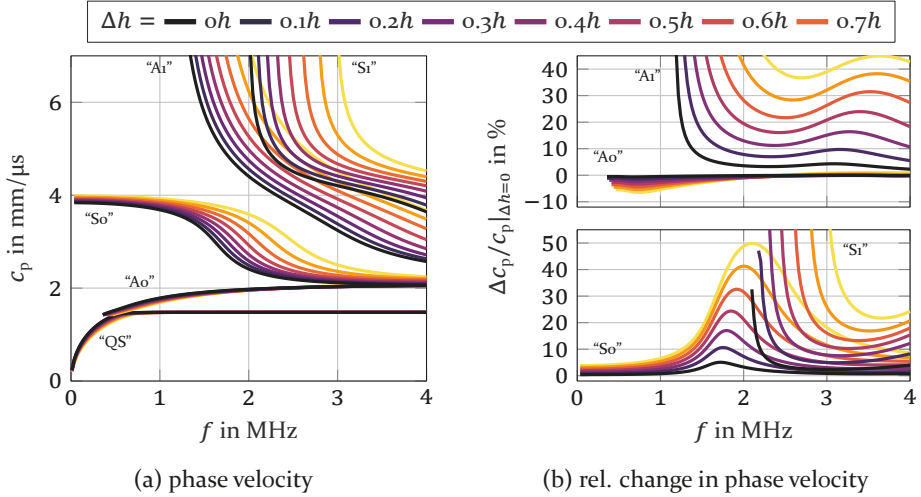


Figure 7.7: Dezincification: change of phase velocity with increasing dezincification thickness Δh . A layer of copper is thereby deposited on the pipe wall of thickness $0.57\Delta h$. The brass pipe wall thickness is $h = 1$ mm.

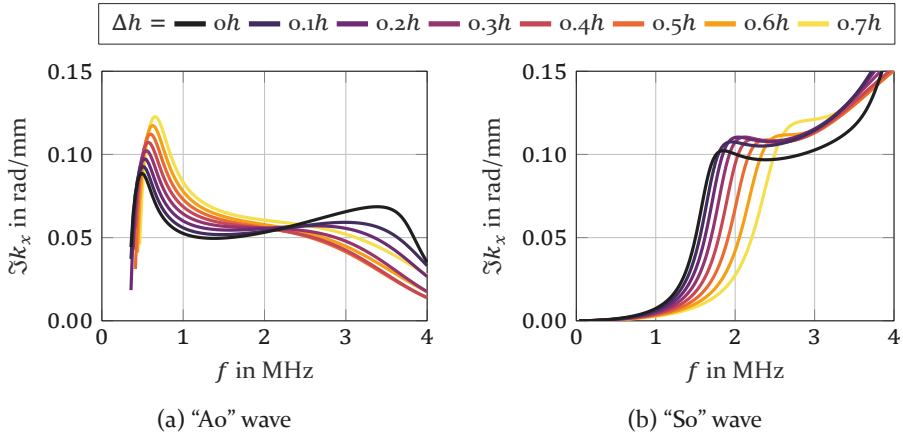


Figure 7.8: Dezincification: radiation rate changes with increasing dezincification corrosion thickness Δh of the pipe wall (brass pipe with thickness $h = 1$ mm).

Another process that forms a layer on the pipe wall is *dezincification* of a brass pipe [178]. This corrosion process of the copper-zinc alloy exhibits two forms [178]: (i) oxidation and dissolution of zinc into the water, or (ii) both copper and zinc oxidate and dissolve, whereby the copper precipitates again onto the pipe wall. In both cases, zinc is preferentially dissolved into the water, leading to a layer of copper on top of the brass material. Note that the copper

may settle with different structures, e.g., dense or porous. The process may occur uniformly on the whole pipe's area (layer dezincification) or locally (plug dezincification), thereby forming holes [179]. Any type of dezincification may be accompanied by the deposition of *meringue* [178], which mainly consists of environmentally hazardous zinc carbonate with inclusions. Both dezincification and meringue formation are not well understood. Many factors affect the process, for instance, the brass alloy (composition, phase and doping), chemistry of the water (pH, hardness, chloride) and physical factors (water flow velocity, contact to other metals, surface structure of the pipe) [178]. Moreover, dezincification leads to interior mechanical stresses [180], which may change the wave propagation inside the pipe wall [142, P2].

For simplicity, we assume that the plate thickness reduces due to corrosion, while at the same time a homogeneous and isotropic layer of copper is deposited. That is, ideal layer dezincification without meringue buildup is considered. If the loss in pipe wall thickness is Δh , then the deposited copper layer will be of thickness $0.57\Delta h$. This relationship has been determined by stoichiometry of a CuZn37 brass alloy using the molar volumes of copper and zinc.

The resulting phase velocities of the bi-layered waveguide are presented in Fig. 7.7a and the corresponding relative changes with respect to no dezincification are shown in Fig. 7.7b. The higher order modes are highly affected by dezincification. On the other hand, fundamental modes are only moderately changed considering that dezincification of up to 70% is considered.

The radiation rate of dezincified brass is given in Fig. 7.8. The effect is not as detrimental as for calcite layer formation. Note that the "Ao" at 1 MHz, for instance, exhibits increasing radiation. A relatively stable operating point with respect to changes in radiation rate of the "Ao" wave is encountered at about 2.2 MHz.

7.4 Temperature cross-sensitivity

The effect of temperature on the system is of particular interest. In conventional transit-time UFM, temperature compensation is primordial for accurate flow metering [1, 2]. It is desirable to design a robust system capable of operating in a very wide temperature range, e.g., 0 °C to 100 °C. These environmental conditions are encountered in practice and may change during operation.

Temperature affects all components of the system. We discuss only the effects on ultrasonic wave propagation. As shown in Fig. 7.2, it is affected in three

ways by temperature, namely, changes in (i) the fluid wave speed c_f , (ii) the pipe wall material parameters c, ρ , and (iii) the pipe wall thickness h . The latter can be studied using the thermal expansion coefficient of the material together with the analysis from Subsec. 7.3.1. We found that the effect of thermal expansion is much smaller as compared to (i) and (ii) and will be neglected. The remaining two effects are discussed in the following.

7.4.1 Temperature dependence of the pipe material

Change of the material parameters has been discussed in Subsec. 7.3.2. This can be used to analyze the effect of temperature $\mathcal{T} = \mathcal{T}_0 + \Delta\mathcal{T}$ on wave propagation in the pipe wall. We are mostly concerned with the deviation $\Delta\mathcal{T}$ from the reference temperature $\mathcal{T}_0 = 20^\circ\text{C}$. The dominant effect is on the Young's modulus, i.e., $E = E(\mathcal{T})$. From (7.9) we have

$$\epsilon_{c_p}^{\mathcal{T}} \stackrel{\text{def}}{=} \frac{\Delta c_p}{c_p} = \frac{1}{2} \frac{c_p}{c_e} \frac{\partial E}{\partial \mathcal{T}} \frac{\Delta \mathcal{T}}{E}, \quad (7.10)$$

where $\frac{\partial E}{\partial \mathcal{T}}$ is the temperature coefficient of the material. Metals have negative coefficients [181] and the relevant ones are explicitly provided in Appendix A. Note that all variables in (7.10) are taken to be at the reference temperature \mathcal{T}_0 (except $\Delta\mathcal{T}$).

The relative change in phase velocity per unit change in temperature is shown in Fig. 7.9. The effect seems to be rather low. However, the temperature may deviate as much as 80 K. For this reason, it is important to consider this effect in order to obtain an accurate model for UFM devices.

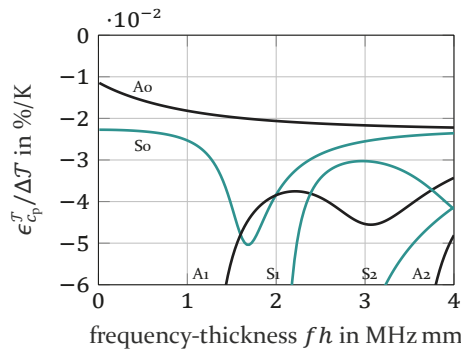


Figure 7.9: Temperature induced change in phase velocity of Lamb waves (brass pipe).

The calculation in Fig. 7.9 is a linear approximation using free Lamb waves. The exact calculation obtained by calculating the QGWs with varying $E(T)$ is displayed in Fig. 7.10. Except for the additional QS mode and the low frequency region of the Ao' wave, the linear approximation agrees very well to the full model. For instance, setting $\Delta T = 100^\circ\text{C}$ in Fig. 7.9 corresponds to the yellow curves in Fig. 7.10b.

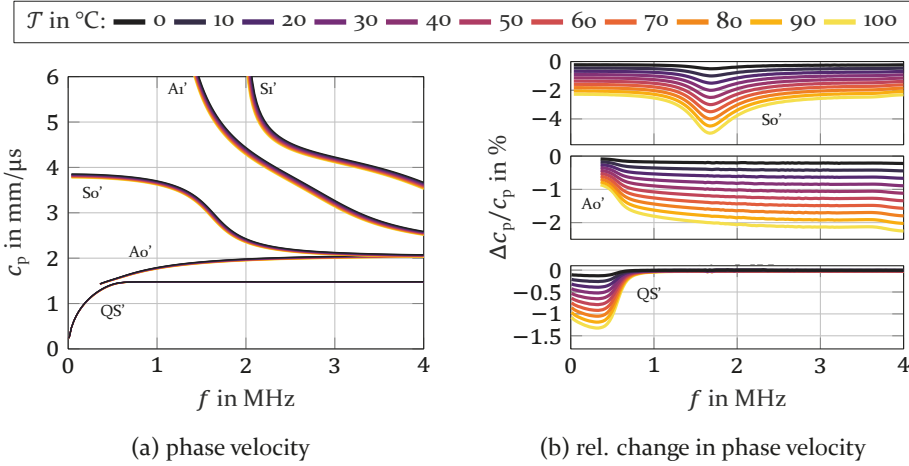


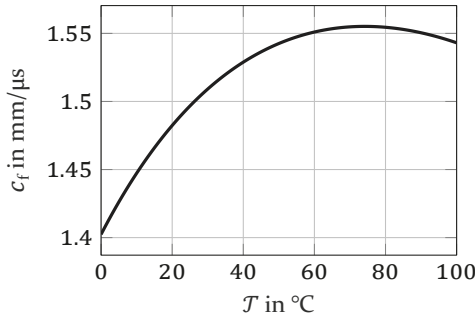
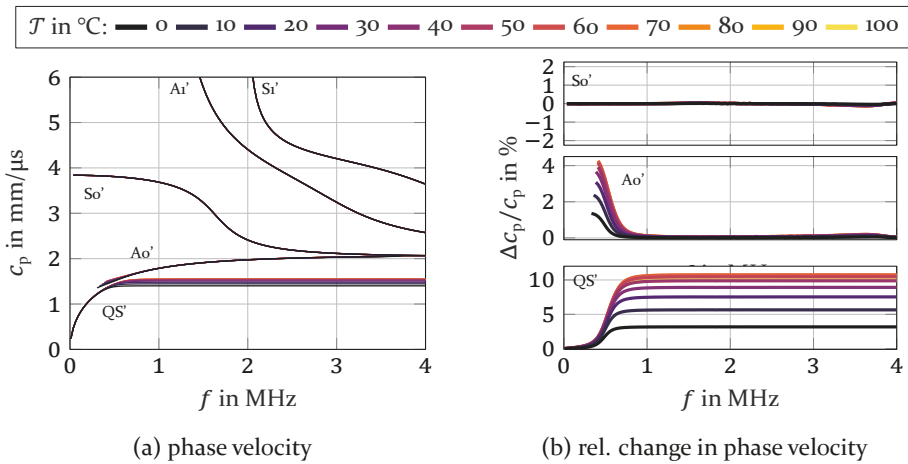
Figure 7.10: Temperature affecting $E(T)$: the phase velocity changes due to changes in the Young's modulus $E(T)$ (1 mm brass).

We may conclude that the phase velocity of waves in the pipe wall changes linearly with temperature. This is not too surprising given the fact that we are using a linear temperature coefficient. Note, however, that the Young's modulus $E(T)$ does not factorize in the QGW stiffness operators given in Subsec. 3.2.2 or 3.2.3 and they are, hence, not exactly proportional to $E(T)$. This is due to the fluid degree of freedom, which is independent of $E(T)$.

7.4.2 Temperature dependence of the fluid wave speed

The wave speed c_f in water is highly dependent on temperature, i.e., $c_f = c_f(T)$. We use a phenomenological model obtained by Bilaniuk and Wong [182, 183]. They fit a fifth order polynomial to measured data (see Appendix A) valid from 0°C to 100°C . The temperature-dependent speed of sound in water is depicted in Fig. 7.11. Note that it exhibits a maximum at $T \approx 74^\circ\text{C}$.

The fluid wave velocity affects the QGW dispersion curves, which are shown for the full temperature range in Fig. 7.12a and the corresponding relative changes with respect to $T = 0^\circ\text{C}$ in Fig. 7.12b. Only the mostly water-born waves are

Figure 7.11: Temperature-dependence of the wave speed c_f in water.Figure 7.12: Temperature affecting $c_f(T)$: the phase velocity changes due to changes in wave speed $c_f(T)$ of water (1 mm brass).

affected, i.e., the high frequency QS' wave as well as the low frequency Ao' wave. The temperature-dependence $c_f(T)$ seen in Fig. 7.11 directly affects the high frequency region of the QS' wave. In particular, its phase velocity exhibits a maximum where $c_f(T)$ shows the maximum.

In practice, both the pipe wall $E(T)$ and the fluid wave speed $c_f(T)$ are affected by temperature. Assuming that the temperature distributes uniformly, both effects superpose to give the dispersion curves in Fig. 7.13a. The relative changes with respect to $T = 0^\circ\text{C}$ are shown in Fig. 7.13b. Note that in practice, the temperature might not distribute uniformly. In this case, it might be more appropriate to assume the pipe wall and the fluid to be at different (maybe homogeneous) temperatures.

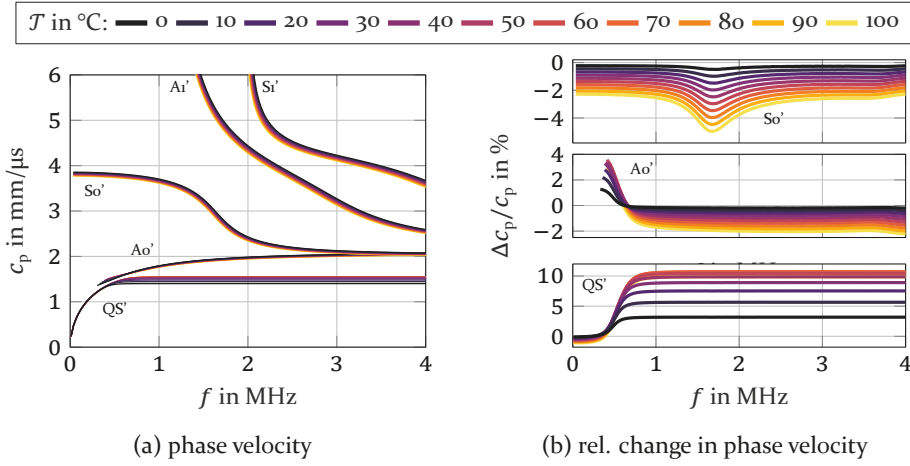


Figure 7.13: Temperature affecting $E(T)$ and $c_f(T)$: the phase velocity changes due to changes in the Young's modulus $E(T)$ of the pipe wall and the sound speed $c_f(T)$ in water (1 mm brass).

7.4.3 Overall differential effect of temperature

Henceforth the model is simplified by assuming that the QGW's phase velocity is independent of the fluid wave speed c_f . According to Fig. 7.12, this is justified for all waves except the QS mode and the Ao' wave close to its coincident frequency. Hence, c_p is only affected by changes of the Young's modulus $E(T)$. Note that this situation was also considered when deriving the cross-sensitivities of the volumetric flow rate in (7.5).

Using (7.5) and (7.10), the differential measurement error due to temperature is $\epsilon_Q^J = \epsilon_Q^{E(T)} + \epsilon_Q^{c_f(T)}$, where

$$\epsilon_Q^{E(T)} \stackrel{\text{def}}{=} \epsilon_Q^{c_p} \epsilon_{c_p}^J = \frac{-c_p^3}{2c_e(c_p^2 - c_f^2)} \frac{\partial E}{\partial T} \frac{\Delta T}{E}, \quad (7.11)$$

and

$$\epsilon_Q^{c_f(T)} \stackrel{\text{def}}{=} \epsilon_Q^{c_f} \epsilon_{c_f}^J = + \frac{2c_f^2 - c_p^2}{c_p^2 - c_f^2} \frac{c_f(T) - c_f}{c_f}. \quad (7.12)$$

It is worth inspecting each of the effects (7.11) and (7.12) separately. They are shown in Fig. 7.14a and Fig. 7.14b, respectively. While the former is linear in T , the latter is not – hence the surface plots in the T - f -plane.

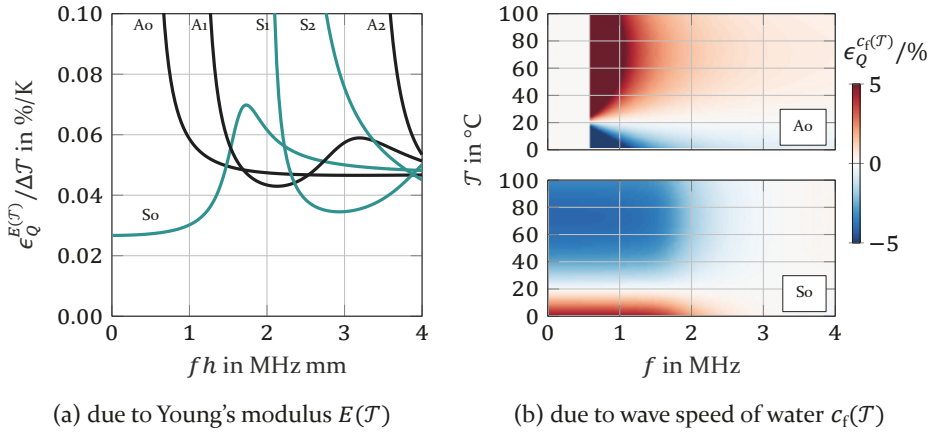


Figure 7.14: Relative error $\epsilon_Q = \frac{Q_m - Q}{Q}$ due to temperature. Effects acting through E and c_f are segregated. Water measurement in a 1 mm brass pipe.

Observe in Fig. 7.14a that the deviation due to $E(\mathcal{T})$ is positive, while the error due to $c_f(\mathcal{T})$ seen in Fig. 7.14b might be negative. As a consequence, the two effects compensate in regions where this is the case.

Lastly, Fig. 7.15 shows the total relative measurement error, i.e., $\epsilon_Q^{\mathcal{T}} = \epsilon_Q^{E(\mathcal{T})} + \epsilon_Q^{c_f(\mathcal{T})}$. The low frequency and high temperature region of the So' wave profits slightly of the mentioned compensation effect, resulting in lower errors than in Fig. 7.14b. Note the additional downward-going frequency-dependent zero-error band in the \mathcal{T} - f -plane of the So' wave in Fig. 7.15. This is due to the "sweet spot" marked in Fig. 7.1b.

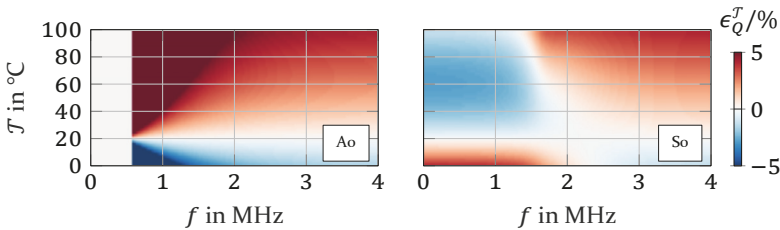


Figure 7.15: Total relative error $\epsilon_Q = \frac{Q_m - Q}{Q}$ of the measured flow rate due to temperature (1 mm brass pipe with water).

7.5 Flow meter sensitivity including temperature

Making use of the analysis in Sec. 7.4, the effect of temperature can now be included in the expression for the flow meter's sensitivity \mathcal{S} . With the simplification $\sin \theta(\mathcal{T}) = \frac{c_f(\mathcal{T})}{c_p(\mathcal{T})}$, it is given by³

$$\mathcal{S}(\mathcal{T}) = \frac{1}{4} K d c_f(\mathcal{T}) \sqrt{c_p^2(\mathcal{T}) - c_f^2(\mathcal{T})} \quad (7.13a)$$

$$= \frac{1}{4} K d \frac{c_f^2(\mathcal{T})}{\tan \theta(\mathcal{T})}, \quad (7.13b)$$

in terms of c_f and c_p or c_f and θ , respectively. Therein, $c_f(\mathcal{T})$ is given by the polynomial fit discussed in Subsec. 7.4.2 and $c_p(\mathcal{T})$ is determined by (7.10) as

$$c_p(\mathcal{T}) = c_p + \frac{1}{2} \frac{c_p^2}{c_e} \frac{\partial E}{\partial \mathcal{T}} \frac{\Delta \mathcal{T}}{E}. \quad (7.14)$$

Note that (7.13) can be used for simple *temperature compensation*: after measuring \mathcal{T} , the corresponding sensitivity $\mathcal{S}(\mathcal{T})$ can be used to determine the flow rate Q .

Let's discuss the impact of temperature on different UFM systems. Eq. (7.13b) is valid for piston transducer devices in V-path arrangement except that the radiation angle θ remains constant thereby⁴. As a consequence, the sensitivity changes as $c_f^2(\mathcal{T})$ and is accordingly highly temperature-dependent [2].

In contrast to this, the radiation angle $\theta(\mathcal{T})$ of Lamb wave-based devices adjusts with temperature such that the sensitivity changes according to the factor $c_f(\mathcal{T}) \sqrt{c_p^2(\mathcal{T}) - c_f^2(\mathcal{T})}$ in (7.13a). Note that the phase velocity decreases with temperature⁵. As a consequence, on the range 0 °C to 74 °C – where c_f increases monotonically – the square root is guaranteed to decrease and (partly) compensates the growth of the $c_f(\mathcal{T})$ -factor. We conclude that the variation of $\mathcal{S}(\mathcal{T})$ with temperature is less than that of $c_f(\mathcal{T})c_f(\mathcal{T}_0)$. As a result, Lamb wave-based flow meters are much less affected by temperature than conventional piston transducer UFM devices ($\mathcal{S} \sim c_f^2(\mathcal{T})$).

³ Note: the first expression makes use of $\cos \arcsin \frac{c_f}{c_p} = \sqrt{1 - \frac{c_f^2}{c_p^2}}$.

⁴ The radiation angle is fully determined by the transducer's orientation.

⁵ Remember that metals exhibit negative temperature coefficients $\frac{\partial E}{\partial \mathcal{T}}$, see Sec. 7.4.1.

To give an impression, the temperature-dependent sensitivity $\mathcal{S}(\mathcal{T})$ of (i) a steel pipe Ao wave, (ii) a brass pipe Ao wave, and (iii) a traditional piston transducers UFM device are compared in Fig. 7.16a. Moreover, the relative change of their sensitivity with respect to 20 °C, i.e., $\frac{\mathcal{S}(\mathcal{T})}{\mathcal{S}(20^\circ\text{C})} - 1$, is shown in Fig. 7.16b. While the relative change in sensitivity of piston transducer devices is as large as 10 %, a flow meter exploiting the Ao wave in a steel pipe exhibits deviations below 2.5 %.

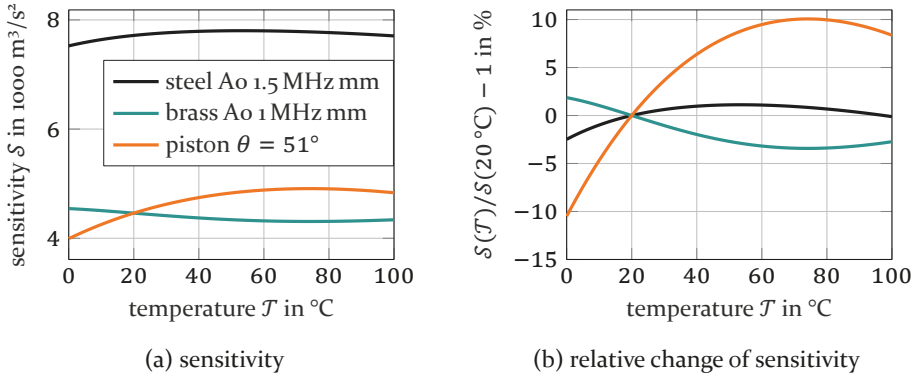


Figure 7.16: Temperature-dependence of the flow meter sensitivity $\mathcal{S}(\mathcal{T})$.

Furthermore, as seen in Fig. 7.16a, the Ao wave in steel profits from its higher phase velocity (lower radiation angle), which leads to a larger overall sensitivity and is less affected by temperature in relative terms. However, this yields correspondingly lower differential time of flights $\Delta\tau_p = Q/\mathcal{S}$. That is, the effect of convection on the transmitted signals will be *maximized* when \mathcal{S} is minimized. It must be ensured that the system is capable of acquiring $\Delta\tau_p$ with sufficient accuracy.

Note that the slope at 20 °C seen in Fig. 7.16 is negatively proportional to the local sensitivity defined in (7.4). The relation to the corresponding “sweet spot” $c_p = \sqrt{2}c_f$ found in Fig. 7.1b should be established. While the brass meter has $c_p < \sqrt{2}c_f$, for the steel meter $c_p > \sqrt{2}c_f$. This results in the different sign of the slope seen in Fig. 7.16b. Remember that the sweet spot describes a local zero-sensitivity to changes in c_f while c_p is assumed constant. Correspondingly, for such an operating point, $\mathcal{S}(\mathcal{T})$ exhibits a stationary point at 20 °C when $\frac{\partial E}{\partial \mathcal{T}}$ is set to zero. However, at this point the effect of $c_p(\mathcal{T})$ is dominant when $\frac{\partial E}{\partial \mathcal{T}} \neq 0$ and its consideration substantially changes $\mathcal{S}(\mathcal{T})$. As a consequence, a global temperature-dependent analysis including both the effect on c_f and c_p is indispensable to find a good operating point and appropriately model $\mathcal{S}(\mathcal{T})$ for temperature compensation.

The variation of sensitivity $\mathcal{S}(\mathcal{T})$ over the entire temperature range is analyzed systematically in a quantitative way by inspecting the root mean square error due to temperature. For this, we define the (squared) deviation as

$$(\Delta\mathcal{S})^2 \stackrel{\text{def}}{=} \frac{1}{100^\circ\text{C}} \int_{0^\circ\text{C}}^{100^\circ\text{C}} [\mathcal{S}(\mathcal{T}) - \mathcal{S}(20^\circ\text{C})]^2 d\mathcal{T}, \quad (7.15)$$

and the corresponding relative error by

$$F_{\text{rel}} = \frac{\Delta\mathcal{S}}{\mathcal{S}(20^\circ\text{C})}, \quad (7.16)$$

which corresponds to the root mean square of the curves in Fig. 7.16b. Note that \mathcal{S} and consequently F_{rel} does not only depend on c_p , but also on c_e according to (7.14), i.e., on the dispersive behavior of waves inside the pipe wall.

The resulting dispersion curves of the relative error is depicted exemplarily for a brass and a steel plate in Fig. 7.17. It is remarkable that the global error due to temperature tends to stay below about 3% for the steel setup, which compares to 7.8% for a piston transducer setup. We note that the curves depend quite strongly on the temperature coefficient $\frac{\partial E}{\partial \mathcal{T}}$. However, even for $\frac{\partial E}{\partial \mathcal{T}} = 0 \text{ GPa/K}$, they stay strictly below 4%, except for the A_0 wave at coincidence.

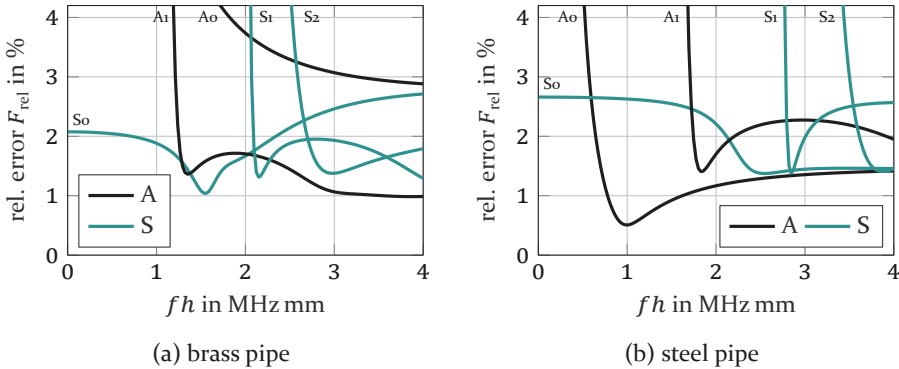


Figure 7.17: Relative root mean square error due to temperature.

Concluding, it may be stated that it is worth inspecting the temperature-dependence of the pipe's mechanical parameters in order to find a temperature-insensitive operating point. In any case, Lamb wave-based UFM is always less dependent on temperature than conventional flow meters. If required, the model developed in this section can be used for active temperature compensation.

8 Flow meter: model validation and measurements

The models developed in the previous chapters will be validated against experimental data in the following. For this purpose, a prototype of the Lamb wave-based UFM device [19, 20] has been built by the project partner¹. Photographs are shown in Fig. 8.1. The steel pipe (Appendix A) has a wall thickness $h = 1.5$ mm. The rectangular cross section is of inner dimensions $b = 1.5$ cm and $d = 1$ cm.

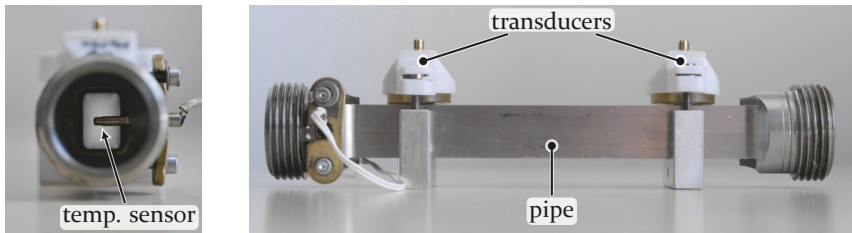


Figure 8.1: Flow meter prototype built by Diehl Metering GmbH.

First, the model is validated in Sec. 8.1 against measurements with the prototype. Then, the inverted model is used to determine the flow rate in Sec. 8.2 and the temperature in Sec. 8.3. Lastly, a general inversion scheme with automatic error compensation is proposed in Sec. 8.4.

8.1 Validation: experimental data of a prototype

Two kind of measurements are used to validate the model: (i) LDV measurements of the pipe wall vibrations and (ii) pitch-catch measurements with controlled temperature and flow rate. These are discussed separately in the following.

8.1.1 LDV measurements

First, the LDV measurements (see Sec. 5.2) are presented in Fig. 8.2. A comb array transducer (see Subsec. 5.1.2) matched to the A_0 wave is driven with a 1 MHz Gaussian sinusoidal burst shown in Fig. 8.2b (scaled amplitude). The peak amplitude is approx. 100 V. The signal recorded at about 9 cm from

¹ Diehl Metering GmbH, Ansbach, Germany

the transducer's center exhibits two pulses that clearly separate in time: the direct path wave and the V-path wave. Scanning a line along the pipe axis gives the $x-t$ data from Fig. 8.2c. A $\mathcal{F}_x\text{-}\mathcal{F}_t$ -Fourier transform of the latter yields the $f\text{-}\mathcal{R}k_x$ -spectrum depicted in Fig. 8.2d.

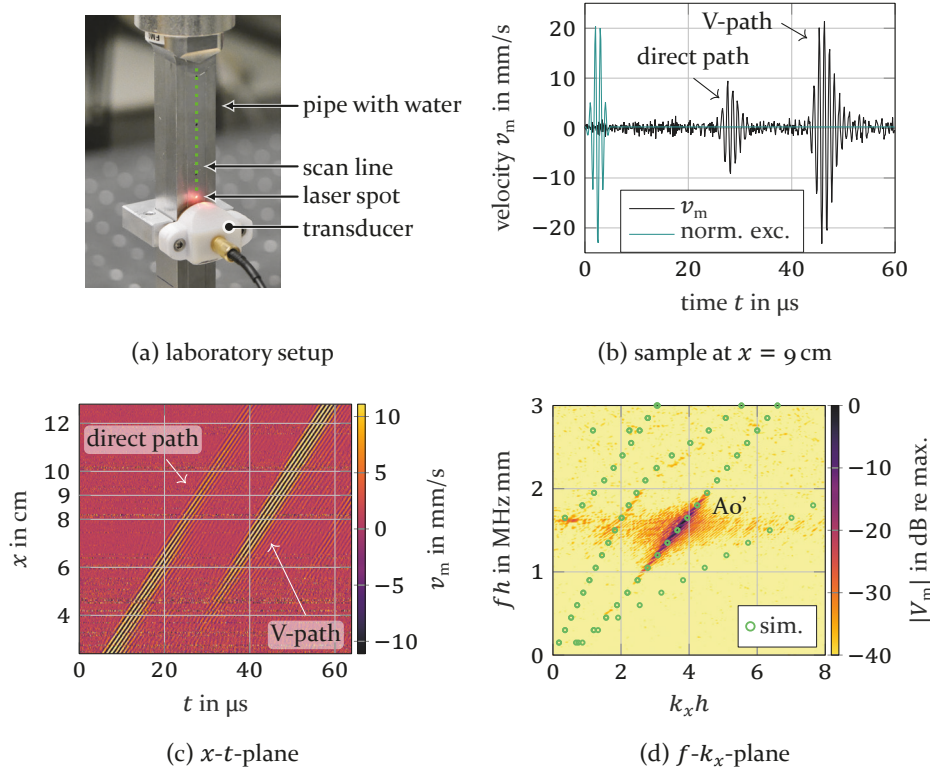


Figure 8.2: LDV measurement of a sinusoidal burst propagating along the pipe wall.

The quasi-guided wave model from Sec. 3.2 yields the wavenumbers superimposed in Fig. 8.2d. The match to the experimentally obtained wavenumbers is very good. This confirms that the quasi-guided plate wave model developed in this monograph is valid to describe waves in the pipe wall of the flow meter prototype.

The measurement data from Fig. 8.2d demonstrates that an almost pure Ao' wave (see Subsec. 3.2.6) is excited by the transducer. Moreover, no reflections from the pipe end can be observed in the considered time interval. These are excellent circumstances to operate the setup as a flow meter.

8.1.2 Ultrasonic pitch-catch measurements

Second, ultrasonic pitch-catch measurements under controlled temperature and flow rate conditions were performed² at the project partner's test facility. The water temperature and flow rate are adjusted by the facility's main controller to the desired nominal values \mathcal{T}_{nom} and Q_{nom} , respectively. Moreover, it provides the current actual flow rate Q_{ref} , which serves as reference for the measurement value Q_{m} determined by the device under test. The reference temperature \mathcal{T}_{ref} , on the other hand, is obtained by the flow meter itself using a negative temperature coefficient thermistor introduced into the flow meter pipe.

Two Ao' wave comb array transducers (see Subsec. 5.1.2) are mounted on the flow meter prototype with an axial separation of $D = 9$ cm. They are alternately excited with a 1 MHz sinusoidal burst using a specialized microcontroller, while the other one serves as a receiver. The microcontroller is also in charge of analogue to digital conversion of the received signals. In this way, the ultrasonic upstream signal $s^{\text{u}}(t)$ and downstream signal $s^{\text{d}}(t)$ are obtained. Multiple measurements are recorded during one test cycle, i.e., at fixed Q_{nom} and \mathcal{T}_{nom} .

The test facility was used to record a set of upstream and downstream signals for a number of operating points. The target values for the volumetric flow rate Q_{nom} in L/h were 6.4, 63, 630, 4000, 5000, and 6000; while the temperature \mathcal{T}_{nom} was set from 10 °C to 90 °C in steps of 10 °C. Each signal is sampled at 8 MHz with 321 points in total.

Recorded signals

In order to gain understanding, the recorded signals are presented qualitatively prior to reducing them to a scalar time of flight. As a first example, the upstream and downstream signals for $Q_{\text{ref}} = 6021$ L/h and $\mathcal{T}_{\text{ref}} = 19.9$ °C are plotted in Fig. 8.3a. Note that both direct wave signals coincide, as expected. The V-path wave, on the other hand, exhibits a clear phase difference between the upstream and downstream recordings.

² The raw data was obtained by the project partner Diehl Metering GmbH, Ansbach, Germany. The signal analysis and evaluation is performed by the author.

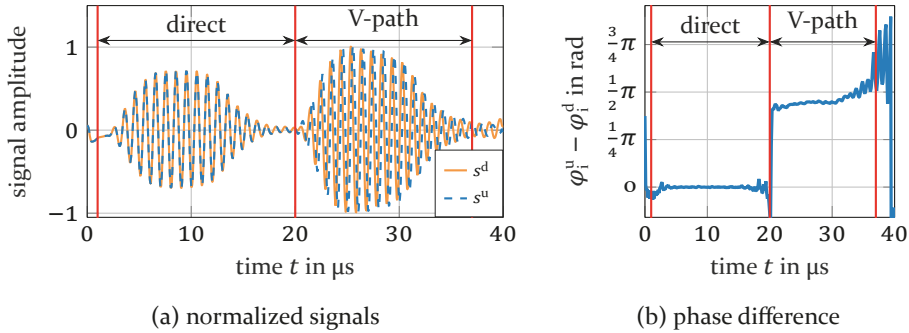


Figure 8.3: Recorded ultrasonic upstream and downstream signals at $Q_{\text{ref}} = 6021 \text{ L/h}$ and $T_{\text{ref}} = 19.9 \text{ }^\circ\text{C}$.

The difference in “instantaneous phase”³ $\varphi_i^u(t) - \varphi_i^d(t)$ of the signals is depicted in Fig. 8.3b. It is estimated by

$$\varphi_i^u(t) - \varphi_i^d(t) = \arg\{s_a^d s_a^{u*}\}, \quad (8.1)$$

where $s_a = s(t) - i\mathcal{H}s(t)$ is the analytic signal⁴ corresponding to s , and \mathcal{H} denotes the Hilbert transform defined as $\mathcal{H}s(t) \stackrel{\text{def}}{=} \text{p.v.} \frac{1}{\pi} \int_{-\infty}^{\infty} \frac{s(\tau)}{t-\tau} d\tau$ [184].

Second, two downstream signals at different temperature but same flow rate are presented in Fig. 8.4a. Their respective instantaneous phase difference $\Delta\varphi_i = \varphi_i^d(40 \text{ }^\circ\text{C}) - \varphi_i^d(20 \text{ }^\circ\text{C})$ is shown in Fig. 8.4b. Temperature affects both the direct as well as the V-path pulses. Thereby, phase delays due to flow rate and temperature combine in the V-path signal.

Time-of-flight evaluation of phase fronts

The phase difference of the signals with respect to a chosen reference signal is obtained from their respective fast Fourier transform (FFT) at fixed frequency (at the magnitude’s maximum 1.018 MHz). Evaluating the V-path downstream signals s^d with respect to a sample at $T_{\text{nom}} = 70 \text{ }^\circ\text{C}$ and $Q_{\text{nom}} = 630 \text{ L/h}$ yields the measured time-of-flight values τ_p^m plotted in Fig. 8.5a. The reference sample is arbitrary and was chosen close to the stable temperature (where the

³ Note that in a Fourier-frequency sense, “instantaneous phases” do not exist, since this is an infinite-time process. In fact, a time-frequency uncertainty holds instead [184].

⁴ The negative sign is due to the sign convention in the definition of the temporal Fourier transform given in Subsec. 2.2.1.

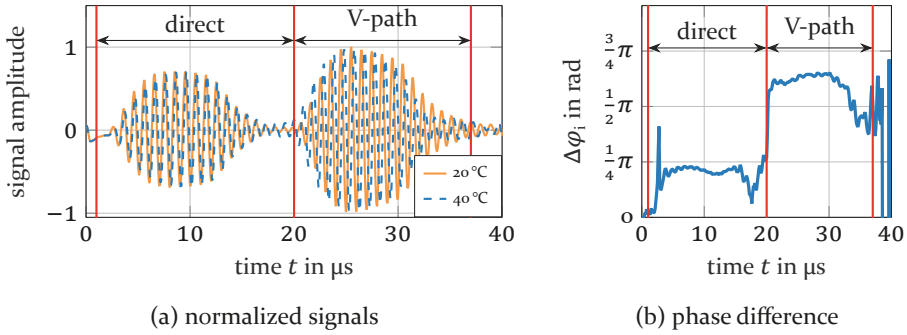


Figure 8.4: Recorded ultrasonic downstream signals at two different temperatures with $Q_{\text{ref}} = 6.4 \text{ L/h}$.

wave speed of water does not change) and with a medium level of flow rate. Incorporating the effect of temperature into (6.12) results in

$$\tau_p(v_o, \mathcal{T}) = \frac{D - 2b \tan \theta(\mathcal{T})}{c_p(\mathcal{T})} + \frac{2b}{c_f(\mathcal{T}) \cos \theta(\mathcal{T})} \left(1 - \frac{v_o}{c_p(\mathcal{T})} \right) + \tau_0, \quad (8.2)$$

where τ_0 is an unknown constant offset. The model (8.2) is also shown in Fig. 8.5a and the measured values τ_p^m – which are periodic in $T \approx 1 \mu\text{s}$ – have been unwrapped around it.

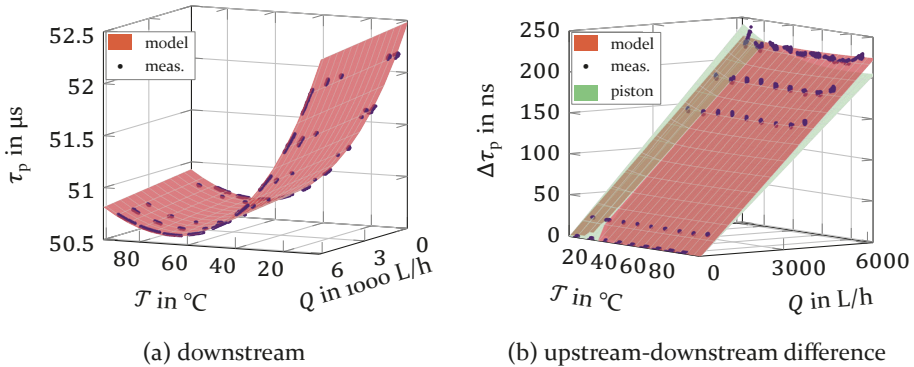


Figure 8.5: Model vs. measurement of the absolute and differential time of flight of the V-path Ao' wave.

The surface's curvature in Fig. 8.5a is determined by both $c_f(\mathcal{T})$ and $c_p(\mathcal{T})$. The only parameter with high degree of uncertainty is $\frac{\partial E}{\partial \mathcal{T}}$ from (7.14). Minimizing the target function $\tau_p(\frac{\partial E}{\partial \mathcal{T}}) - \tau_p^m$ yields $\frac{\partial E}{\partial \mathcal{T}} = -0.0993 \text{ GPa/K}$. After fitting this single scalar parameter, we obtain the excellent agreement between measured

data and model that can be observed in Fig. 8.5a, exhibiting a root-mean-square error of 5.8 ns. Henceforth, the above given value of $\frac{\partial E}{\partial \mathcal{T}}$ will be used for the evaluations.

The measured upstream-downstream differential time of flight $\Delta\tau_p^m$ is obtained in a similar manner using the FFT. Thereby, for every upstream signal, the corresponding downstream signal s^d serves as reference. The measured values depicted in Fig. 8.5b align well with the model surface as predicted by $\Delta\tau_p = \mathcal{S}^{-1}(\mathcal{T})Q$ with $\mathcal{S}(\mathcal{T})$ from (7.13). The root-mean-square error between model and measurements is only 1.8 ns. In contrast to Fig. 8.5a, and as expected from Sec. 7.5, it is barely dependent upon temperature \mathcal{T} . This is a big strength of Lamb wave-based flow meters. For comparison, the expected differential time of flight for a piston transducer UFM is also shown. Thereby, the constant radiation angle $\theta = 35.3^\circ$ corresponds to the Ao' wave's angle at 20 °C. The piston model exhibits a root-mean-square error to the measured data of 7 ns. Most notably, the temperature-dependence expected by this model does not align with the evidenced measurements, as can be observed in Fig. 8.5b. This demonstrates that conventional modeling of ultrasonic flow meters is not appropriate for Lamb wave-based systems.

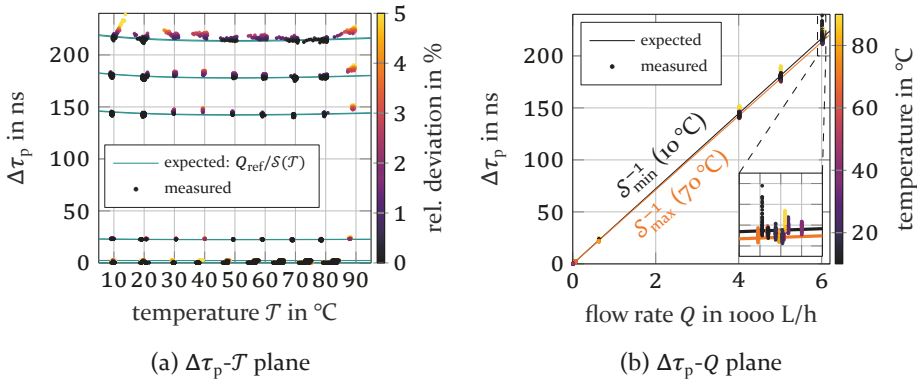


Figure 8.6: Expected vs. measured differential time of flight $\Delta\tau_p$.

The projection of Fig. 8.5b onto the $\Delta\tau_p$ - \mathcal{T} plane is depicted in Fig. 8.6a, while the projection onto the $\Delta\tau_p$ - Q -plane is shown in Fig. 8.6b. Both representations yield valuable insight into the temperature dependence of the model and the variation of the acquired differential time of flight $\Delta\tau_p^m$. The lowest and highest expected slope are drawn into Fig. 8.6b. The variation of the measured values is larger than expected due to temperature and does not correlate with it. The distance correlation coefficient⁵ between $\mathcal{S}_m = Q_{\text{ref}}/\Delta\tau_p^m$ and \mathcal{T}_{ref} is 0.03 and the Pearson correlation coefficient between \mathcal{S}_m and $\mathcal{S}(\mathcal{T}_{\text{ref}})$ is 0.003.

This demonstrates that the variation in $\Delta\tau_p^m$ is mainly caused by other process uncertainties.

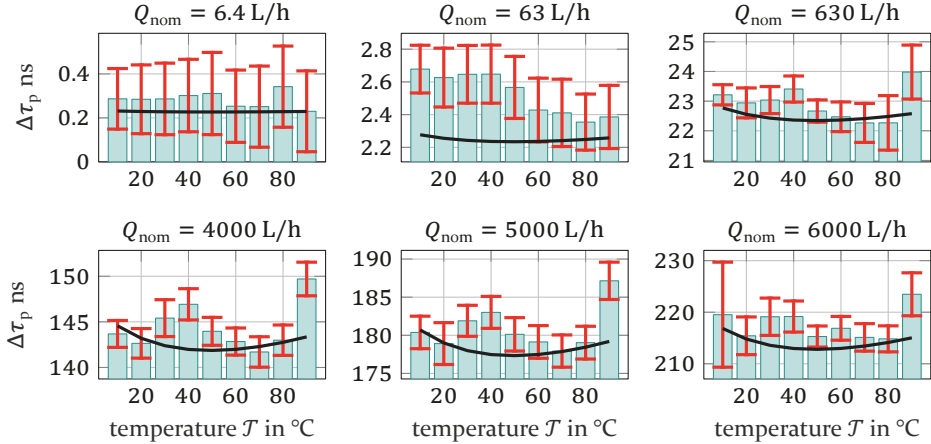


Figure 8.7: Errors in the evaluated upstream-downstream differential time of flight $\Delta\tau_p^m$:
■ mean ┆ 2σ -error bars — model

Lastly, we examine the reliability of the dataset comprising the 7665 measurements and consisting of upstream and downstream signals as well as the accompanying signal processing. Some statistics of the evaluated upstream-downstream differential time of flight $\Delta\tau_p^m$ is presented in Fig. 8.7 along with the expectation from the model. No sort of correction has been made therein. As the hydrodynamic correction is missing, i.e., $K = 1$, the low flow rates are underestimated by the model. While the standard deviation increases in absolute terms with Q_{nom} , it strongly decreases in relative terms. Note that the expected $\Delta\tau_p$ for $Q_{\text{nom}} = 6.4$ L/h is merely 0.23 ns, which equals the 2σ -width of the distribution. Conspicuous is the rather arbitrary temperature dependence of the data. This confirms, again, that the errors should be ascribed to other effects.

This concludes the validation of the Lamb wave-based UFM model developed in this monograph. A physics-based description of the flow rate-dependent time of flight of ultrasonic signals has been attained. Thereby, the effect of temperature from 0 °C to 100 °C has been included in a precise manner. With regard to the upstream-downstream differential time of flight, the prototype was shown to be less affected by temperature than piston transducer flow

⁵ Neither the Pearson nor the Spearman correlation coefficient are appropriate, as the expected relation between the slope \mathcal{S} and temperature \mathcal{T} is nonlinear and nonmonotonic.

meters. The flow rate will be retrieved from the acquired time of flights in the next section.

8.2 Flow rate determination from the V-path

After acquiring the V-path differential time of flight $\Delta\tau_p^m$, the volumetric flow rate can be obtained according to (7.1) by

$$Q_m = S(\mathcal{T})\Delta\tau_p^m. \quad (8.3)$$

Therein, the temperature \mathcal{T}_{ref} acquired by the temperature sensor is utilized. Without hydrodynamic corrections ($K = 1$, see Subsec. 1.2.4), the resulting measurement deviations with respect to the reference flow rate Q_{ref} are presented in Fig. 8.8. A series of histograms is plotted using only the data subset where Q_{nom} is below the indicated values, revealing the flow rate-dependent distribution of deviations. Note that Q_{ref} is not known for each single measurement, but only as a mean value of every tested operating point (Q_{nom} , T_{nom}). Hence, the deviations are not necessarily errors.

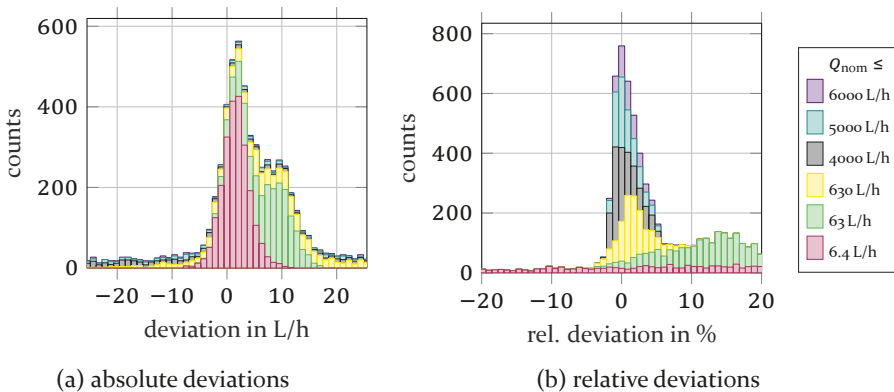


Figure 8.8: Distribution of deviations of the 7665 measurements without hydrodynamic corrections ($K = 1$). Occurrences are accumulated from low to high values of the nominal flow rate Q_{nom} .

The absolute deviations $Q_m - Q_{\text{ref}}$ are seen to increase with the flow rate in Fig. 8.8a. The converse is true for the relative measurement deviations in Fig. 8.8b. This is because for low flow rates, the associated differential time of flight is close to the uncertainty in obtaining the quantity (see Fig. 8.7), which leads to high variations. Nonetheless, the corresponding deviations are small in absolute terms. This is a well-known behavior of transit-time UFM.

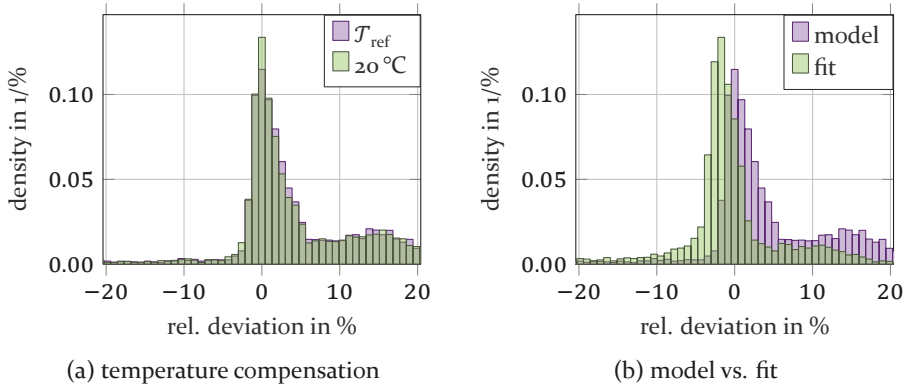


Figure 8.9: Comparison of measurement deviations without hydrodynamic corrections ($K = 1$) using different inversion methods.

Note that the low flow rates are biased towards positive deviations, i.e., they are overestimated. This is attributed to the fact that the calibration factor K has been set to unity, which is a good approximation for turbulent flow only. For flow rates in the laminar and transitional regimes $K(\bar{v}_0) < 1$, which is usually determined experimentally.

The above evaluation requires the temperature \mathcal{T} to be known. As has been shown in Sec. 7.5, the temperature-dependence of \mathcal{S} is low for the prototype under inspection. Moreover, according to Subsec. 8.1.2, the uncertainty in acquiring $\Delta\tau_p^m$ is higher than the effect of temperature. Hence, it is possible to fix \mathcal{S} at $\mathcal{S}_0 = \mathcal{S}(20\text{ }^\circ\text{C})$ and abstain from temperature-compensation. Proceeding in this way avoids the temperature sensor altogether. This results in a very simple measurement at cost of introducing some errors. The overall measurement deviations using either \mathcal{T}_{ref} or $\mathcal{T}_0 = 20\text{ }^\circ\text{C}$ in the computation of Q_m are compared in Fig. 8.9a. This confirms that, in contrast to conventional UFM, temperature compensation is of minor importance with the utilized Lamb wave-based flow meter prototype.

Instead of using the physical model developed in this work, the flow meter could rely on a phenomenological model for flow rate determination. For instance, a function linear in $\Delta\tau_p$ and cubic in \mathcal{T} has been fitted to the $\Delta\tau_p^m - \mathcal{T}_{\text{ref}} - Q_{\text{ref}}$ data set (i.e., the inverted model is fitted) using a least squares method. Using this fit to determine Q_m yields the measurement deviation distribution shown in Fig. 8.9b in comparison to the previous results. Note that the fit tries to minimize the sum of squares by moving down the very high errors at cost of displacing the peak error density, i.e., the maximum in Fig. 8.9b, away from zero. This could be undesired. While the fit is specialized

to the prototype with given geometry and materials, the physical model is universally applicable and can be used for device optimization.

The effect of hydrodynamics shall be illustrated by inspecting the experimentally obtained correction factor $K = \bar{Q}_{\text{ref}}/\bar{Q}_m$. Therein, the $\bar{\cdot}$ refers to the mean over all acquired data at certain Q_{nom} . The results are plotted together with an exponential fit in Fig. 8.10a. The fit is of the form $K(\bar{\Delta\tau}_m) \approx A - B e^{-C\bar{\Delta\tau}_m}$ and results in $A = 0.987$, $B = 0.211$ and $C = 0.344/\text{ns}$. The correction factor exhibits the expected behavior: it increases with the flow rate and saturates in the turbulent flow regime. $K(\bar{\Delta\tau}_m)$ can be used in $\mathcal{S}(\mathcal{J})$, see (7.13), to calculate the flow rate Q_m . The resulting mean relative errors with respect to Q_{ref} are shown in Fig. 8.10b. Depending on T_{nom} , the errors are still substantial. In practice, the correction factor K should be made temperature-dependent because the dynamic viscosity of water depends on it, which results in a shift of the transitional and turbulent flow regimes. As a consequence, \mathcal{S} will also depend on temperature through $K(\Delta\tau, \mathcal{J})$.

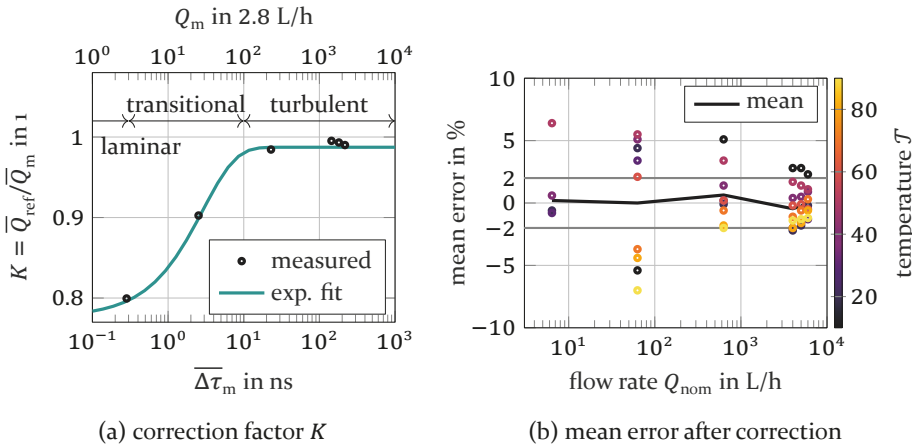


Figure 8.10: Correction factor and mean errors.

This section showed that the theoretical time-of-flight model is quite appropriate to determine the flow rate Q_m . Two main reasons are identified for the relatively high measurement errors with the prototype. One is the low wave convection effect (\mathcal{S} too high) compared to the accuracy with which the differential time of flight is acquired. This can be resolved by choosing another operating point with lower \mathcal{S} , see Chap. 7. The other source of errors are hydrodynamic effects, which affect the results because it has been neglected in the inverted model. Accurate flow measurements will only be possible if a calibration is performed to compensate this effect. This is the conventional

procedure in UFM, but the implementation of a detailed compensation is outside the scope of this monograph.

8.3 Temperature determination from direct path

The ultrasonic system is additionally able to determine the temperature from the direct path wave. This signal component is particularly suited because it is expected to be independent of the fluid flow. The Ao' wave's change in time of flight with respect to $\tau_p^d(\mathcal{T}_0)$, i.e., the time of flight at $\mathcal{T}_0 = 20^\circ\text{C}$, is

$$\Delta\tau_p^d(\mathcal{T}) \stackrel{\text{def}}{=} \tau_p^d(\mathcal{T}) - \tau_p^d(\mathcal{T}_0) = \frac{D}{c_p(\mathcal{T})} - \frac{D}{c_p}, \quad (8.4)$$

where $c_p = c_p(\mathcal{T}_0)$. With $c_p(\mathcal{T})$ given in (7.14), we obtain

$$\Delta\tau_p^d(\mathcal{T}) = \frac{D}{c_p + \frac{1}{2} \frac{c_p^2}{c_e} \frac{\partial E}{\partial \mathcal{T}} \frac{\Delta \mathcal{T}}{E}} - \frac{D}{c_p} \approx -\frac{D}{2c_e} \frac{\partial E}{\partial \mathcal{T}} \frac{\Delta \mathcal{T}}{E}. \quad (8.5)$$

With manufacturer provided material data (Appendix A: $\frac{\partial E}{\partial \mathcal{T}} = -0.075 \text{ GPa/K}$), the expected slope $\frac{\Delta\tau_p^d}{\Delta\mathcal{T}}$ is 5.18 ns/K, which compares to 5.43 ns/K using material data from Ref. [185] (Appendix A: $\frac{\partial E}{\partial \mathcal{T}} = -0.0787 \text{ GPa/K}$) obtained by measurement of Lamb waves on a plate of the same material. This demonstrates that the effect is sufficiently large to be exploited using current transit-time UFM hardware.

The model is compared to the measured time delay $\Delta\tau_{pm}^d = \frac{\Delta\varphi^d}{\omega}$ of the direct path wave in Fig. 8.11a. Thereby, the direct-path phase difference $\Delta\varphi^d$ is obtained from the phase of the Fourier transform of the signals at $f = 1.018 \text{ MHz}$ with respect to 20°C . In general, good agreement is found. The data aligns quite well on a line with slope $\approx 5.36 \text{ ns/K}$ ($R^2: 0.9992$, root mean square error: 3.79 ns). According to (8.5), this corresponds to $\frac{\partial E}{\partial \mathcal{T}} = -0.0777 \text{ GPa/K}$.

Unexpectedly, the direct path wave is seen to be slightly dependent on the flow rate. This is presumably due to flow rate-dependent systematic deviations between the acquired temperature \mathcal{T}_m and its reference \mathcal{T}_{ref} . For instance, in general, the temperature of the pipe wall (\mathcal{T}_m) will be different to the one of the water (\mathcal{T}_{ref}). As our test system applies high flow rates only for a short time,

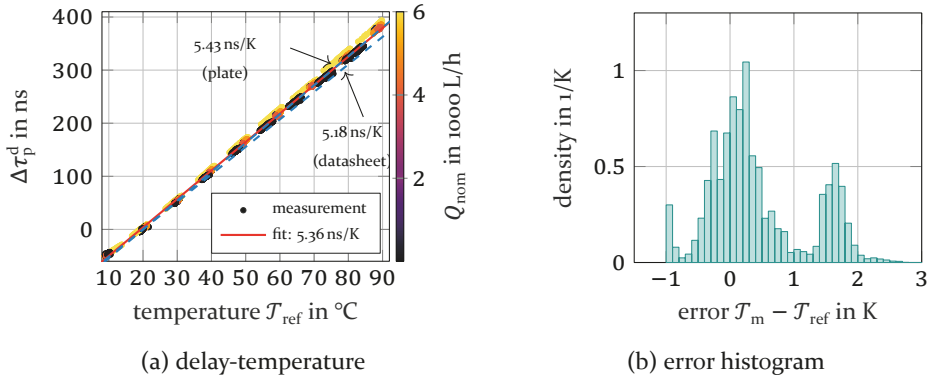


Figure 8.11: Temperature evaluation from the direct path wave.

T_m might not settle into its steady state, which indirectly leads to a flow-rate dependence.

The temperature can be obtained from (8.5) given the measured delay $\Delta\tau_{pm}^d$. It is determined by

$$T_m = T_0 - \frac{2c_e E}{D \frac{\partial E}{\partial T}} \Delta\tau_{pm}^d. \quad (8.6)$$

The calculation has been performed for the acquired data. The error between measured temperature T_m and reference temperature T_{ref} is shown in the histogram of Fig. 8.11b. Typical errors are below 2 K. This could be improved upon by revoking the assumption that $T_m = T_{ref}$ and, instead, considering that the plate will be in thermal equilibrium between the water temperature T_{ref} and the ambient temperature.

The obtained temperature estimate can be used for temperature-compensated flow measurements, thereby eliminating the need for a dedicated temperature sensor. As the meter's cross-sensitivity of flow rate to temperature is low (see Sec. 7.5), the achieved accuracy in determining T might be sufficient for the desired compensation effect. In view of the fact that conventional systems need very accurate dedicated temperature sensors – which are rather expensive and require perforation of the pipe – this represents a remarkable improvement for UFM systems.

8.4 A general inversion method: compensation of arbitrary effects

An alternative approach to determine the flow rate Q is sketched in the following. So far, it has been assumed that the sensitivity \mathcal{S} is known and can be used for direct determination of Q . This might, however, not be the case because of uncertainties in the system parameters and environmental influences.

In a very general setting, what is known is the dependence of the time of flight τ – given in (8.2) – on the unknown parameters of interest, which hereinafter are collected into the vector \underline{p} . One of them should be the flow rate Q , as this is what is to be measured. Other parameters of particular interest are the temperature \mathcal{T} and the phase velocity $c_p(\mathcal{T})$, as has been demonstrated in Chap. 7. If we are able to estimate these two, it will be possible to compensate most environmental influences and uncertainties on the flow meter.

Multiple signal components reach the receiver as contributions due to different waves and wave paths. These have been modeled systematically in the previous chapters. Each of them leads to a time-of-flight expression $\tau_n(\underline{p})$, i.e., a system of equations is obtained that is collected in the vector $\underline{\tau}(\underline{p})$. The task finally consists in inverting the system, yielding the desired parameters \underline{p} (one of them being the flow rate Q). Note that this results in *automatic compensation of all undesired effects* due to parameters included in \underline{p} .

The inversion does not need to be done explicitly in advance – it might not even be possible to do so. Instead, once the corresponding measurement values $\underline{\tau}^m$ have been acquired, the cost function

$$F(\underline{p}) = (\underline{\tau}(\underline{p}) - \underline{\tau}^m)^2 \quad (8.7)$$

can be minimized on-line to obtain the best approximation \underline{p}_m .

At least as many independent time-of-flight quantities need to be used as number of parameters in \underline{p} . If more are used, (8.7) can be solved in a least square sense and this might be of convenience. It is crucial to choose the quantities such that an invertible and well conditioned system of equations is obtained, i.e., the τ_n should be independent. For each leaky Lamb wave, possible time-of-flight quantities are the phase and energy transit times ($\times 2$), each of them as direct or V-path signal ($\times 2$). The latter can additionally be obtained as upstream or downstream signals ($\times 2$). The same applies for trapped waves (e.g., QS mode) except that no V-path signal exists.

Considering only the fundamental leaky waves Ao' / So' and the QS mode, this gives a total of 14 possible time-of-flight quantities shown schematically in Fig. 8.12. These cannot all be used in practice because (i) not all of them are excited, (ii) the contributions need to be separable and (iii) some have inappropriate physical properties for the setup (e.g., wavelength/radiation rate).

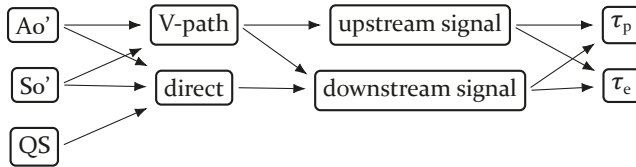


Figure 8.12: Theoretically available time-of-flight quantities (14 in total).

It is pertinent to restrict to phase delays, since these can be measured more accurately than envelope/energy delays. Moreover, it is reasonable to use only upstream-downstream time differences for V-path signals. For direct path waves, the upstream and downstream signals are the same and we need to consider the absolute time of flight for one of them instead. The overall resulting reduction is depicted in Fig. 8.13.

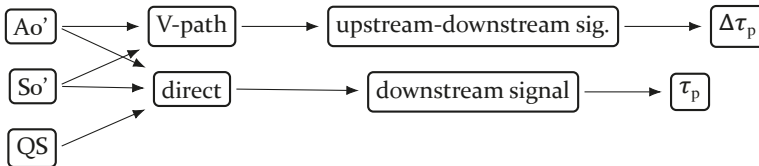


Figure 8.13: Available differential time of flights for phase fronts only (5 in total).

As a proof of concept, the time-of-flight models $\underline{\tau} = [\Delta\tau_p^{Ao,V}, \Sigma\tau_p^{Ao,V}, \tau_p^{So,d} - \tau_p^{So,d}(20^\circ\text{C})]^T$ have been used, where \bullet^V and \bullet^d denote the V-path and direct path, respectively. Moreover, $\Sigma\tau_p$ denotes the sum of upstream and downstream transit times. The method was tested against synthesized measurement data with $\pm 0.5\%$ random errors in $\underline{\tau}^m$. Moreover, the parameters were $\underline{p} = [v_o, \mathcal{T}]^T$, i.e., the flow velocity and temperature. A “trust-region-reflective” optimization algorithm is capable of determining \underline{p} with 0.5% accuracy. Note, however, that it is necessary to minimize the cost functional on both sides of the maximum of $c_f(\mathcal{T})$ separately, as otherwise a local minimum is found. This illustrates the problematic behavior of $c_f(\mathcal{T})$, which is not invertible.

For now, direct inversion as presented in Sec. 8.2 is preferred due to its simplicity. As low-cost computational power becomes readily available on digital

signal processors, the method sketched above might gain interest in the near future. Its strength lies in its generality, as it is capable of determining the best estimates for all parameters of interest. This avoids additional sensors, e.g., for temperature, and leads to automatic compensation of cross-sensitivities. Accurate modeling of all wave modes and paths – as presented in this monograph – is the foundation that enables this alternative approach.

9 Conclusions and outlook

Ultrasonic flow meters fully play off their strengths in a non-invasive configuration, i.e., when the pipe's interior is not perforated and the transducers are mounted on the outside. This comes, however, at the price of more intricate physical models required to appropriately describe the wave propagation. This is the case because the non-invasive system is dependent upon the dynamics of the pipe wall, which is an elastodynamic system exhibiting pronounced resonances, denoted here as *quasi-guided waves*.

Models based on quasi-guided waves, e.g., leaky Lamb waves, account for the *exact pipe wall mechanics*. Such models were formulated in this monograph for all arising wave paths through the flow metering device in a consistent manner. This includes structure-borne ultrasound (direct path) as well as waves going through the fluid medium (V-path). Thereby, we included and assessed the effect of

- convection in the flowing medium,
- temperature (acting on the fluid and the pipe),
- pipe material parameters and thickness (uncertainty and aging), and
- deposition of a layer in the pipe (e.g., scaling or dezincification).

In this way, an extensive picture of the flow meter's response to its environment – whether the effect is desired or not – was obtained. The assessment allows to choose an operating point with good sensitivity and low cross-sensitivities.

The effect of temperature is of major interest, as it needs to be actively compensated in conventional ultrasonic meters. We found that Lamb wave-based devices intrinsically exhibit a passive compensation mechanism, leading to a significantly *reduced cross-sensitivity to temperature*. This is the result of a complex interplay between the quasi-guided waves in the pipe wall and the fluid medium. Albeit the reduced cross-sensitivity is already obtained by considering the temperature-dependence of water alone, it has been shown that the temperature-dependence of the pipe's material is also relevant.

Strictly speaking, the *time of flight in Lamb wave-based flow meters is different* to that in piston type transducer systems. The latter sense a time of flight that changes with the fluid flow, whereby the length of the propagation path remains effectively unchanged. In contrast to this, the Lamb wave-based

meters exhibit flow-independent transit times through the fluid but the ultrasonic beam will be axially displaced when reaching the pipe wall and coupling back as a quasi-guided wave. The Lamb wave receiver still perceives a change in transit time because the convected wave has coupled back closer or further away from the transducer. This means that Lamb wave-based flow meters sense the beam displacement by means of conventional ultrasonic ranging of the point of incidence on the pipe wall. In contrast to conventional setups, in the extreme laminar and turbulent flow regimes the transit time is perfectly linear in the flow velocity.

The developed concepts and models were *verified experimentally*. The wavenumbers obtained from the plane quasi-guided wave problem were validated with laser Doppler vibrometer measurements on fluid loaded plates. Such measurements also confirm that the pipe wall of the prototype flow meter can, in very good approximation, be regarded as a plane waveguide. Schlieren photographs were taken to reveal the radiation field of leaky waves and non-specular reflection phenomena, both effects arising in flow meter systems. Time-of-flight measurements on a prototype device agree well with the flow- and temperature-dependent transit time model. It can, hence, readily be used to determine the flow rate from the acquired transit times. However, the conventional hydrodynamic calibration is still required.

Quasi-guided waves for flow meter modeling

Central to the developed model and many of the performed studies is the knowledge of the quasi-guided wave field, in particular, the frequency-dependent wavenumbers and the radiation rate. These are waves propagating along a mechanical structure that is in contact with an infinite fluid medium (that is, larger than the wave packet itself). In general, they can be classified into three categories: (i) perfectly guided waves, which are also called *trapped waves*; (ii) *leaky waves* that radiate into the fluid; and (iii) incoming waves, which appear due to lack of a radiation condition. The former two are of interest in flow metering, with emphasis on leaky waves, as they can fully insonify the interior of the pipe.

We have argued that leaky waves are a very useful concept for flow metering because they form a *rapidly converging discrete basis* (albeit for the pipe wall only). Nonetheless, they are physically very intricate and insufficiently well understood. This is because they represent eigensolutions of a non-conservative system, i.e., energy may leak out of the pipe wall into the infinite fluid medium. As a consequence, many of the conventional mathematical concepts and tools, e.g., modal expansion and perturbation, are not directly

applicable. The concept of leaky waves could be avoided by using a modal basis instead, the so-called radiation modes. However, this basis is continuous, resulting in an integral representation of the wave field. With such a representation, assessment of the flow meter behavior would be rather difficult – if not impossible.

Quasi-guided waves are described by a *nonlinear eigenvalue problem* in the axial wavenumber, which is unusual and difficult to solve. We developed a *new solution procedure* based on a change of variable which linearizes the problem in case of a plane waveguide, i.e., for plates. Conventional linear eigenvalue solvers can then be used to robustly and reliably obtain the solutions. In contrast to conventional methods, our technique guarantees to find all solutions and is applicable to any combination of pipe and fluid parameters.

A *simulation toolbox* named Elastodynamic Acoustic Toolbox (EDAT) was implemented. It is capable of solving guided and quasi-guided wave problems in plane structures based on a spectral collocation scheme and the above mentioned change of variable. It can handle generally anisotropic, dissipative, multi-layered and fluid loaded plates. The analysis presented in this monograph has entirely been carried out with this toolbox.

Outlook

In addition to the flow rate, other parameters can also be valuable to the end user. A method that simultaneously solves for multiple parameters has already been introduced in Sec. 8.4. It could be worth developing a device geometry and excitation where sufficiently many waves are received to apply this method. In principle, only (i) the flow rate, (ii) the wave speed in water, and (iii) the phase velocity in the pipe wall need to be accounted for in order to obtain a system which is robust against most environmental influences (including temperature, scaling, sedimentation and aging). In this way, a *self-calibrating* flow meter is obtained. Such meters do already exist. It is, however, worth remarking that the framework developed in this work is also well suited to achieve this goal.

Additionally, *broadband excitation* could also be used to increase the information at the receiver, i.e., exploiting the dispersive propagation of quasi-guided waves. Dispersion is already accounted for in the models. However, it would also need to be considered in the signal processing schemes. Several such methods have been developed in the literature, one promising example being the dispersive Radon transform [186].

Only metallic pipes were considered for the flow meter. Devices based on polymer pipes may exhibit better transmission into the pipe's interior. The implemented EDAT toolbox enables the development and optimization of polymer-based meters, including fiber-reinforced composites, which represent a challenge due to their strong interaction with the fluid, dissipation and anisotropy.

The herein developed solver for quasi-guided waves is restricted to plane waveguides loaded with one fluid, either on one or both sides of the plate (which can be rather arbitrary). Adapting the change of variable, it might be possible to extend the method to different fluids on both sides or even loading the plate by solid half-spaces. On the other hand, extending the method to more general waveguide geometries might be more difficult, if not impossible. In such a case, nonlinear eigenvalue solvers as found in the literature [91, 187] could still be used.

Some of our analysis still rely on perturbation of guided waves instead of the quasi-guided ones, e.g., the effect of temperature on the pipe. This assumes that the field of fluid loaded and free elastic waves are similar, which is not the case for strongly fluid-coupled structures like a polymer pipe containing water. Instead of perturbation analysis, it would be feasible to solve the full wave problem iteratively for every parameter value (e.g., temperature) in order to assess its influence. This, however, hides the analytical relation between the parameter and the resulting wave propagation characteristics. Therefore, it would be desirable to resolve these limitations as discussed next.

As to date, no theory exists to perform a formally sound field expansion in terms of leaky elastic waves. Consequently, perturbation theory is not possible and the excitation of leaky waves by the transducer cannot be computed. These handicaps of leaky wave theory are due to lack of an orthogonality relation. We conjecture that these difficulties can be resolved by developing a quasinormal mode theory of the elastodynamic quasi-guided waves, as this has successfully been done in other disciplines [76].

A Appendix: Material data

Fibre reinforced graphite/epoxy (GREP)

Voigt notated stiffness tensor in GPa:

$$\underline{\underline{C}} = \begin{bmatrix} 109 & 6.50 & 6.50 & 0 & 0 & 0 \\ 6.50 & 14.3 & 6.78 & 0 & 0 & 0 \\ 6.50 & 6.78 & 14.3 & 0 & 0 & 0 \\ 0 & 0 & 0 & 3.76 & 0 & 0 \\ 0 & 0 & 0 & 0 & 5.27 & 0 \\ 0 & 0 & 0 & 0 & 0 & 5.27 \end{bmatrix}, \quad (\text{A.1})$$

Density: $\rho = 1540 \text{ kg/m}^3$.

Source: [58].

Brass CuZn37

λ_L in GPa	μ_L in GPa	ρ in kg/m^3	$\frac{\partial E}{\partial T}$ in GPa/K
87.2	41.0	8440	-0.05

Source: [188].

Aluminum EN AW-5754

λ_L in GPa	μ_L in GPa	ρ in kg/m^3	$\frac{\partial E}{\partial T}$ in GPa/K
51.4	26.5	2680	-

Poly(methyl methacrylate) – PMMA

λ_L in GPa	μ_L in GPa	ρ in kg/m^3	$\frac{\partial E}{\partial T}$ in GPa/K
4.22	2.34	1190	-

Source: Comsol material data.

Calcite

λ_L in GPa	μ_L in GPa	ρ in kg/m ³	$\frac{\partial E}{\partial T}$ in GPa/K
106.2	35	2710	-

Source: [189].

Copper EN-DLP

λ_L in GPa	μ_L in GPa	ρ in kg/m ³	$\frac{\partial E}{\partial T}$ in GPa/K
104.7	49.3	8940	-

Source: www.wieland.com.

Steel X6CrNiMoTi17-12-2

λ_L in GPa	μ_L in GPa	ρ in kg/m ³	$\frac{\partial E}{\partial T}$ in GPa/K
115.6	79.0	7900	-0.075 [190], -0.0787 [185]

Source: [185, 190].

Water

Speed of sound in m/s (temperature-dependent):

$$\begin{aligned}
 c_f(T) = & 1.402\,387\,44 \cdot 10^3 + 5.038\,361\,71 T - 5.811\,729\,16 \cdot 10^{-2} T^2 + \\
 & + 3.346\,381\,17 \cdot 10^{-4} T^3 - 1.482\,596\,72 \cdot 10^{-6} T^4 \\
 & + 3.165\,850\,20 \cdot 10^{-9} T^5,
 \end{aligned} \tag{A.2}$$

Speed of sound at room temperature: $c_f(20^\circ\text{C}) = 1482$ m/s,

Density: $\rho = 1000$ kg/m³.

Source: [182, 183].

Glycerol

Speed of sound: $c_f = 1920$ m/s,

Density: $\rho = 1260$ kg/m³.

Bibliography

References

- [1] S. J. Rupitsch. *Piezoelectric Sensors and Actuators - Fundamentals and Applications*. Topics in Mining, Metallurgy and Materials Engineering. Springer, Aug. 2018.
- [2] O. Fiedler. *Strömungs- und Durchflussmesstechnik*. Oldenbourg Industrieverlag, 1992.
- [3] J. Gätke. *Akustische Strömungs- und Durchflussmessung*. Wiley-VCH Verlag, Jan. 1991.
- [4] M. A. Linnert. “Energieeffiziente Felderzeugung für die magnetisch-induktive Durchflussmessung”. Dissertation. Erlangen: University of Erlangen-Nürnberg, Mar. 2020.
- [5] *Flow Meter Market Size, Share Analysis with Industry Forecast to 2026*. URL: <https://www.alliedmarketresearch.com/flow-meter-market> (visited on 05/14/2021).
- [6] *Ultrasonic Flow Meter Market Trends to Watch Through 2024*. URL: <https://www.marketsandmarkets.com/Market-Reports/ultrasonic-flow-meter-market-168677264.html> (visited on 05/14/2021).
- [7] J. McGlade et al. *Measuring water use in a green economy, A Report of the Working Group on Water Efficiency to the International Resource Panel*. United Nations Environment Programme (UNEP), 2012.
- [8] S. Tanverakul and J. Lee. “Impacts of Metering on Residential Water Use in California”. In: *Journal - American Water Works Association* 107 (Feb. 2015). DOI: 10.5942/jawwa.2015.107.0005.
- [9] *Water conservation report 2018*. Department of Environment, Food and Rural Affairs, 2018.
- [10] C. Maaß, J. Zedelius, and B. Uhlmann. *Wasser sinnvoll zählen – und weniger zahlen*. Hamburg: Hamburg Institut, May 2017.
- [11] W. C. Wong, H. T. Ng, R. Chan, B. Evain, and H. Ang. “Going real time in water conservation – the Singapore experience”. In: *Water Practice and Technology* 14.1 (Dec. 2018). DOI: 10.2166/wpt.2018.117.

- [12] *Use of freshwater resources in Europe*. European Environment Agency. Dec. 2019. URL: <https://www.eea.europa.eu/data-and-maps/indicators/use-of-freshwater-resources-3/assessment-4> (visited on 05/15/2021).
- [13] A. D. Pierce. *Acoustics: An Introduction to its Physical Principles and Applications*. 3rd ed. Acoustical Society of America, 1994.
- [14] J. Massaad Mouawad. “High-precision Versatile Ultrasonic Flow Meters Based on Matrix Transducer Arrays”. Dissertation. Delft: Delft University of Technology, 2021. DOI: 10.4233/UUID:E930DACE-0655-4B4C-9B4B-F5D846414FE7.
- [15] P. Ploß. “Untersuchung von Clamp-on-Ultraschalldurchflussmessgeräten im k-Raum”. Dissertation. Erlangen: University of Erlangen-Nürnberg, 2016.
- [16] K. Conrad and L. Lynnworth. “Fundamentals of ultrasonic flow meters”. In: *American School of Gas Measurement Technology* 1 (2002).
- [17] L. C. Lynnworth and Y. Liu. “Ultrasonic flowmeters: Half-century progress report, 1955–2005”. In: *Ultrasonics* 44 (Dec. 2006). DOI: 10.1016/j.ultras.2006.05.046.
- [18] O. Keitmann-Curdes and B. Funck. “A new calibration method for ultrasonic clamp-on transducers”. In: *2008 IEEE Ultrasonics Symposium*. Nov. 2008. DOI: 10.1109/ULTSYM.2008.0125.
- [19] M. Mayle and P. Ploss. “Ultraschallzähler und Verfahren zur Erfassung einer Durchflussgröße”. German pat. 102017004038A1. Diehl Metering GmbH. Aug. 2018.
- [20] M. Mayle and P. Ploss. “Ultrasonic meter and method for sensing a flow variable”. U.S. pat. 10989578B2. Diehl Metering GmbH. Apr. 2021.
- [21] *MSP430FR6047 Ultrasonic Sensing MSP430™ Microcontrollers for Water-Metering Applications*. Texas Instruments. Sept. 2017.
- [22] *HYDRUS 1.3 - Ultrasonic Meter Datasheet*. Diehl Metering. Mar. 2021.
- [23] X. Gu and F. Cegla. “Modeling Surface Roughness-Related Uncertainties of Leaky Lamb Wave Clamp-on Ultrasonic Flowmeters”. In: *IEEE Transactions on Instrumentation and Measurement* 69.9 (Sept. 2020). DOI: 10.1109/TIM.2020.2975389.
- [24] M. Bächle, D. A. Schwär, and F. Puente León. “Analytic wavelet packets for robust ultrasonic flow measurement”. In: *tm - Technisches Messen* 87.1 (Jan. 2020). DOI: 10.1515/teme-2019-0093.

- [25] J. Massaad, P. L. M. J. van Neer, D. M. van Willigen, M. A. P. Pertijs, N. de Jong, and M. D. Verweij. “Suppression of Lamb wave excitation via aperture control of a transducer array for ultrasonic clamp-on flow metering”. In: *The Journal of the Acoustical Society of America* 147.4 (Apr. 2020). DOI: 10.1121/10.0001135.
- [26] R. A. Kippersund, K. E. Frøysa, and P. Lunde. “Flow measuring apparatus”. U.S. pat. 8141434B2. TeCom AS. Mar. 2012.
- [27] B. Koenig, Y. Hoog, C. Gittinger, and Y. Fuchs. “Device for determining properties of a medium”. U.S. pat. 9581572B2. Bürkert Werke GmbH and Co KG. Feb. 2017.
- [28] R. Ladwa. “ROSEN EMAT flowmeter”. Presentation. Aberdeen, Sept. 2015.
- [29] *FLOWave SAW flowmeter Datasheet*. Christian Bürkert GmbH & Co. KG. Apr. 2021.
- [30] Z. Fan, W. Jiang, and W. M. D. Wright. “Non-contact ultrasonic gas flow metering using air-coupled leaky Lamb waves”. In: *Ultrasonics* 89 (Sept. 2018). DOI: 10.1016/j.ultras.2018.04.008.
- [31] M. Aanes, R. A. Kippersund, K. D. Lohne, K.-E. Frøysa, and P. Lunde. “Time-of-flight dependency on transducer separation distance in a reflective-path guided-wave ultrasonic flow meter at zero flow conditions”. In: *The Journal of the Acoustical Society of America* 142.2 (Aug. 2017). DOI: 10.1121/1.4996851.
- [32] P. Ploß, M. Mayle, and A. Benkert. “Ultrasonic flow measuring device with a rectangular cross-section passage having recesses in two side-walls other than the sidewalls in which the transducers are located”. U.S. pat. 10746578B2. Diehl Metering GmbH. Aug. 2020.
- [33] J. L. Rose. *Ultrasonic Guided Waves in Solid Media*. Cambridge University Press, Aug. 2014.
- [34] P. Ploss and M. Mayle. “Method and measuring device for determining measurement information”. U.S. pat. 10852171B2. Diehl Metering GmbH. Dec. 2020.
- [35] K.-J. Langenberg, R. Marklein, and K. Mayer. *Theoretische Grundlagen der zerstörungsfreien Materialprüfung mit Ultraschall*. De Gruyter Oldenbourg, 2009.
- [36] K.-J. Langenberg, R. Marklein, and K. Mayer. *Ultrasonic Nondestructive Testing of Materials: Theoretical Foundations*. CRC Press, Feb. 2012. DOI: 10.1201/b11724.

- [37] B. A. Auld. *Acoustic Fields and Waves in Solids*. 2nd ed. Vol. 1. Krieger Publishing Company, 1990.
- [38] J. D. Achenbach. *Wave Propagation in Elastic Solids*. North Holland, Nov. 1987.
- [39] D. T. Blackstock. *Fundamentals of Physical Acoustics*. John Wiley & Sons, Apr. 2000.
- [40] M. A. Biot. “General Theorems on the Equivalence of Group Velocity and Energy Transport”. In: *Physical Review* 105.4 (Feb. 1957). DOI: 10.1103/PhysRev.105.1129.
- [41] B. A. Auld. *Acoustic Fields and Waves in Solids*. 2nd ed. Vol. 2. Krieger Publishing Company, 1990.
- [42] N. F. Declercq, R. Briers, J. Degrieck, and O. Leroy. “The history and properties of ultrasonic inhomogeneous waves”. In: *IEEE Transactions on Ultrasonics, Ferroelectrics, and Frequency Control* 52.5 (May 2005). DOI: 10.1109/TUFFC.2005.1503963.
- [43] V. G. Mozhaev and M. Weihnacht. “Subsonic leaky Rayleigh waves at liquid–solid interfaces”. In: *Ultrasonics* 40.1 (May 2002). DOI: 10.1016/S0041-624X(02)00233-0.
- [44] A. Bernard, M. J. S. Lowe, and M. Deschamps. “Guided waves energy velocity in absorbing and non-absorbing plates”. In: *The Journal of the Acoustical Society of America* 110.1 (July 2001). DOI: 10.1121/1.1375845.
- [45] K. J. Langenberg, R. Marklein, and K. Mayer. “Energy vs. group velocity for elastic waves in homogeneous anisotropic solid media”. In: *2010 URSI International Symposium on Electromagnetic Theory*. Berlin, Germany: IEEE, Aug. 2010. DOI: 10.1109/URSI-EMTS.2010.5637253.
- [46] N. Marcuvitz. “On field representations in terms of leaky modes or eigenmodes”. In: *IRE Transactions on Antennas and Propagation* 4.3 (July 1956). DOI: 10.1109/TAP.1956.1144410.
- [47] F. Hernando Quintanilla, M. J. S. Lowe, and R. V. Craster. “Full 3D dispersion curve solutions for guided waves in generally anisotropic media”. In: *Journal of Sound and Vibration* 363 (Feb. 2016). DOI: 10.1016/j.jsv.2015.10.017.
- [48] V. Pagneux and A. Maurel. “Determination of Lamb mode eigenvalues”. In: *The Journal of the Acoustical Society of America* 110.3 (Aug. 2001). DOI: 10.1121/1.1391248.

- [49] A. Bonnet-Ben Dhia, G. Dakhia, C. Hazard, and L. Chorfi. “Diffraction by a Defect in an Open Waveguide: A Mathematical Analysis Based on a Modal Radiation Condition”. In: *SIAM Journal on Applied Mathematics* 70.3 (Jan. 2009). DOI: 10.1137/080740155.
- [50] V. Maupin. “The radiation modes of a vertically varying half-space: a new representation of the complete Green’s function in terms of modes”. In: *Geophysical Journal International* 126.3 (Sept. 1996). DOI: 10.1111/j.1365-246X.1996.tb04701.x.
- [51] L. Margerin. “Generalized eigenfunctions of layered elastic media and application to diffuse fields”. In: *The Journal of the Acoustical Society of America* 125.1 (Jan. 2009). DOI: 10.1121/1.3021312.
- [52] J. Hu and C. R. Menyuk. “Understanding leaky modes: slab waveguide revisited”. In: *Advances in Optics and Photonics* 1.1 (Jan. 2009). DOI: 10.1364/AOP.1.000058.
- [53] E. Ayryan, D. Divakov, A. Egorov, K. Lovetskiy, and L. Sevastianov. “Modelling Leaky Waves in Planar Dielectric Waveguides”. In: *EPJ Web of Conferences* 226 (2020). DOI: 10.1051/epjconf/202022602003.
- [54] P. T. Leung, S. S. Tong, and K. Young. “Two-component eigenfunction expansion for open systems described by the wave equation I: completeness of expansion”. In: *Journal of Physics A: Mathematical and General* 30.6 (Mar. 1997). DOI: 10.1088/0305-4470/30/6/034.
- [55] H.-P. Nollert. “Quasinormal modes: the characteristic sound of black holes and neutron stars”. In: *Classical and Quantum Gravity* 16.12 (Nov. 1999). DOI: 10.1088/0264-9381/16/12/201.
- [56] R. Courant and D. Hilbert. *Methods of Mathematical Physics*. Wiley, Apr. 1989. DOI: 10.1002/9783527617210.
- [57] D. P. Stowell and J. Tausch. “Variational Formulation for Guided and Leaky Modes in Multilayer Dielectric Waveguides”. In: *Communications in Computational Physics* 7 (July 2010). DOI: 10.4208/CICP.2009.09.043.
- [58] B. Dubuc, A. Ebrahimkhanlou, and S. Salamone. “Computation of propagating and non-propagating guided modes in nonuniformly stressed plates using spectral methods”. In: *The Journal of the Acoustical Society of America* 143.6 (June 2018). DOI: 10.1121/1.5040140.
- [59] I. A. Viktorov. *Rayleigh and Lamb Waves: Physical Theory and Applications*. Red. by L. Balamuth. 2nd ed. Plenum Press, 1970.

- [60] F. Simonetti and M. J. S. Lowe. “On the meaning of Lamb mode non-propagating branches”. In: *The Journal of the Acoustical Society of America* 118.1 (June 2005). DOI: 10.1121/1.1938528.
- [61] C. Grünsteidl, T. Berer, M. Hettich, and I. Veres. “Determination of thickness and bulk sound velocities of isotropic plates using zero-group-velocity Lamb waves”. In: *Applied Physics Letters* 112.25 (June 2018). DOI: 10.1063/1.5034313.
- [62] F. Hernando Quintanilla, M. J. S. Lowe, and R. V. Craster. “The symmetry and coupling properties of solutions in general anisotropic multilayer waveguides”. In: *The Journal of the Acoustical Society of America* 141.1 (Jan. 2017). DOI: 10.1121/1.4973543.
- [63] M. Manav, G. Reynen, M. Sharma, E. Cretu, and A. S. Phani. “Ultra-sensitive resonant MEMS transducers with tuneable coupling”. In: *Journal of Micromechanics and Microengineering* 24.5 (May 2014). DOI: 10.1088/0960-1317/24/5/055005.
- [64] H. Überall, B. Hosten, M. Deschamps, and A. Gérard. “Repulsion of phase-velocity dispersion curves and the nature of plate vibrations”. In: *The Journal of the Acoustical Society of America* 96.2 (Aug. 1994). DOI: 10.1121/1.411434.
- [65] H. Lamb. “On waves in an elastic plate”. In: *Proceedings of the Royal Society A* 93.648 (Mar. 1917). DOI: 10.1098/rspa.1917.0008.
- [66] F. B. Cegla, P. Cawley, and M. J. S. Lowe. “Material property measurement using the quasi-Scholte mode—A waveguide sensor”. In: *The Journal of the Acoustical Society of America* 117.3 (Mar. 2005). DOI: 10.1121/1.1841631.
- [67] E. V. Glushkov, N. V. Glushkova, and O. A. Miakisheva. “Backward waves and energy fluxes excited in acoustic medium with an immersed plate”. In: *Ultrasonics* 94 (Apr. 2019). DOI: 10.1016/j.ultras.2018.10.001.
- [68] C. Prada, D. Clorennec, and D. Royer. “Local vibration of an elastic plate and zero-group velocity Lamb modes”. In: *The Journal of the Acoustical Society of America* 124.1 (July 2008). DOI: 10.1121/1.2918543.
- [69] F. Legrand, B. Gérardin, J. Laurent, C. Prada, and A. Aubry. “Negative refraction of Lamb modes: A theoretical study”. In: *Physical Review B* 98.21 (Dec. 2018). DOI: 10.1103/PhysRevB.98.214114.
- [70] G. S. Kino. *Acoustic Waves: Devices, Imaging, and Analog Signal Processing*. Prentice Hall, Jan. 1987.

- [71] W. B. Fraser. “Orthogonality relation for the Rayleigh–Lamb modes of vibration of a plate”. In: *The Journal of the Acoustical Society of America* 59.1 (Jan. 1976). DOI: 10.1121/1.380851.
- [72] J. E. Murphy, G. Li, and S. A. Chin-Bing. “Orthogonality relation for Rayleigh–Lamb modes of vibration of an arbitrarily layered elastic plate with and without fluid loading”. In: *The Journal of the Acoustical Society of America* 96.4 (Oct. 1994). DOI: 10.1121/1.410103.
- [73] J. L. Rose. *Ultrasonic Waves in Solid Media*. Cambridge University Press, Sept. 2004.
- [74] J.-L. Akian. “A proof of the completeness of Lamb modes”. preprint. Apr. 2021. DOI: 10.22541/au.161771284.45509849/v1.
- [75] M. Gallezot, F. Treysède, and L. Laguerre. “Contribution of leaky modes in the modal analysis of unbounded problems with perfectly matched layers”. In: *The Journal of the Acoustical Society of America* 141.1 (Jan. 2017). DOI: 10.1121/1.4973313.
- [76] E. S. C. Ching, P. T. Leung, A. Maassen van den Brink, W. M. Suen, S. S. Tong, and K. Young. “Quasinormal-mode expansion for waves in open systems”. In: *Reviews of Modern Physics* 70.4 (Oct. 1998). DOI: 10.1103/RevModPhys.70.1545.
- [77] P. T. Leung, S. Y. Liu, and K. Young. “Completeness and orthogonality of quasinormal modes in leaky optical cavities”. In: *Physical Review A* 49.4 (Apr. 1994). DOI: 10.1103/PhysRevA.49.3057.
- [78] P. T. Leung, W. M. Suen, C. P. Sun, and K. Young. “Waves in open systems via a biorthogonal basis”. In: *Physical Review E* 57.5 (May 1998). DOI: 10.1103/PhysRevE.57.6101.
- [79] P. T. Kristensen, K. Herrmann, F. Intravaia, K. Busch, and K. Busch. “Modeling electromagnetic resonators using quasinormal modes”. In: *Advances in Optics and Photonics* 12.3 (Sept. 2020). DOI: 10.1364/AOP.377940.
- [80] P. T. Leung, S. S. Tong, and K. Young. “Two-component eigenfunction expansion for open systems described by the wave equation II: linear space structure”. In: *Journal of Physics A: Mathematical and General* 30.6 (Mar. 1997). DOI: 10.1088/0305-4470/30/6/035.
- [81] S. H. Schot. “Eighty years of Sommerfeld’s radiation condition”. In: *Historia Mathematica* 19.4 (Nov. 1992). DOI: 10.1016/0315-0860(92)90004-U.

- [82] G. Ciruolo and R. Magnanini. “A radiation condition for uniqueness in a wave propagation problem for 2-D open waveguides”. In: *Mathematical Methods in the Applied Sciences* 32.10 (2009). DOI: 10.1002/mma.1084.
- [83] F. Treyssède, K. L. Nguyen, A. .-. Bonnet-BenDhia, and C. Hazard. “Finite element computation of trapped and leaky elastic waves in open stratified waveguides”. In: *Wave Motion* 51.7 (Nov. 2014). DOI: 10.1016/j.wavemoti.2014.05.003.
- [84] M. Gallezot, F. Treyssède, and L. Laguerre. “A modal approach based on perfectly matched layers for the forced response of elastic open waveguides”. In: *Journal of Computational Physics* 356 (Mar. 2018). DOI: 10.1016/j.jcp.2017.12.017.
- [85] F. Hernando Quintanilla. “Pseudospectral collocation method for viscoelastic guided wave problems in generally anisotropic media”. PhD Thesis. London: Imperial College London, Feb. 2016.
- [86] P. Zuo and Z. Fan. “SAFE-PML approach for modal study of waveguides with arbitrary cross sections immersed in inviscid fluid”. In: *Journal of Sound and Vibration* 406 (Oct. 2017). DOI: 10.1016/j.jsv.2017.06.001.
- [87] K. L. Nguyen, F. Treyssède, and C. Hazard. “Numerical modeling of three-dimensional open elastic waveguides combining semi-analytical finite element and perfectly matched layer methods”. In: *Journal of Sound and Vibration* 344 (May 2015). DOI: 10.1016/j.jsv.2014.12.032.
- [88] V. Mehrmann and H. Voss. “Nonlinear eigenvalue problems: a challenge for modern eigenvalue methods”. In: *GAMM-Mitteilungen* 27.2 (Dec. 2004). DOI: 10.1002/gamm.201490007.
- [89] V. Hernandez, J. E. Roman, and V. Vidal. “SLEPc: A Scalable and Flexible Toolkit for the Solution of Eigenvalue Problems”. In: *ACM Trans. Math. Softw.* 31.3 (Sept. 2005). DOI: 10.1145/1089014.1089019.
- [90] H. Gravenkamp, C. Birk, and C. Song. “Numerical modeling of elastic waveguides coupled to infinite fluid media using exact boundary conditions”. In: *Computers & Structures* 141 (Aug. 2014). DOI: 10.1016/j.compstruc.2014.05.010.
- [91] M. Mazzotti, I. Bartoli, A. Marzani, and E. Viola. “A coupled SAFE-2.5D BEM approach for the dispersion analysis of damped leaky guided waves in embedded waveguides of arbitrary cross-section”. In: *Ultrasonics* 53.7 (Sept. 2013). DOI: 10.1016/j.ultras.2013.03.003.
- [92] A. Hood. “Localizing the eigenvalues of matrix-valued functions: analysis and applications”. PhD Thesis. Ithaca: Cornell University, Jan. 2017.

- [93] V. Mehrmann and D. Watkins. “Polynomial eigenvalue problems with Hamiltonian structure”. In: *Electronic Transactions on Numerical Analysis* 13 (2002).
- [94] D. Mackey, N. Mackey, C. Mehl, and V. Mehrmann. “Structured Polynomial Eigenvalue Problems: Good Vibrations from Good Linearizations”. In: *SIAM Journal on Matrix Analysis and Applications* 28.4 (Jan. 2006). DOI: 10.1137/050628362.
- [95] A. Freedman. “Effects of fluid-loading on Lamb mode spectra”. In: *The Journal of the Acoustical Society of America* 99.6 (June 1996). DOI: 10.1121/1.414948.
- [96] A. L. Shuvalov, O. Poncelet, and M. Deschamps. “Analysis of the dispersion spectrum of fluid-loaded anisotropic plates: flexural-type branches and real-valued loops”. In: *Journal of Sound and Vibration* 290.3 (Mar. 2006). DOI: 10.1016/j.jsv.2005.05.015.
- [97] X. L. Bao, H. Franklin, P. K. Raju, and H. Überall. “The splitting of dispersion curves for plates fluid-loaded on both sides”. In: *The Journal of the Acoustical Society of America* 102.2 (Aug. 1997). DOI: 10.1121/1.419939.
- [98] K. Rostyne Van de, C. Glorieux, W. Gao, W. Lauriks, and J. Thoen. “Experimental investigation of leaky Lamb modes by an optically induced grating”. In: *IEEE Transactions on Ultrasonics, Ferroelectrics, and Frequency Control* 49.9 (Sept. 2002). DOI: 10.1109/TUFFC.2002.1041541.
- [99] M. Mazzotti, I. Bartoli, and A. Marzani. “Ultrasonic leaky guided waves in fluid-coupled generic waveguides: hybrid finite-boundary element dispersion analysis and experimental validation”. In: *Journal of Applied Physics* 115.14 (Apr. 2014). DOI: 10.1063/1.4870857.
- [100] I. A. Nedospasov, V. G. Mozhaev, and I. E. Kuznetsova. “Unusual energy properties of leaky backward Lamb waves in a submerged plate”. In: *Ultrasonics* 77 (May 2017). DOI: 10.1016/j.ultras.2017.01.025.
- [101] O. A. Sapozhnikov, A. A. Karabutov Jr., and V. G. Mozhaev. “Experimental Evidence for a Growing Surface Wave and Acoustic Beam Narrowing upon Reflection from Fluid-Solid Interfaces”. In: *2007 IEEE Ultrasonics Symposium Proceedings*. Oct. 2007. DOI: 10.1109/ULTSYM.2007.107.
- [102] S. I. Rokhlin, D. E. Chimenti, and A. H. Nayfeh. “On the topology of the complex wave spectrum in a fluid-coupled elastic layer”. In: *The Journal of the Acoustical Society of America* 85.3 (Mar. 1989). DOI: 10.1121/1.397490.

- [103] A. Freedman. “Anomalies of the Ao leaky lamb mode of a fluid-loaded, elastic plate”. In: *Journal of Sound and Vibration* 183.4 (June 1995). DOI: 10.1006/jsvi.1995.0282.
- [104] J. Dickey, G. Maidanik, and H. Überall. “The splitting of dispersion curves for the fluid-loaded plate”. In: *The Journal of the Acoustical Society of America* 98.4 (Oct. 1995). DOI: 10.1121/1.413283.
- [105] B. N. Pavlakovic. “Leaky guided ultrasonic waves in NDT.” PhD Thesis. London: Imperial College London, Jan. 1999.
- [106] J.-P. Sessarego, J. Sagéoli, C. Gazanhes, and H. Überall. “Two Scholte–Stoneley waves on doubly fluid-loaded plates and shells”. In: *The Journal of the Acoustical Society of America* 101.1 (Jan. 1997). DOI: 10.1121/1.418014.
- [107] P. Guo, B. Deng, X. Lan, K. Zhang, H. Li, Z. Tian, and H. Xu. “Water Level Sensing in a Steel Vessel Using Ao and Quasi-Scholte Waves”. In: *Journal of Sensors* (Dec. 2017). DOI: <https://doi.org/10.1155/2017/2596291>.
- [108] T. Tamir and A. Oliner. “Guided complex waves. Part 1: Fields at an interface”. In: *Proceedings of the Institution of Electrical Engineers* 110.2 (Feb. 1963). DOI: 10.1049/piee.1963.0044.
- [109] J. Rautenberg, S. Olfert, F. Bause, and B. Henning. “Validation of analytically modeled Leaky Lamb radiation using Schlieren photography”. In: *2012 IEEE International Ultrasonics Symposium*. Oct. 2012. DOI: 10.1109/ULTSYM.2012.0204.
- [110] X. Jia. “Modal analysis of Lamb wave generation in elastic plates by liquid wedge transducers”. In: *The Journal of the Acoustical Society of America* 101.2 (Feb. 1997). DOI: 10.1121/1.418041.
- [111] M. O. Deighton, A. B. Gillespie, R. B. Pike, and R. D. Watkins. “Mode conversion of Rayleigh and Lamb waves to compression waves at a metal-liquid interface”. In: *Ultrasonics* 19.6 (Nov. 1981). DOI: 10.1016/0041-624X(81)90014-7.
- [112] H. Dabirikhah and C. W. Turner. “Anomalous behaviour of flexural waves in very thin immersed plates”. In: *IEEE 1992 Ultrasonics Symposium Proceedings*. Oct. 1992. DOI: 10.1109/ULTSYM.1992.275989.
- [113] H. Dabirikhah and C. W. Turner. “The coupling of the Ao and interface Scholte modes in fluid-loaded plates”. In: *The Journal of the Acoustical Society of America* 100.5 (Nov. 1996). DOI: 10.1121/1.416985.

- [114] R. D. Watkins, W. H. B. Cooper, A. B. Gillespie, and R. B. Pike. "The attenuation of Lamb waves in the presence of a fluid". In: *Ultrasonics* 20.6 (Nov. 1982). DOI: 10.1016/0041-624X(82)90046-4.
- [115] E. M. Viggen and H. K. Arnestad. "Understanding sound radiation from surface vibrations moving at subsonic speeds". In: *Proceedings of the 44th Scandinavian Symposium on Physical Acoustics*. Feb. 2021.
- [116] A. Schoch. "Der Schalldurchgang durch Platten". In: *Acta Acustica united with Acustica* 2.1 (Jan. 1952).
- [117] B. Pavlakovic, M. J. S. Lowe, D. Alleyne, and P. Cawley. "Disperse: A General Purpose Program for Creating Dispersion Curves". In: *Review of Progress in Quantitative Nondestructive Evaluation*. Ed. by D. O. Thompson and D. E. Chimenti. Vol. 16. Springer, 1997. DOI: 10.1007/978-1-4615-5947-4_24.
- [118] M. J. S. Lowe. "Matrix techniques for modeling ultrasonic waves in multilayered media". In: *IEEE Transactions on Ultrasonics, Ferroelectrics, and Frequency Control* 42.4 (July 1995). DOI: 10.1109/58.393096.
- [119] M. F. M. Osborne and S. D. Hart. "Transmission, Reflection, and Guiding of an Exponential Pulse by a Steel Plate in Water. I. Theory". In: *The Journal of the Acoustical Society of America* 17.1 (July 1945). DOI: 10.1121/1.1916293.
- [120] A. Grabowska. "Propagation of elastic wave in solid layer-liquid system". In: *Archives of Acoustics* 4.1 (1979).
- [121] A. T. I. Adamou and R. V. Craster. "Spectral methods for modelling guided waves in elastic media". In: *The Journal of the Acoustical Society of America* 116.3 (Sept. 2004). DOI: 10.1121/1.1777871.
- [122] C. Hakoda, C. Lissenden, and J. Rose. "Weak form implementation of the semi-analytical finite element (SAFE) method for a variety of elastodynamic waveguides". In: *AIP Conference Proceedings*. American Institute of Physics, 2018. DOI: 10.1063/1.5031648.
- [123] T. Hayashi and D. Inoue. "Calculation of leaky Lamb waves with a semi-analytical finite element method". In: *Ultrasonics* 54.6 (Aug. 2014). DOI: 10.1016/j.ultras.2014.04.021.
- [124] M. Mazzotti, A. Marzani, I. Bartoli, and E. Viola. "Guided waves dispersion analysis for prestressed viscoelastic waveguides by means of the SAFE method". In: *International Journal of Solids and Structures* 49.18 (Sept. 2012). DOI: 10.1016/j.ijsolstr.2012.04.041.

- [125] L. Gavrić. “Finite Element Computation of Dispersion Properties of Thin-Walled Waveguides”. In: *Journal of Sound and Vibration* 173.1 (May 1994). DOI: 10.1006/jsvi.1994.1221.
- [126] L. Gavrić. “Computation of propagative waves in free rail using a finite element technique”. In: *Journal of Sound and Vibration* 185.3 (Aug. 1995). DOI: 10.1006/jsvi.1995.0398.
- [127] F. Hernando Quintanilla, M. J. S. Lowe, and R. V. Craster. “Modeling guided elastic waves in generally anisotropic media using a spectral collocation method”. In: *The Journal of the Acoustical Society of America* 137.3 (Mar. 2015). DOI: 10.1121/1.4913777.
- [128] J. E. Lefebvre, V. Zhang, J. Gazalet, and T. Gryba. “Legendre polynomial approach for modeling free-ultrasonic waves in multilayered plates”. In: *Journal of Applied Physics* 85.7 (Mar. 1999). DOI: 10.1063/1.369699.
- [129] J. E. Lefebvre, V. Zhang, J. Gazalet, and T. Gryba. “Conceptual advantages and limitations of the Laguerre polynomial approach to analyze surface acoustic waves in semi-infinite substrates and multilayered structures”. In: *Journal of Applied Physics* 83.1 (Jan. 1998). DOI: 10.1063/1.366697.
- [130] P. Packo, T. Uhl, and W. J. Staszewski. “Generalized semi-analytical finite difference method for dispersion curves calculation and numerical dispersion analysis for Lamb waves”. In: *The Journal of the Acoustical Society of America* 136.3 (Sept. 2014). DOI: 10.1121/1.4892778.
- [131] S.-E. Hebaz, F. Benmeddour, E. Moulin, and J. Assaad. “Semi-analytical discontinuous Galerkin finite element method for the calculation of dispersion properties of guided waves in plates”. In: *The Journal of the Acoustical Society of America* 143.1 (Jan. 2018). DOI: 10.1121/1.5021588.
- [132] H. Gravenkamp, F. Bause, and C. Song. “On the computation of dispersion curves for axisymmetric elastic waveguides using the Scaled Boundary Finite Element Method”. In: *Computers & Structures* 131 (Jan. 2014). DOI: 10.1016/j.compstruc.2013.10.014.
- [133] H. Gravenkamp, J. Prager, A. A. Saputra, and C. Song. “The simulation of Lamb waves in a cracked plate using the scaled boundary finite element method”. In: *The Journal of the Acoustical Society of America* 132.3 (Sept. 2012). DOI: 10.1121/1.4740478.
- [134] B. Fornberg. *A Practical Guide to Pseudospectral Methods*. Cambridge Monographs on Applied and Computational Mathematics. Cambridge University Press, 1996. DOI: 10.1017/CBO9780511626357.

- [135] L. N. Trefethen. *Spectral Methods in MATLAB*. Society for Industrial and Applied Mathematics, July 2000. DOI: 10.1137/1.9780898719598.
- [136] J. A. Weideman and S. C. Reddy. “A MATLAB Differentiation Matrix Suite”. In: *ACM Trans. Math. Softw.* 26.4 (Dec. 2000). DOI: 10.1145/365723.365727.
- [137] L. N. Trefethen and D. Bau III. *Numerical Linear Algebra*. Society for Industrial and Applied Mathematics, June 1997.
- [138] G. von Winckel. *Fast Clenshaw-Curtis Quadrature*. MATLAB Central File Exchange. 2005. URL: <https://www.mathworks.com/matlabcentral/fileexchange/6911-fast-clenshaw-curtis-quadrature>.
- [139] M. Berhanu. “The Polynomial Eigenvalue Problem”. PhD Thesis. Manchester: University of Manchester, Aug. 2005.
- [140] T. Betcke, N. J. Higham, V. Mehrmann, C. Schröder, and F. Tisseur. “NLEVP: A Collection of Nonlinear Eigenvalue Problems”. In: *ACM Trans. Math. Softw.* 39.2 (Feb. 2013). DOI: 10.1145/2427023.2427024.
- [141] H. Fassbender and D. Kressner. “Structured Eigenvalue Problems”. In: *GAMM-Mitteilungen* 29.2 (Oct. 2006). DOI: 10.1002/gamm.201490035.
- [142] M. Ponschab. “Ultraschallbasiertes Sensorprinzip für die eingriffsfreie Messung hydrostatischen Drucks (Ultrasonic sensing principle for the measurement of hydrostatic pressure)”. Doctoral dissertation, unpublished. University of Erlangen-Nürnberg, Erlangen, 2021.
- [143] V. M. Ristic. *Principles of Acoustic Devices*. John Wiley & Sons, 1983.
- [144] L. Cremer and M. Heckl. *Körperschall: Physikalische Grundlagen und technische Anwendungen*. Ed. by M. Möser and W. Kropp. 3rd ed. Springer, 2009.
- [145] O. Balogun, T. W. Murray, and C. Prada. “Simulation and measurement of the optical excitation of the S_1 zero group velocity Lamb wave resonance in plates”. In: *Journal of Applied Physics* 102.6 (Sept. 2007). DOI: 10.1063/1.2784031.
- [146] P. D. Wilcox, M. J. S. Lowe, and P. Cawley. “Mode and Transducer Selection for Long Range Lamb Wave Inspection”. In: *Journal of Intelligent Material Systems and Structures* 12.8 (Aug. 2001). DOI: 10.1177/10453890122145348.
- [147] F. L. Degertekin, B. V. Honein, and B. T. Khuri-Yakub. “Efficient excitation and detection of Lamb waves for process monitoring and NDE”. In: *1995 IEEE Ultrasonics Symposium*. Nov. 1995. DOI: 10.1109/ULTSYM.1995.495684.

- [148] V. Giurgiutiu. “Tuned Lamb Wave Excitation and Detection with Piezoelectric Wafer Active Sensors for Structural Health Monitoring”. In: *Journal of Intelligent Material Systems and Structures* 16.4 (Apr. 2005). DOI: 10.1177/1045389X05050106.
- [149] F. Lanza di Scalea, H. Matt, and I. Bartoli. “The response of rectangular piezoelectric sensors to Rayleigh and Lamb ultrasonic waves”. In: *The Journal of the Acoustical Society of America* 121.1 (Jan. 2007). DOI: 10.1121/1.2400668.
- [150] S. P. Pelts, D. Jiao, and J. L. Rose. “A comb transducer for guided wave generation and mode selection”. In: *1996 IEEE Ultrasonics Symposium*. Nov. 1996. DOI: 10.1109/ULTSYM.1996.584128.
- [151] J. L. Rose, S. P. Pelts, and M. J. Quarry. “A comb transducer model for guided wave NDE”. In: *Ultrasonics* 36.1 (Feb. 1998). DOI: 10.1016/S0041-624X(97)00042-5.
- [152] S.-C. Wooh and Y. Shi. “Synthetic phase tuning of guided waves”. In: *IEEE Transactions on Ultrasonics, Ferroelectrics, and Frequency Control* 48.1 (Jan. 2001). DOI: 10.1109/58.896134.
- [153] Y. Shi. “Analysis of optimum Lamb wave tuning”. PhD Thesis. Massachusetts Institute of Technology, 2002.
- [154] *Polytec Scanning Vibrometer PSV-500-3D - Operating Instructions*. Polytec. 2016.
- [155] P. Hora and O. Červená. “Determination of Lamb wave dispersion curves by means of Fourier transform”. In: *Applied and Computational Mechanics* 6 (2012).
- [156] D. Alleyne and P. Cawley. “A two-dimensional Fourier transform method for the measurement of propagating multimode signals”. In: *The Journal of the Acoustical Society of America* 89.3 (Mar. 1991). DOI: 10.1121/1.400530.
- [157] S. Johannesmann, L. Claes, M. Webersen, and B. Henning. “Inverser Ansatz zur akustischen Charakterisierung plattenförmiger Materialproben”. In: *Fortschritte der Akustik - DAGA 2017*. Ed. by G. Schmidt, B. Nolte, and U. Heute. Kiel: Deutsche Gesellschaft für Akustik e.V., Mar. 2017.
- [158] S. Johannesmann, J. Düchting, M. Webersen, L. Claes, and B. Henning. “An acoustic waveguide-based approach to the complete characterisation of linear elastic, orthotropic material behaviour”. In: *tm - Technisches Messen* 85.7 (July 2018). DOI: 10.1515/teme-2017-0132.

- [159] M. Webersen, S. Johannesmann, J. DÜchting, L. Claes, and B. Henning. “Guided ultrasonic waves for determining effective orthotropic material parameters of continuous-fiber reinforced thermoplastic plates”. In: *Ultrasonics* 84 (Mar. 2018). DOI: 10.1016/j.ultras.2017.10.005.
- [160] F. Schöpfer, F. Binder, A. Wöstehoff, T. Schuster, S. v. Ende, S. Föll, and R. Lammering. “Accurate determination of dispersion curves of guided waves in plates by applying the matrix pencil method to laser vibrometer measurement data”. In: *CEAS Aeronautical Journal* 4.1 (Apr. 2013). DOI: 10.1007/s13272-012-0055-7.
- [161] C. Prada, O. Balogun, and T. W. Murray. “Laser-based ultrasonic generation and detection of zero-group velocity Lamb waves in thin plates”. In: *Applied Physics Letters* 87.19 (Nov. 2005). DOI: 10.1063/1.2128063.
- [162] D. Clorennec, C. Prada, D. Royer, and T. W. Murray. “Laser impulse generation and interferometer detection of zero group velocity Lamb mode resonance”. In: *Applied Physics Letters* 89.2 (July 2006). DOI: 10.1063/1.2220010.
- [163] G. S. Settles. *Schlieren and Shadowgraph Techniques: Visualizing Phenomena in Transparent Media*. Springer-Verlag, 2001.
- [164] W. Stößel. *Fourieroptik: Eine Einführung*. Springer-Verlag, 1993. DOI: 10.1007/978-3-662-01618-3.
- [165] C. Unverzagt, S. Olfert, and B. Henning. “A new method of spatial filtering for Schlieren visualization of ultrasound wave fields”. In: *Physics Procedia* 3.1 (Jan. 2010). DOI: 10.1016/j.phpro.2010.01.120.
- [166] L. Chen, S. J. Rupitsch, J. Grabinger, and R. Lerch. “Quantitative reconstruction of ultrasound fields in optically transparent isotropic solids”. In: *IEEE Transactions on Ultrasonics, Ferroelectrics, and Frequency Control* 61.4 (Apr. 2014). DOI: 10.1109/TUFFC.2014.2956.
- [167] S. Tietze and G. Lindner. “Visualization of the interaction of guided acoustic waves with water by light refractive vibrometry”. In: *Ultrasonics* 99 (Nov. 2019). DOI: 10.1016/j.ultras.2019.105955.
- [168] L. Chen, S. J. Rupitsch, and R. Lerch. “A reliability study of light refractive tomography utilized for noninvasive measurement of ultrasound pressure fields”. In: *IEEE Transactions on Ultrasonics, Ferroelectrics and Frequency Control* 59.5 (May 2012). DOI: 10.1109/TUFFC.2012.2276.
- [169] P. Ploß, S. J. Rupitsch, and R. Lerch. “Extraction of Spatial Ultrasonic Wave Packet Features by Exploiting a Modified Hough Transform”. In: *IEEE Sensors Journal* 14.7 (July 2014). DOI: 10.1109/JSEN.2014.2311160.

- [170] *The Acoustics Module User's Guide - The Convected Wave Equation*. Comsol. 2017.
- [171] X. Jia. "Normal-mode theory of nonspecular phenomena for a finite-aperture ultrasonic beam reflected from layered media". In: *Applied Physics Letters* 70.3 (Jan. 1997). DOI: 10.1063/1.118401.
- [172] L. Cremer. "Über die Analogie zwischen Einfallswinkel und Frequenzproblemen". In: *Arch. Electr. Übertragung* 1 (1947).
- [173] *Chebfun guide*. Pafnuty Publications, 2014.
- [174] H. L. Bertoni and T. Tamir. "Unified theory of Rayleigh-angle phenomena for acoustic beams at liquid-solid interfaces". In: *Applied physics* 2.4 (Oct. 1973). DOI: 10.1007/BF00884205.
- [175] A. Schoch. "Der Durchgang von Ultraschall durch Platten". In: *Il Nuovo Cimento (1943-1954)* 7.2 (Mar. 1950). DOI: 10.1007/BF02784326.
- [176] A. Schoch. "Seitliche Versetzung eines total reflektierten Strahls bei Ultraschallwellen". In: *Acta Acustica united with Acustica* 2.1 (Jan. 1952).
- [177] C. S. Richards, F. Wang, W. C. Becker, and M. A. Edwards. "A 21st-Century Perspective on Calcium Carbonate Formation in Potable Water Systems". In: *Environmental Engineering Science* 35.3 (Mar. 2018). DOI: 10.1089/ees.2017.0115.
- [178] E. Sarver, Y. Zhang, and M. Edwards. "Review of Brass Dezincification Corrosion in Potable Water Systems". In: *Corrosion Reviews* 28.3 (2011). DOI: 10.1515/CORRREV.2010.28.3-4.155.
- [179] Deutsches Kupferinstitut. *Kupfer-Zink-Legierungen*. 2007.
- [180] H. Lu, K. Gao, and W. Chu. "Determination of tensile stress induced by dezincification layer during corrosion for brass". In: *Corrosion Science* 40.10 (Oct. 1998). DOI: 10.1016/S0010-938X(98)00063-8.
- [181] J. Rösler, H. Harders, and M. Bäker. *Mechanisches Verhalten der Werkstoffe*. 4th ed. Springer Vieweg, 2012. DOI: 10.1007/978-3-8348-2241-3.
- [182] N. Bilaniuk and G. S. K. Wong. "Erratum: Speed of sound in pure water as a function of temperature [J. Acoust. Soc. Am. 93, 1609–1612 (1993)]". In: *The Journal of the Acoustical Society of America* 99.5 (May 1996). DOI: 10.1121/1.415224.
- [183] N. Bilaniuk and G. S. K. Wong. "Speed of sound in pure water as a function of temperature". In: *The Journal of the Acoustical Society of America* 93.3 (Mar. 1993). DOI: 10.1121/1.406819.

- [184] L. Cohen. "Time-frequency distributions-a review". In: *Proceedings of the IEEE* 77.7 (July 1989). DOI: 10.1109/5.30749.
- [185] T. Burgschneider. "Vermessung temperaturabhängiger Materialkonstanten mittels Lamb-Wellen". Bachelor Thesis. Erlangen: University of Erlangen-Nürnberg, June 2020.
- [186] K. Xu, P. Laugier, and J.-G. Minonzio. "Dispersive Radon transform". In: *The Journal of the Acoustical Society of America* 143.5 (May 2018). DOI: 10.1121/1.5036726.
- [187] M. Mazzotti, A. Marzani, and I. Bartoli. "Dispersion analysis of leaky guided waves in fluid-loaded waveguides of generic shape". In: *Ultrasonics* 54.1 (2014). DOI: 10.1016/j.ultras.2013.06.011.
- [188] *Datasheet CuZn37*. Deutsches Kupferinstitut. 2005.
- [189] *Calcite Optical Material Datasheet*. Crystran Ltd. 2011.
- [190] *Datasheet stainless steel X6CrNiMoTi7-12-2*. Lucefin S.p.A. 2018.

Publications

Journal articles

- [P1] M. Wormser, D. A. Kiefer, S. J. Rupitsch, and C. Körner. “Comparison of Transmission Measurement Methods of Elastic Waves in Phononic Band Gap Materials”. In: *Materials* 14.5 (Feb. 2021). DOI: 10.3390/ma14051133.
- [P2] M. Ponschab, D. A. Kiefer, and S. J. Rupitsch. “Simulation-Based Characterization of Mechanical Parameters and Thickness of Homogeneous Plates Using Guided Waves”. In: *IEEE Transactions on Ultrasonics, Ferroelectrics, and Frequency Control* 66.12 (Dec. 2019). DOI: 10.1109/TUFFC.2019.2933699.
- [P3] D. A. Kiefer, M. Ponschab, S. J. Rupitsch, and M. Mayle. “Calculating the full leaky Lamb wave spectrum with exact fluid interaction”. In: *The Journal of the Acoustical Society of America* 145.6 (June 2019). DOI: 10.1121/1.5109399.
- [P4] D. A. Kiefer, M. Fink, and S. J. Rupitsch. “Simultaneous Ultrasonic Measurement of Thickness and Speed of Sound in Elastic Plates Using Coded Excitation Signals”. In: *IEEE Transactions on Ultrasonics, Ferroelectrics, and Frequency Control* 64.11 (Nov. 2017). DOI: 10.1109/TUFFC.2017.2746900.

Submitted:

- [P5] D. A. Kiefer, M. Ponschab, and S. J. Rupitsch. “From Lamb waves to quasi-guided waves: On the wave field and radiation of elastic and viscoelastic plates”. submitted for publication. DOI: 10.13140/RG.2.2.32631.44968.

Conference proceedings

- [P6] M. Ponschab, L. Petzold, D. A. Kiefer, and S. J. Rupitsch. “Guided Wave Based Characterization of Mechanical Parameters and Wall Thickness of Metal Tubes”. In: *SMSI 2020 - Measurement Science*. June 2020. DOI: <http://dx.doi.org/10.5162/SMSI2020/D6.3>.
- [P7] M. Ponschab, D. A. Kiefer, and S. J. Rupitsch. “Towards an Inverse Characterization of Third Order Elastic Constants Using Guided Waves”. In: *2019 IEEE International Ultrasonics Symposium (IUS)*. Glasgow, Oct. 2019. DOI: 10.1109/ULTSYM.2019.8926294.

- [P8] M. Ponschab, D. A. Kiefer, and S. J. Rupitsch. “Berechnung der Auswirkung mechanischer Spannungen auf die Ausbreitung von Lamb-Wellen”. In: *Fortschritte der Akustik - DAGA 2019*. Rostock: Deutsche Gesellschaft für Akustik e.V., Mar. 2019.
- [P9] D. A. Kiefer, M. Ponschab, and S. J. Rupitsch. “Berechnung der vollständigen Dispersionscharakteristik von abstrahlenden Lambwellen mittels Variablentransformation”. In: *Fortschritte der Akustik - DAGA 2019*. Rostock: Deutsche Gesellschaft für Akustik e.V., Mar. 2019.
- [P10] M. Ponschab, D. A. Kiefer, and S. J. Rupitsch. “The Influence of Temperature on the Frequency Dependent Directivity of Ultrasonic Transducers - An Indirect Acquisition Technique”. In: *Sensors and Measuring Systems; 19th ITG/GMA-Symposium*. Nuremberg: VDE Verlag GmbH, June 2018.
- [P11] D. A. Kiefer, M. Ponschab, and S. J. Rupitsch. “Berechnung der Abstrahldämpfung in ebenen Wellenleitern aufgrund eines angrenzenden Fluids”. In: *Fortschritte der Akustik - DAGA 2018*. Ed. by B. Seeber. Munich: Deutsche Gesellschaft für Akustik e.V., Mar. 2018.
- [P12] D. A. Kiefer, M. Fink, and S. J. Rupitsch. “Simultane Bestimmung der Plattendicke und Schallgeschwindigkeit mit codierten Ultraschallsignalen”. In: *Tagungsband Innovation Messtechnik*. Ed. by B. G. Zagar. Vol. 5. Vienna: Shaker Verlag, Nov. 2017.

Presentations

- [P13] D. A. Kiefer, M. Ponschab, and S. J. Rupitsch. *Geführte Wellen in fluidgekoppelten Platten (Guided waves in fluid-coupled plates)*. Presentation. 5. Doktorandentreffen – Akustische Wellenleiter. Delbrück, Germany, Oct. 2019.
- [P14] D. A. Kiefer, M. Ponschab, and S. J. Rupitsch. *Calculating the full leaky Lamb wave dispersion characteristics*. Presentation. 177th ASA Meeting. Louisville, KY, USA, May 2019. DOI: 10.1121/1.5101549.
- [P15] D. A. Kiefer, M. Ponschab, and S. J. Rupitsch. *Berechnung der vollständigen Dispersionscharakteristik von abstrahlenden Lambwellen mittels Variablentransformation (Calculation of the full dispersion characteristics of leaky Lamb waves using a change of variables)*. Presentation. DAGA 2019 – 45. Deutsche Jahrestagung für Akustik. Rostock, Mar. 2019.

- [P16] D. A. Kiefer, M. Ponschab, and S. J. Rupitsch. *Berechnung der Abstrahldämpfung in ebenen Wellenleitern aufgrund eines angrenzenden Fluids (Calculation of the attenuation of waves in a plane waveguide due to radiation into an adjacent fluid)*. Presentation. DAGA 2018 – 44. Deutsche Jahrestagung für Akustik. Munich, Mar. 2018.
- [P17] D. A. Kiefer, M. Fink, and S. J. Rupitsch. *Simultane Bestimmung der Plattendicke und Schallgeschwindigkeit mit codierten Ultraschallsignalen (Simultaneous determination of plate thickness and speed of sound using coded ultrasonic signals)*. Presentation. DEGA-Workshop „Schallfeldbasierte Messverfahren - vom Transducer bis zur praktischen Anwendung“. Drübeck, Germany, July 2017.
- [P18] D. A. Kiefer, M. Fink, and S. J. Rupitsch. *Simultane Bestimmung der Plattendicke und Schallgeschwindigkeit mit codierten Ultraschallsignalen (Simultaneous determination of plate thickness and speed of sound using coded ultrasonic signals)*. Presentation. Innovation Messtechnik. Vienna, May 2017.

List of supervised student theses

- [S1] J. Freitag. “Entwurf, Aufbau und Verifikation akustischer Hologramme unter Berücksichtigung von Festkörpermechanik (Design, implementation and verification of acoustic holograms considering full solid mechanics)”. Master Thesis. University of Erlangen-Nürnberg, Sept. 2020.
- [S2] L. Vogl. “Messen von Fluideigenschaften mittels der quasi-Scholte Plattenmode (Measurement of fluid properties with the quasi-Scholte plate mode)”. Master Thesis. University of Erlangen-Nürnberg, Aug. 2020.
- [S3] S. Sivanesan. “Simulation und Einsatz räumlicher Lichtmodulatoren für Schlieren-optische Aufnahme von Ultraschall (Simulation and utilization of spatial light modulators for schlieren-optical imaging of ultrasound)”. Master Thesis. University of Erlangen-Nürnberg, Aug. 2020.
- [S4] H. Dai. “Messen der Dispersionskurven geführter Wellen in fluidbelasteten Platten (Measurement of dispersion curves of guided waves in fluid-coupled plates)”. Project Thesis. University of Erlangen-Nürnberg, Feb. 2020.
- [S5] C. Ittner. “Entwurf, Fertigung und Verifikation eines akustischen Hologramms (Design, fabrication and verification of an acoustic hologram)”. Master Thesis. University of Erlangen-Nürnberg, July 2019.
- [S6] O. Umbeer. “Messung der Dispersionskurven von mechanischen Wellen in einer Platte (Measurement of the dispersion curves of mechanical waves in a plate)”. Master Thesis. University of Erlangen-Nürnberg, July 2019.
- [S7] J. R. Herterich. “Entwurf, Aufbau und Verifikation eines Keilwandlers zur Erzeugung von Lambwellen (Design, implementation and verification of a wedge transducer for Lamb wave generation)”. Master Thesis. University of Erlangen-Nürnberg, Feb. 2019.
- [S8] D. Heilmeyer. “Mikrocontrollerunterstützte Laufzeitmessung von Ultraschallsignalen (Microcontroller-based time of flight measurements of ultrasonic signals)”. Bachelor Thesis. University of Erlangen-Nürnberg, Oct. 2018.
- [S9] K. Schmid. “Schlierenoptische Messungen zur Abstrahlung von Plattenwellen in ein Fluid (Schlieren-optical imaging of the radiation of plate waves into a fluid)”. Bachelor Thesis. University of Erlangen-Nürnberg, Oct. 2018.

- [S10] L. Vogl. “Simulationsbasierter Entwurf, Aufbau und Verifikation eines Elektromagnetisch-akustischen Wandlers zur Erzeugung von Lamb-Wellen (Simulation-based design, implementation and verification of an electromagnetic acoustic transducer for generation of Lamb waves)”. Bachelor Thesis. University of Erlangen-Nürnberg, Apr. 2018.

Table of symbols

Mathematical notation

Example	Meaning	Description
$\stackrel{\text{def}}{=}$	definition	
a	scalar	italic
\mathbf{a}	tensor of order ≥ 1	bold
\underline{a}	vector	single underline
$\underline{\underline{a}}$	matrix	double underline
a_i	fixed index	upright index
a_i	running index: $i \in \{x, y, z\}$	italic index, except: x, y, z
$a_i b_i = \sum_i a_i b_i$	summation convention	repeated dummy index
\mathbf{ab}	dyadic product	e.g., $a_i b_j \mathbf{e}_i \mathbf{e}_j$
$\mathbf{a} \cdot \mathbf{b}$	contraction	dot product
$\mathbf{a} : \mathbf{b}$	double contraction	double dot product
$\mathbf{a} \vdots \mathbf{b}$	triple contraction	triple dot product
$\underline{\underline{a}} \otimes \underline{\underline{b}}$	Kronecker product	
\mathbf{a}^{1342}	permutation of a tensor	$(\mathbf{e}_a \mathbf{e}_b \mathbf{e}_c \mathbf{e}_d)^{1342} = \mathbf{e}_a \mathbf{e}_c \mathbf{e}_d \mathbf{e}_b$
\mathbf{a}^\top	transposition	permutation \mathbf{a}^{21}
$\text{tr } \mathbf{a} = \mathbf{I} : \mathbf{a}$	trace	sum of diagonal elements
$ \mathbf{a} = a$	magnitude of a	vectors only

Mathematical notation (continuation)

Example	Meaning	Description
$\Re a$	real part of a	
$\Im a$	imaginary part of a	
$\arg a$	argument (phase) of a	
a^*	complex conjugation	$(\Re a + i\Im a)^* = \Re a - i\Im a$
$a(x)$	functional dependence of a on x	
$a _x$	evaluate a at x	
dx	differential element	
$d^3\mathbf{x}$	diff. volume element	$d^3\mathbf{x} = dx dy dz$
$\frac{d}{di}$	total derivative w.r.t. i	
$\partial_i a$	partial derivative of a w.r.t. i	$\frac{\partial a}{\partial i}$
$\nabla = \partial_i \mathbf{e}_i$	Nabla operator	$\mathbf{e}_x \partial_x + \mathbf{e}_y \partial_y + \mathbf{e}_z \partial_z$
$\nabla_{\mathbf{k}} = \partial_{k_i} \mathbf{e}_i$	Nabla- \mathbf{k} operator	$\mathbf{e}_x \partial_{k_x} + \mathbf{e}_y \partial_{k_y} + \mathbf{e}_z \partial_{k_z}$
\mathcal{G}	waveguide operator	$\mathbf{e}_x i k_x + \mathbf{e}_y \partial_y + \mathbf{e}_z \partial_z$
$\int_a^b u(x) dx$	integral of u w.r.t. x from a to b	
$\mathcal{F}_x a$	Fourier transform of a w.r.t. x	
$\mathcal{H} a$	Hilbert transform of a w.r.t. t	
\mathbb{R}	set of real numbers	
\mathbb{C}	set of complex numbers	

Mathematical constants

Name	Meaning
$e \approx 2.718\ 28$	Euler's number
$\pi \approx 3.141\ 59$	Archimedes' constant
$i = \sqrt{-1}$	imaginary unit

Common indices and notation

Index	Meaning
a_f	fluid quantity
$\underline{\underline{a}}_d$ or $\underline{\underline{a}}^d$	discretized quantity
\bar{a}	mean value of a
a_{nom}	nominal value of a
a_{ref}	reference value of a
a_m or a^m	measured value of a
a^u, a^d	upstream / downstream quantity a

Signals

Symbol	Meaning	Units
s	signal	e.g., V
S	signal spectrum magnitude	e.g., V s
D	pulse duration	s
B	bandwidth	Hz
g_e	spatial-envelope	1
g_t	time-envelope	1

Unit vectors and tensors, identities

Symbol	Meaning	Comment
δ_{ij}	Kronecker delta	
δ	Dirac delta function	
\mathbf{e}_i	unit directional vector i	
$\mathbf{I} = \delta_{ij}\mathbf{e}_i\mathbf{e}_j$	2nd order unit tensor	

Elastodynamic field and waves

Symbol	Meaning	Units
t	time	s
\mathbf{x}	spatial position vector	m
x, y, z	Cartesian components of \mathbf{x}	m
\mathbf{u}	particle displacement vector	m
\mathbf{v}	particle velocity vector	m/s
\mathbf{j}	linear momentum	kg/(s ² m ²)
\mathbf{T}	stress tensor (2nd order)	N/m ² = Pa
\mathbf{S}	strain tensor (2nd order)	1
\mathbf{f}	volume force density	N/m ³
\mathbf{t}	traction, i.e., force area density	N/m ² = Pa
p	acoustic pressure	N/m ² = Pa
$\bar{\mathbf{p}}$	average power flux density vector	W/m ²
$\mathcal{K}, \mathcal{E}, \mathcal{H}$	kinetic, elastic and total energy density	J/m ³
H	total stored energy	J or J/m
ρ	mass density	kg/m ³
\mathbf{s}	compliance tensor (4th order)	m ² /N
\mathbf{c}	stiffness tensor (2th order)	N/m ² = Pa
λ_L, μ_L	Lamé parameters	N/m ² = Pa
E, ν	Young's modulus, Poisson's ratio	N/m ² = Pa, 1
κ	adiabatic compressibility	m ² /N
Z_f	acoustic wave impedance	kg/(m ² s)

Elastodynamic field and waves (continuation)

Symbol	Meaning	Units
f, ω	frequency, angular frequency	Hz, rad/s
$T = 1/f$	period	s
\mathbf{k}, k	wave vector, wavenumber	rad/m
$\lambda = \frac{2\pi}{k}$	wavelength	m
$\mathbf{s} = \mathbf{k}/\omega$	slowness vector	s/m
φ	phase	rad
c_l, c_t	longitudinal/transverse wave speed	m/s
κ_l, κ_t	homogeneous longitudinal/transverse wavenumber	rad/m
\mathbf{c}_p, c_p	(vectorial) phase velocity	m/s
\mathbf{c}_e, c_e	(vectorial) energy velocity	m/s
\mathbf{c}_g, c_g	(vectorial) group velocity	m/s
\mathbf{D}	Kelvin-Christoffel tensor (2nd order)	e.g., 1/s ²

Waveguide description

Symbol	Meaning	Units
h	thickness	m
k_x	axial wavenumber	rad/m
k_y	transversal wavenumber	rad/m
\mathbf{W}	wave tensor (2nd order)	e.g., 1/s ²
\mathbf{B}	waveguide boundary operator	N/m ³
\mathbf{L}_i	waveguide stiffness operator	N/m ²
γ	QGW eigenvalue	1
\underline{q}	QGW eigenvector	m
$\underline{\underline{Q}}_i$	QGW stiffness operators	N/m ² = Pa
$\underline{\underline{D}}_i$	QGW boundary operators	N/m ² = Pa
$\underline{\underline{G}}_i$	QGW stiffness operators after transform	depends
$\underline{\underline{\Gamma}}_i$	QGW boundary operators after transform	depends
$\overline{P} = \overline{P}_n$	average power flux along the waveguide	W/m
θ	radiation angle	rad
α	radiation rate	1/m
\underline{P}	waveguide BCs matrix	
A, S	antisymmetric and symmetric char. eq.	

Discretization

Symbol	Meaning	Units
$\underline{\underline{D}}_y, \underline{\underline{D}}_{yy}$	differentiation matrices	1/m
$\underline{\underline{I}}_d$	identity matrix on collocation points	1
N	discretization order (number of collocation points)	1

Normal mode theory

Symbol	Meaning	Units
$A_n(x)$	modal envelope along the waveguide	1
$a_n(x)$	axial variations along the waveguide	1
f_{sn}, f_{vn}	surface/volume waveguide source	W/m ²
w	transducer aperture	m
w_p	transducer periodicity length	m

Flow meter

Symbol	Meaning	Units
b	inner pipe width (rectangular)	m
d	inner pipe depth (rectangular)	m
Q	volumetric flow rate	m ³ /s
\bar{v}_A	area average of flow velocity	m/s
\bar{v}_0	ray path average of flow velocity	m/s
Re	Reynolds number	1
ν_f	dynamic viscosity of the fluid	m ² /s
K	flow profile calibration constant	1
L_0, L	ray path length through fluid (without/with) flow	m
l_0	axial propagation distance of beam	m
Δl	axial convection distance	m
D	axial distance between transducers	m
\mathbf{v}_o, v_o	(vectorial) fluid flow velocity	m/s
\mathbf{x}_p	point on wave front	m
\mathbf{v}_p, v_p	(vectorial) ray velocity	m/s
γ	convection angle	rad
τ_f	transit time through the fluid	s
τ_p, τ_e	time of flight (phases, energy)	s
$\Delta\tau_p, \Delta\tau_e$	differential time of flight (phases, energy)	s

Sensitivity analysis

Symbol	Meaning	Units
S	sensitivity of the flow meter	m^3/s^2
Δa	change/perturbation in a	units of a
$a' = a + \Delta a$	perturbed a	
$\epsilon_a = \frac{\Delta a}{a}$	relative deviation in a	1
ϵ_a^b	relative deviation in a due to b	1
p	arbitrary parameter	(any)
$T = T_0 + \Delta T$	temperature	$^{\circ}\text{C}$ or K
$T_0 = 20^{\circ}\text{C}$	reference temperature	$^{\circ}\text{C}$ or K
$\frac{\partial E}{\partial T}$	temperature coefficient of Young's modulus	Pa/K
F, F_{rel}	error function / relative error function	any, 1
σ	standard deviation	any

Glossary

- BC** boundary condition. 42, 48, 72, 82, 83, 85, 87, 88, 119
- EDAT** Elastodynamic Acoustic Toolbox. 37, 59, 81, 90, 128, 155
- EVP** eigenvalue problem. 29, 37, 57–60, 81, 87–90
- FE** finite element. 71, 72, 84, 85, 103, 108, 109, 119
- FFT** fast Fourier transform. 142, 143
- LDV** laser Doppler vibrometer. 91, 95, 96, 98, 99, 139, 140
- PML** perfectly matched layer. 54, 55, 72
- PMMA** poly(methyl methacrylate). 78
- QGW** quasi-guided wave. 39, 51, 53–61, 65, 68, 70–76, 87–90, 96, 98, 100, 103–105, 110, 114–117, 120, 132, 133
- QNM** quasinormal mode. 53
- QS** quasi-Scholte. 65, 68, 69, 73
- SC** spectral collocation. 59, 84, 85, 90
- SH** shear-horizontal. 39–41, 43, 51
- UFM** ultrasonic flow metering. 1–4, 7, 8, 19, 35, 105, 107–109, 111, 112, 120, 121, 123, 128–130, 132, 136–139, 143–146, 148, 149

A non-invasive ultrasonic flow meter is studied for which the pipe remains unperforated and without obstructions in its interior. Elastic waves that are excited inside the pipe wall interact with the adjacent fluid to form quasi-guided waves. These can be either of leaky or trapped kind. The radiation of the leaky waves is exploited to insonify the pipe's interior. The quasi-guided waves are studied in-depth with particular emphasis on their radiation behavior. Highly reliable and efficient computational methods are developed for this purpose. The ultrasonic transit time in the flow meter is modeled systematically based on the aforementioned waves. Thereby, the effects of fluid flow and temperature are included explicitly in an analytical manner. Compared to conventional ultrasonic flow meters, we find that devices based on quasi-guided waves exhibit a strongly reduced cross-sensitivity to temperature, which is also confirmed experimentally. The developed analytical and numerical techniques enable a systematic optimization of such devices with regard to their temperature-dependent behavior, geometrical uncertainties, material aging, as well as scaling and deposition of other layers.

